

Measurements and modelling of residual stresses during quenching of thick heat treatable aluminium components in relation to their precipitation state

THÈSE N° 6559 (2015)

PRÉSENTÉE LE 6 MARS 2015

À LA FACULTÉ DES SCIENCES ET TECHNIQUES DE L'INGÉNIEUR
LABORATOIRE DE SIMULATION DES MATÉRIAUX
PROGRAMME DOCTORAL EN SCIENCE ET GÉNIE DES MATÉRIAUX

ÉCOLE POLYTECHNIQUE FÉDÉRALE DE LAUSANNE

POUR L'OBTENTION DU GRADE DE DOCTEUR ÈS SCIENCES

PAR

Nicolas Paul Henry CHOBAUT

acceptée sur proposition du jury:

Prof. P. Muralt, président du jury
Dr J.-M. Drezet, Dr D. Carron, directeurs de thèse
Dr J. Cugnoni, rapporteur
Prof. O. Keßler, rapporteur
Prof. M. Perez, rapporteur



ÉCOLE POLYTECHNIQUE
FÉDÉRALE DE LAUSANNE

Suisse
2015

« Je prends beaucoup plus de plaisir à m'instruire moi-même
que non pas à mettre par écrit le peu que je sais. »
René Descartes

ACKNOWLEDGEMENTS

This work is funded by the Competence Center for Materials Science and Technology (<http://www.ccmx.ch/>) involving EPF Lausanne, PSI Villigen, Univ. Bretagne-Sud Lorient, Constellium and ABB Turbosystems AG. The Gleeble 3500 machine of Université de Bretagne-Sud was co-financed by European Regional Development Fund (ERDF). The Institut Laue-Langevin (ILL) in France, the Swiss Spallation Neutron Source (SINQ) in Switzerland and the Forschungs-Neutronenquelle Heinz Maier-Leibnitz (FRM II) in Germany are gratefully acknowledged for neutron beam time.

On top of the above mentioned institutes and companies, I would like to thank:

- my PhD committee for accepting to review my work: Prof. Paul Murali (EPFL), Prof. Michel Perez (INSA Lyon), Prof. Olaf Keßler (Univ. Rostock) and Dr. Joël Cugnoni (EPFL).
- Prof. Michel Rappaz (EPFL) for having given to me the opportunity to perform this PhD in his group at LSMX (Laboratoire de simulation des matériaux),
- my thesis director and principal investigator of this CCMX project, Prof. Jean-Marie Drezet (LSMX), for allowing me to work alongside him and for his guidance,
- my thesis co-director Dr. Denis Carron (Univ. Bretagne Sud), for his expertise in thermo-mechanical tests, for his countless work on DSC and Gleeble measurements and for fruitful discussions,
- Sylvie Arsène and Dr. Christophe Sigli (Constellium C-TEC, Voreppe) for their great interest and expertise in residual stresses and precipitation,
- Dr. Peter Sälzle (ABB Turbo Systems Ltd.) for his deep involvement in the project and for the supervision of many tasks including temperature measurements, heat treatments and FE simulations,
- Prof. Philippe Pilvin (Univ. Bretagne-Sud) for providing SiDoLo software and for fruitful discussions,
- Dr. Muriel Carin and Prof. Philippe Le Masson (Univ. Bretagne-Sud) for their expertise in heat transfer modelling,
- Prof. Jon Danzig (LSMX and Univ. Illinois) for his wise advice especially on inverse methods,
- Jean Costa and William Berckmans (Univ. Bretagne-Sud) for the instrumentation of the Gleeble specimens and technical help during the Gleeble tests,
- the team of the ATMX workshop (atelier de l'institut des matériaux) of EPFL for their irreproachable machining work,
- Prof. Andreas Mortensen (EPFL) and his group for having given to me access to the facilities of his laboratory,

- beamline scientists Thilo Pirling (SALSA, France), Dr. Michael Hoffman (STRESS-SPEC, Germany) and Dr. Vadim Davydov (POLDI, Switzerland) for technical help during neutron diffraction experiments,
- Dr. Julia Repper (PSI) for her work on the measurement of residual stresses in forgings by neutron diffraction,
- my bachelor/master students Leonard Antoinat (Ecole des Mines d'Albi), Gunnar Steinberg (KIT), Emanuel Ris (EPFL) and Gilles Michel (EPFL) for their kind and active commitment,
- all my colleagues for their support, especially Christophe Mondoux (LSMX) for having supported me during the last four years in the same office and Anne Roy (LSMX) for the administrative aspects.

My last thanks go to my friends and my family, who made all this possible, and also to the woman I love for her incommensurable help during every second of my PhD time.

ABSTRACT

In the fabrication of heat treatable aluminium parts, solutionising and quenching are key steps in order to obtain the required mechanical characteristics. Fast quenching is necessary to avoid coarse precipitation as this one reduces the mechanical properties after heat treatment. However fast quenching gives birth to high residual stresses, which cause unacceptable distortions during machining and can reduce service life drastically. For this reason, plates and forgings such as those considered in this thesis are subjected to a stress relieving operation, removing most of the residual stresses after quenching. For thick products, fast quenching throughout the thickness is no longer possible owing to the high but still limited thermal diffusivity of aluminium alloys, but residual stress occurrence remains problematic.

The objective of this work is to develop a comprehensive model of quenching including precipitation effects for understanding the development of residual stresses in thick heat treatable aluminium components.

Two industrial contexts are studied in this work:

- the cold-water quenching of hot-rolled AA7040 and AA7449 thick plates for aerospace applications,
- the boiling-water quenching of large AA2618 compressor wheel forgings used in turbochargers.

Besides an accurate knowledge of the thermal field in the components during quenching, this work has involved an extensive thermo-mechanical characterisation of the three alloys in different precipitation states by interrupted quench-tests achieved in a Gleeble machine. Plastic strain recovery at high temperature is considered in a simple way in the description of the material behaviour and the Bauschinger effect is neglected as suggested by dedicated experiments. Three numerical models are developed to predict as-quenched residual stresses:

- a thermo-mechanical model ignoring precipitation,
- a physically-based thermo-metallurgical-mechanical model where a yield strength model is coupled with a precipitation model,
- a thermo-mechanical model accounting for precipitation in a simple but realistic way. Instead of modelling precipitation that occurs during quenching, the model parameters are identified using a limited number of tensile tests achieved after representative interrupted cooling paths in a Gleeble machine.

The results are compared to as-quenched residual stress measurements achieved by neutron diffraction and layer removal in thick AA7449 and AA7040 plates and in large AA2618 forgings. The thermo-mechanical model ignoring precipitation is found to be sufficient for relatively thin products. For thicker products, precipitation hardening by small precipitates is found to increase as-quenched residual stresses. Since the thermo-mechanical model ignoring precipitation underestimates these residual stresses, precipitation must thus be accounted for.

The second model gives an excellent agreement between measurements and simulations provided that the precipitation model is well calibrated. This physically-based

model is necessary for modelling complex parts with different thicknesses. Nevertheless, a lot of effort has to be dedicated to the characterisation and modelling of the precipitation of metastable non-stoichiometric phases and GP zones during quenching. This tedious work is not needed for the third model which requires only a few interrupted quench-tests while giving an excellent agreement between measurements and simulations for all the investigated components. In particular, it is verified that the two models taking into account precipitation give identical residual stress profiles in thick AA7449 plates.

Keywords: aluminium alloys, quenching, residual stresses, precipitation, solid solution strengthening, Gleeble machine, interrupted quench, neutron diffraction, resistivity, differential scanning calorimetry, finite element modelling, inverse method.

RÉSUMÉ

Lors des différentes étapes du cycle de fabrication de pièces en alliage d'aluminium à durcissement structural, le traitement de mise en solution et la trempe sont des étapes primordiales pour l'obtention des caractéristiques mécaniques désirées. Une trempe rapide est nécessaire pour éviter de former des précipités grossiers car ceux-ci diminuent les propriétés mécaniques après traitement thermique. Cependant, une trempe rapide donne naissance à des contraintes résiduelles élevées qui peuvent conduire à des distorsions géométriques sévères pendant usinage et à une durée de vie considérablement amoindrie. Ainsi, la trempe est suivie d'une étape visant à réduire la plus grande partie des contraintes résiduelles, telle que le détensionnement pour des tôles. Pour des produits épais, une trempe rapide dans toute l'épaisseur n'est plus possible en raison de la conductivité thermique élevée mais limitée des alliages d'aluminium.

Cette étude vise à comprendre la genèse des contraintes résiduelles lors de la trempe de produits épais en alliages d'aluminium à durcissement structural. L'objectif est de prendre en compte les phénomènes physiques présents lors de la trempe, notamment la précipitation, afin de prédire l'état de contraintes résiduelles dans des produits épais.

Deux problématiques industrielles sont considérées :

- la trempe en laboratoire de tôles épaisses d'alliages d'aluminium de la série 7xxx principalement utilisées dans l'aéronautique,
- la trempe industrielle de pièces forgées de grande taille utilisées dans des turbo-compresseurs.

En plus d'une bonne connaissance du champ thermique dans les pièces étudiées, l'étude a nécessité une campagne de caractérisation thermo-mécanique conséquente des trois alliages dans différents états de précipitation au moyen de trempes interrompues réalisées à l'aide d'une machine Gleeble.

Le phénomène de non-cumulation de la déformation plastique à haute température est pris en compte de manière simplifiée dans l'équation constitutive décrivant le comportement mécanique du matériau. L'effet Bauschinger est négligé comme suggéré par des essais dédiés montrant le faible écrouissage cinématique pendant la trempe.

Trois modèles numériques sont développés afin de prédire les contraintes résiduelles à l'état brut de trempe:

- un modèle thermo-mécanique ne tenant pas compte de la précipitation,
- un modèle thermo-métallurgique-mécanique physique couplant un modèle de limite élastique à un modèle de précipitation.
- un modèle thermo-mécanique prenant en compte la précipitation de façon simple mais réaliste. Au lieu de modéliser la précipitation durant la trempe, les paramètres du modèle sont identifiés en utilisant un nombre limité d'essais mécaniques. Ceux-ci sont effectués après des trempes interrompues représentatives de chemins de refroidissement réels reproduits dans la machine Gleeble.

Les contraintes résiduelles simulées sont comparées aux mesures réalisées par diffraction neutronique et méthode du barreau à l'état brut de trempe sur des tôles épaisses en alliages d'aluminium 7449 et 7040 et sur des pièces forgées en alliage d'aluminium 2618.

Le modèle thermo-mécanique ne tenant pas compte de la précipitation se révèle suffisant pour des produits relativement minces. Pour des produits plus épais, le durcissement par formation de précipités fins mène à une augmentation des contraintes résiduelles à l'état brut de trempe. Pour les produits épais, la précipitation doit donc être prise en compte car un modèle thermo-mécanique sans précipitation sous-estime les contraintes résiduelles.

Le deuxième modèle fournit un excellent accord entre les contraintes résiduelles mesurées et simulées pourvu que le calage du modèle de précipitation soit satisfaisant. Ce modèle physique est nécessaire pour modéliser la trempe de pièces de formes complexes présentant des épaisseurs variables. Néanmoins, la mise au point du modèle de précipitation nécessite beaucoup d'efforts de caractérisation et de modélisation de la précipitation des phases métastables non-stœchiométriques et des zones GP pendant la trempe. Ce travail fastidieux n'est pas nécessaire pour le troisième modèle qui ne requiert que quelques essais de caractérisation mécanique en trempe interrompue. De plus, cette approche simplifiée fournit un excellent accord entre les contraintes résiduelles mesurées et simulées pour toutes les pièces étudiées. En particulier, il est vérifié que les deux modèles prenant en compte la précipitation donnent des profils de contraintes résiduelles identiques dans des tôles épaisses en alliage 7449.

Mots-clés : alliages d'aluminium, trempe, contraintes résiduelles, précipitation, durcissement par solution solide, machine Gleeble, trempe interrompue, diffraction neutronique, résistivité, calorimétrie différentielle à balayage, modélisation par éléments finis, méthode inverse.

CONTENTS

1. Introduction and context	13
1.1. Contexts, motivation and objective	14
1.2. General literature review	16
1.2.1. Literature survey on quench induced residual stresses	16
1.2.2. Precipitation in the investigated heat treatable aluminium alloys	19
1.3. Thesis outline	24
2. Materials, heat transfer and RS measurements.....	27
2.1. Materials	27
2.2. Quenching of industrial parts.....	29
2.2.1. Literature review on heat transfer during quenching.....	29
2.2.2. Quenching of plates by vertical immersion in 20°C water	31
2.2.3. Quenching of large forging in boiling water.....	33
2.3. Measurement of residual stress by layer removal.....	37
2.3.1. Principle of the layer removal method	37
2.3.2. Results for a 75 mm thick AA7449 plate.....	38
2.4. Measurement of residual stress by neutron diffraction	39
2.4.1. Principle	39
2.4.2. Experimental campaign of residual strain measurements by ND	42
2.4.3. Results in as-quenched thick plates	47
2.4.4. Results in forgings.....	49
2.5. Summary of chapter 2	54
3. Characterisation and modelling of precipitation during quenching	55
3.1. State of the art	55
3.1.1. Differential scanning calorimetry	55
3.1.2. Resistivity.....	56
3.1.3. Small Angle X-ray Scattering	57
3.2. Precipitation kinetics in AA2618 by DSC	61
3.2.1. Principle and setup.....	61
3.2.2. Results.....	64
3.3. Precipitation kinetics in AA2618 by <i>in situ</i> resistivity	68
3.3.1. Experimental procedure	68
3.3.2. Results.....	69
3.4. Modelling precipitation.....	74
3.4.1. Precipitation model.....	74
3.4.2. Identification of precipitation model parameters for <i>S</i> phase in AA2618....	75
3.5. Summary of chapter 3	80
4. Thermo-mechanical behaviour	81
4.1. State of the art	81
4.1.1. Phenomenological models	81
4.1.2. Physically-based models.....	84
4.1.3. Temperature dependence of yield strength	90
4.1.4. Conclusion and limitation of previous works	93
4.2. Thermo-mechanical testings in the Gleeble.....	95
4.2.1. Gleeble thermo-mechanical simulator and sample configuration.....	95
4.2.2. Requirements and setup for Gleeble tests	96
4.2.3. Identification using SiDoLo	98
4.3. Results and discussion.....	102
4.3.1. Fast interrupted quenches on AA7449, AA7040 and AA2618	102
4.3.2. Evolution of yield strength	105
4.3.3. Mechanical behaviour of AA7449.....	107

4.3.4.	Identification of model parameters	116
4.3.5.	Behaviour after coolings similar to the industrial ones.....	119
4.3.6.	Identification of the parameters of the yield strength model.....	123
4.3.7.	Determination of onset of accumulation of inelastic deformation	133
4.4.	Summary of chapter 4.....	136
5.	RS predictions by finite element simulations	137
5.1.	Thermo-mechanical models of quenching.....	137
5.1.1.	Cold-water quenching of thick plates	137
5.1.2.	Boiling-water quenching of forgings	141
5.2.	RS predictions using the TM model without precipitation	142
5.2.1.	As-quenched thick plates	142
5.2.2.	As-quenched forgings	144
5.3.	RS predictions with precipitation	148
5.3.1.	Taking into account precipitation without precipitation model	148
5.3.2.	Taking into account precipitation with a precipitation model: TMM model with one-way coupling.....	152
5.3.3.	Application of the TMM model to thicker AA7449 plates	156
5.4.	Summary of chapter 5.....	157
6.	Conclusion and perspectives	159
6.1.	Conclusion	159
6.2.	Perspectives	161
7.	Appendixes	162
7.1.	Properties of 2618, 7040 and 7449 alloys	162
7.2.	Choice of NGV for RS measurements by ND.....	164
7.3.	Principle of parameter identification by SiDoLo	166
7.4.	Gleeble specimen geometries.....	169
7.5.	Influence of presolutionising and sampling on flow stress	178
7.6.	Gleeble results for AA7040	180
7.6.1.	AA7040 at $T \geq 400^{\circ}\text{C}$	180
7.6.2.	AA7040 at $T < 350^{\circ}\text{C}$	183
7.6.3.	AA7040 determination of T_{cum}	185
7.6.4.	Effect of non-monotonic load on RS for AA7040 – Bauschinger effect...	188
7.7.	Gleeble results for AA2618	190
7.7.1.	AA2618 at $T \geq 400^{\circ}\text{C}$	190
7.7.2.	AA2618 at 350°C	191
7.7.3.	AA2618 at $T < 350^{\circ}\text{C}$	192
7.7.4.	AA2618 determination of T_{cum}	194
7.8.	Application of isothermal model to non-isothermal testing.....	198
7.9.	Validation of yield strength model	202
7.10.	Predicted vs measured as-quenched RS in large forging	206
	BIBLIOGRAPHY	208
	ACRONYMS AND ABBREVIATIONS	217
	LATIN CHARACTERS	218
	GREEK CHARACTERS.....	220
	NOTATION	221
	GLOSSARY	222

1. Introduction and context

The present study was carried out in the frame of a CCMX (Competence Center for Material Science and Technology) project involving Ecole Polytechnique Fédérale de Lausanne, PSI Villigen, Université de Bretagne-Sud Lorient and two industrials, Constellium C-TEC, Voreppe and ABB Turbosystems AG, Baden. It deals with measurements and modelling of residual stress (RS) during quenching of thick heat treatable aluminium components. Besides the technological need for better predictions of macroscopic RS in these components, an understanding of the influence of subnanometer-size precipitates on these RS was required. Due to the multi-scale dimension of the work and the fact that three alloys (AA7449, AA7040 and AA2618) were on the agenda, two PhD works were launched together in 2011. The work-sharing between the two PhD works is shown schematically in *Figure 1-1*.

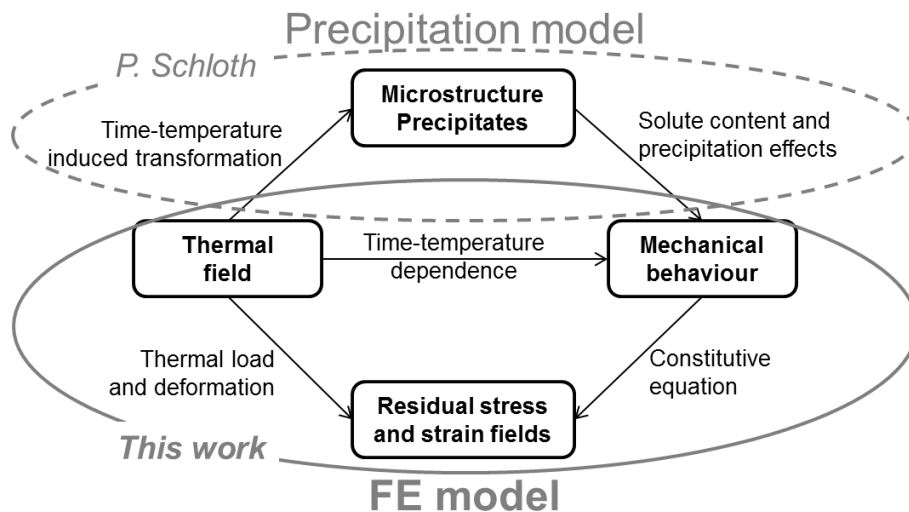


Figure 1-1 – Work-sharing between the PhD work of P. Schloth and this work.

While the present PhD work mainly addresses macroscopic aspects, the second PhD work of P. Schloth focuses on microstructural aspects at lower scales down to the subnanometer, mostly on AA7449. Both works being complementary, they are intimately related and therefore continuously referred to each other. In particular, this work makes use of the findings of P. Schloth in order to account for microstructural aspects in residual stress predictions at the macro-scale.

As will be shown hereafter in the literature survey, the problem addressed here belongs to an extensively studied subject since, even reduced by stress relief, undesirable RS can remain after quenching in large and complex aluminium alloy products. Thus, quench induced RS has been for more than 30 years a favourite subject of many scientists at Ecole des Mines de Nancy, including G. Beck, A. Simon, P. Archambault, S. Denis, E. Aeby-Gautier and D. Godard. In fact, the problem for plates was almost solved in 1999 – at least numerically – in the PhD work of Godard who found out that RS in 7xxx aluminium alloy are mainly influenced by the small precipitates or GP zones which happened to be co-discovered by A. Guinier from Nancy. Therefore, the work of Godard and co-workers will be also referred to many times throughout the present study

1.1. Contexts, motivation and objective

Presentation of the industrial contexts

Constellium, the largest supplier of aluminium plates in Europe, owe their leadership to the continuous development and design of new aluminium alloys at Constellium C-TEC, Voreppe, previously Alcan CRV (Centre de Recherche de Voreppe). Several years of intense research led to a better understanding of the many factors that influence residual stresses and helped to product optimisation and in-service property improvement. Nevertheless the thick plate market is demanding for high strength products having minimal residual stress (reduction of distortion during machining for example) and a better understanding of the interactions between microstructure evolution and stress generation during heat treatment is required to go a step forwards in thick product development. The processing-route for heat treatable aluminium alloy plates is shown schematically in *Figure 1-2*.

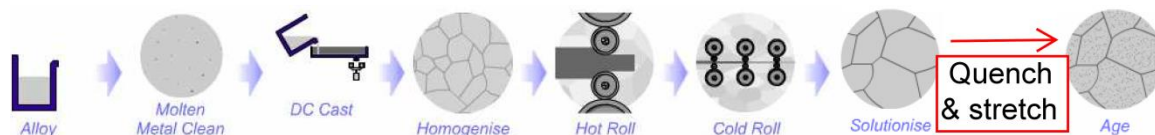


Figure 1-2 – Schematic processing-route for heat treatable aluminium alloys plates. Adapted from <http://aluminium.matter.org.uk/>.

The first steps – casting, homogenising and hot/cold rolling – control the material chemical composition and grain structure. The last steps – solutionising, quenching (focus of this work) and ageing – constitute the age-hardening treatment and control the precipitation state mainly responsible for the mechanical properties. Plates are stretched after quenching for stress relief.

ABB Turbo Systems Ltd. is the worldwide leader in turbocharging diesel and gas engines with power output of 400 kW and above. Turbochargers (*Figure 1-3*) increase the specific power output of engines while reducing their fuel consumption.

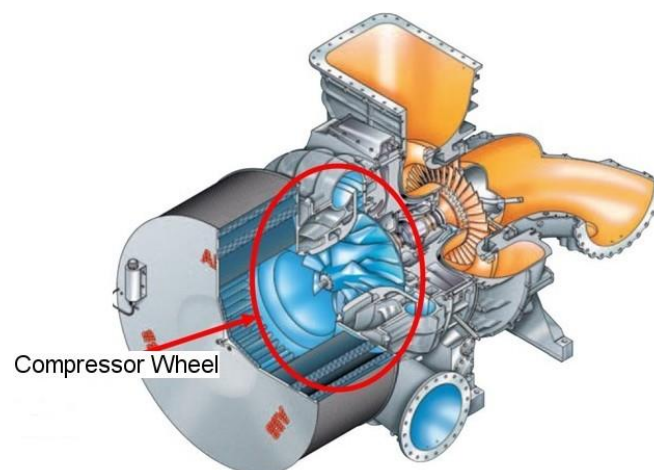


Figure 1-3 – Cut view of a turbocharger with the compressor side in blue and the turbine side in yellow (courtesy of ABB Turbo Systems Ltd.).

Highest performance and operational reliability are achieved by a sophisticated development and production process of the turbocharger components. Special emphasis is given on large compressor wheels (also called impellers) made of the Al-Cu-Mg-based AA2618 alloy owing to its high creep resistance [1]. The size of these parts requires a thorough understanding of the heat treatment process with its implications on residual stresses and material properties. Thereby simulations of this production step are essential in order to achieve both minimum residual stresses and high material strength. Since the turbocharger market asks for even bigger impellers in the future, numerical optimisation of the heat treatment process and the subsequent machining step will become more and more important.

Forgings of different sizes depending on the application are received right after the shaping process by ABB Turbosystems which performs an age-hardening treatment to reach desired mechanical properties. Although very large forgings (up to 1 meter in diameter) are pre-machined before solutionising, the forgings investigated in this work (< 0.6 meters in diameter) are directly subjected to the age-hardening treatment shown schematically in *Figure 1-4*.

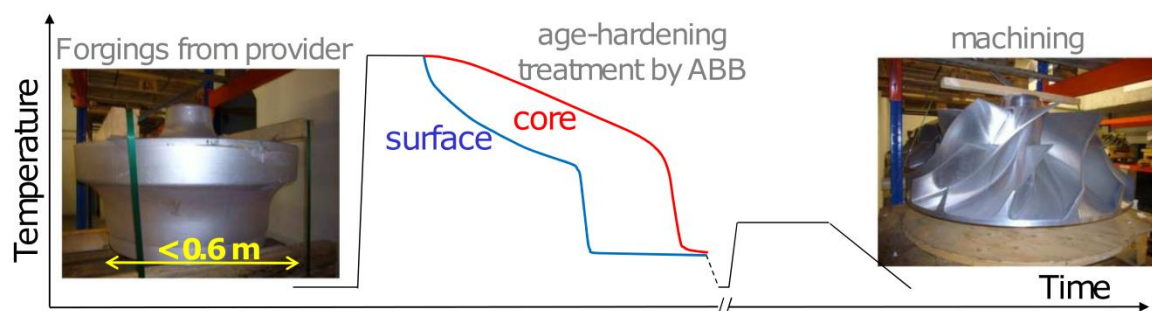


Figure 1-4 – Thermo-mechanical treatment from forgings to impellers performed by ABB (images: courtesy of ABB Turbosystems).

Forgings are solutionised, quenched in boiling water, aged to the desired temper and machined to the final contour.

Motivation

In the fabrication of heat treatable aluminium parts, solutionising – also called solution heat treatment (SHT) – and quenching are key steps in order to obtain the required mechanical characteristics. The SHT objective is to obtain a solid solution at equilibrium. Quenching aims at cooling the material to room temperature as fast as possible to obtain a state at the end of quench called in this work non-equilibrium solid solution (neSS) as close as possible to solid solution at equilibrium before quench. Quenching should thus be fast in order to avoid or limit precipitation. However, high thermal gradients through thickness cause non-homogeneous plastic strain resulting in RS after quenching. Robinson, Tanner and Truman [2] showed that surface RS measured by X-ray diffraction on AA7010 cold-water quenched rectilinear blocks increase when the thickness increases from 16 mm to 124 mm. Quenching is thus followed by a stress relief [2-5]. For plates, this is achieved by stretching which reduces residual stresses by a factor of

approximately 10 as shown by Boyer and Boivin [4] and by Prime and Hill [5]. For forgings, residual stresses are controlled by a pre-machining step before solutionising and by spinning the wheel at high rotation speed after the ageing treatment. The ageing treatment is performed to transform elements in solid solution into fine hardening precipitates and thus increase the yield strength. In thick 7xxx highly alloyed wrought products, even reduced by stress relief, the RS at final temper can lead to distortions during machining of large and complex parts, see for example Dubost *et al.* [6]. Likewise, RS in large forgings can lead to distortions during final machining.

Precipitation phenomena may affect RS. For instance it is well known for thick plates that the cooling during quenching is not fast enough at mid-thickness to prevent any precipitation. This decreases the efficiency of ageing [2] but also may affect the as-quenched yield strength and consequently the RS distribution according to the calculations of Godard and co-workers [7]. In 7xxx alloys, two types of precipitation may occur during quenching depending on the cooling rate, see for instance Dumont *et al.* [8]. For low cooling rates, a first precipitation occurs at intermediate temperature, typically 400-250°C for AA7010 [9] and AA7449 [10]. The large precipitates formed are undesirable since they reduce the amount of elements in solid solution and do not harden the material significantly. A second precipitation occurs at low temperature, typically below 220°C as evidenced by Godard *et al.* [11] for AA7010 and below 300-250°C for AA7449 according to Schloth *et al.* [10]. In the case of 200 mm thick AA7010 water-quenched plates, Godard and co-workers [7] have shown that the resulting effect of these two types of precipitation is an increase of the yield strength at plate surface after quenching compared to that of the neSS.

For the prediction of RS, it is thus important to be able to model the full process and particularly the quenching with consideration of potential precipitation phenomena. It is the first step since a stress relief model has to use RS after quenching as its initial state in a Through Process Modelling.

Objective of this work

With regards to the motivations presented above, the objective of this work is to develop a comprehensive model of quenching including precipitation effects for understanding the development of RS. The result of this work – a model capable of predicting the final properties after quenching of thick heat treatable aluminium components, knowing their history – will be the starting point for both industrial partners Constellium and ABB Turbosystems to improve their processing route for the production of thicker components, according to the desired properties.

1.2. General literature review

1.2.1. Literature survey on quench induced residual stresses

The literature on quenching of heat treatable AA is profuse. An extended technology review is provided by Shuey and Tiryakioglu [12] and a bibliographical review of the finite element (FE) methods applied to the simulation of quenching is given by Mackerle [13].

The latest experimental and numerical state of the art on RS in heat treatable AA is available in a special issue of *Strain* journal in 2014 by Robinson, Tanner and Truman [2] who worked for more than 15 years on this topic and carried out many RS measurements using neutron diffraction (ND).

Phenomena occurring during quenching and their modelling

Quenching of metallic alloys with phase transformations is a thermo-metallurgical-mechanical coupled problem. The interactions between the main phenomena occurring during quenching of metallic alloys are shown schematically in *Figure 1-5*.

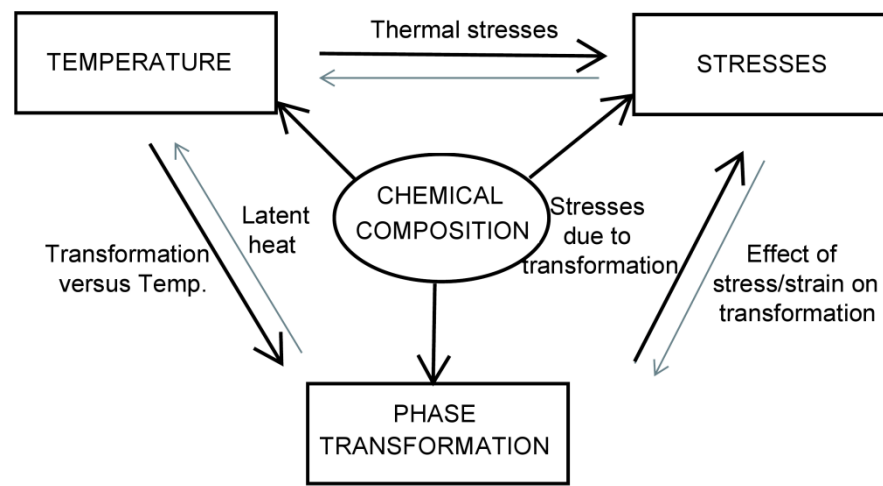


Figure 1-5 – Schematics of the interactions between the main phenomena occurring during quenching of metallic alloys. Light grey arrows indicate weak coupling generally neglected for heat treatable aluminium alloys. Adapted from [14].

The various thermal cooling paths within a component lead to thermal stresses and phase transformations as shown by the thick black arrows starting from the box “temperature” and pointing towards the boxes “stresses” and “phase transformation” respectively. Unlike phase transformations in steels such as martensitic or bainitic transformations [15, 16], precipitation in heat treatable aluminium alloys leads to negligible volume changes [17]. Therefore, the thick black arrow starting from “phase transformation” and pointing towards “stresses” refers only to the variations of mechanical properties induced by precipitation. In heat treatable AA, the heat released by precipitation is low as indicated by the light grey (= weak coupling) arrow starting from “phase transformation” and pointing towards “temperature”. Stresses and strains influence phase transformation as evidenced by Deschamps *et al.* [18] with dynamic precipitation in AA7xxx alloys. However, this is usually neglected (light grey arrow in *Figure 1-5*) during quenching of heat treatable AA due to the low strains (~1%) encountered [17]. The heat associated with deformation is negligible during quenchingⁱ (light grey arrow from “stresses” to “temperature”). Thick black arrows starting from the box “chemical composition” and pointing towards the three other boxes refer to

ⁱ this would not be the case for extrusion at high speed where the die and the extruded part heat up significantly due to large deformation and friction.

microstructural, thermal and mechanical changes due to macrosegregation resulting from solidification.

Thanks to the above mentioned simplifications for quenching of heat treatable AA, a full coupling is not necessary: the one-way coupling temperature→precipitation→stresses is enough and requires two models, a precipitation model and a mechanical model [19]. The general approach to treat precipitation is to use yield strength and strain hardening models where the flow stress depends on the precipitation state calculated by a precipitation model, e.g. as in Deschamps *et al.* [20]. Archambault *et al.* [21] neglected the effect of precipitation on strain hardening and used a physically-based model for the yield strength. This model required an extensive mechanical characterisation of the influence of precipitation on flow stress as shown in the work of Godard *et al.* [22].

The physics behind RS build-up during quenching

The generation of RS in aluminium alloys has been widely studied and many researchers have implemented models to predict RS build-up in thick components [3, 17, 23-26]. A summary of recent finite element (FE) models of quenching is given in Ref. [2]. After quenching, natural ageing is not simulated since RS do not evolve at room temperature. Qualitatively, the core is reported to be in tension and the surface in compression after cooling. This is referred to as the “skin-core” effect [23, 26]. The stress magnitude depends on the quench rate: the higher the quench rate, the higher the RS [25, 27, 28]. The physics of RS build-up is now well understood. During quenching, cooling is not homogeneous. A thermal gradient exists between core and surface, leading to differential thermal deformation accommodated by elastic and plastic deformation to satisfy compatibility of deformation. Whenever the material yields, RS remain after quenching due to irreversibility of plastic deformation. Quenching of thick aluminium plates leads to plastic deformation resulting in surface compressive stresses balanced by core tensile stresses after quench [4]. In the particular case of cold-water quenching of thick plates, the surface deforms plastically at high temperature but also at low temperature as shown by Godard [7] in his PhD work. The magnitude of the surface compressive stress depends thus on the yield strength but also on the plastic deformation accumulated during quenching at the plate surface. The plate mid-thickness area may also deform plastically down to room temperature but less than the surface. Around quarter-thickness, the material straining remains purely elastic at low temperature.

Effect of precipitation during quenching

Precipitation changes the flow stress and as a consequence the generation of residual stresses. For thin plates, a thermo-mechanical model ignoring precipitation is sufficient to predict as-quenched RS satisfactorily. This is because quenching is fast so that precipitation is inhibited and plastic flow does not occur at low temperature [3]. In the case of highly alloyed AA7xxx thick plates, a thermo-mechanical model that does not

account for the increase of yield strength by precipitation hardening underestimates RS as shown in Ref. [29].

Godard and co-workers [7, 17] stated that RS in AA7010 thick plates is influenced by precipitation only when the material experiences plastic deformation. While heterogeneous precipitation slightly lowers residual stresses, homogeneous precipitation leads to an increase of RS [17]. During quenching, it is usually assumed that precipitation only modifies yield strength [7, 17]. The influence of quench rate on strain hardening rate is generally considered to be negligible in comparison to its strong influence on the yield strength [17, 30].

To account for precipitation, a number of techniques that monitor precipitation kinetics have been developed. Besides the direct observation of precipitates by means of microscopy to identify their nature and composition [30], indirect techniques based on the measurement of properties affected by precipitation are available, such as differential scanning calorimetry (DSC), resistivity [12, 31-33], yield strength or toughness [12]. The slower the quench, the higher the solute loss and as a consequence the lower the yield stress reachable after ageing. Indeed, solute trapped in quench-induced precipitates is no longer available for hardening as coarse precipitates do not evolve significantly after quenching [12, 34, 35]. Vacancy density can also be measured to assess the quality of quenching (a perfect quench is associated with a high vacancy concentration). This is the scope of positron annihilation lifetime spectroscopy, a technique mostly used during natural ageing, which measures the lifetime of a positron before being trapped by a vacancy [36].

Residual stress measurements

A wide range of methods are available to measure RS: hole drilling [37], layer removal [3], crack compliance [5], ultrasounds [38], diffraction [39]. These measurements can be used to improve and validate numerical models. For thick components where long penetration paths are required, ND has proved to be a suitable method as aluminium is rather transparent to neutrons. Uncertainties in RS lower than 10 MPa have been obtained [40, 41]. A recent summary of cold-water quenched RS measurements in heat treatable AA plates and forgings found in the literature is given by Robinson, Tanner and Truman [2]. Prime and Hill [5] quenched a hot-rolled 760 × 760 × 78 mm AA7050 plate and measured RS by crack compliance in artificially overaged (not stress relieved) state. Although the in-plane directions were equivalent (width and length equal), residual stresses in the rolling direction were greater (~40%) than in the transverse long direction, mainly due to plastic anisotropy. For non-rolled heat treatable AA quenched plates this plastic anisotropy is not expected.

1.2.2. Precipitation in the investigated heat treatable aluminium alloys

Heat treatable aluminium alloys feature high strengths obtained by the precipitation from a supersaturated solid solution of fine (a few nm) hardenable precipitates of thermodynamically metastable phases. Among the three series featuring age-hardening, 2xxx, 6xxx and 7xxx, this work focuses on 2xxx and 7xxx series with the investigation of:

- Al-Cu-Mg-Fe-Ni forging AA2618 alloy developed for engine components,
- Al-Zn-Mg-Cu AA7040 and AA7449 alloys developed for ultra-thick plates used in the aerospace industry.

In order to obtain the desired mechanical properties, an ageing treatment is performed purposely at temperatures ranging typically from 120°C to 200°C (artificial ageing) as shown in *Figure 1-6* for AA7449 (left) and AA2618 (right).

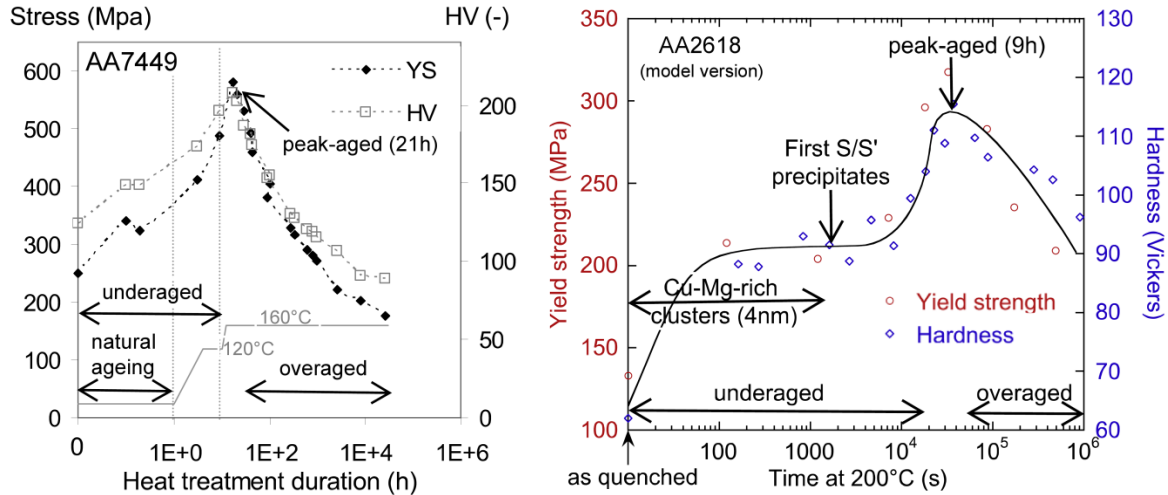


Figure 1-6 – Evolution of yield strength and hardness during ageing treatment of AA7449 (left – adapted from [42]) and AA2618 (right – adapted from [43] with original references given in this paper).

During ageing treatment, yield strength and hardness increase to reach a maximum called peak-aged or T6-temper (or state). This corresponds to the maximal achievable yield strength after perfect quenching. The peak-aged strength (or hardness) being 2-3 times higher than the as-quenched value, heat treatable AA components are usually used in a temper close to T6. For high temperature applications such as turbochargers, T6-state might evolve in-service at long times with a decrease of yield strength due to the formation of coarse precipitates (overaged state). In fact, a slightly overaged state is often preferred to the T6-state to improve the stress corrosion cracking resistance.

The different regimes in the yield strength evolution shown in *Figure 1-6-right* are due to different types of precipitates [43] as explained hereafter. It is also worth mentioning that yield strength increases – to a lesser extent – even at room temperature (natural ageing) [26] as shown in *Figure 1-6-left* for AA7449 and in *Figure 1-8-left* for AA7010.

The role of each alloying element is well described in the literature and shortly described hereafter. The major elements Zn, Mg and Cu are in solid solution during solutionising and form precipitates upon cooling, such as η ($\text{Mg Zn}_{2(1-z)} \text{Cu}_z \text{Al}_z$), S ($\text{Al}_2 \text{Cu Mg}$) and T ($\text{Mg}_{32} (\text{Al}, \text{Zn})_{49}$) phases in AA7xxx and S and θ ($\text{Al}_2 \text{Cu}$) phases in AA2618. These phases are formed from metastable (semi)-coherent precursors labelled by a ' (for example η' or S'). They originate from clusters of solute atoms or GP zones named after their discoverers in 1938, Guinier (1911-2000) and Preston (1896-1972). It is generally acknowledged that the homogeneous precipitation sequence is: clusters/GP zones – metastable (semi)-coherent precursors – incoherent equilibrium precipitates. This is shown schematically in *Figure 1-7*.

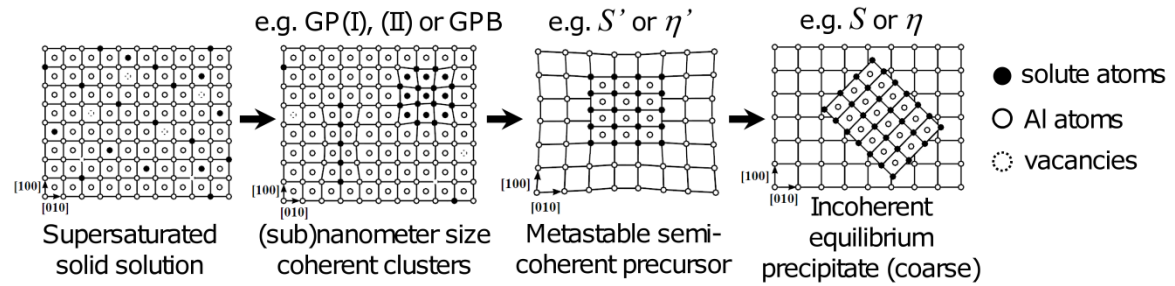


Figure 1-7 – Schematic homogeneous precipitation sequence in heat treatable AA, starting from a supersaturated solid solution obtained after quenching. Adapted from Maisonnnette [44].

The supersaturated solid solution corresponds to the solid solution after solutionising and perfect quenching. Therefore, it is out of thermodynamic equilibrium and very unstable. In this work, the term non-equilibrium solid solution (neSS) is used instead. In *Figure 1-7*, several dashed open symbols at positions of Al atoms can be seen in the first two sketches. They correspond to vacancies “frozen” during quenching. These so-called quench-induced vacancies increase diffusion at low temperature and are believed to be responsible for rapid agglomeration of solute atoms [45] to form clusters or GP zones which are fully coherent with the matrix (second sketch in *Figure 1-7*). Coherent precipitates have the same crystallographic structure as the matrix but different lattice parameters resulting in a slight lattice distortion also represented in *Figure 1-7*. The different names used in the literature for Guinier Preston zones refer to different crystallographic structures. In Al-Cu-Mg alloys such as AA2618, the zones are named GPB after Bagaryatsky who proposed the first structure for the arrangement of Cu and Mg atoms in nanometer-size platelet or rod-like clusters. Debate remains about their exact structure which is still under investigation, see for instance Wang, Starink and Gao [46]. In Al-Zn-Mg-Cu alloys such as AA7449, two types of GP zones have been evidenced in the literature:

- GP(I) zones are spherical (up to 2 nm in diameter) and form between room temperature and 120-150°C. Their exact composition is still debated.
- GP(II) zones are non-spherical Zn-rich clusters forming above 70°C [47].

As precipitates become larger and change in chemical composition, their crystallographic structure changes and the misfit between the two lattices (matrix and precipitate) increases. Coherency is lost in one direction and precipitates are therefore semi-coherent (third sketch in *Figure 1-7*). They are generally considered as the main hardening phases. The last sketch in *Figure 1-7* shows incoherent coarse precipitates which form after long artificial ageing times. While this precipitation sequence applies for temperatures below ca. 250°C, heterogeneous nucleation is favoured at higher temperature with the precipitation of incoherent phases as observed for instance by Godard *et al.* in AA7010 [11] (*Figure 1-8-right*).

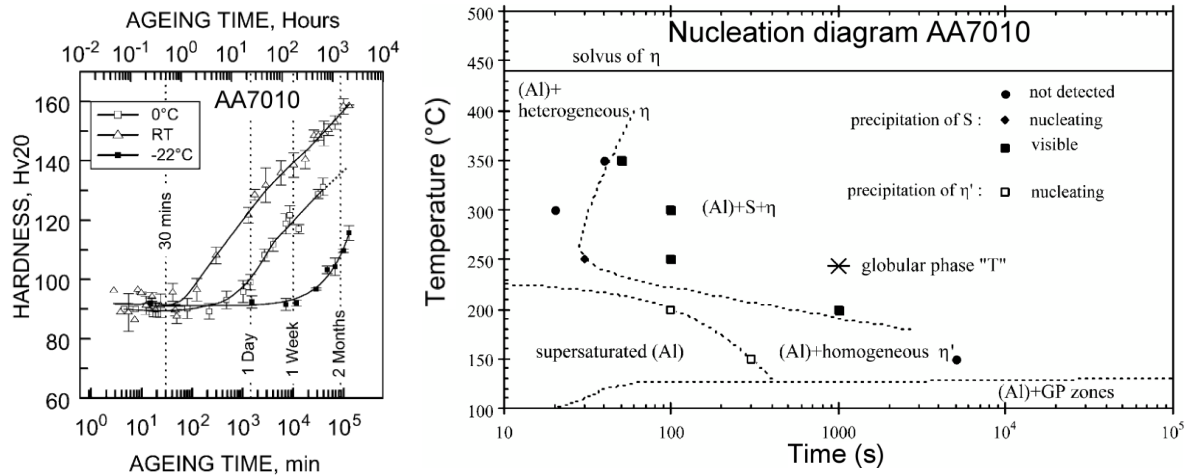


Figure 1-8 – Evolution of hardness after quenching of AA7010 [26] (left). Nucleation diagram of AA7010 determined by Godard *et al.* [11] (right).

Coarse precipitates η (~200 nm in diameter [8]) form when the material explores high temperatures for a too long time (10 sec), i.e. for slow quenching. Since S and T phases form for quenching paths that are rarely encountered in industrial cases (very slow quench), they are usually not considered in precipitation models.

Other alloying elements than Zn, Mg and Cu do not dissolve during solutionising due to their low solubility limit at high temperature. Fe, Si and Ni form large intermetallic precipitates (such as $\text{Al}_7\text{Cu}_2\text{Fe}$ or Mg_2Si) and small precipitates called dispersoids are formed from Cr, Ti and Zr. While the former precipitates are usually avoided by Fe, Si and Ni contents as low as possibleⁱ, the latter are desired since they act as nucleation sites in the subsequent ageing stage.

The composition determines to a great extent the quench-sensitivity of the alloy, related to the drop in strength after ageing due to inadequate quenching. Quench sensitivity is then a relative measure of the solute loss from solid solution when precipitation occurs during slow cooling. It is reported in the literature that high sensitivity is due to high amount of Zn+Mg+Cu elements, low ratio Zn/Mg, presence of Cr instead of Zr elements and high recrystallisation fraction, see for example Liu *et al.* [48]. Hence, AA7449 is more quench sensitive than AA7040 and AA2618. AA7040 has a lower solute content than AA7449 since it has been designed for very thick plates requiring a low quench-sensitivity. Efforts are done to develop and patent alloys with little or no quench-sensitivity [49], a useful tool to assess quench-sensitivity being Time-Temperature-Properties (TTP) diagrams. Robinson *et al.* [35] established by Jominy end quench procedure the time temperature indentation hardness diagram of AA7449 in overaged (6 hours at 120°C followed by 10 hours at 160°C) condition shown in Figure 1-9-left. The continuous cooling precipitation diagram of AA7449 determined in the PhD work of P. Schloth [50] is given in Figure 1-9-right for comparison.

ⁱ though they can help to control grain size and impede dislocation motion. In AA2618, Fe and Ni are added in equal amounts (1.1 wt.%) to reach the maximum age hardening through the formation of Al_3NiFe .

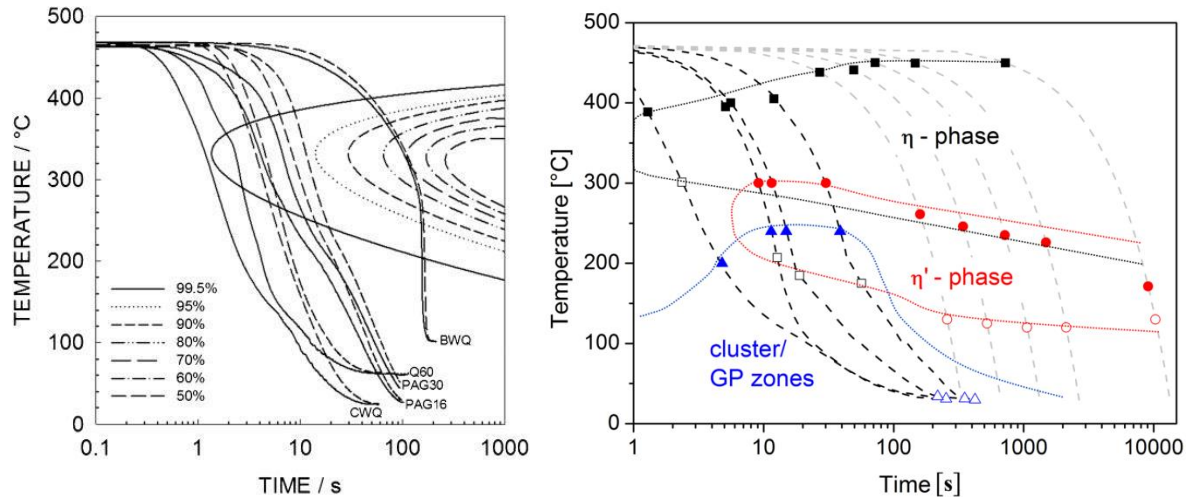


Figure 1-9 – TTP diagram (C-curves) of AA7449 together with various cooling paths; the legend is given in Robinson et al. [51] (left). Continuous cooling precipitation diagram of AA7449 determined by Schloth [50] (right).

Except for boiling water quenching (BWQ), all other coolings shown in Figure 1-9-left lead to a high hardness after ageing. BWQ leads to precipitation of η precipitates at high temperature that decreases matrix supersaturation by pumping solute, and hence decreases the hardening potential (softening). While the TTP diagram in Figure 1-9-left refers to solute pumped mainly by η precipitates, the continuous cooling precipitation diagram in Figure 1-9-right also shows the precipitation domains of η' and GP zones/clusters in AA7449. For low cooling rates, a first precipitation occurs at intermediate temperature, typically 400-250°C for AA7010 [9] and AA7449 [10]. The large precipitates formed are undesirable since they reduce the amount of elements in solid solution and do not harden the material significantly. A second precipitation occurs at low temperature, typically below 220°C for AA7010 (Figure 1-8-right) and below 300-250°C for AA7449 (Figure 1-9-right). In the case of a 200 mm thick AA7010 water-quenched plate, Godard and co-worker [7] have shown that the resulting effect of these two types of precipitation is an increase of the yield strength at plate surface after quenching compared to that of the neSS. To our knowledge, no such diagrams exist in the literature for AA7040 and AA2618 and yet, they are important to know the time-temperature window where precipitates are likely to occur upon cooling, but also to predict the effect of quenching on strength, which is the scope of the Quench Factor Analysis [52].

1.3. Thesis outline

Novelty and focus of this work

Considering the literature survey and the objectives of this work, it is obvious that the novelty of the present work will not be in the FE simulations of stress build-up during quenching of thick components, which are firmly established in the literature. In particular, it is well known that the solution procedure to take into account precipitation in RS simulations is based on a thermo-metallurgical-mechanical model. Initially, the goal of the CCMX project involving two PhD students was to implement such a model. However, this classical approach remained challenging since it requires the calibration of a precipitation and a yield strength model. To achieve this initial goal, an extensive characterisation work was carried out, while keeping an open eye to search for a simpler solution which would not require a coupling with a precipitation model. Eventually, a model accounting for precipitation in a simple way is proposed. This simple model constitutes the major novelty of this work.

Besides this novelty, the main efforts of this work are on the experimental investigation by making use of the latest available techniques in order to characterise residual stresses, precipitation states and mechanical properties for AA7449, AA7040 and AA2618. Thus, special attention is paid to the:

- determination of thermal properties – especially heat transfer coefficients which are difficult to obtain for complex coolings – in order to have an accurate knowledge of the temperature field evolution in the components,
- measurement of RS – delicate for high thicknesses where neutron diffraction (ND) gives poor statistics – in order to validate FE quenching simulations,
- determination of mechanical properties of non-equilibrium solid solutions – challenging for high quench-sensitive alloys – in order to feed thermo-mechanical and thermo-metallurgical-mechanical models.

Detailed contents

Most of the experimental results are given in chapters 2 (Materials, heat transfer and RS measurements), 3 (Characterisation and modelling of precipitation during quenching) and 4 (Thermo-mechanical behaviour) with the exception of the mechanical behaviour of AA7040 and AA2618 given in appendixes 7.6 and 7.7 respectively.

In details, the experimental tasks performed in this work are:

- temperature measurements in thick plates and forgings (part 2.2),
- RS measurement of as-quenched thick AA7449 and AA7040 plates and AA2618 forgings mainly by ND at large scale facilities (part 2.4),
- comparison between neutron diffraction RS measurements from different diffractometers and a destructive technique (part 2.4),
- characterisation of precipitation upon cooling in AA2618 by DSC (part 3.2),

- characterisation of precipitation in AA2618 by isothermal quenching resistivity measurements in a Gleeble machine (part 3.1),
- characterisation of the mechanical behaviour of the three alloys in different precipitation states typical of quenching by thermo-mechanical tests in a Gleeble machine (chapter 4),

This work also refers to the pioneering characterisation of precipitation in AA7449 and AA7040 by *in situ* SAXS measurements performed by P. Schloth [50] in his PhD work (section 3.1.3).

On the numerical part, several optimisations are performed by inverse method, namely:

- identification using Isight of heat transfer coefficients (section 2.2.3) used in chapter 5,
- identification using Matlab of precipitation model parameters for *S* phase in AA2618 (section 3.4.2) – not used in chapter 5,
- identification using SiDoLo of the parameters of a phenomenological constitutive equation for the three alloys (section 4.3.4) – used in chapter 5,

The other (simpler) optimisation problems are either solved by curve fitting (using Origin) or by hand (using the Manipulate function of Mathematica) as for the calibration of the yield strength model (section 4.3.6) used in chapter 5.

The calibration of the precipitation model – considering only GP(I) zones – used in chapter 5 was performed by hand (trial and error) in the work of P. Schloth [50].

All these optimisations make the connection between the measurements given in chapters 2, 3 and 4 and the FE quenching simulations given in chapter 5. This final chapter collects all the information gathered in the previous chapters necessary for the simulations performed using three different models increasing in complexity, namely:

- A Thermo-Mechanical model ignoring precipitation (TM model) – part 5.2,
- A Thermo-Mechanical model taken into account precipitation in a simple-way using a few Gleeble interrupted quench-tests (TMG model) – section 5.3.1,
- A Thermo-Metallurgical-Mechanical model taken into account precipitation using a precipitation model in a one-way coupling temperature→precipitation→stresses (TMM model) – section 5.3.2.

While the FE quenching simulations with the TM and TMG models are performed for AA7449 and AA7040 plates and for AA2618 forgings, those with the TMM model are carried out for AA7449 plates only as summarised in *Table 1-1*.

Model Alloy	TM model Thermo-Mechanical model without precipitation	TMG model Thermo-Mechanical model with precipitation from Gleeble tests	TMM model Thermo-Metallurgical- Mechanical model with precipitation model
AA7449	✓	✓	✓
AA7040	✓	✓	✗
AA2618	✓	✓	✗

Table 1-1 – Overview of the three models used for finite element simulations of quenching in the three investigated alloys. The green symbols and the red crossse indicate the performed simulations and the work left as a perspective respectively.

The conclusion of this manuscript (chapter 6) presents the main results obtained in this work and opens on perspectives.

2. Materials, heat transfer and RS measurements

This chapter presents the materials, their quenching method and the residual stress measurements. While the heat transfer coefficients determined in part 2.2 are input for the simulations of quenching, the RS measurements in parts 2.2 and 2.4 are used for comparison with the predicted as-quenched residual stresses to validate the models used in the simulations.

2.1. Materials

The chemical composition of the three alloys used in this work is given in *Table 2-1* together with their processing temperatures.

Al-balanced	AA2618	AA7040		AA7449	
wt. %	measured	Min	Max	Min	Max
Si	0.2	0.1		0.12	
Fe	1.1	0.13		0.15	
Cu	2.4	1.5	2.3	1.4	2.1
Mn	0.01	0.04		0.20	
Mg	1.55	1.7	2.4	1.8	2.7
Cr	0.004	0.04		-	
Ni	1.1	-		-	
Zn	0.1	5.7	6.7	7.5	8.7
Ti	0.06	0.06		0.25	
Zr	0.001	0.05	0.12		
solutionising (°C)	530	470	490	460	490
quenching (°C)	100	20		20	
artificial ageing treatment	20 hours at 195-200°C	120-160°C		120-160°C	

Table 2-1 – Chemical composition and processing temperatures of the three investigated alloys.

The chemical composition measured by optical emission spectrometer in the AA2618 forgings was uniform. The composition ranges given for AA7040 and AA7449 correspond to the limits of the international specifications. These chemical compositionsⁱ will be used (in at.%) in the yield strength model presented in chapter 4 and used in chapter 5 for simulations of quenching with the TMM model.

20 mm and 75 mm thick AA7449 and 75 and 140 mm thick AA7040 hot-rolled plates were supplied by Constellium. The microstructure after quenching of a 75 mm thick AA7449 plate was characterised by P. Schloth [50]. It consists of grains elongated in the rolling direction (1000 µm in length and 100-200 µm in thickness) comprising subgrains with an average size of ~2 µm. Some recrystallised grains with a grain size of 150-200 µm and without subgrain structure were also observed. In addition, Al₇Cu₂Fe and Mg₂Si intermetallic phases were found through the thickness in rather low quantities.

For machining the Gleeble tests specimens, the 75 mm thick hot rolled plates were used directly. For RS measurements, hot-rolled plates were vertically quenched by immersion

ⁱ For the plates, the chemical composition used in this work is position dependent according to internal Atome Probe Tomography measurements performed on 75 mm thick AA7449 plates.

2. Materials, heat transfer and RS measurements

in an experimental medium size agitated 20°C water quench device. Two as-quenched plates were measured directly (no machining); the other as-quenched plates were cut in order to obtain smaller plates easier to manipulate for ND measurements. The as-quenched plate dimensions are given in *Table 2-2*.

Alloy	Dimensions for quenching (L) × (LT) × (ST) in mm	Dimensions for RS measurement after machining (L) × (LT) × (ST) in mm	Technique of RS measurement
AA7449	500 × 300 × 20	500 × 300 × 20 (no machining)	ND at POLDI
	640 × 510 × 75	640 × 510 × 75 (no machining)	ND at SALSA
	640 × 510 × 75	310 × 310 × 75	ND at SALSA
	640 × 510 × 75	310 × 310 × 75	ND at POLDI
	700 × 405 × 75	2 bars 30 × 250 × 75 2 bars 250 × 30 × 75	Layer Removal by Constellium
AA7040	1000 × 500 × 75	310 × 310 × 75	ND at POLDI and SALSA
	1000 × 730 × 140	600 × 400 × 140	ND at SALSA

Table 2-2 - Dimensions of the different hot-rolled 7xxx plates used in this work.

AA2618 forgings of different sizes (small, large and very large) were provided by ABB Turbo Systems in annealed state, i.e. containing coarse precipitates formed during slow cooling. The grain size was estimated by P. Schloth to be about 40 µm from electron backscatter diffraction images.

For machining the Gleeble tests specimens, the forgings in annealed state were used directly. For temperature and RS measurements, the forgings (one small and one large) were quenched individually by immersion in an industrial agitated boiling water bath. For T6 RS measurements, the large forging was heat treated according to the specifications given in *Table 2-1*.

2.2. Quenching of industrial parts

In order to predict the as-quenched RS, one needs to have an accurate knowledge of the temperature field evolution in the components. In the case of cold-water quenched plates, the efforts should be on the cooling experienced by the surface as it imposes its stress.

2.2.1. Literature review on heat transfer during quenching

Four different regimes can operate successively during quenching as shown in Figure 2-1 and Figure 2-2.

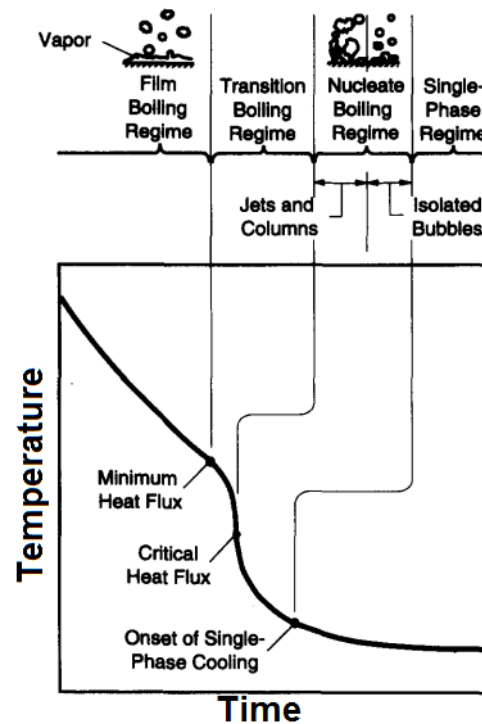


Figure 2-1 – Boiling regimes associated with pool quenching a small metallic mass [53].

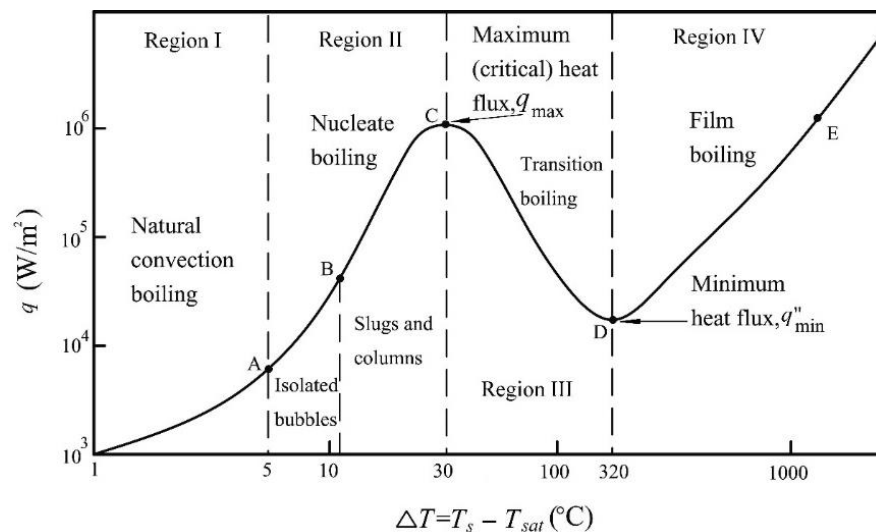


Figure 2-2 – Pool boiling curve for saturated water showing heat flux versus excess temperature [54].

In the single-phase regime occurring at low excess temperature (difference between quenchant and surface temperature less than 5°C [54]), natural convection is dominant with a low rate of heat transfer.

In the nucleate boiling regime, heat transfer is fast with vapour bubbles forming at nucleation sites and carrying heat away from the surface. The film formed by bubbles intermittently collapses and reappears, which makes difficult to determine the heat transfer in this regime. The maximal heat flux occurs at low excess temperature for quenching in boiling water (30°C in Figure 2-2). This maximum is shifted towards higher excess temperatures for colder quenchants [55, 56].

In the transition boiling regime, bubbles start to form an unstable vapour film with a thermal conductivity lower than the liquid, thus reducing heat transfer by acting like a blanket.

Film boiling regime starts at the Leidenfrost temperature (point D in Figure 2-2) when the vapour blanket becomes stable enough to cover entirely the surface and allow constant heat transfer by conduction through the vapour. With increasing excess temperature, radiation becomes more and more important, leading to a heat flux increase.

Surface heat flux is estimated from temperature measurements by inverse method using a nonlinear FE model that solves the heat equation:

$$\rho c_p \frac{\partial T}{\partial t} + \text{div}(-k \underline{\nabla} T) = 0 \quad \text{Eq. 2-1}$$

where ρ is the density (in kg.m^{-3}), c_p the specific heat capacity (in $\text{J.kg}^{-1}.\text{K}^{-1}$) and k the thermal conductivity (in $\text{W.m}^{-1}.\text{K}^{-1}$). Instead of using a Neumann (heat flux) boundary condition, a Cauchy boundary condition is often preferred:

$$q = \text{HTC}(T_s - T_0) \quad \text{Eq. 2-2}$$

where q is the heat flux (in W.m^{-2}), HTC the heat transfer coefficient (in $\text{W.m}^{-2}.\text{K}^{-1}$), T_s the surface temperature of the component (in Kelvin) and T_0 the quenchant temperature (in Kelvin). Knowing the heat transfer coefficient, the resolution of the heat equation gives the thermal field $T(P,t)$ at each position P and time t , which is an input for metallurgical and mechanical models.

A review of recent FE models with their heat transfer coefficient was recently made by Robinson et al. [2]. *Figure 2-3* shows heat transfer coefficients for immersion quenching of aluminium alloy plates in 20°C water obtained by inverse method.

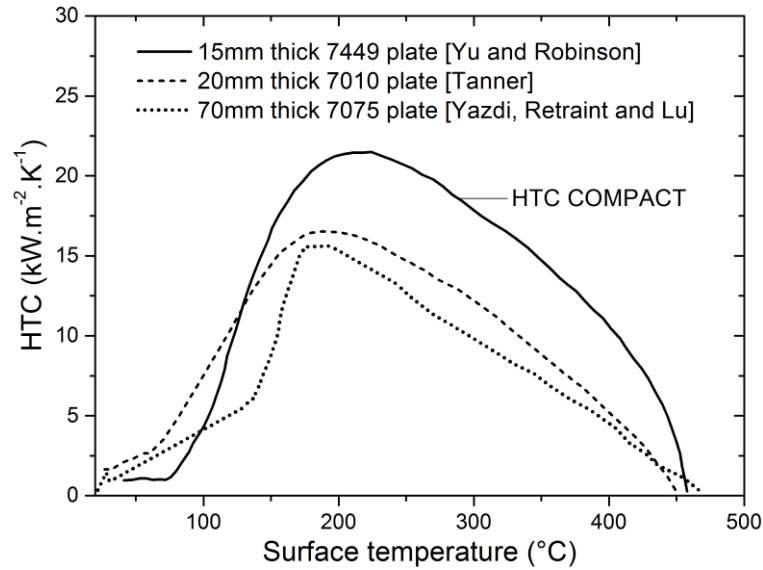


Figure 2-3 – Heat transfer coefficients for immersion of AA plates in 20°C water [55-57].

Yazdi, Retraint and Lu [57] quenched a 500 x 500 x 70 mm plate equipped with four thermocouples at 0, 17.5, 26 and 34 mm from the surface. Plates were quenched horizontally, i.e. the large face with a thermocouple at ca. 0.5 mm from the surface entered the quenchant first, in the works of Tanner (60 x 60 x 20 mm plate) [55] and Yu and Robinson (105 x 105 x 15 mm plate) [56]. The later authors found the same HTC (later called “HTC COMPACT” as it was determined in the frame of the European project COMPACTⁱ) with or without water agitation but pointed out that more massive components are likely to cool down slower without agitation. The three HTC curves present a maximum at 190-215°C. The differences can be due to different alloys, sample dimensions, surface conditions, or quenching conditions. The high HTC values in Figure 2-3 together with the relatively high thickness of the plates give a Biot number much larger than 0.1, meaning that a thermal gradient in the plate thickness is present [58]. In this case, instead of inserting thermocouples in holes parallel to the thermal gradient (as this is the case in [55-57]), it is preferable to drill holes perpendicular to the thermal gradient.

2.2.2. Quenching of plates by vertical immersion in 20°C water

The industrial quench by water spray was not considered in this work for the sake of simplicity. Instead, plates were quenched by immersion in a lab water pool. A 350 x 400 x 75 mm 7449 plate (plate1) was drilled perpendicular to the thermal gradient at 3, 15 and 37.5 mm from the surface and equipped with three Chromel-Alumel (type-K) thermocouples (TCs) of diameter 1mm inserted in the holes (*Figure 2-4-left*). An inorganic ceramic adhesive was applied at the surface of the holes to fix thermocouples and prevent water from going into the holes. The plate was vertically quenched by immersion in agitated 20°C water, i.e. the small face entered the quenchant first. Two

ⁱ A COncurrent approach to Manufacturing induced Part distortion in Aerospace ComponenTs

quenches were performed successively for reproducibility purpose and an additional TC was placed outside the plate close to its center in order to determine the begin of quenching. This TC showed that water temperature remained inferior to 35°C during quenching.

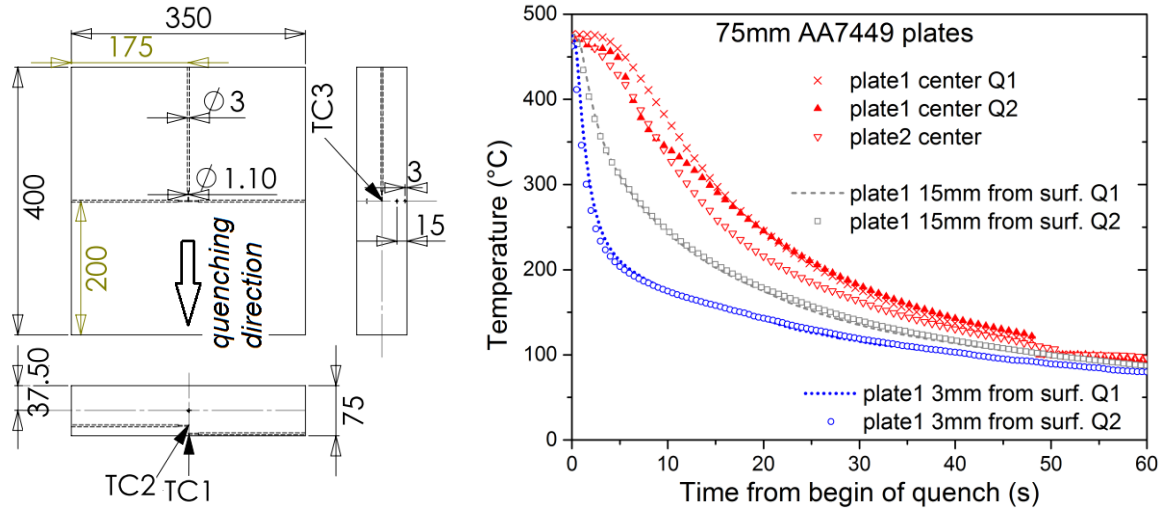


Figure 2-4 – 75 mm thick AA7449 plate (plate1) equipped with three TCs (a) and temperature measurements during vertical immersion quenching in agitated cold water (b).

Reproducibility was good at 3 mm and 15 mm from the plate surface but poor at the center. The temperature measured at the center of another plate (plate2) drilled parallel to the thermal gradient is also shown in *Figure 2-4-right*. The differences at plate center can be due to possible poor connection between thermocouple and aluminium in plate1 as suggested by the unlikely abrupt temperature drops between 5 and 10 seconds during Q2 and at ca. 50 seconds during Q1 and Q2.

A FE simulation using HTC COMPACT determined by Yu and Robinson [56] fits relatively well our temperature measurements as shown in *Figure 2-5*.

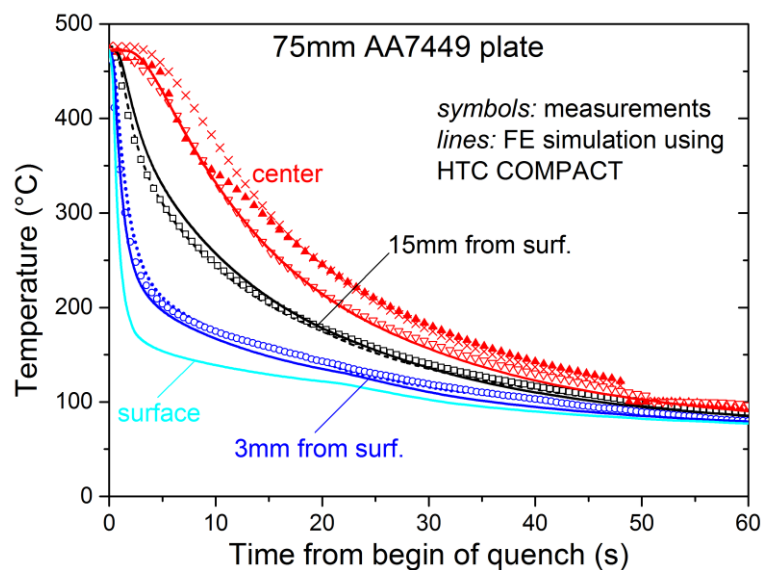


Figure 2-5 – Measured and simulated cooling curves for immersion quench in 20°C water.

The simulated cooling using HTC COMPACT is slightly too fast at 3 mm from the surface but slightly too slow at 15 mm from the surface. This indicates that the agreement between measurements and simulation cannot be improved significantly by changing HTC COMPACT. The overall fit may be improved by adjusting thermal diffusivity, but this is not done since the fit at 3 mm from the surface is already good. HTC COMPACT with a quenchant temperature of 20°C was used to calculate the surface cooling as shown in *Figure 2-5* for the 75 mm thick AA7449 plate. It is assumed to be identical for the 20 mm thick AA7449 plate, 75 mm and 140 mm thick AA7040 plates.

2.2.3. Quenching of large forging in boiling water

For temperature measurements, a large forging was equipped by ABB with 20 type-K thermocouples. In *Figure 2-6-top*, one can distinguish six groups at the external surfacesⁱ and three TCs inside the forging. Instead of being on the same plane (e_r, e_z), TCs are positioned at different angles, ϕ , as shown schematically in *Figure 2-6-bottom*, in order to maximise the distance between two drillingsⁱⁱ and thus diminish the influence of the drillings on the surrounding TCs. The forging was quenched by immersion in an industrial boiling water bath with a water jet facing to group 6.

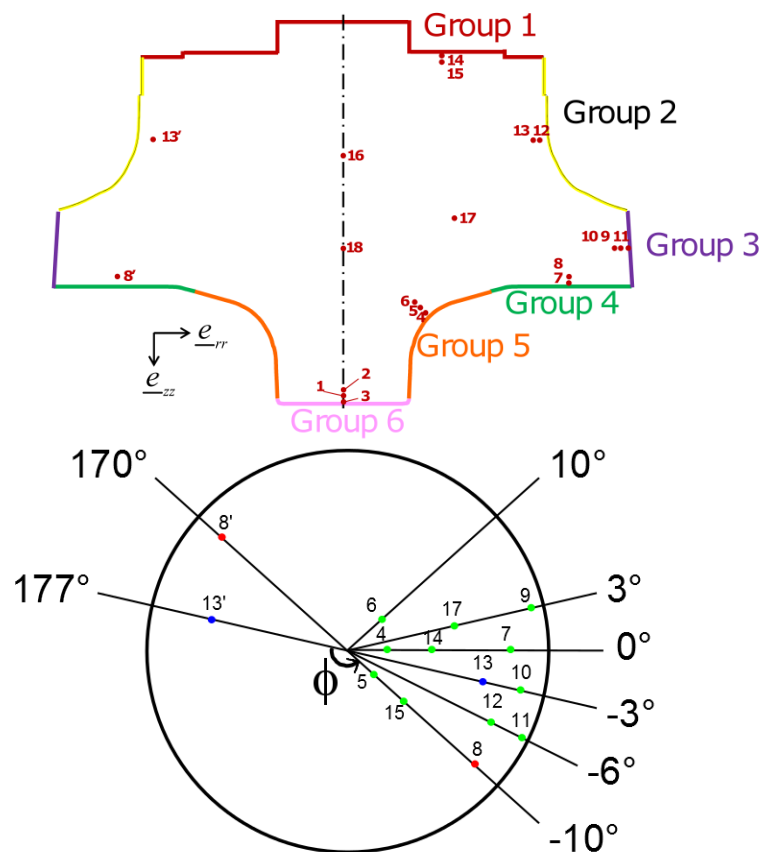


Figure 2-6 – Position of the thermocouples in the large forging in cut view (top) and in top view (bottom) where the angles ϕ and the dimensions are not to scale.

ⁱ TCs are aligned in a row of two or three in order to capture the surface thermal gradient.

ⁱⁱ The air present in the drillings decreases heat transfer.

Figure 2-6-bottom also shows that TCs 8' and 13' are positioned at $\phi = 180^\circ$ from TCs 8 and 13 respectively in order to check the cooling axisymmetric hypothesis. This is the case for TCs 8 and 8' whose cooling curves are almost superimposed (Figure 2-7).

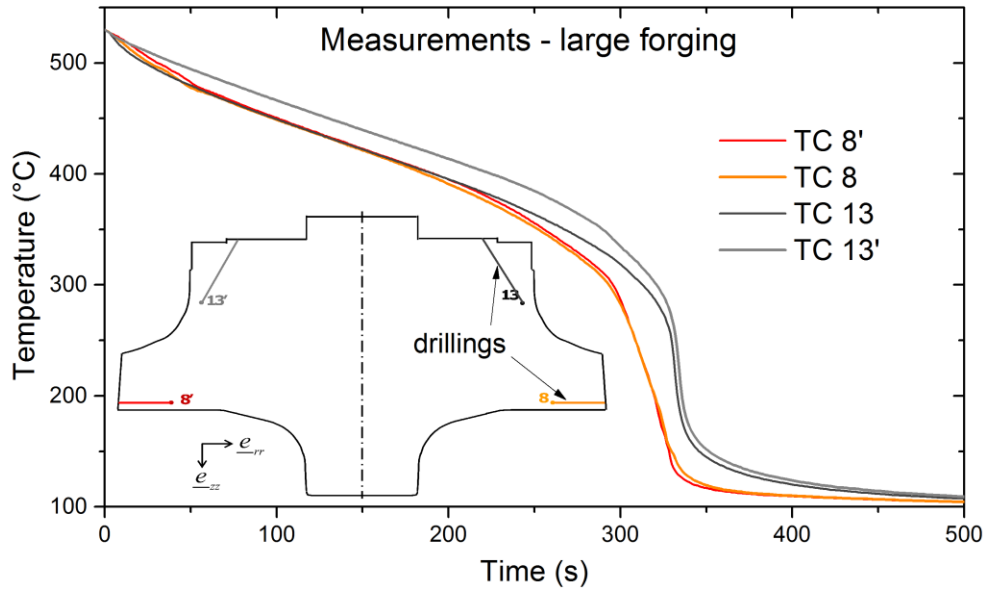
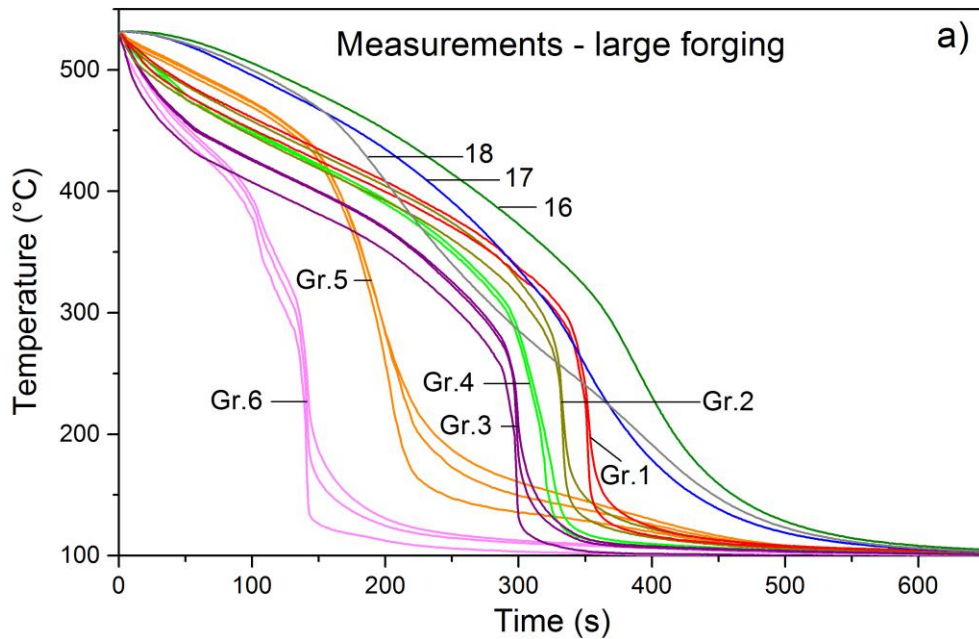


Figure 2-7 – Temperature evolution of two TCs at same radial distance but at $\phi = 180^\circ$ from each other to check the cooling axisymmetric hypothesis.

The fact that the cooling curves of TCs 13 and 13' are not superimposed may come from the position of those thermocouples which could be not exactly symmetrical. This might be due to the fact that the drilling is done at an angle of 62.5° from the top for TCs 13 and 13', whereas it is perpendicular to the lateral surface 3 for the TCs 8 and 8'.

Figure 2-8 shows that cooling is strongly dependant on position.



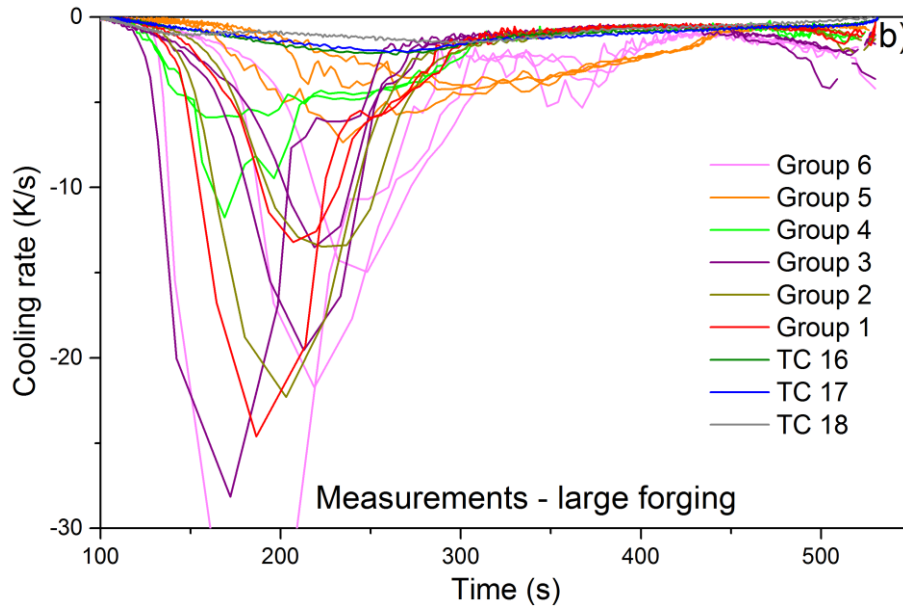


Figure 2-8 – Measured cooling curves in boiling-water quenched large forging (a) and corresponding cooling rates (b).

From the solutionising temperature, temperature begins to decrease almost linearly with time but is not uniform within the forging. Above ca. 300°C, the measured cooling rates are around 1 K/s at forging center (TCs 16 to 18) and always lower than 5 K/s in the forging (Figure 2-8-b). The side facing the water jet (groups 5 and 6) cools faster (1-5 K/s) than the other faces (~1 K/s).

From ca. 300-400°C depending on position, temperature drops dramatically but not at the same time within the forging resulting in huge temperature gradients. The highest cooling rates (20-30 K/s) occur between 150°C and 250°C. At forging center, the cooling rates are always lower than 2 K/s.

As temperature approaches 100°C, the quenchant temperature, natural convection takes place with all cooling curves tending towards the same value. Temperature is almost uniform after ca. 650 seconds so that internal stresses will no longer evolve due to thermal gradients.

In order to simulate this strongly position-dependant quenching, one HTC per group of TCs was defined in the FE model. A parameterisation of the 6 HTCs was used to decrease the number of design variables to optimise by inverse method:

$$HTC(T) = \alpha_0 + \alpha_1 \exp\left(-\left(\frac{T - T_0}{T_n}\right)^{\alpha_2}\right) \quad \text{Eq. 2-3}$$

where α_0 and $\alpha_0 + \alpha_1$ are the values at high temperature and at the quenchant temperature, T_0 , respectively. T_n determines the rate of decay of the exponential and α_2 the slope at T_0 .

Rather than optimising simultaneously the 24 design variables (4 variables times 6 HTC), a two-steps optimisation method was performed in the master project of G. Michel [59]. The first step consists in solving independently the local heat equations for the 6 surfaces described by their parameterised HTC.

In the second step, the quenching simulation of the entire forging is run to account for interactions between the 6 surfaces and limit the variation of the design variables in the local optimisation (first step). The optimised HTCs are given in *Figure 2-9* together with the measured and simulated temperature evolutions.

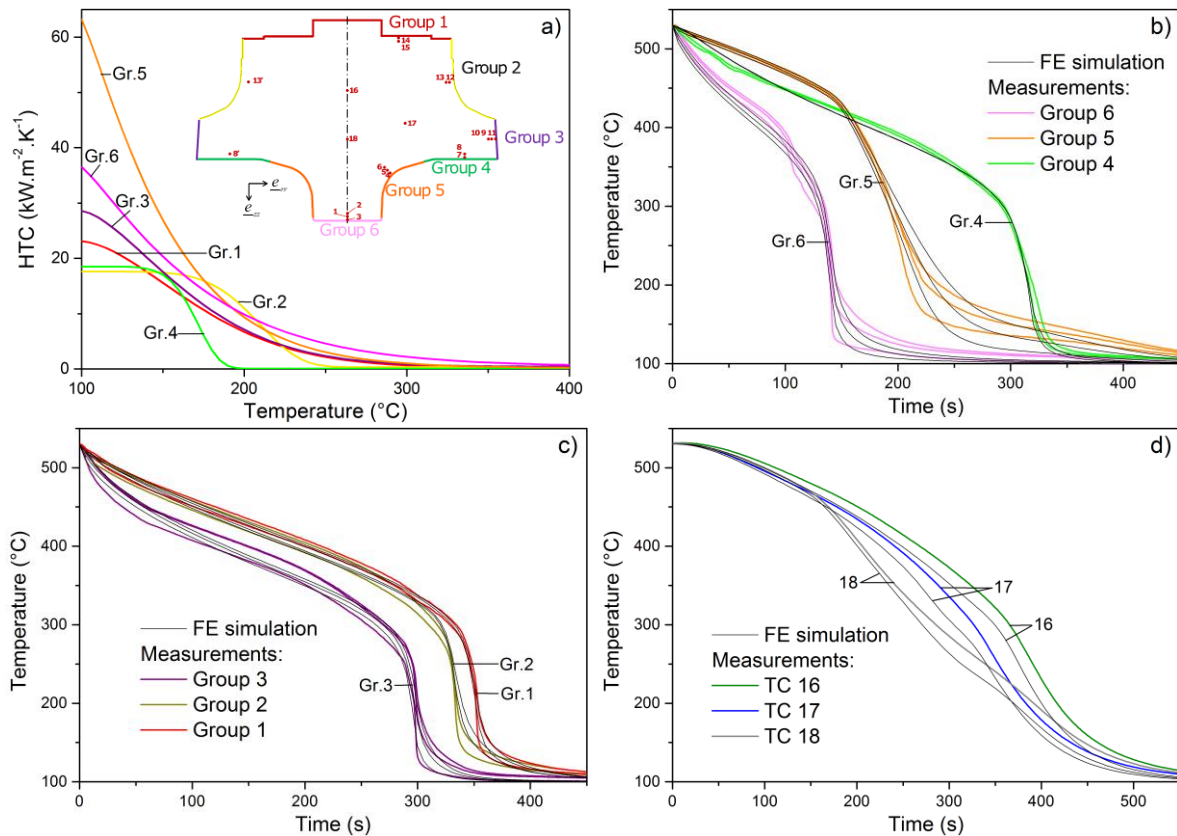


Figure 2-9 – HTCs vs. surface temperature obtained by inverse method (a) using an axisymmetric model of quenching in boiling water; comparison between temperature measurements and simulation (b, c and d).

The overall agreement between measurements and simulation is good, except at low temperature ($< 150^{\circ}\text{C}$) where the simulated curves are below the measured ones. This is due to the fact that the parameterisation is not realistic since HTC is expected to decrease as the surface temperature approaches the quenchant temperature (*Figure 2-3*). In order to evaluate the effect of this simplification on the residual stresses, HTCs were manually lowered below 130°C . This resulted in maximal differences of about 5.8 MPa. The identified HTCs given in *Figure 2-9* are assumed to be identical for the small forging whose shape differs only slightly from the large one.

2.3. Measurement of residual stress by layer removal

2.3.1. Principle of the layer removal method

As its name itself suggests, this method consists in measuring the deflection or the strain resulting from successive layer removal and calculating RS using the elasticity theory. This relaxation method originally based on the work of Rosenthal and Norton on heavy section weldments [60] has been used for decades to determine RS profile in thick aluminium plates [3, 24].

Two full thickness rectangular bars are taken in the L and LT directions of the middle of the plates. For RS measurements, these bars are machined down the ST direction step by step. After each step the bar thickness and the strain are recorded. Strain measurements are performed by a one-way strain gauge with thermal expansion compensation bound to the surface opposite to the machined surface as shown in *Figure 2-10*.

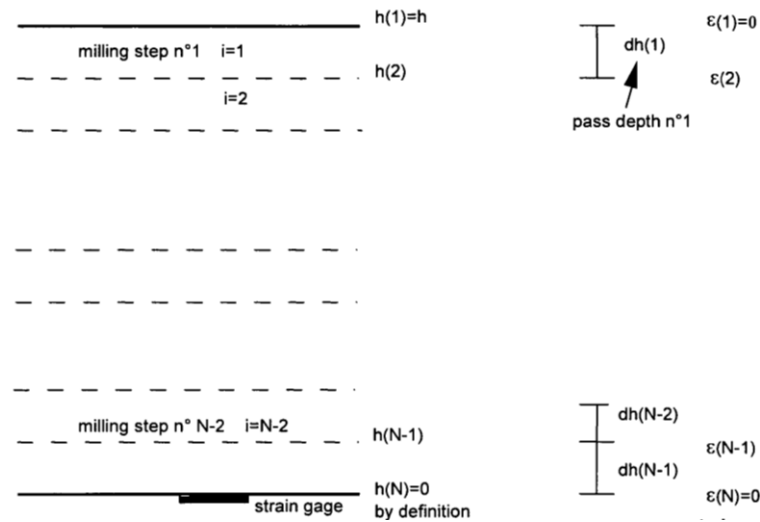


Figure 2-10 - Schematic representation of the measurement and calculation sequences to determine a residual stress profile using the layer removal method [61].

Recommendations for bar dimensionsⁱ and machining conditions are given in the patent [61] and in Ref. [3].

For each bar, after each machining step i , the average stress in the layer removed, $s(i)$, is calculated according to [61]:

$$s(i) = -E \frac{(\varepsilon_{SG}(i+1) - \varepsilon_{SG}(i))(h(i+1))^2}{[h(i) - h(i+1)][3h(i) - h(i+1)]} - \Sigma_s(i) \quad \text{Eq. 2-4}$$

where $\varepsilon_{SG}(i)$ is the strain gauge reading and $h(i+1)$ is the bar thickness after step i and E is the Young's modulus of the alloy.

ⁱ The machining of the bars in the plates leads to a mechanical re-equilibrium: the in-plane stress in the direction of the width of the bars is near zero and the in-plane stress in the direction of the length of the bars is almost not affected by machining provided that the bars are long enough.

$$\Sigma_s(i) = E \sum_{k=1}^{i-1} (\varepsilon_{SG}(k+1) - \varepsilon_{SG}(k)) \left(1 - \frac{3h(k)[h(i) + h(i+1)]}{[h(k+1)][3h(k) - h(k+1)]} \right) \quad \text{Eq. 2-5}$$

The stress profiles $s_L(i)$ and $s_{LT}(i)$ obtained for the two bars in the L and LT directions respectively are used to calculate the stress profiles in the plate, $\sigma_L(i)$ and $\sigma_{LT}(i)$:

$$\sigma_L(i) = \frac{s_L(i) + \nu s_{LT}(i)}{1 - \nu^2} \quad \text{and} \quad \sigma_{LT}(i) = \frac{s_{LT}(i) + \nu s_L(i)}{1 - \nu^2} \quad \text{Eq. 2-6}$$

where ν is the Poisson's ratio of the alloy.

If the initial bars are not perfectly flat, the first milling step will be not uniform in thickness. This makes the first point difficult to obtain. For the last milling step, the bars are not stiff enough. Thus, deformations slightly depend on the position of the bars on the milling assembly. Furthermore, the thicker the bars, the lower the deformations and hence the lower the measurement accuracy.

2.3.2. Results for a 75 mm thick AA7449 plate

The layer removal method was used to measure through thickness RS in a 700 mm × 405 mm × 75 mm as-quenched AA7449 plate. Two full thickness rectangular bars were taken in the x (L) and y (LT) directions at the middle of a 75 mm thick AA7449 plate. Two additional bars were used for reproducibility as shown in *Figure 2-11*. The 30 mm × 250 mm × 75 mm bars were machined down the z direction by steps of 2 mm.

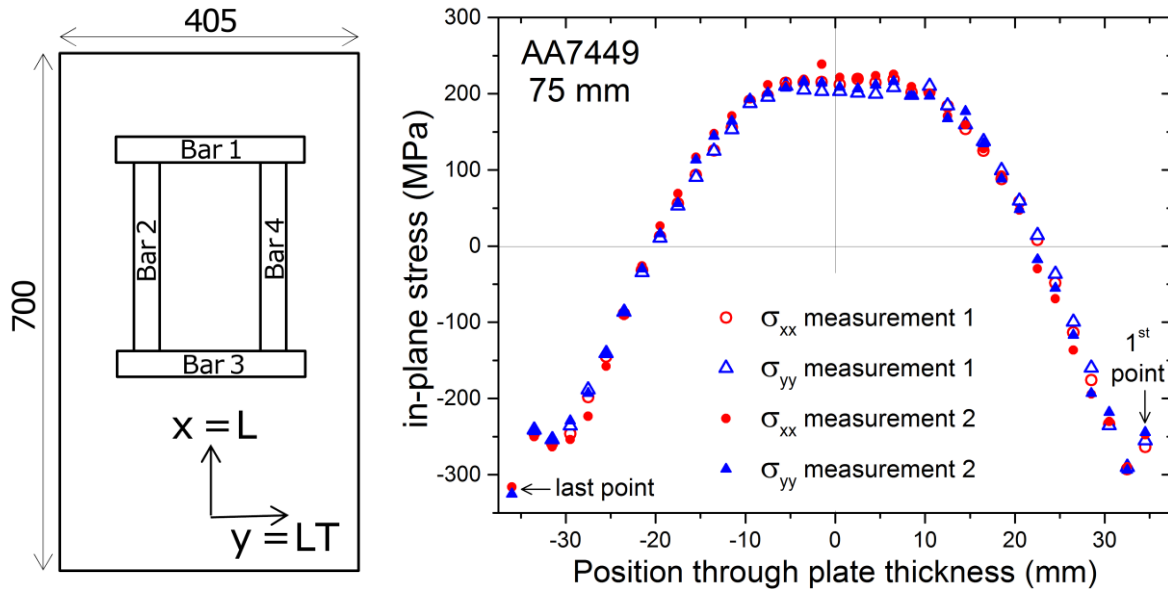


Figure 2-11 – Sketch of 75 mm thick AA7449 plate from which 4 bars are taken for the layer removal method (left) and obtained RS profiles (right).

The skin-core effect appears clearly with about 300 MPa compressive stress at the surface and 200 MPa tensile stress in the centre. Stresses are higher in absolute value at the surface than in the centre due to higher quenching rate [26, 28]. Measurements 1 and 2 are close, showing the good reproducibility of the method, which gives:

$$\sigma_{xx} \approx \sigma_{yy}$$

Eq. 2-7

This means that the effect of the rolling texture on macroscopic residual stresses is low. This is in agreement with the low stress difference (max. 15 MPa) between transverse long (LT) and rolling (L) sampling directions in AA7449 plate as shown in appendix 7.5.

2.4. Measurement of residual stress by neutron diffraction

2.4.1. Principle

Strains are obtained by measuring with high accuracy the interplanar spacing of the crystal lattice which acts as an internal strain gauge. Diffractionⁱ techniques based on interferenceⁱⁱ phenomena allow measuring inter-atomic distances (in the order of 10^{-10} m). One of the required conditions for constructive interference is expressed by Bragg's law which writes for (hkl) planes:

$$n_{dif} \lambda = 2d^{hkl} \sin(\theta)$$

Eq. 2-8

Bragg diffraction condition states that the optical path difference $2d^{hkl} \sin(\theta)$ shown in Figure 2-12 must be equal to an integer multiple n_{dif} of the wavelength λ .

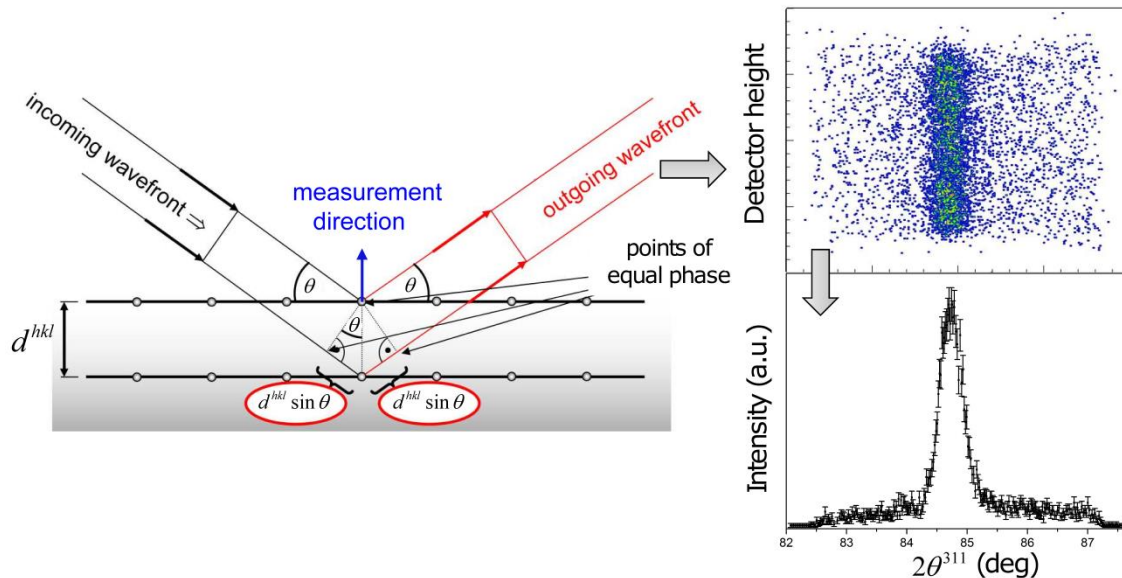


Figure 2-12 - Schematic of wave scattering at two atomic planes showing first order diffraction ($n_{dif} = 1$); example of 2D-detector signal at SALSA integrated over its height to obtain the Intensity- 2θ plot.

One distinguishes monochromatic from polychromatic time-of-flight techniques. In the monochromatic angular dispersive diffraction technique, wavelength is fixed and diffraction angle is measured. Hence, only one diffraction peak is recorded, usually the

ⁱ Deviation of the light (or electrons/neutrons) propagation compared to the predictions of geometrical optics, when wave fronts interact with obstacles with size close to their wavelength.

ⁱⁱ Interaction of two or more radiation sources resulting in an intensity distribution, which differs from the sum of the intensities of the single sources.

(311) reflection for face-centered cubic metals like aluminium since it exhibits low intergranular strains and elastic properties close to the ones of the bulk material [62].

In the polychromatic time-of-flight, diffraction angle is fixed and wavelength (proportional to the time-of-flight of neutrons according to de Broglie relationship) is measured. This allows investigating multiple Bragg reflections at the same time by recording simultaneously a large number of diffraction peaks corresponding to several families of diffracting planes. This technique gives insight on texture and enables the calculation of an average lattice parameter using a full diffraction pattern Pawley analysis [63].

In the x directionⁱ, the component of the elastic strain tensor, ε_{xx} , is derived from the interplanar spacing d_x , as follows:

$$\varepsilon_{xx}^{hkl} = \frac{d_x^{hkl} - d_0^{hkl}}{d_0^{hkl}} = \frac{\Delta\lambda}{\lambda} - \cot\theta \Delta\theta \quad \text{Eq. 2-9}$$

where Eq. 2-8 has been used and the subscript 0 refers to the absence of macroscopic stress. The reference interplanar spacing can be measured on small coupons cut from a companion component. Usually, the same piece is used for d_x^{hkl} and d_0^{hkl} measurements. After d_x^{hkl} measurements in a first session, the piece is cut for d_0^{hkl} measurements in a second session. d_0^{hkl} is known to vary with solute content, i.e. with macrosegregation.

The stress-free reference value can also be determined using the fact that normal stress is zero or using mechanical equilibrium. In large plates, the measured spatial variation in d_0^{hkl} can be compared to the values calculated using [29]:

$$d_0^{hkl} = \frac{2\nu}{(1+\nu)} d_x^{hkl} + \frac{(1-\nu)}{(1+\nu)} d_z^{hkl} \quad \text{Eq. 2-10}$$

With d_x and d_z the interplanar spacing in the x and z directions.

In a polycrystal, only the grains with plane normal parallel to the scattering vector diffract into the detector. Hence, finer grain microstructure yields better statistics.

Although elastic strains should be compared when confronting measurements with simulations, stresses are more meaningful for engineers. Stress components are calculated using the generalised Hooke's law, which writes for an isotropic material using Einstein's summation convention:

$$\sigma_{ij} = \frac{E}{1+\nu} \varepsilon_{ij} + \frac{E\nu}{(1+\nu)(1-2\nu)} \text{Tr}(\varepsilon) \delta_{ij} \quad \text{Eq. 2-11}$$

where $i, j = 1, 2, 3$ indicate the components relative to chosen orthogonal axes. E and ν are the Young's modulus and Poisson's ratio respectively.

The measurement of six strain components in six different directions is thus necessary to calculate the full stress tensor. The trace being an invariant, strain measurements in three mutually orthogonal directions are actually enough to calculate stresses (not

ⁱ The measurement direction corresponds to the direction bisecting the directions of incident and diffracted beams (direction of the scattering vector).

necessarily principal) in these directions without knowledge of the shear strain components.

The residual stresses are usually classified into three orders, depending on the scale of consideration as shown in *Figure 2-13*.

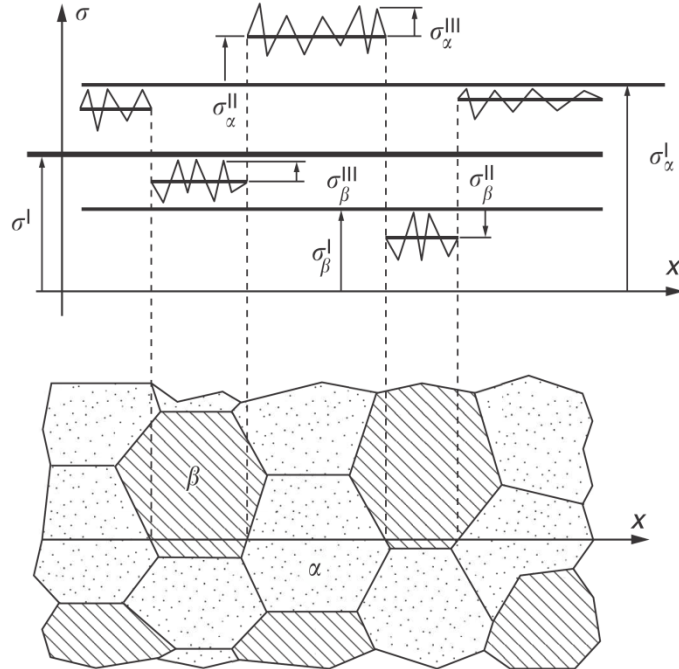


Figure 2-13 – Schematics of the three orders of residual stresses [64].

Although macrostresses (superscript I in *Figure 2-13*) originating from processing (i.e. from quenching in this work) are the main interest here, it should be kept in mind that they are influenced by stresses at lower scales (superscripts II and III). Type II and type III microstresses originate from incompatibility of strain between neighbouring grains and at inhomogeneously distributed dislocation arrangements respectively.

Stress calculation leads to two potential errors. The first one comes from the elastic constants E and ν . At the atomic scale, the elastic constants depend on crystal orientation and may differ from the macroscopic constants. The diffraction peak-specific elastic constants E^{hkl} and ν^{hkl} for texture-free materials can be measured (e.g. $E^{311} = 69.0$ GPa for aluminium [65]). Here, the values calculated using Kröner modelⁱ were used ($E^{311} = 70.2$ GPa and $\nu^{311} = 0.35$ for aluminium [62]) for stress calculations. Here, it should be kept in mind that microstructure and alloy composition affect the elastic constants. The second error comes from the trace in Hooke's law which propagates any error in one strain component to all stress components. These two sources of error make stress calculations less trustworthy than strain measurements.

While X-ray is the most common radiation source, it is limited to low penetration depths of a few micrometers in most metals [62]. On the other hand, neutrons feature high penetration depths due to their neutral electric charge, relatively high mass and small

ⁱ The model assumes that the grains are spherical and randomly oriented and takes into account stress and strain continuity at grain boundaries.

radius (6.10^{-16} m). Aluminium being relatively transparent to neutrons, residual stress measurements in large billets could be performed with a maximal beam path of ca. 300 mm by neutron diffraction [39].

2.4.2. Experimental campaign of residual strain measurements by ND

Residual strains were measured at three different diffractometers:

- i. SALSA (Strain Analyser for Large and Small scale engineering Applications) located at the Institut Laue-Langevin (ILL) in Grenoble, France,
- ii. STRESS-SPEC located at FRM II in Garching, Germany,
- iii. POLDI (Pulse OverLap Diffractometer) located at SINQ in Villigen, Switzerland.

Measurements at i. and ii. were performed using the (311) aluminium reflection with a scattering angle of ca. 84.8° at SALSA and ca. 88.8° at STRESS-SPEC. These two continuous source based diffractometers, were chosen for their high neutron flux. This, together with their large 2D-area detectors ($8 \times 8 \text{ cm}^2$ at SALSA and $30 \times 30 \text{ cm}^2$ at STRESS-SPEC) provided good counting statistics in a reasonable measurement time. Diffraction peaks recorded by the 2D-detectors of SALSA and STRESS-SPEC are integrated over the height of the detector to obtain Intensity- 2θ diffraction peaks as shown in *Figure 2-12*. Error bars represent the statistical uncertainty associated with the integration over the height of the detector. For these two strain scanners at constant wavelength, $\Delta\lambda = 0$ and Eq. 2-9 becomes $\varepsilon_{xx} = -\cot(\theta) \Delta\theta$.

The time-of-flight diffractometer POLDI was chosen for its ability to investigate multiple Bragg reflections at the same time but at the cost of a lower neutron flux (ca. 10 times lower than SALSA). This, together with the one-dimensional detector of POLDI, leads to a lower counting statistics compared to SALSA or STRESS-SPEC. For this pulsed beam instrument, $\Delta\theta = 0$ and Eq. 2-9 becomes $\varepsilon_{xx} = \Delta\lambda/\lambda$.

After quadratic baseline subtraction, peaks are fitted using a pseudo-Voigt function which is a linear combination of a Gaussian and a Lorentzian function. The result of the peak analysis is the peak position, 2θ , and the associated errorⁱ, $Er(2\theta)$. This statistical error of the peak position, estimated by the fitting algorithm, is used to calculate the statistical errors on strains – e.g. $Er(\varepsilon_{xx})$ for ε_{xx} – from Eq. 2-9 [64]:

$$Er(\varepsilon_{xx}) = \sqrt{\left(\frac{\sin \theta_0 \cos \theta_x}{\sin^2 \theta_x} Er(\theta_x)\right)^2 + \left(\frac{\cos \theta_0}{\sin \theta_x} Er(\theta_0)\right)^2} \quad \text{Eq. 2-12}$$

This error due to counting statistics is propagated on stresses from Eq. 2-11:

$$Er(\sigma_{xx}) = \frac{E}{1+\nu} \sqrt{\left(\frac{1-\nu}{1-2\nu} Er(\varepsilon_{xx})\right)^2 + \left(\frac{\nu}{1-2\nu} Er(\varepsilon_{yy})\right)^2 + \left(\frac{\nu}{1-2\nu} Er(\varepsilon_{zz})\right)^2} \quad \text{Eq. 2-13}$$

ⁱ estimate of the expected variation due to counting statistics if the peak were observed many times

The measurements performed on as-quenched AA7040 and AA7449 plates of different thicknesses and on AA2618 forgings of different size in different states are summarised in *Table 2-3*.

	as-Q AA7040 plates	as-Q AA7449 plates	AA2618 forgings
STRESS SPEC			-as-Q small -T6 large
SALSA	-75 mm (LT, ST) -140 mm (LT, ST, d_0)	-75 mm (L, LT, ST)	-as-Q large
POLDI	-75 mm (LT, ST)	-75 mm (LT, ST, d_0) -20 mm (LT, ST)	

Table 2-3 – Overview of residual strain measurements by ND. L, LT and ST refer to the measured components in plates. d_0 indicates stress-free reference measurements.

Experimental setup for plates

The plates were placed vertically on the sample table as shown schematically in *Figure 2-14-a* and *b*. Measurements are performed at the center of the plate through the thickness from A to B (*Figure 2-14-c*).

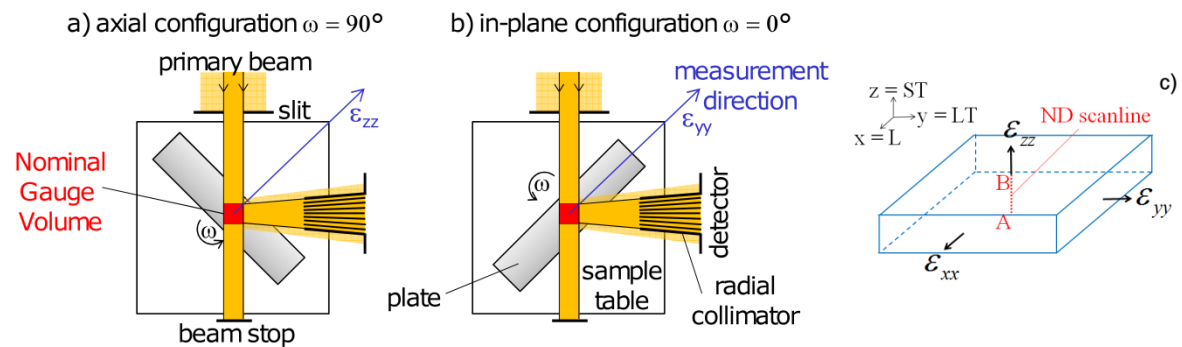


Figure 2-14 – Schematic view of the setup for plates in axial (a) and in-plane (b) configurations. The nominal gauge volume is not to scale. The through plate thickness scanline is shown in (c).

Compared to the axial configuration, the configuration for the in-plane components measurement is achieved by a table rotation of an angle, ω , of 90° .

The slit on the primary beam together with the radial collimator on the diffracted beam (detector-side) define the nominal gauge volume (NGV). The slit, which defines two dimensions of the NGV, was positioned as close as possible to the plate due to the horizontal and vertical beam divergence ($\pm 1^\circ$). The third dimension of the NGV is defined by the radial collimator. The 3.8 mm radial collimator of POLDI was used to define a NGV of 3.8 mm \times 1.5 mm \times 6 mm. The 2 mm radial collimator of SALSA was used to define a NGV of 2 mm \times 2 mm \times 15 mm. In both cases, the long direction of the

NGV is orthogonal to the scattering planeⁱ and corresponds to the rolling direction of the plates along which strains are almost invariant.

As chemical inhomogeneities have been reported by Godard through the thickness of thick aluminium hot-rolled plates, reference comb specimens (see picture in *Figure 2-15*) were machined out from two plates using electro-discharge machining, which is known for its little influence depth on the material (< 0.1 mm). These specimens were used to measure the variation of the stress-free reference value through plate thickness. The NGV was carefully positioned to be fully immersed in the comb in order to avoid spurious shift of the diffraction peak due to partially filled gauge volume [66].

The measured d_0^{311} values in *Figure 2-15-a* are close to the calculated ones using Eq. 2-10. This experimental verification of Eq. 2-10 means that no reference specimen is needed in the case of the 75 mm thick plate.

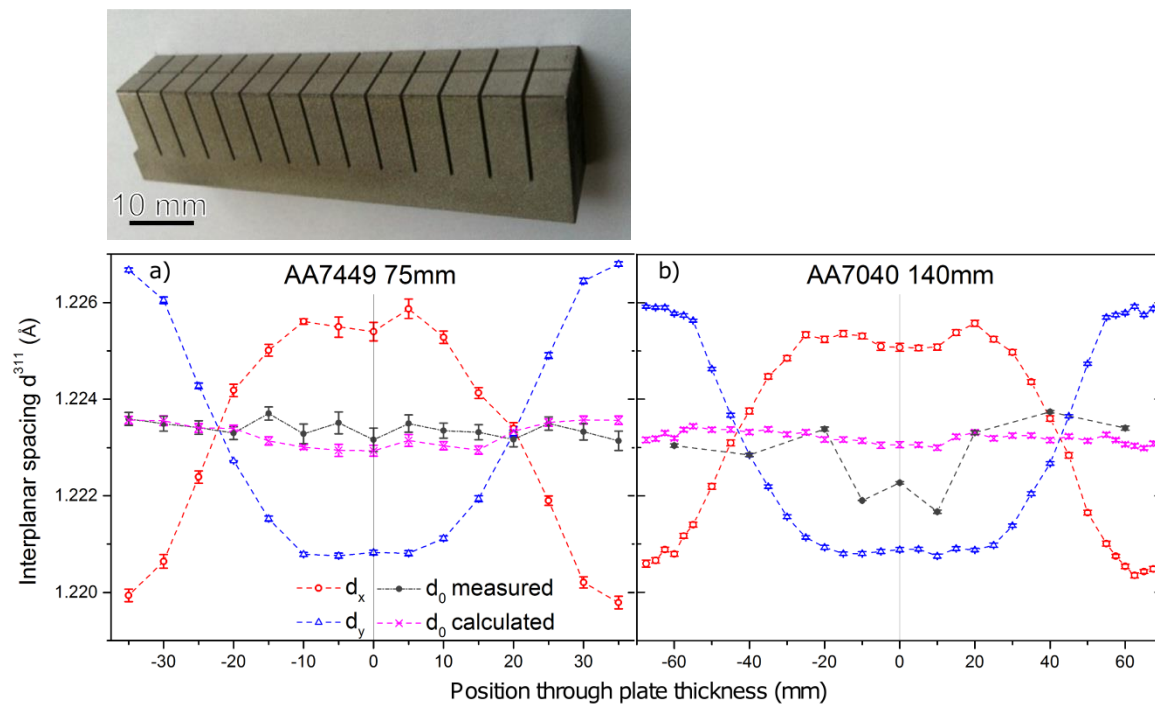


Figure 2-15 – top: picture of reference comb in 75 mm thick AA7449 plate; bottom: interplanar spacing in 75 mm thick AA7449 (a) and 140 mm thick AA7040 (b) plates. The legend in (a) also applies to (b).

In the 140 mm thick plate, the measured d_0^{311} values in *Figure 2-15-b* differ significantly from the calculated ones close to the center. This, together with the slight decrease of d_y close to the center, may be due to magrosegregation present in such thick plates. For strain and stress calculations, the calculated reference value was used to guarantee that $\sigma_{zz}(z) = 0$, as assumed in the model.

ⁱ defined by the primary and diffracted beams.

Experimental setup for forgings

The forgings were placed horizontally on the sample table (i.e., forging axis parallel to the scattering plane) in order to minimise the beam path in the material as shown exemplarily at SALSA diffractometer in *Figure 2-16*.

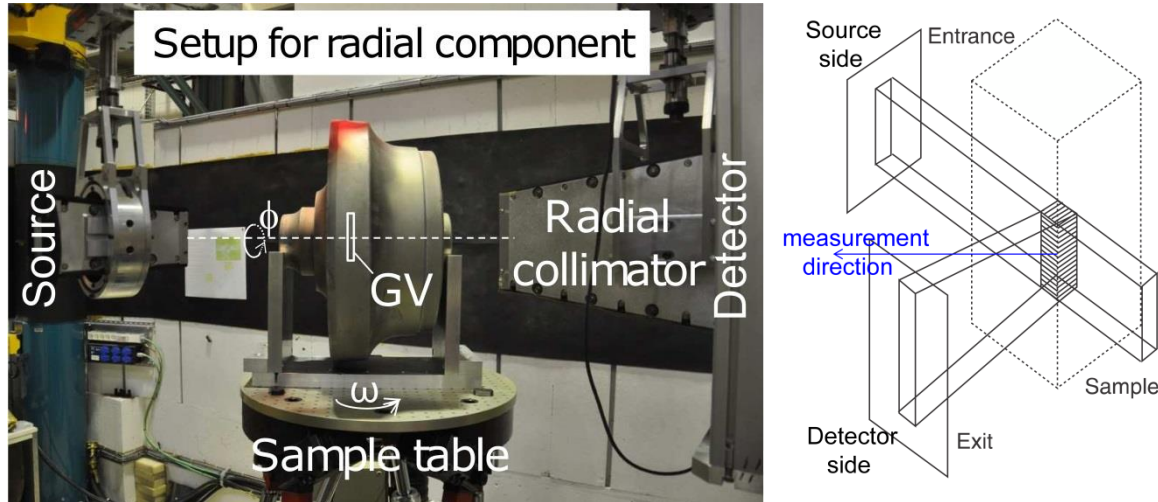


Figure 2-16 – Setup at SALSA diffractometer in the radial configuration (left) and schematic of the nominal gauge volume elongated vertically (right) adapted from [64].

Compared to the radial configuration ($\omega = 0^\circ$), the configuration for the axial component measurement is achieved by a table rotation of an angle, ω , of 90° . The configuration for the hoop component is achieved by a forging rotation of an angle, ϕ , of 90° about its axis with $\omega = 0^\circ$.

The choice of the NGV was delicate due to the large dimensions of the forgings. A radial collimator was used on the diffracted beam (detector-side in *Figure 2-16*) to minimise divergenceⁱ as recommended in [64].

For the two forgings measured at STRESS-SPEC, a 5 mm radial collimator was used to define a NGV of 5 mm × 5 mm × 5 mm allowing for both a reasonable spatial resolution and a satisfying counting statistics.

At SALSA a 2 mm radial collimator was used on the detector side. The first measurements were performed with a 2 mm radial collimator on the primary beam for a high spatial resolution. The resulting NGV of 2 mm × 2 mm × 2 mm appeared to be too small to give a sufficient signal-to-noise ratio for accurate peak fitting. Thus, the NGV was extended vertically as recommended in [64] to gain intensity by removing the collimator on the primary beam. This resulted in a NGV of 2 mm × 2 mm × 15 mm as shown schematically in *Figure 2-16-right* and in *Figure 2-17-b* and *c*. Since strains are averaged over the gauge volume, the elongated direction should correspond to a direction along which strains are almost invariant. This is the case in the axial and radial directions due to axisymmetry but not in the hoop direction where strains are experimentally smoothed along [AB] and [CD]. This elongated NGV was used at SALSA for the as-quenched large forging.

ⁱ at the cost of a longer measurement time.

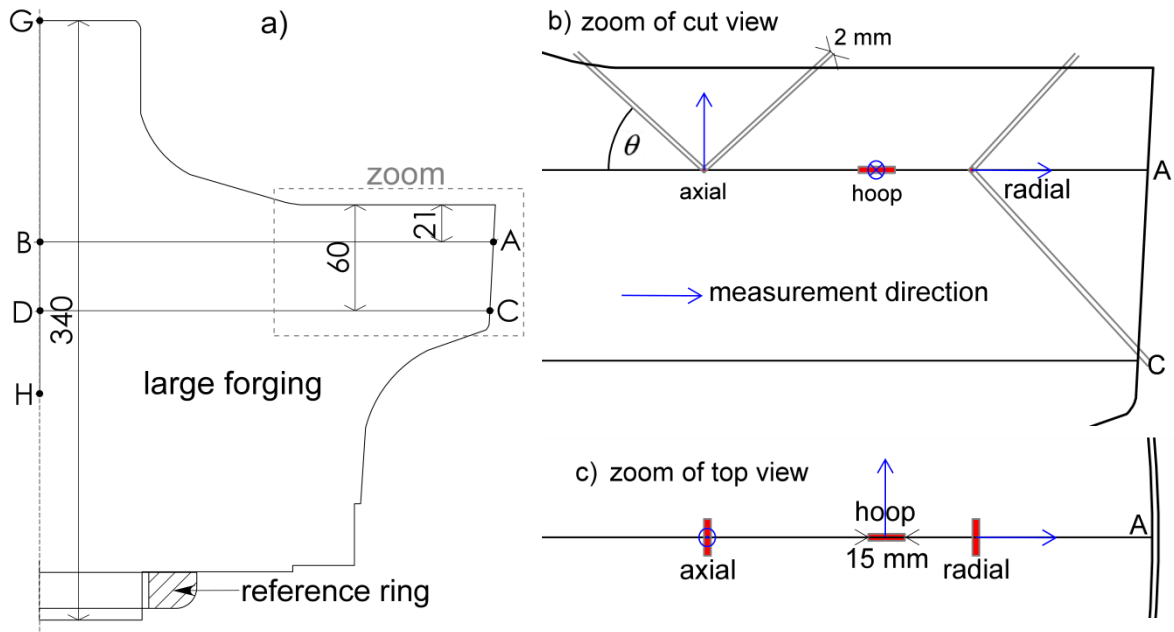


Figure 2-17 – Large forging (a) magnified to illustrate the 2 mm x 2 mm x 15 mm NGV used at SALSA in cut view (b) and in top view (c). Dimensions in mm.

Figure 2-17 shows the specimen geometry with the three segments scanned by ND at SALSA. Only [GH] was scanned at STRESS-SPEC in the T6 state. Figure 2-17-b and c show the NGV at SALSA in axial, radial and hoop configurations.

Due to the geometry of the forgings, the beam path in the axial configuration is generally shorter than in the hoop and radial configurations. Thus, a lower attenuation and consequently a higher signal-to-noise ratio are to be expected in the axial configuration. For the small forging (Figure 2-18), a NGV of 5 mm x 5 mm x 5 mm was chosen.

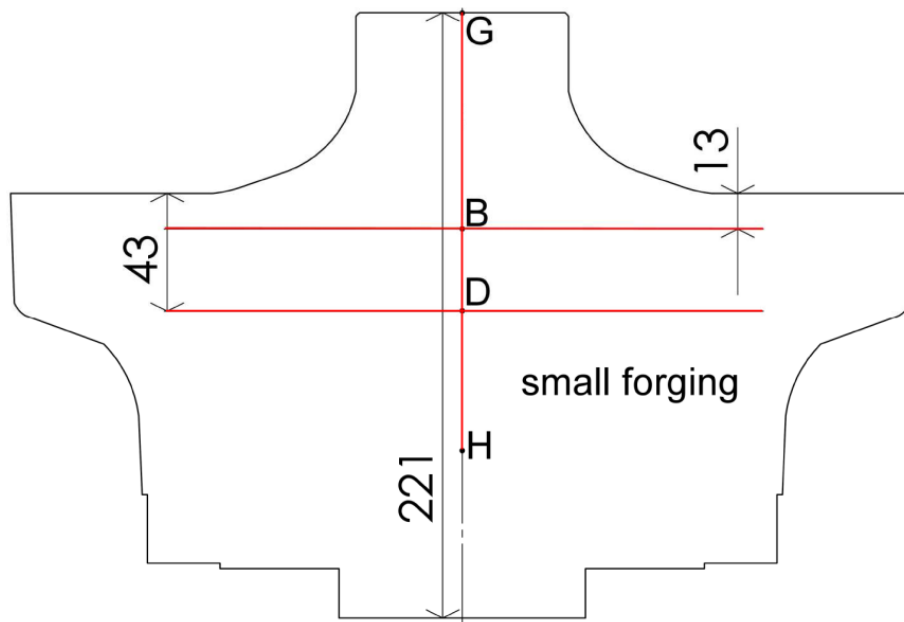


Figure 2-18 – Geometry of small forging showing the three scanlines for ND measurements. Dimensions in mm.

2.4.3. Results in as-quenched thick plates

Six plates, whose dimensions are given in *Table 2-2*, were measured by neutron diffraction. The residual strain measurements are given in *Figure 2-19*.

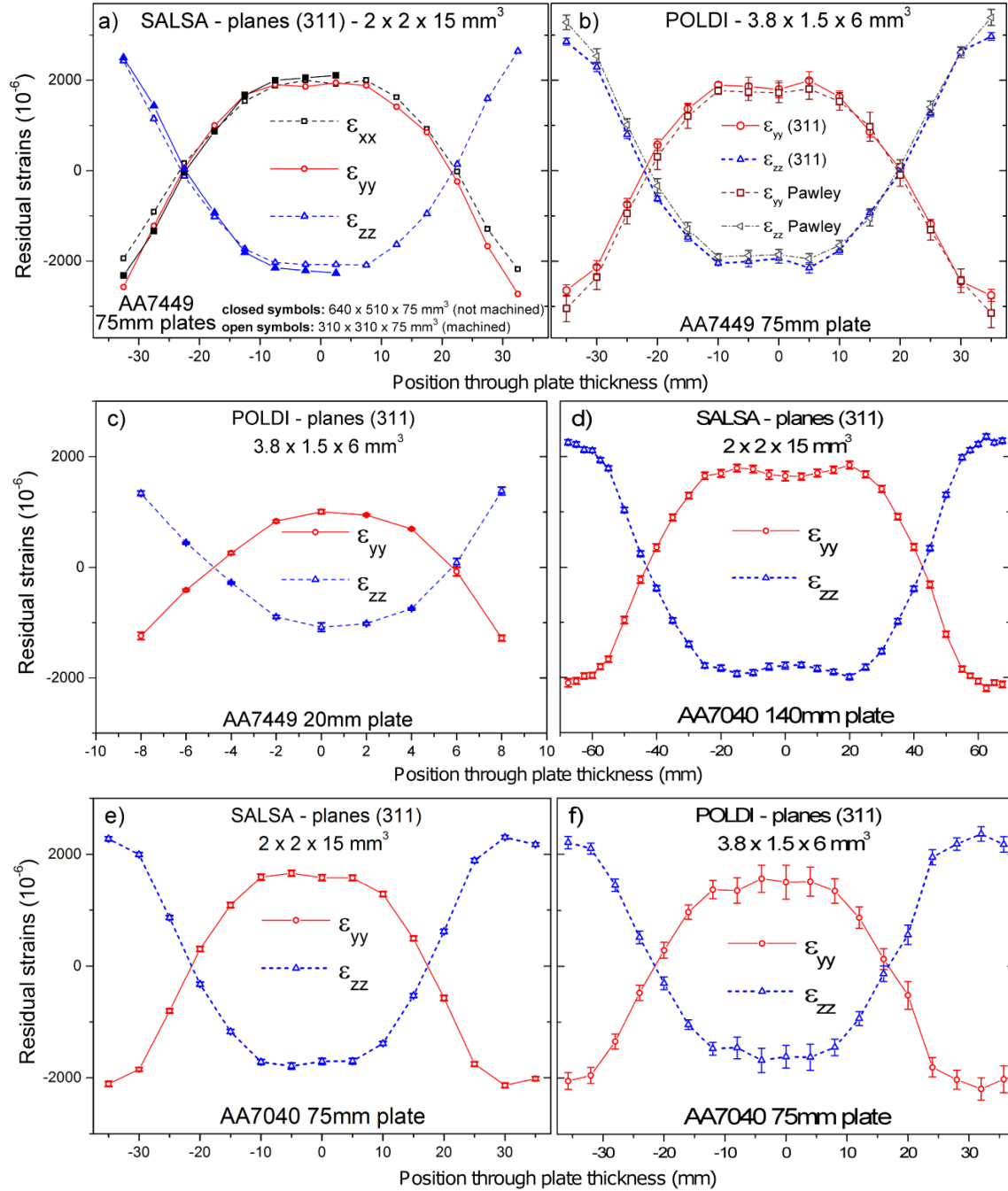


Figure 2-19 - Measured residual elastic strains through the thickness of as-quenched plates.

In *Figure 2-19-a*, the strain profiles (ϵ_{xx} and ϵ_{zz}) are very close in the two plates of different dimensions but identical thickness. This indicates that cutting the $640 \times 510 \times 75 \text{ mm}^3$ plate to obtain the $310 \times 310 \times 75 \text{ mm}^3$ plate (easier to manipulate) has little impact on residual strains at plate center. The measurements in three perpendicular directions

(Figure 2-19-a) show that the in-plane strain components are almost equal in the 310 × 310 × 75 mm³ AA7449 plate:

$$\varepsilon_{xx} \approx \varepsilon_{yy} \quad \text{Eq. 2-14}$$

Eq. 2-14 was assumed to be also valid for the other plates for which only two strain components, ε_{yy} and ε_{zz} , were measured as shown in Figure 2-19-b to f. Figure 2-19 also shows that the following equation holds for all the measurements:

$$\varepsilon_{zz} \approx -\varepsilon_{yy} \quad \text{Eq. 2-15}$$

At POLDI, although some texture was evidenced in the 75 mm thick AA7449 plate [29], data statistics was sufficiently good to carry out single peak analysis on individual Bragg reflections. Figure 2-19-b shows that residual strains calculated using a single peak corresponding to (311) planes are almost equal to those calculated by multiple peak (Pawley) analysis using 11 peaks.

The residual strains in the AA7449 (a and b) and AA7040 (e and f) 75 mm thick plates measured at SALSA and POLDI are close to each other. The lower error bars at SALSA (too small to be clearly seen in Figure 2-19) compared to those at POLDI are explained by the larger NGV (60 mm³ against 34.2 mm³ at POLDI), the higher neutron flux and the use of a 2D detector at SALSA instead of a 1D detector at POLDI. SALSA was thus chosen for the 140 mm thick plate. In-plane strains being equal, Hooke's law becomes:

$$\sigma_{yy} = \frac{E}{1+\nu} \varepsilon_{yy} + \frac{E\nu}{(1+\nu)(1-2\nu)} (2\varepsilon_{yy} + \varepsilon_{zz}) \quad \text{Eq. 2-16}$$

Using Eq. 2-16, the RS measurements are given in Figure 2-20.

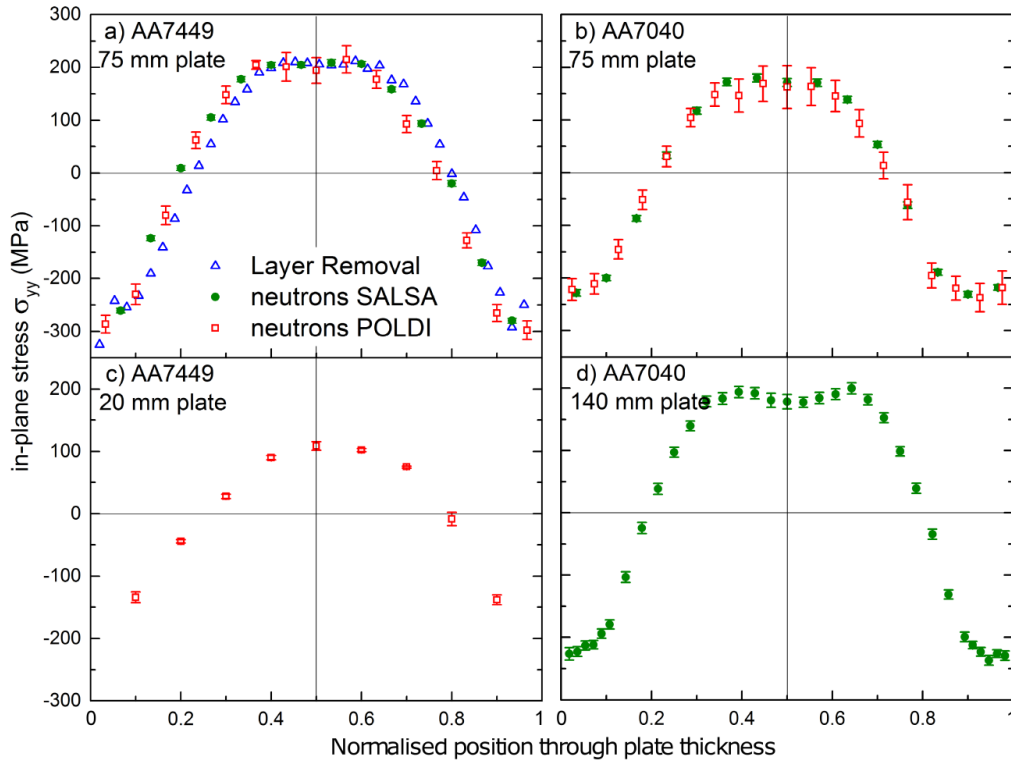


Figure 2-20 – Residual stress in as-quenched (a) 75 mm thick AA7449, (b) 75 mm thick AA7040, (c) 20 mm thick AA7449 and (d) 140 mm thick AA7040 plates. Measurement legend is given in (a).

The skin-core effect appears clearly. Stresses are higher in absolute value at the surface than in the centre since the quenching rate is higher.

The agreement is excellent between measurements by neutron diffraction and layer removal (mean of two measurements) in the 75 mm thick AA7449 plate (a) and between ND measurements performed at two different diffractometers (a and b). RS are higher in the 75 mm thick AA7449 plate (a) than in the 75 mm thick AA7040 plate because AA7449 contains more alloying elements than AA7040.

2.4.4. Results in forgings

Results along forging axis (segment GH)

The 2θ -profiles along the axis of the forgings are shown in *Figure 2-21*.

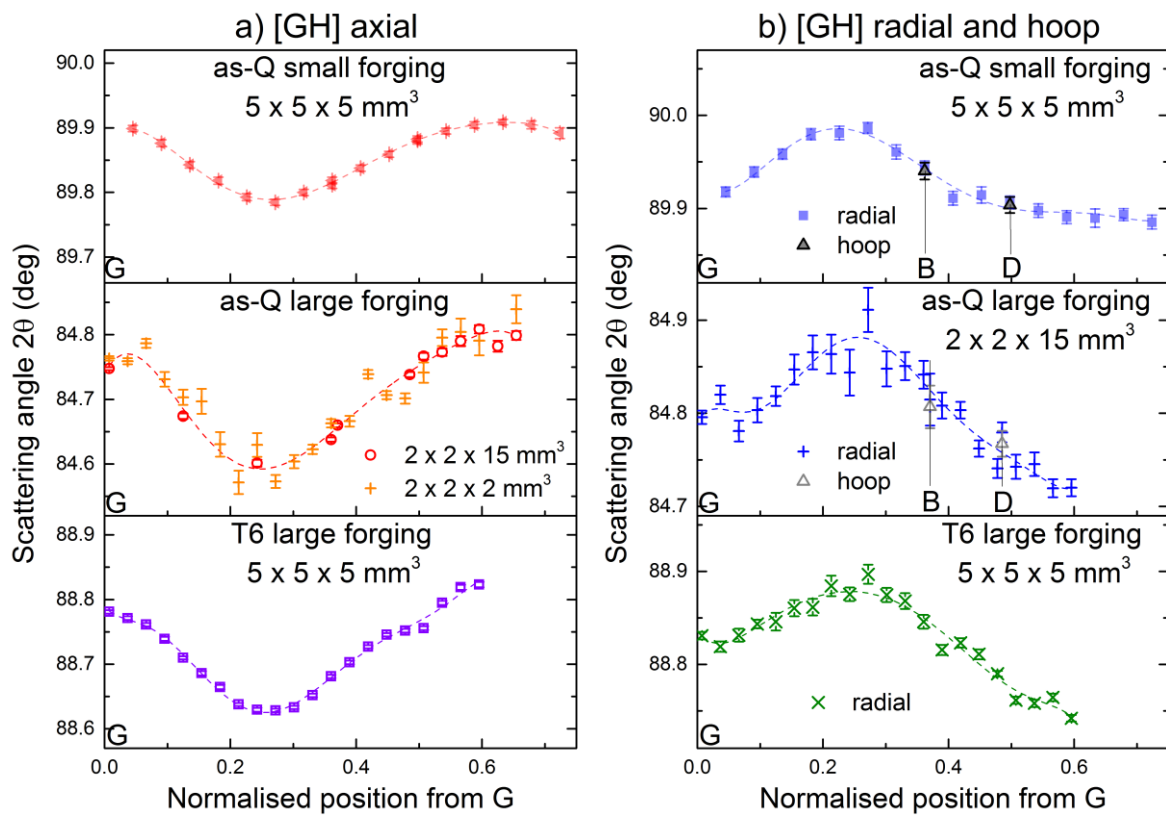


Figure 2-21 – Evolution of 2θ along [GH] in axial (a) and radial/hoop (b) configurations together with 7th order polynomial fit (dashed lines) for residual stress calculation.

The 2θ -profiles have a similar shape for the three forgings. The different 2θ -values for the two different diffractometers are due to the use of different wavelengthsⁱ. The amplitude of 2θ -profile of the small forging is lower than that of the large forgings. This indicates that RS in the small forging will be lower than RS in the large ones.

The main difference between the results in *Figure 2-21* is in the error bars which represent the statistical error of the peak position determined by peak analysis. Selected diffraction peaks are given in appendix 7.2 in order to understand the differences in the

ⁱ This does not influence the calculated strain according to Eq. 2-9.

errors. They show that the larger the gauge volume and the shorter the beam path are, the better the signal-to-noise ratio is. In *Figure 2-21-b*, the lower error bars at STRESS-SPEC (as-Q small and T6 large forgings) compared to those at SALSA (as-Q large forging) are explained by both the larger NGV (125 mm³ against 60 mm³ at SALSA) and the larger area of the 2D detector at STRESS-SPEC. In the measurements, it is verified at positions B and D (*Figure 2-21-b*) that radial and hoop components are almost equal. Residual strains are calculated using the data in *Figure 2-21*, Eq. 2-8 and Eq. 2-9. The stress-free reference value is adjusted to approach zero normal stress close to the surface (position G). Radial and hoop strains being equal along [GH], Hooke's law becomes:

$$\sigma_{ij} = \frac{E}{1+\nu} \varepsilon_{ij} + \frac{E\nu}{(1+\nu)(1-2\nu)} (2\varepsilon_{rr} + \varepsilon_{zz}) \quad \text{Eq. 2-17}$$

In order to decrease the variations of stress due to the trace in Hooke's law, the 7th order polynomial fits of the 2 θ -profiles in *Figure 2-21* are used instead of the raw data to calculate residual stresses. The results are shown in *Figure 2-22*.

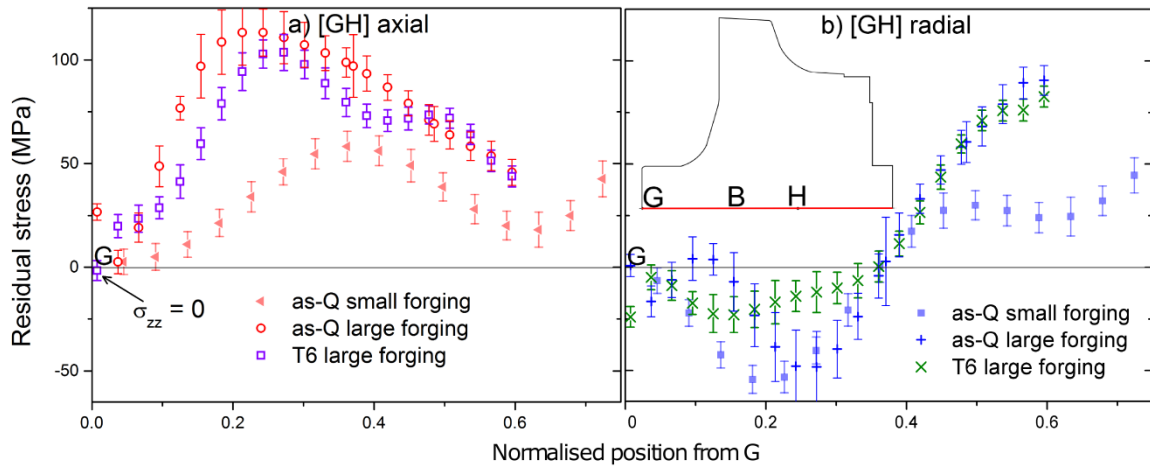


Figure 2-22 – Axial (a) and radial (b) residual stress components along [GH] using $\theta_0 = 89.91^\circ$, $\theta_0 = 84.79^\circ$ and $\theta_0 = 88.806^\circ$ for the as-Q small, as-Q large and T6 large forgings respectively.

The residual stress profiles of the three measurements have two similar features:

- Close to the surface, the forging is in a bi-axial compression state (radial and hoop stress components are between ca. -50 and 0 MPa).
- The core of the forging (from a normalised position of ca. 0.5 from G) is in tri-axial tension.

In the large forging, RS in the T6-state are lower than those in the as-quenched state (max. 35 MPa difference). This is attributed to relaxation during artificial ageing.

In the as-quenched state, tensile RS in the large forging are about two times higher than those in the small forging.

Results along forging radius [AB] and [CD]

The 2 θ -profiles along the radius of the as-quenched forgings are shown in *Figure 2-23*.

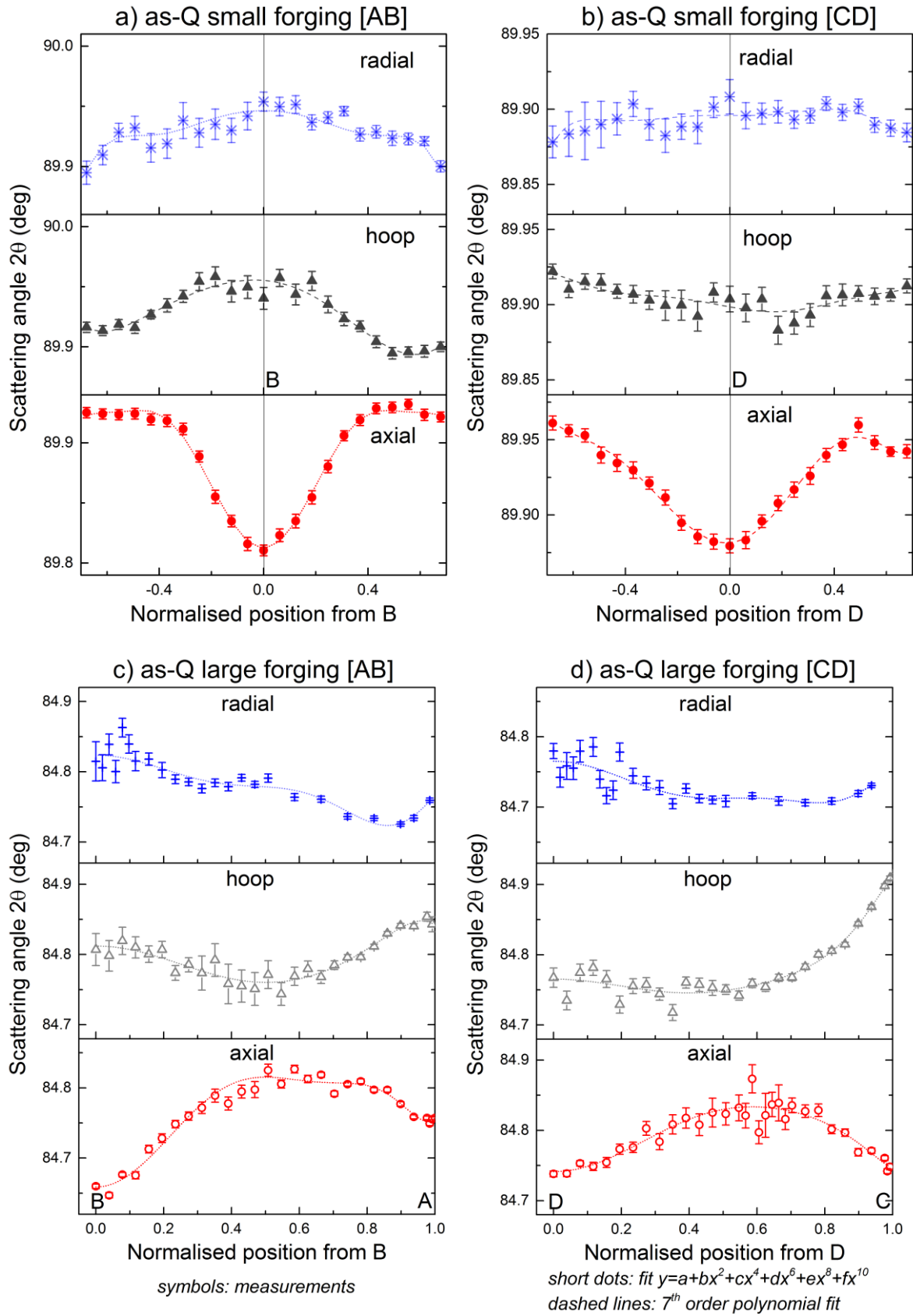


Figure 2-23 – Evolution of 2θ along radius of as-Q small forging (a) and (b) and as-Q large forging (c) and (d). The legend in (c) and (d) applies to the four graphs.

The measurements on the small forging give almost symmetrical results about the axis in radial and axial configurations on [AB] (a). Thus, these 2 θ -profiles are fitted with an even polynomial function (short dots) for residual stress calculation. Due to their slight asymmetry, the other 2 θ -profiles in the small forging are fitted with a 7th order polynomial (dashed lines). Similarly to [GH], the 2 θ -profiles on [AB] and [CD] have a similar shape for the two forgings. As expected by counting statistics considerations, the low signal-to-noise ratio gives poor peak fits in the radial and hoop configurations close to the center of the large forging. Residual strains are calculated using the stress-free reference value so that radial stress approaches zero close to the surface (positions A and C in large forging). Since no close-to-surface measurements were performed on the radial scanlines of the small forging, normal stress at position G was taken.

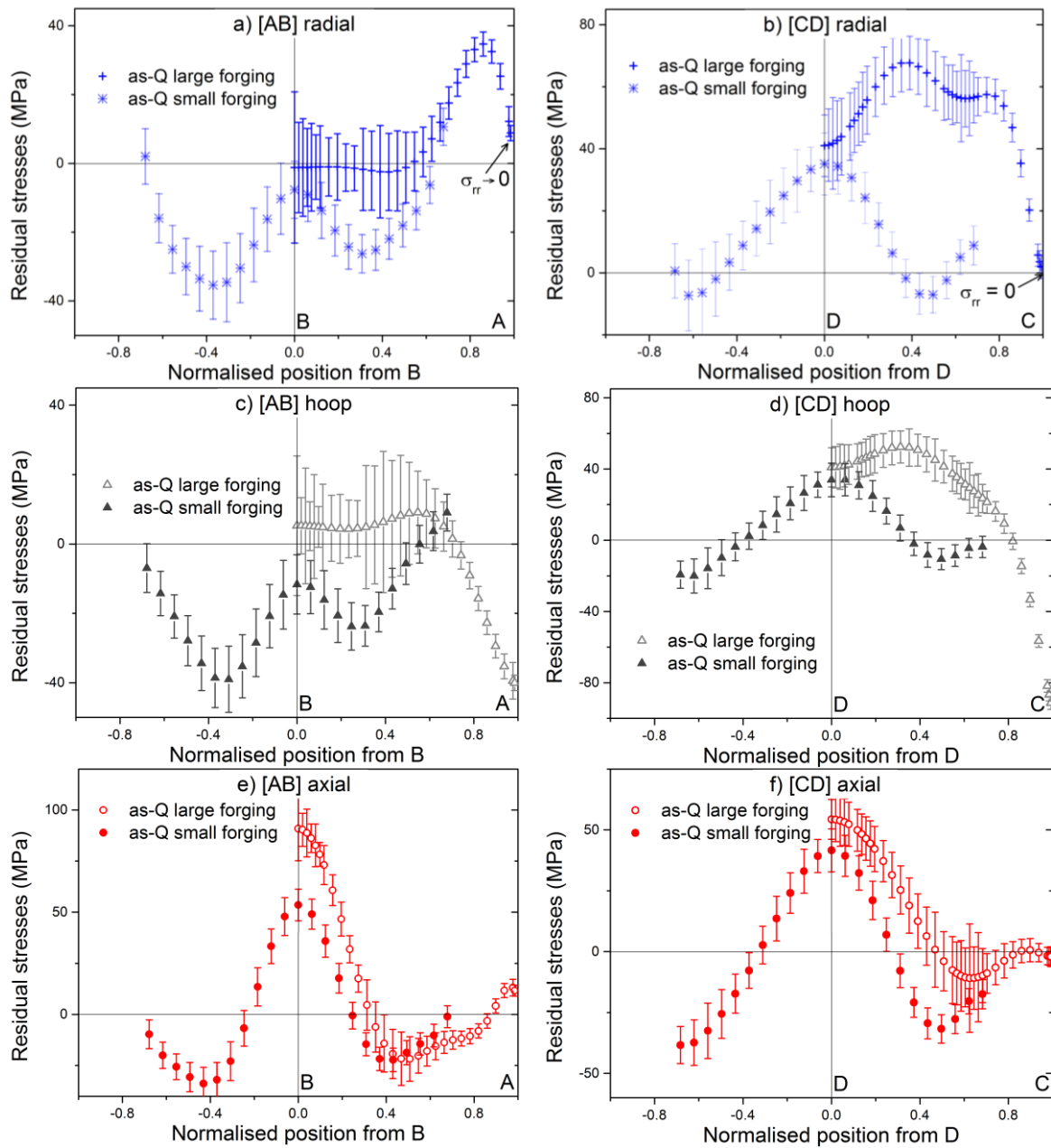


Figure 2-24 – Residual stress components along [AB] (left) and [CD] (right) using $\theta_0 = 89.91^\circ$ and $\theta_0 = 84.782^\circ$ for the as-Q small and large forgings respectively.

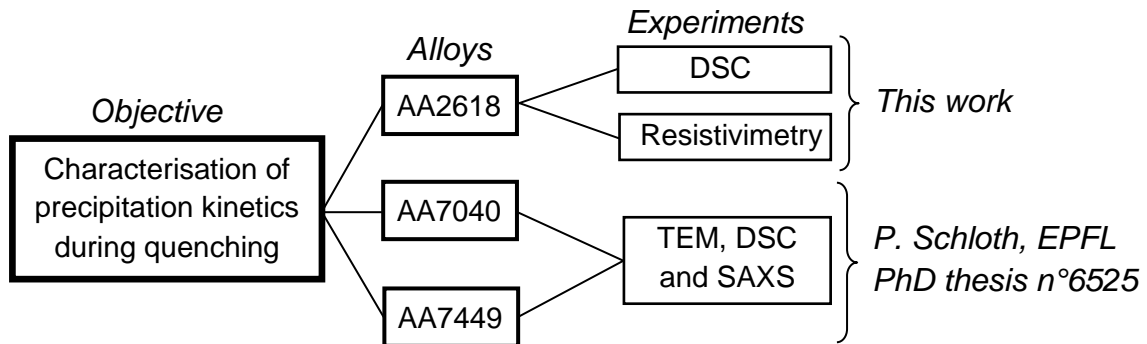
In the small forging, the three RS components are slightly asymmetric as expected by the slight asymmetry of the 2θ -profiles. On both radial scanlines, the radial and hoop stress components are almost equal. This is not the case in the large forging. The shape of the radial – (a) and (b) – and hoop – (c) and (d) – stress components is different in the two forgings. The shape of the axial stress component – (e) and (f) – is similar in both forgings.

2.5. Summary of chapter 2

Three heat treatable aluminium alloys are investigated in this work: AA7449, AA7040 and AA2618. According to the literature, AA7449 is the most quench-sensitive and therefore the most difficult to characterise in terms of mechanical behaviour in relation to its precipitation state. Temperature and RS measurements are performed at plate center to get rid of the fact that transition boiling regime is position dependant and also to avoid edge effects. This allows using a global heat transfer coefficient in the simulation of quenching. Temperature measurements in a cold-water quenched 75 mm thick AA7449 plate compare well with the results of a FE simulation using a HTC found in the literature. As expected by the large thermal gradients during cold-water quench, the residual stresses measured in the 75 mm thick AA7449 plates are large (ca. 200 MPa at mid-thickness and -300 MPa at surface). RS are lower in the 75 mm thick AA7040 plate since AA7040 contains less alloying elements than AA7449. RS in two plates of different thicknesses (20 mm and 140 mm) were also measured by ND to later check the validity of the FE model on a large range of thicknesses. In order to be more confident in the RS measurements by ND, it was checked that two different diffractometers, SALSA and POLDI, give the same results. Furthermore, the agreement between these ND results and the results of the layer removal method is excellent.

AA2618 is supposed to be less quench-sensitive than AA7449 and therefore easier to characterise in terms of mechanical behaviour in relation to its precipitation state. Here, the difficulty comes from the complex geometry of the forgings. Temperature measurements in a boiling-water quenched large forging show that cooling can be considered axisymmetric but it is strongly position-dependant. Therefore, six surfaces are defined to apply six different HTCs. Thanks to a parameterisation of the HTCs and a special optimisation procedure, a set of HTCs is found to fit relatively well the measurements. As expected by the use of boiling water instead of cold water, the residual stresses measured in an as-quenched large forging (between ca. -80 and 100 MPa) are lower than those in thick plates. RS measurements on the same forging after artificial ageing show that stress relaxation during T6 treatment is low (max. 35 MPa). RS in a small forging were also measured by ND to later check the validity of the FE model on a range sizes. In this small forging, measurements along two different diameters show that the 2θ -profiles (and hence the strains) are fairly symmetrical about the forging axis. This means that an axisymmetric model of quenching can be used for RS calculations. Due to the trace in Hooke's law which propagates errors, the symmetry in terms of residual stress is poor. Consequently, the residual strains in the forgings should be compared when confronting measurements with simulations.

3. Characterisation and modelling of precipitation during quenching



As sketched above, this work focuses on precipitation in AA2618 and the PhD work of P. Schloth focuses on precipitation in AA7449 and AA7040 [50]. The results for AA7449 and AA7040 come from Transmission Electron Microscopy (TEM), differential scanning calorimetry and small angle X-ray scattering experiments performed by P. Schloth and are therefore given in the state of the art (part 3.1). Measurements performed in the present work were done on AA2618. Differential scanning calorimetry experiments upon cooling are shown in part 3.2. In part 3.3, a Gleeble machine is used to perform isothermal quenching resistivity measurements consisting in quenching the alloy down to a given temperature and holding it at this temperature. Finally, the precipitation model used in the TMM model is shortly presented in part 3.1, together with an example of calibration of its parameters.

3.1. State of the art

3.1.1. Differential scanning calorimetry

Differential scanning calorimetry has been extensively used to quantify precipitate microstructures in heat treatable aluminium alloys. DSC measurements are usually performed upon heating starting from an initial precipitation state to be characterised.

Lu *et al.* [67] performed DSC upon heating at 20 K/min to characterise the precipitation state of AA2618 samples in various conditions (as-quenched and artificially aged at 200°C for various times ranging from 5 minutes to 80 hours). The as-quenched sample featured an exothermic peak at ca. 100°C attributed to the formation of GPB zones. This peak was not observed for the artificially-aged samples since GPB zones had already formed during artificial ageing as expected by the very rapid (within 2 minutes at 200°C) increase in strength measured by Polmear [68] on AA2618. For all conditions, GPB zones dissolved between 160°C and 270°C (endothermic peak). The underaged samples (≤ 20 hours at 200°C) featured a broad exothermic peak between 270°C and 350°C attributed to the precipitation of S and S' phases which dissolve between 350°C and 470°C. No exothermic peak was observed in the overaged samples (≥ 48 hours at

3. Characterisation and modelling of precipitation during quenching

200°C) since the S phase had almost fully precipitated during the long artificial ageing, allowing the S phase only to dissolve during DSC (endothermic peak between 300°C and 470°C).

Similar results on AA2618 were obtained by Oguocha and Yannacopoulos [69] who performed various heating rates in DSC to determine the formation and dissolution kinetics parameters for GPB zones.

The activation energy of GP zones formation and dissolution in AA7449 were determined in the PhD work of P. Schloth [50] by DSC heating runs. These measurements showed that GP zones formation is influenced by quenched-induced vacancies which have to be considered in a precipitation model applied to quenching.

DSC was performed during cooling from the solutionising temperature on 2024 alloy [70], 6xxx series alloys [71, 72], 7020 and 7150 alloys [73-75] and allowed determining the continuous cooling precipitation (CCP) diagrams of these alloys. Such diagrams being absent in the literature for AA7449 and AA2618, DSC measurements upon cooling have been performed in the frame of this CCMX project. In his PhD work, P. Schloth [50] performed DSC upon cooling on AA7449 at constant cooling rate ranging from 2 K/min to 80 K/min. A first exothermic peak at high temperature (starting around 450°C at 2 K/min and 430°C at 80 K/min) was attributed to the formation of η . A second exothermic peak was observed between 260°C and 130°C (typical range of η' formation) with a maximum around 200°C. In AA7449 where 80 K/min is way too slow to avoid precipitation of η , calorimetric reheating experiments would be necessary to monitor precipitation of the low temperature reactions, see for instance Zohrabyan *et al.* [76]. In the present work, to complete DSC experiments of P. Schloth, DSC upon cooling is performed on AA2618 (see section 3.1.1) which is less quench-sensitive than AA7449.

3.1.2. Resistivity

Based on the fact that solute is pumped to form precipitates, a number of methods (Jominy test, resistivity, thermoelectric power) have been developed to measure indirectly the loss of solute during quenching [77, 78]. The traditional way to monitor solute loss is to measure the drop of hardness in T6-state after an isothermal holding at high temperature. Such measurements being time consuming, *in situ* resistivity has proven to be a useful technique to characterise precipitation kinetics in AA [31, 79]. Resistivity is monitored to determine the solute loss associated with the formation of precipitates according to Mathiessen's rule, stating that the effect of dissolved alloying elements on the electrical resistivity of a metallic alloy is linear and additive. Archambault and Godard [31] used a home-made quenching resistivimeter to characterise precipitation kinetics in AA7010. After validating *in situ* resistivity measurements upon cooling at constant cooling rates against DSC measurements, they performed isothermal quenching measurements at different temperatures. The results were used to calibrate a precipitation model and to nucleation diagram of AA7010. Such data is useful to assess the quench sensitivity of heat treatable aluminium alloys and to design adequate heat treatments. Yet isothermal quenching resistivity has remained a minor technique in the

last decade, probably because precise control of isothermal quenching cycle is difficult in conventional resistivimeters. Nevertheless, the Gleeble machine appeared to be capable of characterising precipitation kinetics by isothermal quenching resistivity measurements for relatively low quench-sensitive AA such as AA7010 [9].

Following this validation work, the Gleeble machine was used to perform isothermal quenching resistivity measurements on AA2618 at temperatures higher than the artificial ageing temperature. The results are reported in section 3.3.2.

3.1.3. Small Angle X-ray Scattering

In order to quantify precipitate microstructures and monitor precipitation kinetics, small angle X-ray scattering (SAXS) has been extensively used in the last 50 years both *ex situ* and *in situ* for heat treatable aluminium alloys (except AA6xxx due to their low contrast in atomic number) [80]. In SAXS experiments, the radius of gyration (Guinier radius), r_g is usually given as an estimate of the size of the scattering objects. Indeed, Deschamps and De Geuser [81] showed that r_g provides an estimate with a precision lower than 10% of the average precipitate (moderate aspect ratio) radius, \bar{r} when the precipitate size distribution (PSD) dispersion is 0.2. The Guinier radius being sensitive to the larger precipitates, it overestimates the average precipitate radius for broad PSDs (dispersion > 0.2). The volume fraction of precipitates can be calculated from the scattering signal provided the chemical composition of the precipitates is known. Therefore, the precision on the volume fraction can be estimated to $\pm 10\%$ due to the uncertainties on composition [82].

In the literature, most SAXS experiments are reported in precipitation states different from as-quenched states.

Deschamps *et al.* [43] monitored the precipitation kinetics of AA2618 during artificial ageing at 200°C to understand its two hardening responses: i) a very rapid (within 2 min) increase in strength [68] followed by ii) an extended yield strength plateau that exists until a rise to peak hardness (at 200°C after ca. 2h) [67]. Thanks to SAXS experiments, these features were attributed to i) the formation of Cu-Mg-rich hardening clusters and ii) their continuous domination of the microstructure associated with a compensation of the small loss of cluster by an increase in their size and the formation of the first stable S' precipitates [43].

Fribourg *et al.* [82] performed *in situ* SAXS experiments to monitor the precipitation kinetics during artificial ageing of AA7449 to calibrate a precipitation model [42].

Ex situ SAXS experiments on AA7040 were performed by Dumont *et al.* [8] after slow (~ 7 K/sⁱ) and fast (~ 850 K/sⁱ) quenches followed by 84 hours at room temperature and artificial ageing. The measured radius and volume fraction of η' phase during artificial ageing was found to be identical for both quenches, due to the low quench-sensitivity of AA7040 (critical cooling rate lower than 7 K/s according to Dumont's experiments).

In the recent paper of Schloth *et al.* [10], *in situ* SAXS experiments on AA7449 during fast coolings similar to the ones in thick plates were performed for the first time. These

ⁱ initial values valid down to ca. 250°C

3. Characterisation and modelling of precipitation during quenching

SAXS results are presented hereafter and will be used in the present work for calibration of the yield strength model.

Preliminary SAXS measurements performed by P. Schloth during coolings of AA2618 (not shown here) revealed anisotropic scattering of large objects around 400°C attributed to the formation of δ phase. Isotropic scattering of subnanometer-size objects (Guinier radius ~ 0.4 - 0.5 nm) was measured below ca. 300°C. A cluster volume fraction of ca. 0.4% was reached after cooling similar to the measured ones in forgings [83].

Early precipitation during cooling of AA7449

The results (Guinier radius and volume fraction of precipitates) of the SAXS measurements for AA7449 are shown in *Figure 3-1*. For the sake of brevity, the average radius and the volume fraction of small precipitates calculated using a precipitation model calibrated by P. Schloth in his PhD work [50] are also shown along with the measurements.

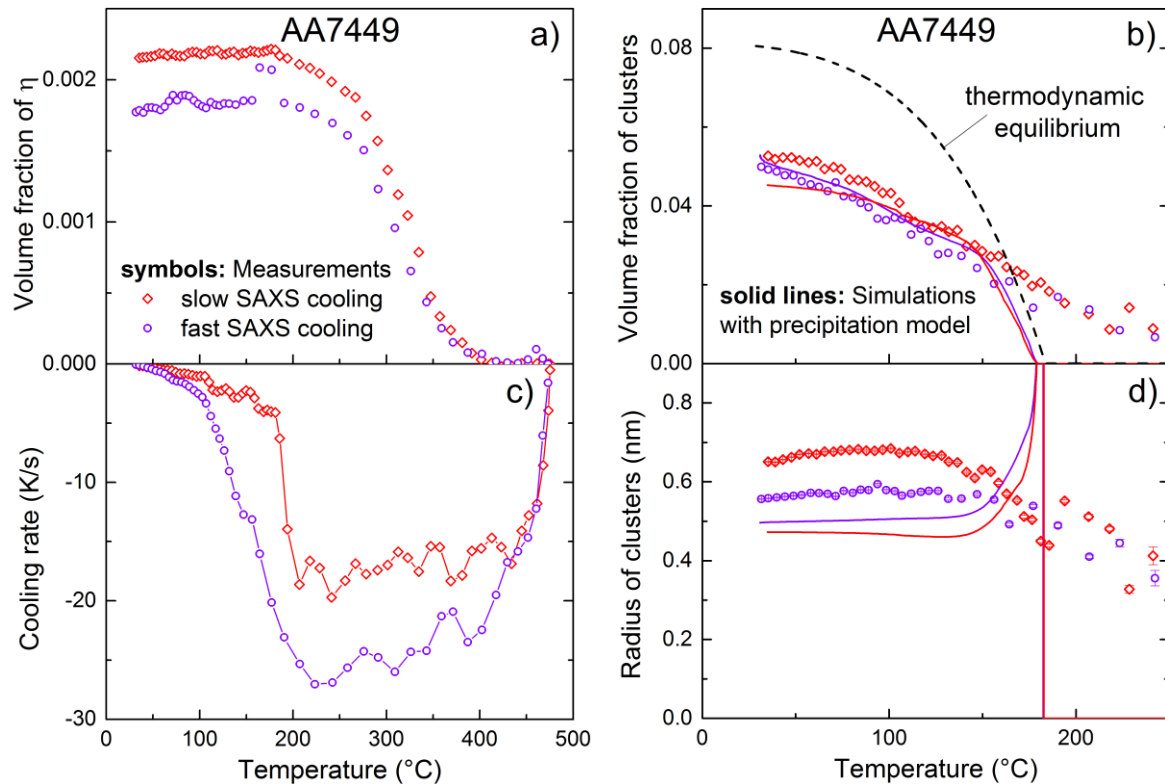


Figure 3-1 – Results of in situ SAXS experiment for AA7449. Measured volume fraction of η phase (a) with corresponding cooling rate (c). Measured and simulated volume fraction (b) and experimental Guinier radius and average simulated radius (d). The legend of the measurements is given in (a) and the legend of the simulations in (b). Adapted from Schloth et al. [10].

During cooling, the scattering of large objects corresponding to the η phase and small objects corresponding to clusters has been recorded. *Figure 3-1-a* shows that precipitation of η starts at ca. 400°C and reaches a maximum volume fraction at about 200°C. Precipitation of clusters starts at ca. 250°C with a continuous increase of volume

3. Characterisation and modelling of precipitation during quenching

fraction down to room temperature (*Figure 3-1-b*) while the Guinier radius is fairly constant below ca. 150°C (*Figure 3-1-d*).

During fast SAXS cooling, *Figure 3-1-a* and *c* show that a cooling rate of ca. 25 K/s is not fast enough to avoid precipitation of the η phase. Therefore, the high temperature critical cooling rate of AA7449 is higher than 25 K/s. The volume fraction of η phase is higher after slow than after fast SAXS cooling which was expected since the slower the cooling is, the more time is available to form large precipitates at high temperature. Nevertheless, for the two coolings, the volume fraction of η is small compared to the value of ~0.08 corresponding to the maximal volume fraction that can be formed after slow cooling (calculated under equilibrium [50]). This, together with the fact that precipitation softening does not have a significant effect on RS as shown by Godard *et al.* [7], justified the choice of P. Schloth to model only one type of precipitates, namely the small ones.

A precipitation model has been calibrated by P. Schloth. The calculated volume fraction and average radius of clusters shown in *Figure 3-1-b* and *d* respectively compares well with the measurements. The average radius calculated by the precipitation model slightly underestimates the measured Guinier radius. This is due to the broader precipitate size distribution (PSD) measured by SAXS compared to the simulated one by the precipitation model as shown in *Figure 3-2*.

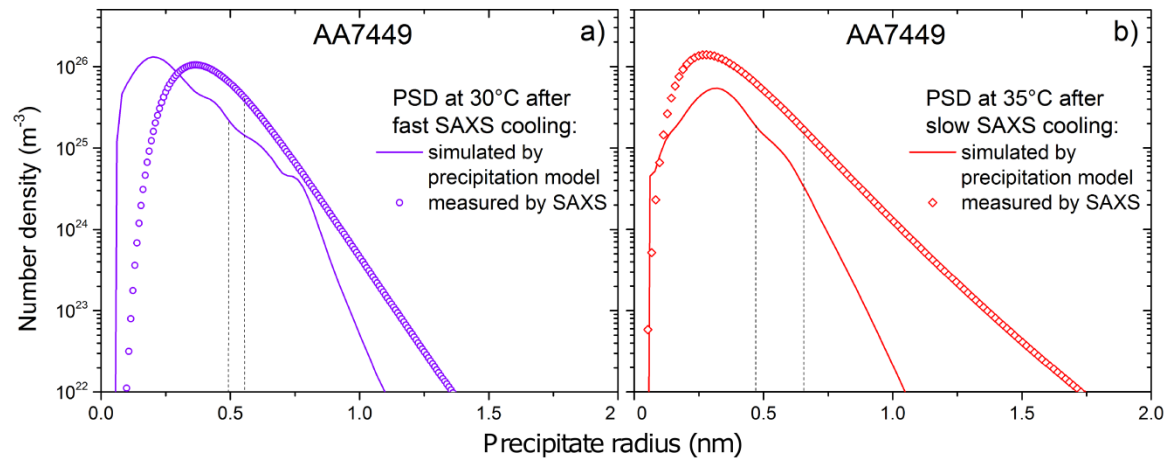


Figure 3-2 – Measured and simulated precipitate size distribution in AA7449 after fast (a) and slow (b) SAXS cooling. Vertical dashed lines: average radius from simulation and Guinier radius from measurements. Adapted from Schloth [50].

The measured PSD is broader after slow than after fast SAXS cooling. Although this was expected due to fact that the slower the cooling, the larger the precipitates, this result is not predicted by the simulation. The larger precipitates of the PSD are not predicted because no precipitation arises above 180°C due to the thermodynamic description used in the model (see section 3.4.1) which considers only GP(I) zones and not η' , that might form between 200-270°C.

Early precipitation during cooling of AA7040

Similar SAXS measurements were also performed by P. Schloth on AA7040. The results of these measurements for AA7040 are shown in *Figure 3-3* together with the simulations using the precipitation model which considers only GP(I) zones [50].

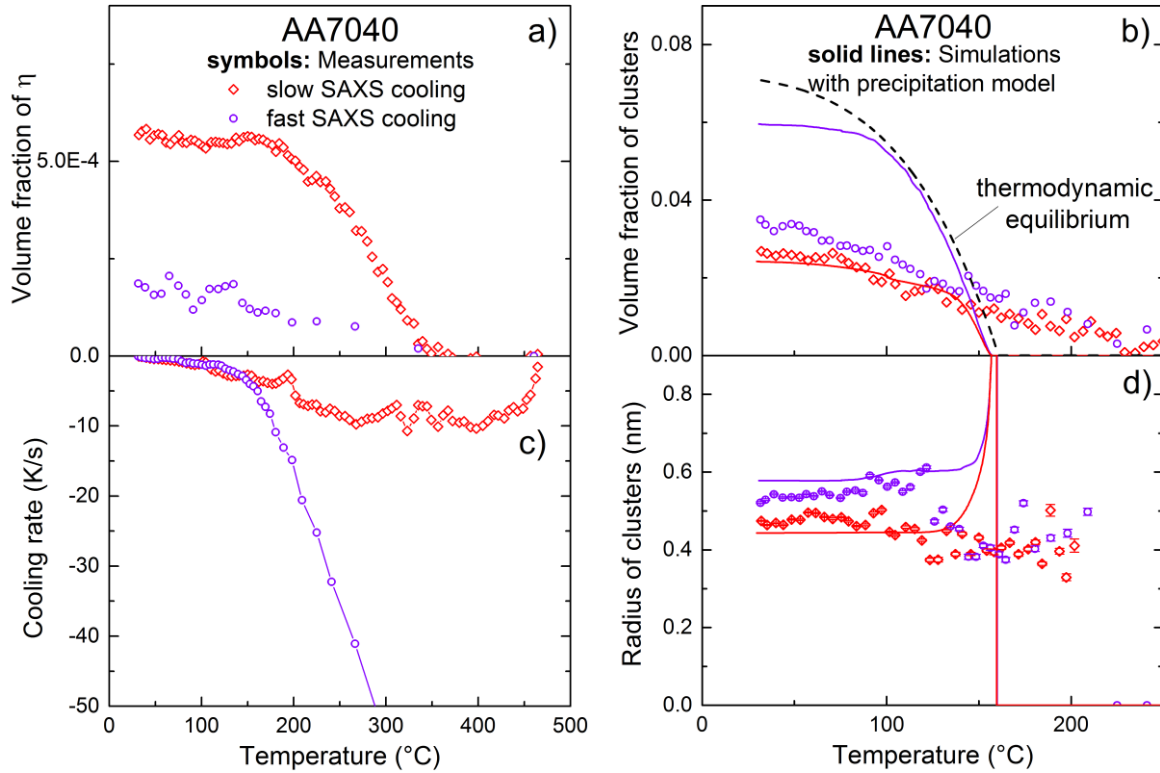


Figure 3-3 – Results of in situ SAXS experiment for AA7040. Measured volume fraction of η phase (a) with corresponding cooling rate (c). Measured and simulated volume fraction (b) and experimental Guinier radius and average simulated radius (d) of clusters. The legend of the measurements is given in (a) and the legend of the simulations in (b). Adapted from Schloth [50].

For AA7040, precipitation of η starts at ca. 350°C and reaches a maximum volume fraction at about 150°C. Precipitation of clusters starts at ca. 250°C with a continuous increase in volume fraction down to room temperature while the radius is fairly constant below ca. 100°C. The volume fractions of small and large precipitates are lower for AA7040 than for AA7449 since the latter alloy contains more solute elements available for precipitation. During fast SAXS cooling, it seems that the cooling rate of ~40-50 K/s is high enough to avoid precipitation of the η phase at high temperature (*Figure 3-3-a* and *c*). Therefore, the high temperature critical cooling rate of AA7040 should be close to 50 K/s.

As expected, the volume fraction of η phase is higher after slow than after fast SAXS cooling (*Figure 3-3-a*). Again, for the two coolings, the volume fraction of η phase is small compared to the value of 0.071 corresponding to the maximal volume fraction that can be formed after slow cooling (equilibrium). The simulated volume fraction and average radius of clusters shown in *Figure 3-3-b* and *d* respectively compare very well with the measurements during slow SAXS cooling. The agreement is poor for the volume

3. Characterisation and modelling of precipitation during quenching

fraction of clusters during fast SAXS cooling which is overestimated by a factor 2 by the simulation with the precipitation model. A better agreement could be found by adjusting the precipitation model parameters to better fit the volume fraction of clusters after fast SAXS cooling. Instead, it has been chosen to use the same calibrated parameters of clusters GP(I) zones in AA7449 and AA7040 (see section 3.4.1). This is physically sound but it overestimates the volume fraction of clusters after AA7040 fast SAXS cooling. This cooling being very close to that experienced by the surface of a 75 mm plate, this means that the yield strength predicted by the yield strength model and hence residual stresses will be overestimated by the thermo-metallurgical-mechanical model for 75 mm thick AA7040 plate.

The Guinier radii and volume fractions of clusters measured during slow and fast SAXS coolings for AA7449 and during slow SAXS cooling for AA7040 will be used in section 4.3.6 to calibrate the yield strength model. Furthermore, these three cooling conditions representative of industrial quenches will be reproduced in the Gleeble to obtain the corresponding yield strength values necessary for the calibration of the yield strength model.

3.2. Precipitation kinetics in AA2618 by DSC

Precipitation upon cooling has been characterised by DSC on AA2618 with various constant cooling rates. The first goal is to determine the high temperature critical cooling rate of AA2618 necessary to avoid precipitation of the stable *S* phase. The second goal is to provide experimental data that could be used to calibrate a precipitation model.

3.2.1. Principle and setup

A Netzsch 204F1 Phoenix® heat flow differential scanning calorimeter with AA2618 cylindrical samples was used - see *Figure 3-4*.

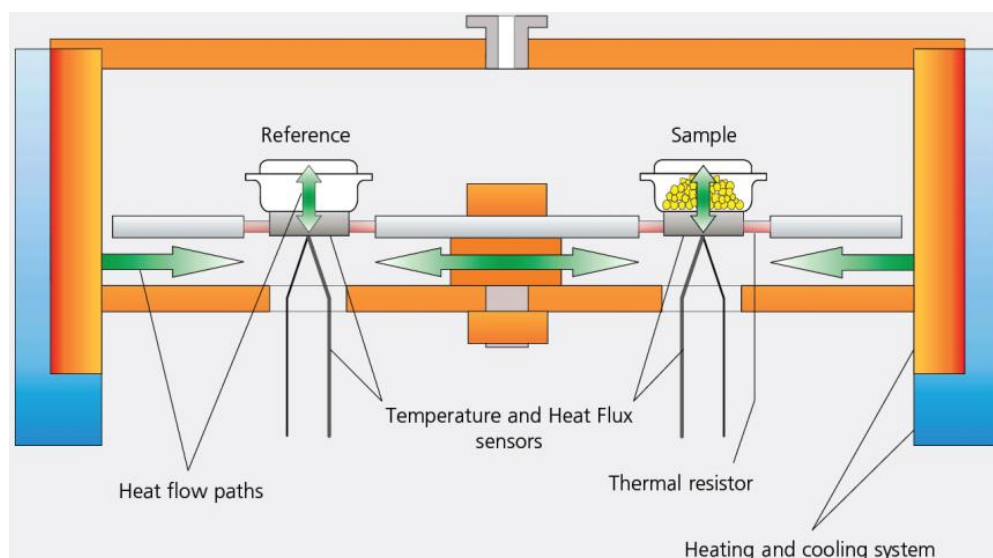
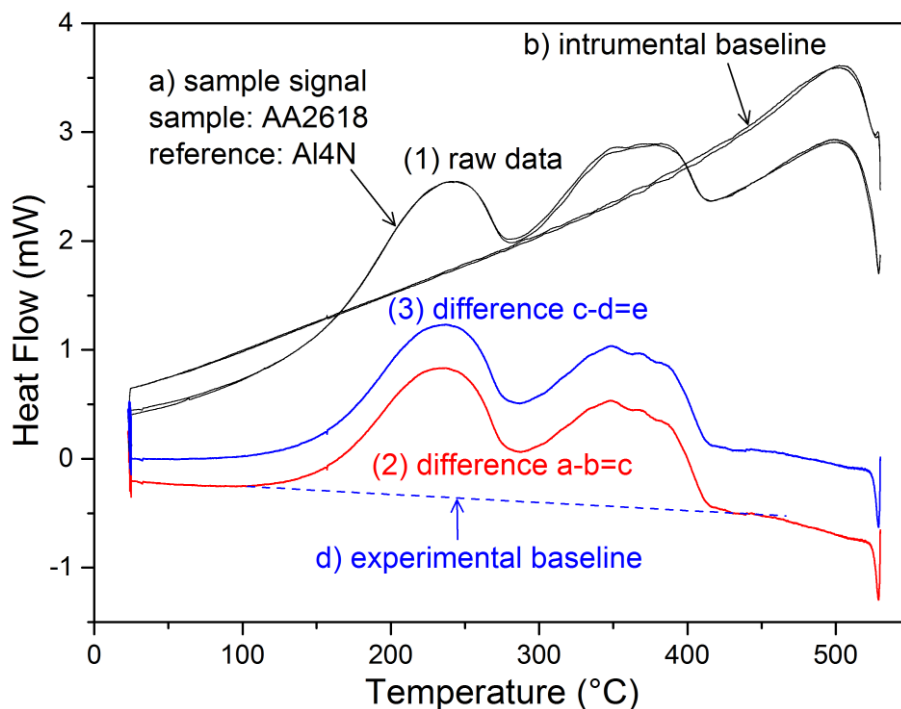


Figure 3-4 – Principle of the heat flow DSC. <http://www.netzsch-thermal-analysis.com>

3. Characterisation and modelling of precipitation during quenching

Based on a homogeneous temperature field in the furnace of the DSC, equal heat flows along the disk-shaped sensor are directed to the sample and reference sides. If the heat capacities of the sample and reference sides differ, or if the sample shows a change in heat absorption or loss due to transitions or reactions, the subsequent different heat flow causes temperature gradients at the thermal resistances of the sensor. Based on the works of Milkereit *et al.* [71, 84], the experimental procedure was defined as follows:

- the AA2618 samples have dimensions of about 4.5 mm in diameter and 1.9 mm in height, which results in a sample mass of approximately 82 mg. They were machined out from a block taken in a large forging in annealed state,
- a high purity aluminium Al4N reference sample with the same mass was placed in the reference furnace,
- the samples were placed in standard aluminium crucibles (ca. 39 mg, pierced lid),
- measurements were done at ambient pressure and under nitrogen as protective gas,
- prior to cooling, *in situ* solutionising treatment was achieved in the calorimeter at 530°C for 2h,
- two successive complete thermal cycles were achieved for each sample in order to check reproducibility,
- baseline correction was done as shown in *Figure 3-5-top*.



3. Characterisation and modelling of precipitation during quenching

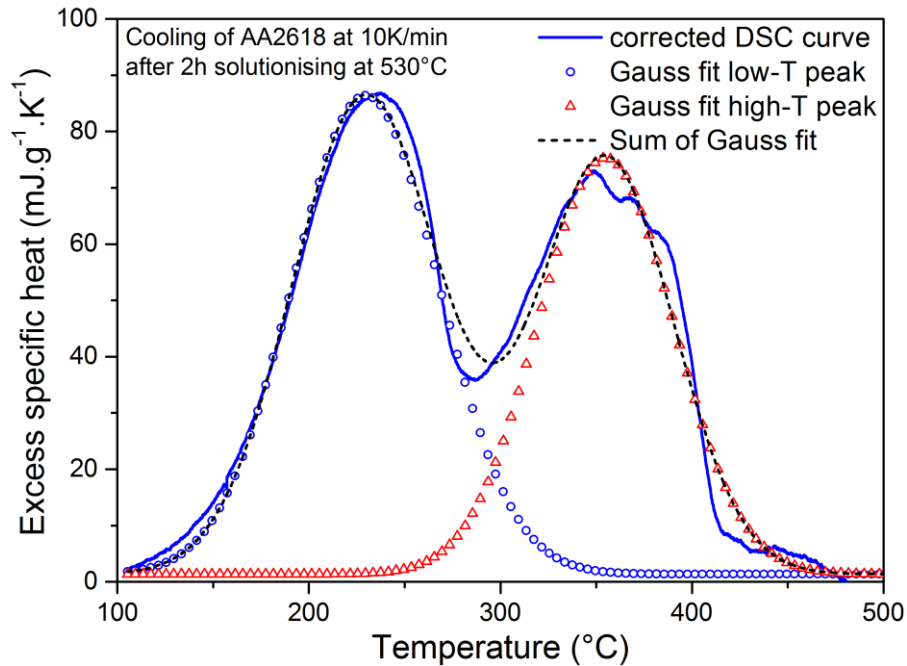


Figure 3-5 – Example of baseline correction (top) and peak fitting (bottom) for AA2618 cooled at 10 K/min.

Firstly, an instrumental baseline measurement is performed for each cooling rate with Al4N samples in reference and sample furnaces. To avoid baseline drift problems, sample and baseline measurements are done directly after each other.

Secondly, the heat-flow curve of an instrumental baseline measurement (b) is subtracted from the heat-flow curve of the appropriate sample measurement (a).

Then, the experimental baseline (d) is determined on the resulting curve (c) by taking the two common tangents (at low and high temperature where no metallurgical change occurs).

Thirdly, the experimental baseline (d) is subtracted from (c). DSC signal being proportional to sample mass and scanning rate, the resulting corrected heat flow curve is normalised by dividing by sample mass and cooling rate.

The obtained curve, so-called “excess specific heat capacity”, is fitted by two Gaussian functions as shown in *Figure 3-5-bottom*. The precipitation start and end temperatures are determined from the fit. The area under the peak(s) gives information about the released specific heat called “specific precipitation heat”. This value is a measure of the volume fraction of precipitates.

In order to confirm the DSC curves, five Vickers hardness indentations (1 kg for 20 sec) were performed on each sample after natural ageing at 20°C for 24 h followed by artificial ageing at 200°C for 20 h.

3.2.2. Results

The results are shown in *Figure 3-6* which compares DSC thermograms with various cooling rates between 1 K/min and 70 K/min. The maximal achieved cooling rate of 70 K/min corresponds approximately to the measured cooling rate at the center of the large forging (see section 2.2.3). Precipitation of S and probably S' phases occurs on cooling for all cooling rates. These DSC experiments indicate that precipitation takes place at the center of large forgings.

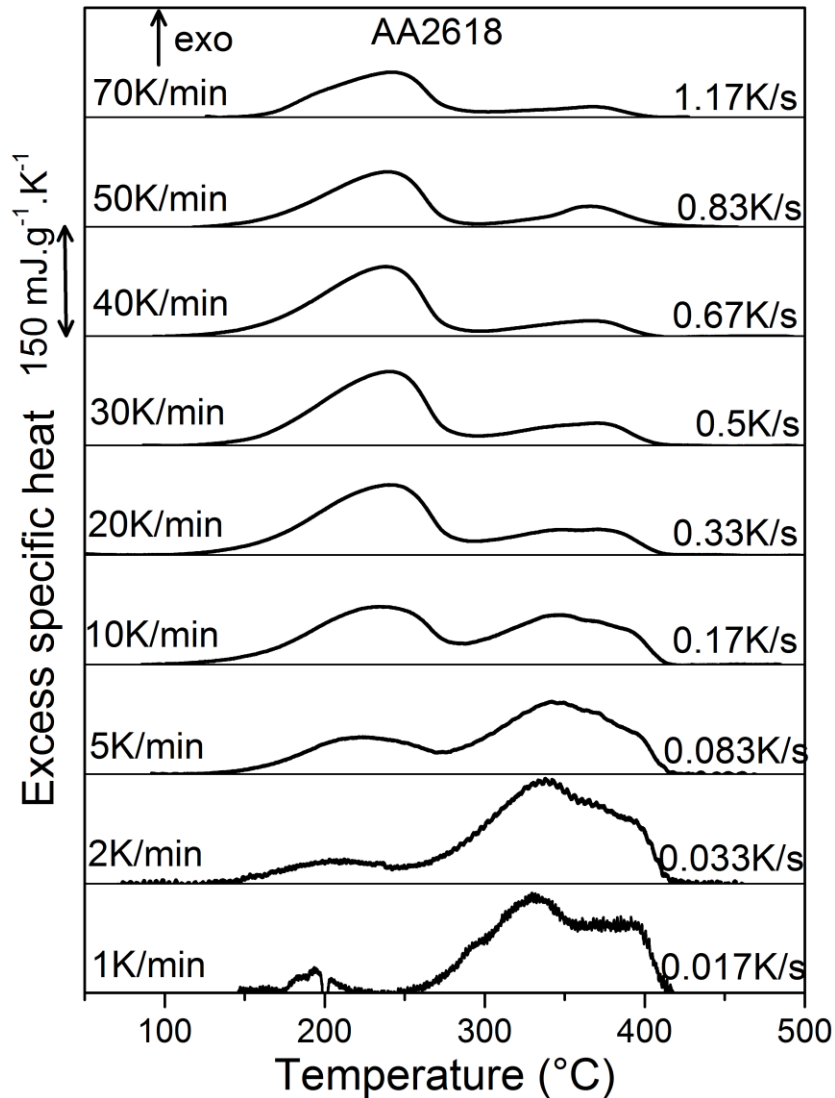


Figure 3-6 – Selected DSC cooling curves of AA2618 at different cooling rates from 1 to 70 K/min after 2 h solutionising at 530°C.

The precipitation start and end temperatures determined from these DSC curves are plotted as a function of time (from begin of cooling) in *Figure 3-7*, together with the corresponding cooling curves. Furthermore, three cooling curves achieved in preliminary SAXS experiments performed by P. Schloth [50] are superimposed with the corresponding start temperatures.

3. Characterisation and modelling of precipitation during quenching

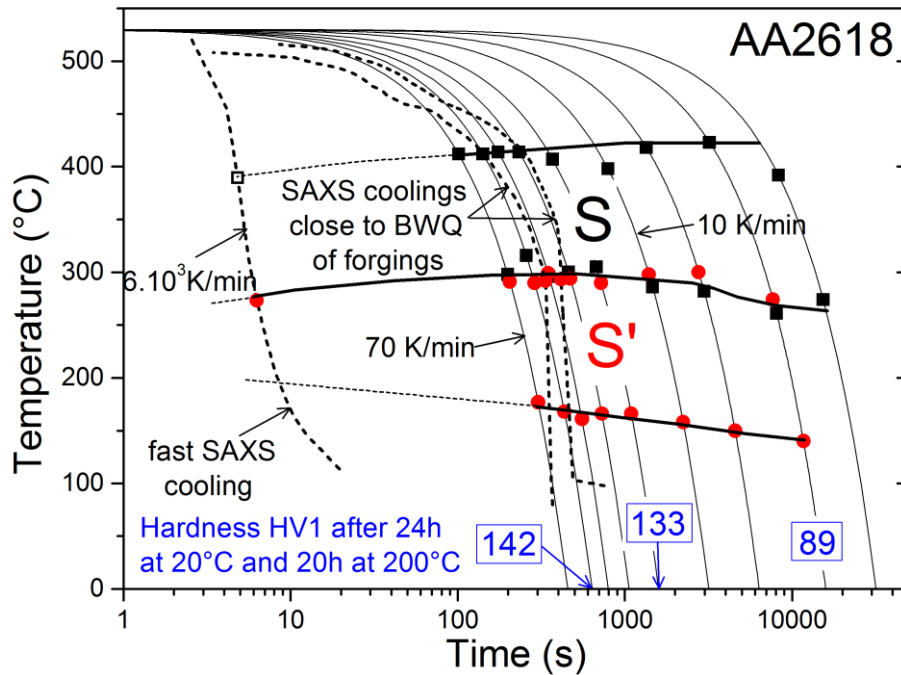


Figure 3-7 – Continuous cooling precipitation diagram of AA2618 obtained with DSC coolings at constant rate together with SAXS coolings performed by P. Schloth [50] at various rates. BWQ: Boiling Water Quench.

For all cooling curves, the onset of precipitation is detected at ca. 390-410°C. Precipitation at such high temperatures is attributed to the formation of the *S* phase in AA2618. This means that the solutionising of AA2618 to dissolve alloying elements could be performed at much lower temperatures (e.g. 480°C) than 530°C. However, Shen [85] showed in his master work that increasing the SHT temperature of AA2618 from 480°C to 530°C increases the yield strength, ultimate tensile strength and elongation by 4.85%, 9.65% and 13.16% respectively. Based on microstructural observations and mechanical properties, he found the optimum solution treatment of AA2618 to be at 530°C for 5h.

The high temperature peak measured by DSC gives an estimation of the end temperature of the *S* phase at ca. 280-310°C. This corresponds to the start temperature of the low temperature peak measured by DSC. The domain of precipitation of the *S* phase is indicated schematically by thick solid lines drawn by hand. During fast SAXS cooling, scattering of large objects was detected (open square in Figure 3-7) but their volume fraction is difficult to estimate because scattering is anisotropic due to the non-spherical shape of *S* precipitates.

The low temperature peak measured by DSC ends at ca. 140-175°C. Precipitation between ca. 290°C and 175°C is attributed to the formation of the *S'* phase in AA2618, whose domain is also indicated in Figure 3-7. Below ca. 175°C, precipitation at high cooling rates revealed by SAXS (not shown here) is attributed to the formation of Cu-Mg-rich clusters according to Deschamps *et al.* [43]. The fast SAXS cooling in Figure 3-7 indicates that 6.10^3 K/min is not fast enough to reach a supersaturated solid solution, i.e. to avoid any precipitation. This means that the low temperature critical cooling rate of

3. Characterisation and modelling of precipitation during quenching

AA2618 is higher than $6 \cdot 10^3$ K/min. *Figure 3-7* also shows the Vickers hardness after three different continuous coolings in DSC followed by artificial ageing. The lower the cooling rate, the lower the hardness in T6 state due to solute loss during cooling.

Specific precipitation heat and peak height are shown in *Figure 3-8* as a function of cooling rate in decreasing logarithmic scale for comparison with the time scale of the continuous cooling precipitation (CCP) diagram.

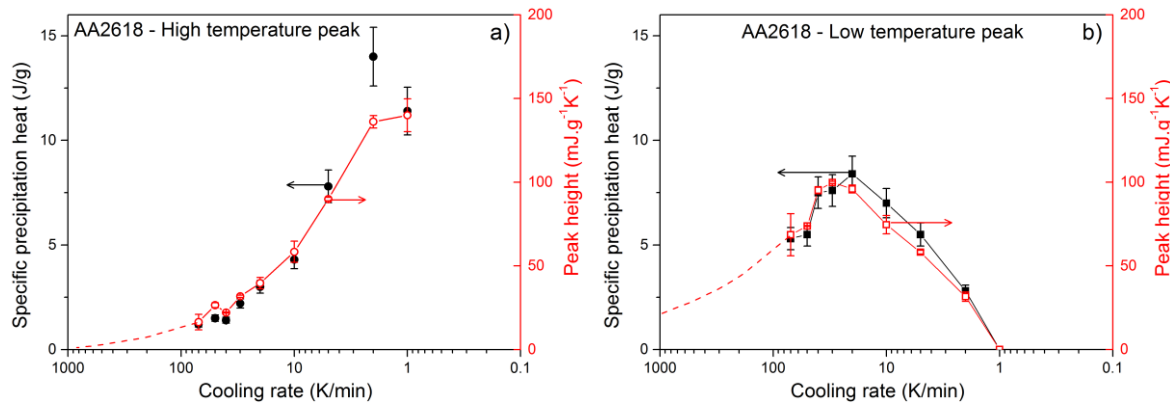


Figure 3-8 - Specific precipitation heat and peak height of high temperature (a) and lower temperature (b) peaks after cooling of AA2618 at various cooling rates from the SHT temperature.

The high temperature precipitation heat (*Figure 3-8-a*) increases with decreasing cooling rate: the slower the cooling, the higher the volume fraction of *S* phase. The cooling rate at which the high temperature precipitation heat reaches zero is defined as the high temperature critical cooling rate. The higher the high temperature critical cooling rate, the more quench sensitive the alloy. *Figure 3-8-a* shows that the high temperature critical cooling rate of AA2618 is higher than 70 K/min. The *S* phase was detected by SAXS at $6 \cdot 10^3$ K/min, although its volume fraction is too low ($< 5 \cdot 10^{-4}$ assuming spherical precipitates) to have a significant effect on the solute content in the matrix. Therefore, the high temperature critical cooling rate of AA2618 is lower than $6 \cdot 10^3$ K/min. The extrapolation of the high temperature precipitation heat (dashed line in *Figure 3-8-a*) assuming a sigmoidal shape gives a high temperature critical cooling rate of AA2618 of ca. 1000 K/min (~ 17 K/s). This value is consistent with the findings of Shen [85] who measured no significant solute loss between 77.5 K/min and $3.8 \cdot 10^3$ K/min.

The low temperature precipitation heat (*Figure 3-8-b*) shows a maximum between 20 and 40 K/min. Cooling slower than 20 K/min leads to large amounts of *S* phase which pumps solute that will not be available for *S'* precipitation at lower temperatures. Cooling faster than 40 K/min, on the other hand, leads to *S'* formation limited by diffusion: the faster the cooling, the lower the volume fraction of *S'* phase. Such a maximum was found at about 10 K/min for AA6005 by Milkereit *et al.* [72] and between 5-20 K/min for AA7150 by Zhang *et al.* [73]. Here, the extrapolation of the low temperature precipitation heat (dashed line in *Figure 3-8-b*) is drawn by hand according to *Figure 3-7* which indicates that the low temperature critical cooling rate of AA2618 is higher than $6 \cdot 10^3$ K/min (100 K/s). The estimated high temperature critical cooling rate (1000 K/min) and low

3. Characterisation and modelling of precipitation during quenching

temperature critical cooling rate (> 6000 K/min) of AA2618 will be used in chapter 4 to define the requirements of the thermo-mechanical tests and to explain qualitatively the measured yield strength values for AA2618.

The combined effect of high and low temperature precipitation is shown in *Figure 3-9* with the total integrated peak area and the corresponding Vickers hardness after artificial ageing.

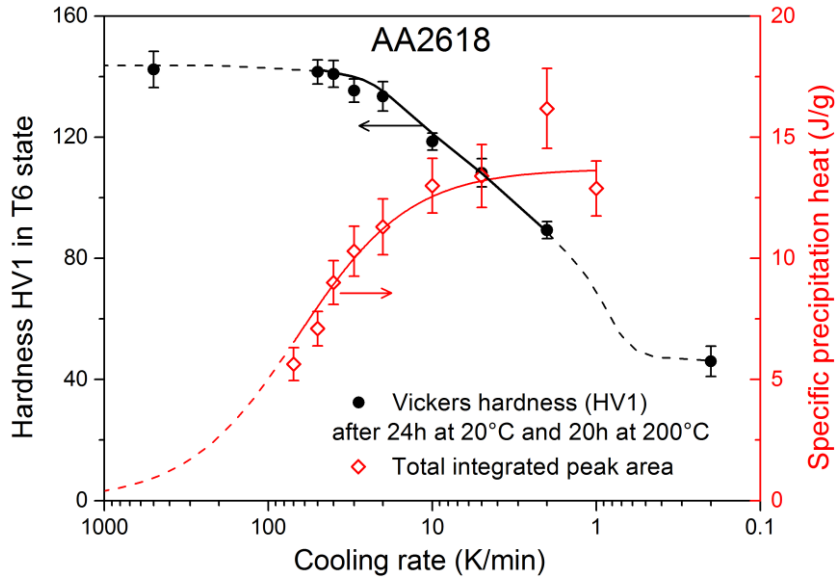


Figure 3-9 - Vickers hardness and specific precipitation heat of DSC samples after natural ageing at 20°C for 24 h followed by artificial ageing at 200°C for 20 h. The hardness error bars correspond to the standard deviation calculated from five indentations.

The hardness increases with increasing cooling rate since the faster the cooling, the lower the solute loss. The T6 hardness values after 0.2 K/min and after ~ 150 K/min were obtained after cooling in a solutionising furnace (switched-off for slow cooling) and after water quench respectively. The dashed lines are drawn by hand to guide the eye. At high cooling rates (> 50 K/min), the dashed line is almost horizontal since Shen [85] measured in AA2618 a slight but not significant T6 hardness increase from 77.5 K/min to $3.8 \cdot 10^3$ K/min. The dashed line between 2 K/min and 0.2 K/min is indicative since no hardness measurements were performed.

The total integrated peak area decreases with increasing cooling rate as explained above. The drop starts at 10-20 K/min while the hardness reaches almost a plateau at 20-30 K/min. This means that the total precipitation heat of ~ 10 J/g measured by DSC at 30 K/min does not correspond to a sufficient solute loss to decrease significantly the T6 hardness. This result is different from the literature where the hardness plateau is usually reached at a cooling rate where the drop in total precipitation heat is significant [72, 73]. These DSC results could be further exploited to determine the volume fraction of S and S' phases or to calibrate a precipitation model by comparing the measured and simulated thermograms. This important task for a TMM model is left as a perspective of this work since precipitation in forgings will be accounted for in FE quenching simulations using a TMG model.

3.3. Precipitation kinetics in AA2618 by *in situ* resistivity

Complementary to DSC measurements, isothermal quenching resistivity measurements on AA2618 have been performed in a Gleeble 3500 machine at Univ. Bretagne Sud. The precipitation kinetics is determined to calibrate a precipitation model.

3.3.1. Experimental procedure

Material

Specimens were machined out from a block taken in a large AA2618 forging in annealed state. All specimens were solutionised in the Gleeble machine for 15 min at 530°C and then quenched to the desired temperature at a cooling rate higher than the HTCRR of AA2618 estimated by DSC at ca. 1000 K/min (~17 K/s) in section 3.1.1.

Resistivity measurements

The Gleeble machine, originally dedicated to thermo-mechanical testing, was selected to carry out the isothermal quenching resistivity measurements because of its reliability in controlling temperature. The specimen is heated via Joule effect using alternative current and cooled by water-cooled grips. Specimen temperature is monitored by three thermocouples fixed to the specimen surface. A closed-loop feedback control system enables precise control of the heat input based on the temperature. Whenever a current is sent through the sample to heat it up, a potential difference is measured between two cooper wires fixed to the specimen's surface at ± 5 mm from the position of the central thermocouple TC1. The electrical resistance is then calculated by the Gleeble system and recorded at 100 Hz to capture the very beginning of precipitation.

A compromise was found between high cooling rates (to avoid precipitation during cooling from the SHT temperature to the isothermals) and low axial thermal gradient in the operating area, i.e. between the two copper wires. This was achieved by using copper grips and an optimised specimen geometry. Cylindrical (6 mm diameter) specimen geometries (*Figure 3-10*) were designed with 3 mm reduced diameter on each side of the operating area as proposed by Samuel and Viswanathan [86].

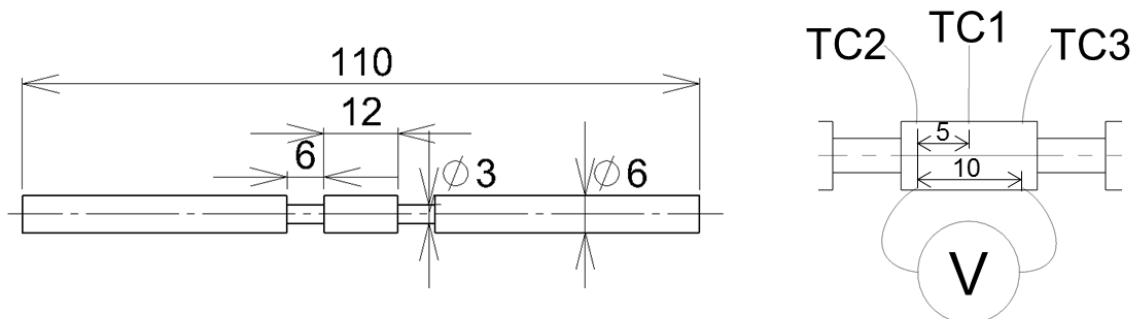


Figure 3-10 – Specimen geometry used for resistivity measurements with dimensions in millimeters (left) and position of thermocouples (right).

3. Characterisation and modelling of precipitation during quenching

The combination of copper grips and the optimised geometry resulted in a maximum temperature difference of 5°C in the operating area between TC2 and TC3 (10 mm in length and 6 mm in diameter) and maximum cooling rates of 20 K/s without additional air cooling. Specimens were held horizontally by copper grips mounted on free jaws that can slide horizontally so that specimens are free to dilate. This assembly called “low force” is proposed by DSI® to measure accurately low forces at elevated temperatures. It was chosen to get rid of any mechanical issue such as buckling of the specimen. All measurements were performed under secondary vacuum (ca. 10^{-1} Pa) to avoid oxidation of the copper wires.

3.3.2. Results

Preliminary measurements were performed on high purity aluminium Al4N and on AA7010 to validate the technique [9]. Then isothermal quenching resistivity measurement was made on AA2618. The results during the first 16 seconds after quench are shown in *Figure 3-11* where the quenches are interrupted at either 510°C, 450°C, 415°C, 400°C, 350°C, 325°C, 300°C, 250°C or 200°C.

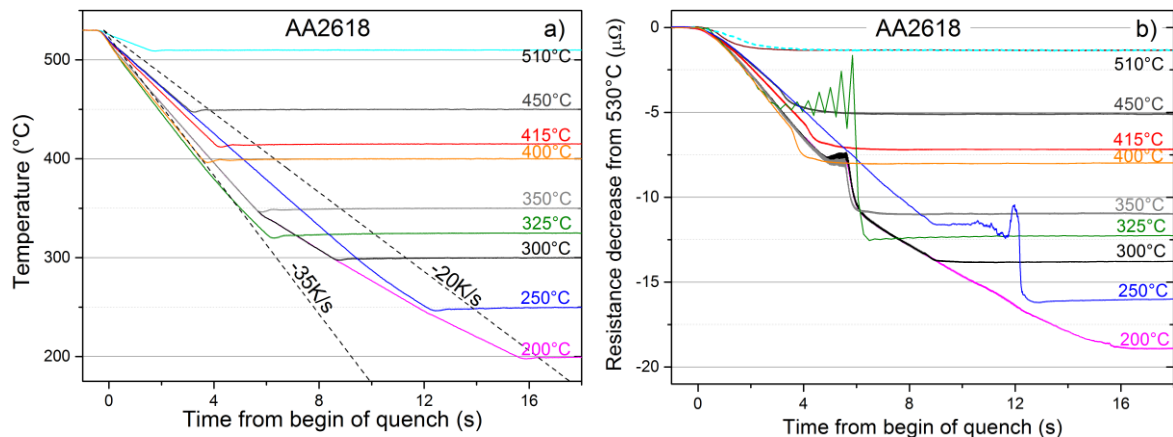


Figure 3-11 – Isothermal quenches achieved with AA2618 Gleeble resistivity specimens; temperature measured by TC1 thermocouple (a) and evolution of resistance decrease from 530°C (b).

Except for the test at 510°C, the imposed cooling rates before the isothermal plateau range from 20 to 35 K/s (*Figure 3-11-a*). Faster coolings can be achieved by turning off the current and using additional air cooling. This was not used because it systematically leads to undesired discontinuities in the measured resistance as shown during cooling down to 325°C and 250°C in *Figure 3-11-b*. The cooling rates were chosen in order to guarantee that a minimum current is sent through the sample during cooling. The resistance decrease shown in *Figure 3-11-b* is obtained by subtracting the resistance value at 530°C from the current resistance value. Resistance is fairly constant during the first seconds on the isothermals since no metallurgical change is detected. This is not always the case for longer times as shown in *Figure 3-12*.

3. Characterisation and modelling of precipitation during quenching

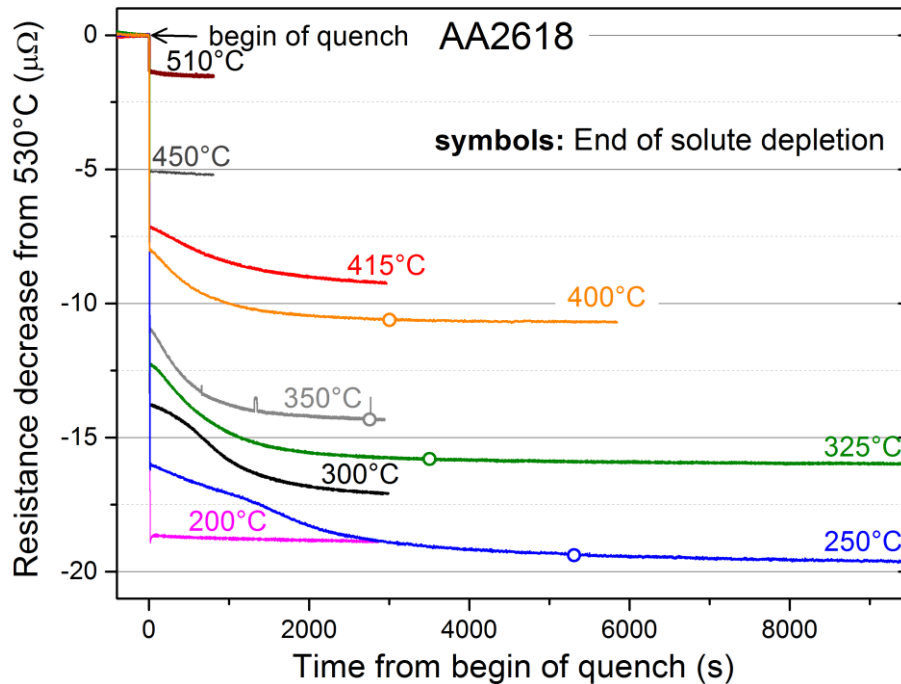


Figure 3-12 – Evolution of resistance decrease from the SHT temperature in AA2618 specimens subjected to isothermal quenching at various temperatures. Raw data (not smoothed).

Again, in the absence of metallurgical change, the resistance should be constant at a given temperature. This is the case for pure aluminium measured in the Gleeble machine [9]: the slight drop of resistance with time (max. $3 \times 10^{-4} \mu\Omega s^{-1}$) gave an estimate of the relative error in the order of 1%. This should be also the case in aluminium alloys at temperatures higher than their solvus. In Figure 3-12, the drop of resistance with time in AA2618 is in the order of $10^{-4} \mu\Omega s^{-1}$ (same operating area as for pure aluminium specimens in [9]) at 510°C and 450°C. This is compatible with the drop of resistance measured in pure aluminium and with the solvus predicted by ThermoCalc software for AA2618, 475°C. The resistance drop value of $10^{-4} \mu\Omega s^{-1}$ is chosen as a criterion to determine the value of the resistance decrease after complete solute depletion of the matrix, R_{end} , indicated by open circles in Figure 3-12.

At temperatures ranging from 250°C to 415°C, precipitation takes place in AA2618 as can be seen by the decrease of resistance on isothermals due to solute loss. The criterion chosen above to determine R_{end} indicates that solute depletion is completed after ca. 3000 sec at 400°C, 2800 sec at 350°C, 3500 sec at 325°C and 5300 sec at 250°C. The isothermal holdings at 415°C and 300°C were too short to reach complete solute depletion.

While resistivity increase is expected at artificial ageing temperatures (200°C for AA2618) due to Bragg scattering by coherent precipitates [87], no precipitation is detected after 50 min at 200°C. Other methods such as small angle scattering experiments have been used in the literature to monitor precipitation at low temperature (see Deschamps *et al.* [43] for SAXS measurements during artificial ageing of AA2618).

3. Characterisation and modelling of precipitation during quenching

Reproducibility was tested on two samples at 250°C (*Figure 3-13*), 325°C, 350°C and 400°C.

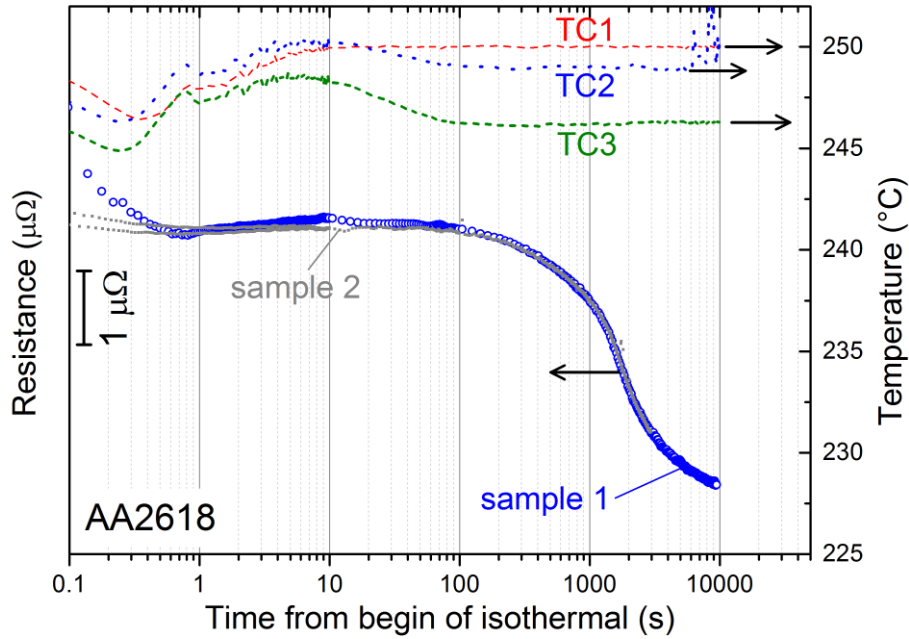


Figure 3-13 – Reproducibility at 250°C using two samples subjected to isothermal quenching after cooling at ca. 30 K/s. TC1, TC2 and TC3 correspond to sample 1.

Resistance in both samples is different during the first seconds due to the slight temperature undershoot (not reproducible). Once temperature stabilises (ca. 10 sec), superposition of both resistance signals is excellent. *Figure 3-13* also shows that temperature in the operating area is almost uniform.

A convenient way to compare results is to calculate the relative resistance decrease, ρ_{el} defined as [9]:

$$\rho_{el}(T, t) = \frac{R(T, t) - R_{start}(T)}{R_{end}(T) - R_{start}(T)} \quad \text{Eq. 3-1}$$

where R_{start} is the value of the resistance decrease of the non-equilibrium solid solution and R_{end} is the value of the resistance decrease after complete solute depletion of the matrix. Since R_{end} was not reached experimentally at 300°C and 415°C (see *Figure 3-12*), it is estimated by extrapolation (not shown here) of the resistance loss defined as the absolute value of the numerator of ρ_{el} . The evolution of the relative resistance decrease of AA2618 is shown in *Figure 3-14*.

3. Characterisation and modelling of precipitation during quenching

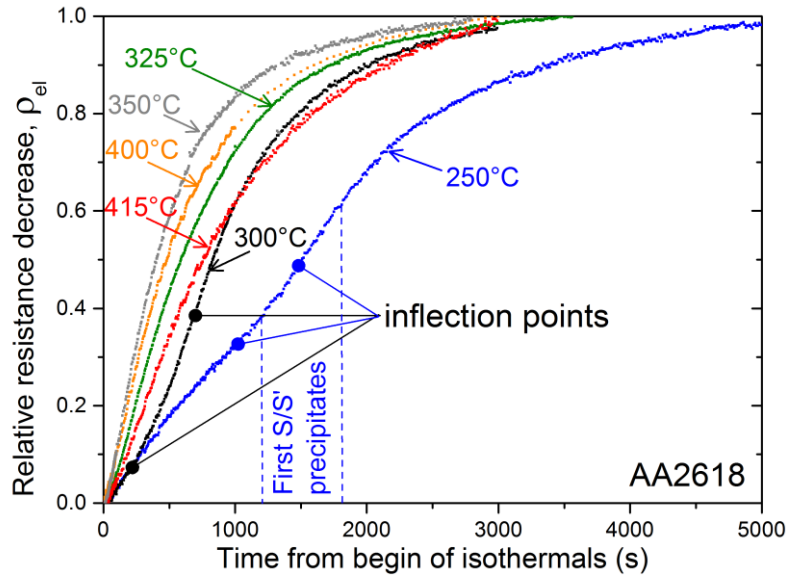


Figure 3-14 – Normalised precipitation kinetics of AA2618 measured by resistivity.

The fastest kinetics is measured at 350°C and the slowest at 250°C where the inflection points suggest that more than one phase is precipitating. This could be attributed to the formation of the first S/S' precipitates observed by Deschamps *et al.* [43] after 20-30 min (dashed vertical lines in Figure 3-14) at 200°C in AA2618. A more striking evidence of the possible precipitation of two phases is given in Log-log representation of $\rho_{el}/(1-\rho_{el})$ versus time as shown in Figure 3-15 which yields straight lines if the diffusion-controlled precipitation reaction (of one phase) obeys Austin-Rickett's law [88].

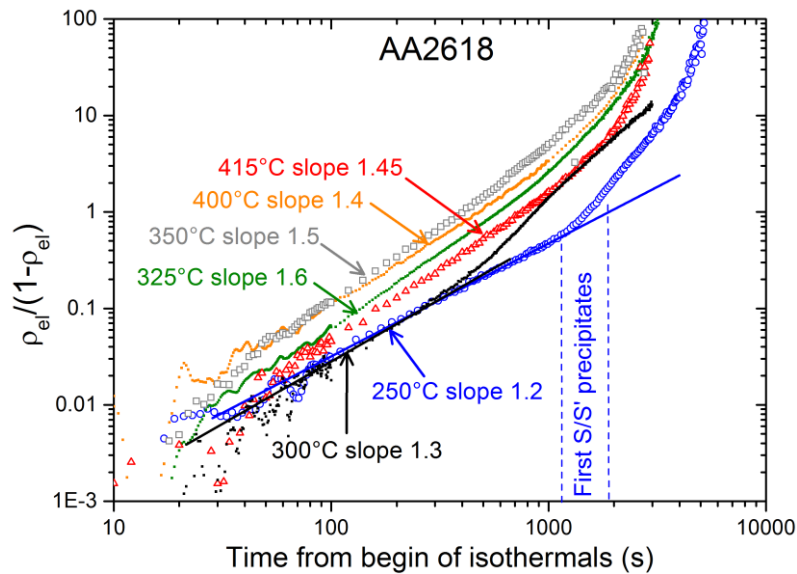


Figure 3-15 – Log-log representation of $\rho_{el}/(1-\rho_{el})$ versus time at various temperatures.

Apart from short times (< 50 sec) where measurements are dispersed, straight lines clearly fit experiments at high temperature ($\geq 325^\circ\text{C}$). This means that the precipitation reaction above 325°C obeys Austin-Rickett's law describing one precipitating phase (S' phase). The slopes, ca. 1.5, are the expected values for diffusion-controlled processes [89].

3. Characterisation and modelling of precipitation during quenching

At low temperature, however, the measurements at 250°C and 300°C deviate from straight lines at times corresponding to the first inflection points shown in *Figure 3-15*, suggesting that more than one phase is precipitating.

The Time-Temperature-Properties (TTP) diagram of AA2618 is derived from *Figure 3-14* by taking the time required to lose 5%, 20%, 50% and 80% of resistance as shown in *Figure 3-16-left*. The continuous cooling precipitation diagram of AA2618 determined in section 3.1.1 is shown *Figure 3-16-right* for comparison. This comparison is only indicative since TTP and CCP diagrams give information on precipitation kinetics during isothermals and continuous coolings respectively.

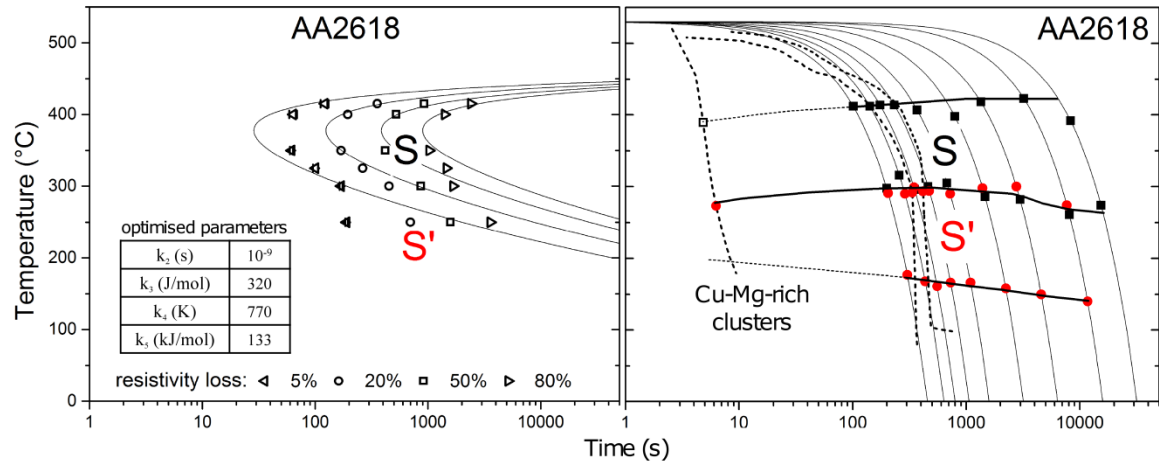


Figure 3-16 – TTP-diagram of AA2618 obtained by resistivity measurements where C-curves represent iso-resistivity loss and corresponding optimised parameters (left). CCP-diagram of AA2618 indicating domains where S and S' are detected by DSC/SAXS (right).

The experimental data above 300°C are fitted using C-curves described by [34]:

$$\tau_c(T) = -k_1 k_2 \exp\left(\frac{k_3 k_4^2}{RT(k_4 - T)^2}\right) \exp\left(\frac{k_5}{RT}\right) \quad \text{Eq. 3-2}$$

where τ_c is the critical time required to precipitate a constant amount of precipitates during the isothermals and k_1 is the natural logarithm of the untransformed fraction. k_2 , k_3 , k_4 and k_5 are fitting parameters related to the reciprocal of the nucleation site density, the energy required to form a nucleus, the solvus temperature and the activation energy for diffusion respectively. The optimised parameters given in *Figure 3-16-left* are in the range of those found in the literature for heat treatable aluminium alloys [12, 51, 90]. At high temperature where only the S phase forms, the fit is acceptable. At low temperature, however, the fit is poor due to precipitation of Cu-Mg-rich hardening clusters and S' phase.

The TTP-diagram of AA2618 given in *Figure 3-16-left* could be used to predict solute loss during non-isothermal coolings by using the additivity principle. This is not done in this work. Instead, the normalised precipitation kinetics of AA2618 given in *Figure 3-14* are used to identify the parameters corresponding to the S phase in a precipitation model (see section 3.4.2).

3.4. Modelling precipitation

In order to predict the precipitation state for any cooling condition, a precipitation model is used. After a very short description of the model, an example of calibration of its parameters is shown using the normalised precipitation kinetics of the S phase in AA2618 determined in the previous section.

3.4.1. Precipitation model

The precipitation model is based on an Euler-like multi-class approach, i.e. the particle size distributions are divided into fixed classes and the flux between the classes is followed. The original model was developed by Serriere [91] for binary alloys. It has been later adapted by Gandin and Jacot [92] to handle non-stoichiometric precipitates formed in multi-component alloys. It is now capable to simulate several families of spherical precipitates in the same primary Al matrix phase. The model is based on classical nucleation and growth theories. The detailed equations are found in Ref. [92] and recalled in the PhD work of P. Schloth [50]. The model was implemented to be coupled with thermodynamic calculations for calculation of the driving forces for nucleation and local equilibrium concentrations.

The following assumptions are used in the model:

- infinite diffusion in the precipitates (uniform composition),
- spherical precipitates,
- no strain misfit between precipitates and matrix,
- local equilibrium at the precipitate/matrix interface.

Inputs of the precipitation model are the chemical composition of the alloy, the diffusion data of each solute element in the matrix and the chemical composition and thermodynamic description of the phases. For each simulated phase, the adjustable parameters are [92]:

- the wetting angle, θ_{wet} used to describe the decrease of the energy barrier for heterogeneous nucleation,
- the nucleation site density ρ_{NS} ,
- the precipitate/matrix interfacial energy.

For homogeneous nucleation of coherent precipitates in aluminium matrix, these parameters are usually [92]:

- fixed to 90° for the wetting angle (i.e. no nucleation barrier reduction),
- fixed to $\sim 10^{28} \text{ m}^{-3}$ for ρ_{NS} (all the atoms are potential nucleation sites),
- adjusted for the interfacial energy in the order of 0.01 J/m^2 .

The main issue when modelling precipitation of metastable coherent precipitates is their unknown chemical composition and thermodynamic description. In his PhD work, P. Schloth [50] derived a thermodynamic description of GP(I) zones (with assumed composition of AlZnMg) using the solubility product approach with two adjustable

3. Characterisation and modelling of precipitation during quenching

parameters, the enthalpy and entropy of formation. Based on dissolution (reversion) experiments performed by P. Schloth [50], these two parameters were adjusted for AA7449 and applied directly for AA7040. The solvus temperature of the GP(I) zones was found to be 184°C in AA7449 and 161°C in AA7040.

Furthermore, P. Schloth took into account the influence of excess vacancies on the diffusion kinetics by increasing the diffusion coefficients (defined by an Arrhenius law in the precipitation model) in the modelⁱ. The adjusted parameters (energy of formation and migration of vacancies and characteristic diffusion length for vacancies) for AA7449 were used to model precipitation in AA7040 (see *Figure 3-3* in section 3.1.3).

The precipitation model calibrated by P. Schloth for the GP(I) zones in AA7449 and AA7040 will be used in the TMM model (section 5.3.2). This precipitation model does not consider the precipitation of η and η' phases above the solvus temperature of the GP(I) zones. Ignoring the η phase is justified by the very small volume fractions measured during SAXS coolings (see section 3.1.3).

As far as the equilibrium phases are concerned (such as η or S), their chemical composition and thermodynamic description are available in commercial databases, for example the Al-Data database from ThermoCalc software. For heterogeneous nucleation of semi/in-coherent precipitates in aluminium matrix, the interfacial energy is higher and the two other parameters (wetting angle and nucleation site density) are lower than those for homogeneous precipitation. Since they are hardly measurable, they must be adjusted to fit the results of indirect measurements such as resistivity (see next section).

The precipitation model gives as main outputs the chemical composition of the matrix, the average precipitate radius and the precipitated volume fraction. These outputs are used as input in a yield strength model. If needed, the PSD is also available as well as the electrical resistivity derived from the chemical composition using Mathiessen's ruleⁱⁱ.

3.4.2. Identification of precipitation model parameters for S phase in AA2618

The normalised precipitation kinetics of AA2618 given in *Figure 3-14* are used to identify by inverse method the parameters corresponding to the S phase. Compared to standard least-squares methods dealing with analytical functions, inverse methods use the numerical solution obtained from direct finite element or finite difference calculations [93]. The cooling curves imposed in the Gleeble isothermal quenchings shown in *Figure 3-11-a* are imposed as thermal load in the precipitation model. The numerical solution of the precipitation model is the electrical resistivity normalised for comparison with the experimental results presented in *Figure 3-14*.

ⁱ excess vacancies are not implemented directly in the precipitation model.

ⁱⁱ assuming that coefficients are valid at high temperature.

3. Characterisation and modelling of precipitation during quenching

For a given isothermal, the identification problem consists in determining the three model parameters (wetting angle, nucleation site density and interfacial energy between S precipitates and matrix, γ_S) which minimise the objective function:

$$G_i^{el}(\theta_{wet}, \rho_{NS}, \gamma_S) = \frac{1}{M_i} \sum_{i=1}^{M_i} \left(\frac{\rho_i^{el,sim} - \rho_i^{el,exp}}{Er(\rho_i^{el,exp})} \right)^2 + \frac{1}{M_i} \sum_{i=1}^{M_i} \left(\frac{\partial_t(\rho_i^{el,sim}) - \partial_t(\rho_i^{el,exp})}{Er[\partial_t(\rho_i^{el,exp})]} \right)^2 \quad \text{Eq. 3-3}$$

where M_i is the number of measurement points, $\rho_i^{el,sim}$ is the normalised electrical resistivityⁱ simulated by the precipitation model, $\rho_i^{el,exp}$ is the experimental relative resistance decrease defined by Eq. 3-1 and $Er(\rho_i^{el,exp})$ is the associated error of measurement. $\partial_t(\rho_i^{el,exp})$ represents the derivative of $\rho_i^{el,exp}$ with respect to time used in the objective function to ensure a good agreement between measurements and simulations in terms of slope. The optimisation is implemented in Matlab using the function *fmincon* to minimise the objective function by an iterative process using constraint gradient-based methods. Within each iteration of *fmincon*, a Matlab script writes the updated input data (with the new parameters) required for the precipitation model and calls the precipitation model n_p+1 times, where n_p is the number of parameters to identify, in order to calculate the partial derivatives for each parameter. The simulated resistivity is then read by the script to compute the objective function in Eq. 3-3. After each iteration (consisting in n_p+1 direct calls), a new set of parameters (θ_{wet} , ρ_{NS} , γ_S) is calculated by the function *fmincon* and the process is repeated. In order to shorten the optimisation process, the time step in the precipitation model is increased for longer times (see Table 3-1) and the inverse method is stopped after N_{DC} direct calls of the precipitation model.

Preliminary optimisations were performed at 325°C with the three parameters ($n_p = 3$), θ_{wet} , ρ_{NS} and γ_S allowed to vary within the closed intervals 20-60°, 10^{19} - $2 \cdot 10^{26}$ m⁻³ and 0.1-0.32 J/m² respectively. N_{DC} was set to 60, thus allowing a maximum of 15 iterations of *fmincon*. Several optimisations were run with different initial parameters. In these calculations, it was found that the precipitation model did not always converge with the chosen time step (min. 0.2 sec), especially for $\theta_{wet} \rightarrow 20^\circ$ and $\rho_{NS} \rightarrow 10^{19}$ m⁻³. Furthermore, several minima were found for many different sets of parametersⁱⁱ, all of which giving acceptable fits of the measurements. In order to obtain a unique minimum, the objective function could be modified by including a maximum a posteriori as shown by Rappaz *et al.* [93]. Instead, it was decided to fix two parameters and identify only the third parameter for a given isothermal.

The strategy used is inspired from the work of Godard *et al.* [94] who adjusted the model parameters for the η phase in AA7010. Above 350°C, they assigned a constant ρ_{NS} value of 10^{19} m⁻³ consistent with density measurements performed on Al₃Zr dispersoids. Below 350°C, they used an increasing ρ_{NS} with decreasing temperature. They took into account the decrease of the nucleation barrier for heterogeneous precipitation with the single

ⁱ normalised electrical resistivity and relative resistance decrease are formally identical

ⁱⁱ no minimum was found for a combination of high θ_{wet} and γ_S values, e.g. 60° and 0.25 J/m²

3. Characterisation and modelling of precipitation during quenching

global parameter $\gamma_S^3 \cdot [2 + \cos(\theta_{wet})] \cdot [1 - \cos(\theta_{wet})]^2 / 2$. This global parameter was considered to increase from 440°C to 350°C in order to model rapid nucleation above 350°C. It was taken constant below 350°C to model instantaneous nucleation.

In this work, θ_{wet} is assigned to 30° at all temperatures. At high temperature ($\geq 325^\circ\text{C}$), γ_S is the only parameter to identify ($n_p = 1$) for each isothermal and ρ_{NS} is set to 10^{21} m^{-3} for heterogeneous precipitation of S phase on defects such as grain boundaries and dispersoids. At lower temperature ($< 325^\circ\text{C}$), γ_S identified at 325°C is taken constant and ρ_{NS} is the parameter to identify. For all optimisations (with one parameter to identify), N_{DC} is set to 32, thus allowing a maximum of 16 iterations of *fmincon*. This criterion was found to be enough to find the minimum of the objective function at all temperatures. The parameters used in the precipitation model are summarised in Table 3-1.

Parameter	Value
Wetting angle, θ_{wet}	30°
Nucleation site density, ρ_{NS}	10^{21} m^{-3} for $T \geq 325^\circ\text{C}$, $5.8 \cdot 10^{20} \text{ m}^{-3}$ otherwise
Molar volume	$1.1 \cdot 10^{-5} \text{ m}^3/\text{mol}$
Diffusion data [95]	pre-exponential (m^2/sec) activation energy (kJ/mol)
Cu	$4.4 \cdot 10^{-5}$ 133.9
Mg	$1.49 \cdot 10^{-5}$ 120.5
Si	$1.38 \cdot 10^{-5}$ 117.6
Number of classes for the PSD	2000
Maximum radius for the PSD	600 nm
Time steps	
from 0 to 200 sec	0.2 sec
from 200 to 400 sec	0.4 sec
from 400 to 1000 sec	0.6 sec
from 1000 to 3000 sec	1.0 sec

Table 3-1 – Parameters used in the precipitation model for the $S(\text{Al}_2 \text{CuMg})$ phase in AA2618.

The results of the optimisation process to find γ_S are shown exemplarily at 325°C in Figure 3-17.

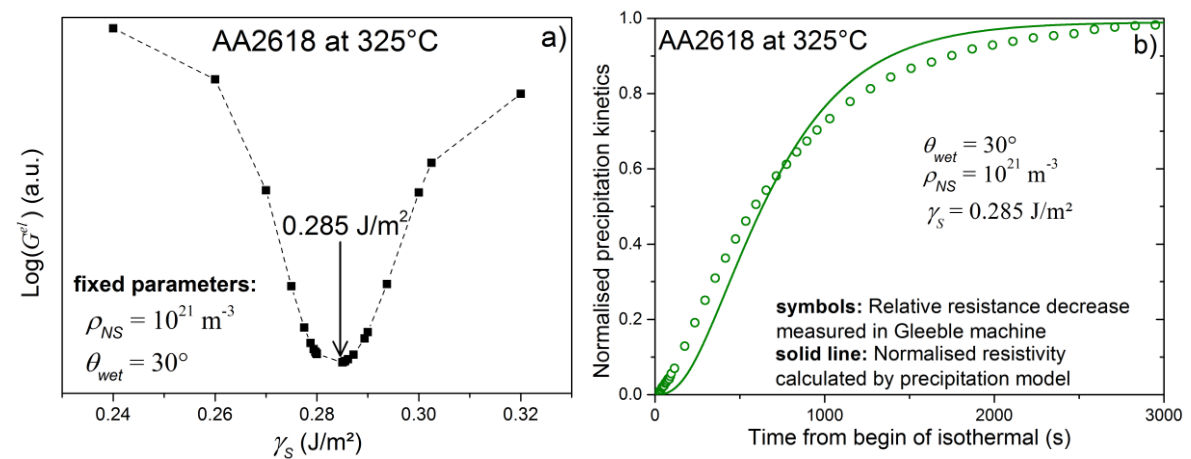


Figure 3-17 – Example of optimisation at 325°C with parameters of Table 3-1: $\text{Log}(G^{el})$ - γ_S plot (a); best fit for $\gamma_S = 0.285 \text{ J/m}^2$ (b).

The minimum of the objective function is reached for an interfacial energy γ_S of ca. 0.285 J/m^2 . Figure 3-17 shows that this minimum is unique in the considered interval (constrained optimisation). The simulation with $\gamma_S = 0.285 \text{ J/m}^2$ reproduces fairly the

3. Characterisation and modelling of precipitation during quenching

experimental measurements. At the very beginning of the isothermal, the simulated precipitation kinetics is late compared to the measurements. The agreement at short times could be improved by increasing ρ_{NS} (while keeping other parameters constant) but this would lead to a poor agreement for longer times (overestimation by the simulation). The discrepancy could be due to the fact that the model considers spherical precipitates which is not the case of the S phase. The optimisation procedure is performed at 350°C, 400°C and 415°C to find γ_S that minimises the objective function with the parameters given in Table 3-1. The results are given in Figure 3-18.

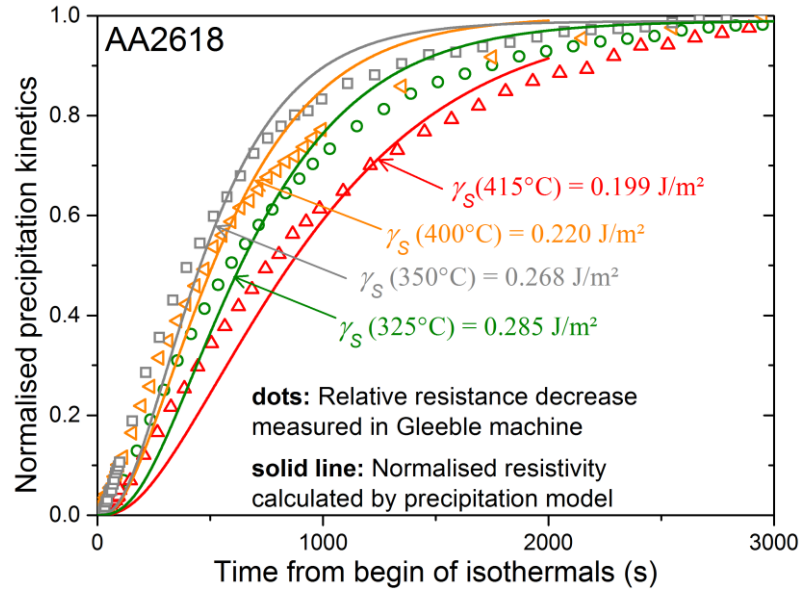


Figure 3-18 - Comparison between measurements and simulations by precipitation model using the parameters of Table 3-1.

The simulation predicts the fastest kinetics at 350°C as found experimentally. The overall trend is fairly captured with an increase of γ_S with decreasing temperature (Figure 3-19) consistent with the findings of Godard *et al.* for the η phase in AA7010 [94].

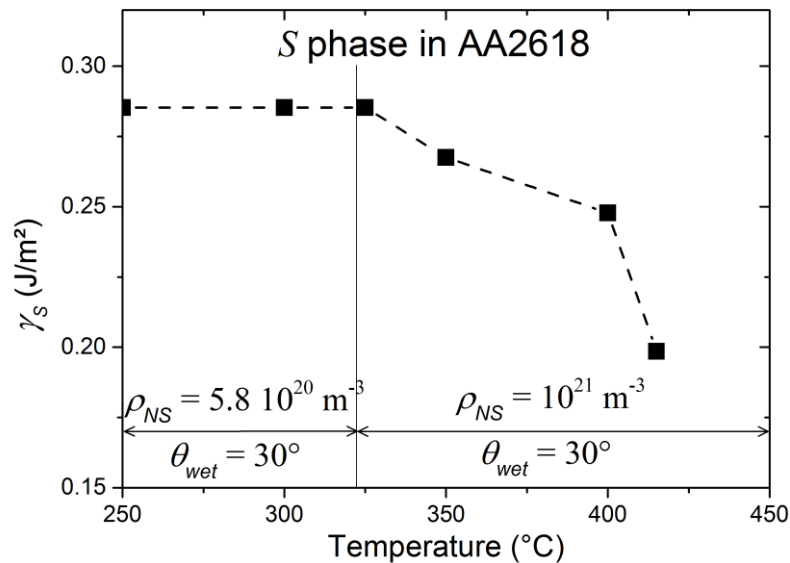


Figure 3-19 - Identified values of γ_S at different temperatures using the parameters of Table 3-1.

3. Characterisation and modelling of precipitation during quenching

In *Figure 3-19*, the nucleation site density below 325°C is the identified value at 300°C with constant interfacial energy, γ_s set to the value identified at 325°C.

At 250°C, the S phase parameters obtained at 300°C are used and the S' phase is included in the precipitation model (2 phases). The model parameters for the S' phase have to be determined. To simplify the optimisation, $\gamma_{S'}$ is the only parameter to identify with θ_{wet} set to 90° and ρ_{NS} set to 10^{28} m^{-3} to account for homogeneous precipitation of S' phase. The results of the optimisation at 300°C and 250°C are shown in *Figure 3-20-a* and *b* respectively.

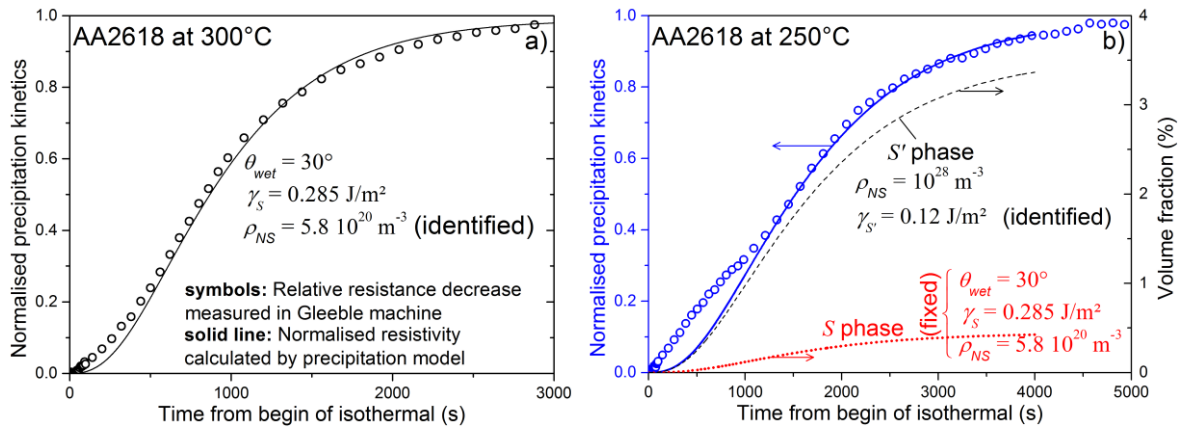


Figure 3-20 – Results of optimisation at 300°C (a) and 250°C (b).

At 300°C, the agreement between measurements and simulation is excellent. However, the identified ρ_{NS} value is slightly lower than that at 325°C which is different from Godard *et al.* [94] who found an increase of nucleation site density with decreasing temperature. At 250°C, the agreement between measurements and simulation is excellent at long times but poor at short times. Indeed, the simulated evolution of the volume fraction of S' phase shown in *Figure 3-20-b* is too slow at short times. The agreement at short times could be improved by decreasing θ_{wet} of S' phase to account for possible heterogeneous nucleation or by introducing another phase for Cu-Mg-rich clusters. This work is left as a perspective.

As a conclusion, the precipitation model with adjusted parameters is able to predict reasonably well the normalised precipitation kinetics determined by *in situ* resistivity. While the presented inverse method considered only resistivity, it would be advantageous to compare the simulated average radius and volume fraction of precipitates against small-angle scattering measurements for instance. Another improvement would be to consider non-spherical precipitates. Furthermore, it should be noted that the determined parameters are model dependent, meaning that they will take other values for other precipitation models.

3.5. Summary of chapter 3

In this chapter, the main precipitation results obtained by P. Schloth were presented. In particular, the following results are used in the present work:

- The measured evolution of the Guinier radius and volume fraction of small clusters during coolings similar to the industrial ones in thick AA7449 and AA7040 plates will be used in section 4.3.6 to calibrate the yield strength model.
- The precipitation model calibrated by P. Schloth for GP(I) zones in AA7449 will be used in sections 5.3.2 and 5.3.3 for a one-way coupling temperature→precipitation→stresses using a TMM model.

Efforts have been put in the present work on the characterisation of precipitation in AA2618 with the following findings:

- The high temperature critical cooling rate of AA2618 is ~1000 K/min (~17K/s). This value will be used in chapter 4 to define the requirements of the thermo-mechanical tests.
- The low temperature critical cooling rate of AA2618 is higher than ca. 6000 K/min (100K/s). This will be used in chapter 4 to explain qualitatively the yield strengths obtained for AA2618.
- During isothermal holding at 250°C, at least two phases precipitate.

An example of precipitation model calibration, mainly for the S phase in AA2618, against resistivity measurements has been shown. Although the overall precipitation kinetics was reasonably well predicted by the precipitation model, some discrepancies were observed and the following limitations were highlighted:

- S precipitates are not spherical as considered in the precipitation model.
- The identified model parameters are not unique and are furthermore model dependent.
- Resistivity is a global measure of solute loss (i.e. volume fraction) which does not allow for comparing precipitate radius and PSD.

For the FE simulations of boiling-water quenching of AA2618 forgings, the calibrated precipitation model for S phase in AA2618 will not be used for simulations with TMM model. This work is left as perspective for time reasons. Instead, a TMG model will be used.

4. Thermo-mechanical behaviour

In this chapter, two thermo-mechanical models (TM and TMG) and one thermo-metallurgical-mechanical (TMM) model are defined to describe the mechanical behaviour during quenching of the three alloys. The TM model to be used for FE simulations without precipitation describes the behaviour of the alloys in non-equilibrium solid solution state. The TMG model to be used for simple (no precipitation model) FE simulations with precipitation (from Gleeble tests) describes the behaviour of the alloys after coolings similar to those experience by the plate surface during quenching. The TMM model to be used for FE simulations with precipitation predicted by the precipitation model (one-way coupling) describes the behaviour of the alloys after every possible cooling condition.

After a short review of the thermo-mechanical and TMM models existing in the literature, the thermo-mechanical tests achieved in this work to identify the model parameters are presented. The experimental results are then given together with the identified parameters.

4.1. State of the art

Mechanical models predict flow stress as a function of temperature (thermo-mechanical models) and microstructure when precipitation is taken into account (TMM models). A number of models have been used in the literature and a brief overview is given hereafter as a guide in the choices made in this work. They are traditionally divided into phenomenological and physically-based models.

4.1.1. Phenomenological models

General overview

Phenomenological models have the general form $\sigma = \sigma(T, \varepsilon^{in}, \dot{\varepsilon}^{in})$ or $\dot{\varepsilon}^{in} = \dot{\varepsilon}^{in}(T, \varepsilon^{in}, \sigma)$ where σ is the flow stress, ε^{in} and $\dot{\varepsilon}^{in}$ are the inelastic strain and strain-rate. While this latter term encompasses plastic, viscoplastic and creep strain-rates in a single expression in unified plasticity models [96], these three contributions are partitioned in non-unified plasticity models. The former approach is mostly used but issues have been raised when the material undergoes both creep at high temperature and plastic deformation at low temperature. During quenching where both high temperature and low temperature deformations are encountered, the classical plasticity theory which relies on the accumulated equivalent inelastic strain, p_{cum} , predicts stresses at low temperature higher than the measured ones [97]. Indeed, Mo and Farup [98] have shown that high temperature strain has no influence on subsequent low temperature mechanical behaviour. This phenomenon is attributed to dislocation annihilationⁱ which is thermally activated and dominates over dislocation storage at high temperature. In contrast, annihilation of dislocations is negligible in the under-aged state as reported by Fribourg

ⁱ dislocations of opposite sign attract each other and can mutually annihilate if they are on the same slip plane.

et al. [82]. To adequately predict stress at low temperature, Haafte *et al.* [99] used a smooth transition from “recovery” above 400°C, where p_{cum} has no influence on the low temperature flow stress, to hardening-dominated behaviour below 250°C, where p_{cum} has a full effect on the flow stress. Taking a sharp transition with a parameter called T_{cum} corresponding to the temperature above which inelastic deformation has no effect on low temperature subsequent behaviour, p_{cum} writes:

$$p_{cum} = \begin{cases} \int \dot{p} dt & \text{when } T < T_{cum} \\ 0 & \text{when } T > T_{cum} \end{cases} \quad \text{with } \dot{p} = \sqrt{\frac{2}{3} \dot{\tilde{\epsilon}}^{in} : \dot{\tilde{\epsilon}}^{in}} \text{ in 3D and } \dot{p} = |\dot{\epsilon}^{in}| \text{ in 1D} \quad \text{Eq. 4-1}$$

where the inelastic strain rate $\dot{\epsilon}^{in}$ is a tensor in 3D, $\dot{\tilde{\epsilon}}^{in}$. This is an alternative to the MATMOD equations used in the literature to overcome this issue [100], or to more complex strain hardening models describing the evolution of dislocation density with strain as a competition between storage and annihilation (see section 4.1.2).

Cold working hardening

Low temperature stress-strain curves exhibit strain hardening, which has been first described by the Ludwig power-law (also called Ramberg-Osgood law [101]):

$$\sigma = \sigma_a + H.(\epsilon^{in})^n \quad \text{Eq. 4-2}$$

where σ_a is the strength in the absence of work hardeningⁱ (at 0% strain offset) and (H , n) are two temperature-dependent parameters. $n = 0$ corresponds to a perfectly plastic behaviour. For most metals, n varies between 0.1 and 0.5 [102]. This law fits well low temperature stress-strain curves at small strains, but predicts an infinite stress when strain tends towards infinity. This is physically not acceptable and the concept of a steady state (or saturation) stress has been introduced by Voce [103] to overcome this problem. This concept was physically explained by the Kocks and Mecking model [104]. Ludwig, Voce and three other models for the strain dependence of cold strain hardening have been used by Suni *et al.* [105] to fit the large experimental database gathered by Alcoa on aluminium alloys at room temperature containing Cu, Mg, Mn and Si solute elements. While Voce’s model gave the worst fit, Ludwig’s model was chosen for its good fitting ability using a global strain hardening exponent, $n(20^\circ\text{C}) = 0.33$ independent of chemical composition since no consistent compositional dependencies was found. Suni *et al.* suggested that H parameter should depend on solute content, whose role is to retard the recovery process by which dislocations accumulated by prior deformation mutually annihilate. H was found to vary as a power to the solute content with an exponent of ~ 0.9 [105]. Zolotarevsky *et al.* [106] found in Al-Cu and Al-Mg alloys that the strain hardening rate increases with increasing solute content. In the literature, H and n are found to decrease with increasing temperature [3, 17, 107].

ⁱ σ_a corresponds physically to the stress needed to free dislocations from a “cloud” of solute.

While Eq. 4-2 is used to model isotropic hardening, the Bauschinger effect may be taken into account by the substitution $\sigma \rightarrow \sigma - X$ in Eq. 4-2 where X is the kinematic hardening variable. While Godard [17] neglected the Bauschinger effect in quenching simulations, Reich and Keßler [108] showed that kinematic strain hardening should be implemented in AA6082 heat treatment simulations. In order to characterise the Bauschinger effect, non-monotonic loads are usually performed at constant temperature [82, 108, 109]. This is not representative of what occurs during quenching where the surface undergoes tension at high temperature followed by compression at low temperature.

High temperature deformation

High temperature stress-strain curves exhibit a strain-rate dependency, which is described in steady state by a Norton-Hoff power law:

$$\sigma = K.(\dot{\epsilon}^m)^{1/N} \quad \text{Eq. 4-3}$$

where K and N are two temperature-dependent parameters. An exponent $N = 1$ corresponds to a Newtonian viscous behaviour and is explained by diffusion creep in solids [110]. A super-plastic behaviour can be found for $0.5 \leq m \leq 0.7$ where $m = 1/N$ characterises the strain-rate sensitivity [110, 111]. Physical models of dislocation creep predict N values ranging from 3 to 8 [110, 112]. N values within the range 5-15 were found by Lagneborg and Bergman [113] from experimental creep data of various precipitation-hardened alloys. Since the power law breaks down at high stresses, Garofalo [114] introduced a hyperbolic sine law which is equivalent to the power law at low stresses. Garofalo's hyperbolic sine law has been adapted by Sellars and McTegart [115] to combine temperature and strain-rate into one single parameter, Z called the Zener-Hollomon parameter:

$$Z = \dot{\epsilon}^m \exp(Q_{HW} / RT) \quad \text{Eq. 4-4}$$

where Q_{HW} is the activation energy for hot working and R is the universal gas constant. Q_{HW} indicates the resistance to plastic deformation and the increase of the flow stress from $0.8 \cdot T_m$, where alloys of the same metal are similar, to $0.5 \cdot T_m$ [116], where T_m is the melting temperature. It is higher in solution treated than in precipitated aluminium alloys because solute elements in solid solution are more effective than precipitates to exert a drag on dislocations at high temperature [117, 118]. For aged 7xxx alloys, Q_{HW} is close to or slightly higher than the activation energy of self-diffusion of pure aluminium, 142 kJ/mol [119]. For solution treated 7xxx alloys, Q_{HW} is within the range 200-260 kJ/mol [118, 120, 121]. The use of the Zener-Hollomon parameter is advantageous since Norton's law rewrites as $Z = A_I \cdot \sigma^{N_I}$ where the parameters A_I and N_I are no longer temperature-dependent.

Combined laws

In order to describe the behaviour of a material over a wide range of temperatures, one has to combine both work hardening and viscoplastic phenomena. Both multiplicative

laws such as Eq. 4-5 [23, 107, 122, 123] and additive laws [15, 17, 124-126] have been used in the literature.

$$\sigma = K_L \cdot (\varepsilon^{in})^{n_L} \cdot (\dot{\varepsilon}^{in})^{m_L} \quad \text{Eq. 4-5}$$

The multiplicative law in Eq. 4-5, where K_L , n_L and m_L are three temperature-dependent parameters, is often preferred. The additive and multiplicative laws are compared in Lemaitre and Chaboche [127]. They are both able to capture strain-hardening, creep and relaxation phenomena. The drawback of these phenomenological laws is that they do not take directly the microstructure into account in the sense that each set of parameters depends on the microstructure but not explicitly.

When precipitation is taken into account by internal or ageing variables, a_{ageing} describing the microstructural evolution, the general formulation becomes $\sigma = \sigma(T, \dot{\varepsilon}^{in}, a_{ageing})$. In his PhD work, Barlas [123] introduced such a variable to account for softening during heating of aluminium casting alloys. This internal variable with no *a priori* physical meaning was linked to the microstructure using the classical theory described hereafter.

4.1.2. Physically-based models

In physically-based models, whose aim is to link microstructure to macroscopic behaviour, internal variables are typically dislocation densityⁱ, ρ_d , or obstacle strength. Indeed, plastic behaviour is satisfactorily understood by dislocation glideⁱⁱ through a field of obstacles such as precipitates, forest dislocations or solute atoms. Kocks and Mecking [128] were the first to propose such a model based on three equations:

$$\sigma^\perp = M \mu b \sqrt{\rho_d} ; \frac{\partial \rho_d}{\partial \varepsilon^{in}} = \frac{1}{M} (\kappa_1 \sqrt{\rho_d} - \kappa_2 (\varepsilon^{in}, T) \cdot \rho_d) ; \sigma = \sigma^\perp \cdot \left(\frac{\dot{\varepsilon}^{in}}{\dot{\varepsilon}_0^{in}} \right)^{m_2} \quad \text{Eq. 4-6}$$

where μ , b and M are the shear modulus, Burgers vector and average Taylor's factor respectively. $\dot{\varepsilon}_0^{in}$ and m_2 are parameters characterising the strain-rate sensitivity. The first equation in Eq. 4-6 describes the relationship between the yield strength due to isotropic work hardening, σ^\perp , and the density of forest dislocations left by prior deformationⁱⁱⁱ. The second equation describes the evolution of ρ_d , where κ_1 is the rate of dislocation storage and κ_2 is the rate of dislocation annihilation by dynamic recovery. A third term corresponding to Orowan loop storage around non-shearable precipitates was introduced by Estrin *et al.* [129]. Zolotarevsky *et al.* [106] found in Al-Cu and Al-Mg alloys that κ_1 increases and κ_2 decreases with increasing solute content. The third equation in Eq. 4-6, derived from Orowan's equation $\dot{\varepsilon}^{in} = \rho_d b v_d$ where v_d is the dislocation velocity, is relevant at high temperature where strain-rate dependency is not negligible.

The interaction between a dislocation and a single type of obstacle has been widely investigated theoretically [130]. The extension to the interaction between dislocations and a statistical field of obstacles of a single type is also available in the literature [131].

ⁱ defined as the number of dislocation lines crossing perpendicularly a plane of unit area.

ⁱⁱ occurs on slip planes in crystallographic directions parallel to the Burgers vector.

ⁱⁱⁱ hardening is due to the difficulty to move dislocations and to a lesser extent due to the difficulty to produce dislocations.

However, the interaction between dislocations and multiple obstacle types is less clear. Kocks, Argon and Ashby [132] proposed to add the strengthening contributions:

- linearly for obstacles with different forces and with very different densities,
- linearly for obstacles with the same force and the same density,
- quadratically for obstacles with the same force and different densities.

More recently, Dong, Nogaret and Curtin [130] calculated that linear addition holds when the ratio of two obstacle densities is larger than ~67 and that quadratic addition holds when the ratio is lower than ~20. In the work of Deschamps and Brechet [20], the room temperature flow stress writes:

$$\sigma = \sigma^{LF} + \sigma^{GB} + \sigma^{SS} + X + \sqrt{(\sigma^{ppt})^2 + (\sigma^{\perp})^2} \quad \text{Eq. 4-7}$$

where σ^{LF} , σ^{GB} , σ^{SS} and σ^{ppt} represent the strengthening contributions of the lattice (Lattice Friction), the grain boundaries (GB), the solid solution (SS) and the precipitates respectively. X is the kinematic hardening variable to account for possible Bauschinger effect. According to Deschamps [133], $\sigma^{LF} + \sigma^{GB} = 10$ MPa for aluminium.

In Eq. 4-7, σ^{ppt} and σ^{\perp} are added quadratically since the density of precipitates is lower than that of forest dislocations, both contributions having a similar force. σ^{SS} and σ^{ppt} are added linearly since solute atoms are relatively weak obstacles but with a very high density compared to precipitates which are stronger obstacles but with a much lower density.

The yield strength at 0% strain offset being difficult to determine experimentally, most authors use the yield strength at 0.2% strain offset, $\sigma_{y0.2}$ in order to identify the parameters associated to σ^{SS} and σ^{ppt} . In his PhD work, Fribourg [42] writes $\sigma_{y0.2}$ at room temperature as:

$$\sigma_{y0.2} = \sigma_{y0.2}^{LF} + \sigma_{y0.2}^{GB} + \sigma_{y0.2}^{SS} + \sigma_{y0.2}^{ppt} \quad \text{Eq. 4-8}$$

While Fribourg took the value of 10 MPa for the matrix contribution (LF and GB) in Eq. 4-8, most authors take a value of ca. 19 MPa measured on pure aluminium.

Next, σ^{SS} and σ^{ppt} are discussed in more details.

Contribution of solid solution to strengthening

Strengthening by solid solution refers to the fact that the strength of pure metals is considerably increased by the addition of solute elements that form solid solution alloys. Several mechanisms have been proposed in the literature to explain solid solution strengthening from the direct interaction between solute atoms and dislocations [134]. They are usually divided into two groups, namely “dislocation locking” where solute atoms diffuse towards dislocations at rest and “dislocation friction” where solute atoms at rest exert a drag on mobile dislocations. For dilute solutions, Cottrell [135] suggested that the strain energy due to distortions around dislocations can be relieved by the segregation of solute atoms around dislocations. Dislocations being locked by their associated solute atoms, deformation at low temperature requires an energy to free dislocations from a “cloud” of solute. For body-centered cubic alloys, this leads to a rapid decrease of yield strength with increasing temperature as explained by Cottrell [135]. For

closed-packed crystals, the yield strength due to dislocation locking by segregated solute atoms is relatively insensitive to temperature according to Suzuki [136]. For highly alloyed solid solutions with short-range orderⁱ, Fisher [137] proposed a complementary strengthening mechanism. According to Fisher, dislocation motion partially destroys the order of short-range order crystals and creates an interface with positive energy. Thus an additional stress is required to force dislocation motion. In its original form, the yield strength (usually at 0.2% strain offset) in annealed temperⁱⁱ (O-temper) of a multi-component alloy with n_s alloying elements is given by Suni *et al.* [105] and writes:

$$\sigma_{y0.2} = \sigma_{y0.2}^{pure} + \sigma_{y0.2}^{SS} \quad \text{with} \quad \sigma_{y0.2}^{SS} = \left\{ \sum_{i=1}^{n_s} \left[a_i^{1/n_{SS}} X_i + \sum_{j=1}^{i-1} \left(a_{ij}^{1/n_{SS}} X_i X_j \right) \right] \right\}^{n_{SS}} \quad \text{Eq. 4-9}$$

where X_i and X_j are the concentrations of elements i and j in the matrix and (a_i, a_{ij}, n_{SS}) are parameters. Solid solution strengthening being the result of the interaction between dislocations and solute elements, it should depend on the number of the solute atoms and not on their mass as pointed out by Bardel [138]. Therefore, the concentration in atomic percent and not in weight percent should be used, which is not always the case in the literature. The interaction terms, a_{ij} account for possible synergism between solutes, such that the strength is higher than the sum of the individual contributions of each solute element. Such synergistic effects reported by Doherty and McBride [139] and Suni *et al.* [105] correspond to structural correlations between solute atoms.

While the solute exponent, n_{SS} , is outside the sum over n_s in Eq. 4-9, many authors used a modified equation [140-142]:

$$\sigma_{y0.2}^{SS} = \sum_{i=1}^{n_s} (a_i X_i^{n_{SS}}) \quad \text{Eq. 4-10}$$

where the interaction terms have been neglected and n_{SS} is inside the sum. Eq. 4-10 is different from Eq. 4-9 as it is no longer additive. This can be checked by considering two isotopes (e.g. ^{63}Cu and ^{65}Cu) with identical solute strengthening parameter a_{Cu} .

A first estimation of the solute exponent, n_{SS} , was made by Mott and Nabarro [143] who found a value of 1. The Mott–Nabarro model was later corrected by Labush [144] who found the value of 2/3. According to Haasen [134], n_{SS} takes the theoretical values of 1/2 when obstacles to dislocation movement are dilute and 2/3 when they are concentrated. a_i and n_{SS} values were initially determined on high-purity binary alloys in which case Eq. 4-9 becomes:

$$\sigma_{y0.2} = \sigma_{y0.2}^{pure} + a.X^{n_{SS}} \quad \text{Eq. 4-11}$$

For classical solute elements in aluminium alloys, a values are given in Ref. [145]. For binary face-centered cubic alloys in general, n_{SS} values of 2/3 or 3/4 were found empirically by Haasen [134]. For Al-Mg and Al-Cu binaries, Suni *et al.* [105] found n_{SS} values close to 2/3. Much higher n_{SS} values than the theoretical ones were found by Ryen *et al.* [146] on Al-Mg and Al-Mn binaries:

ⁱ solute atoms in some alloys occupy preferentially one sub-lattice.

ⁱⁱ without work hardening

$$\sigma_{y,0.2}(20^\circ\text{C}) = 19.5 + 12.1X_{Mg}^{1.14} \text{ and } \sigma_{y,0.2}(20^\circ\text{C}) = 19.4 + 54.8X_{Mn} \quad \text{Eq. 4-12}$$

In Eq. 4-12 the yield strength value for pure aluminium of ca. 19.5 MPa obtained for AA1200 is within the error of the Suni *et al.* value of 18.8 ± 3.2 MPa [105].

While the parameters of Eq. 4-9 are usually determined at room temperature, Godard determined a_{Mg} and n_{SS} as a function of temperature for AA5052 and AA5182 [17]. The solute exponent was found to be almost independent of temperature ($n_{SS} = 0.47$). A value of ca. 38 MPa/(at.%) ^{n_{SS}} was found for a_{Mg} at 250°C and 300°C. This value decreased almost linearly with increasing temperature from 300°C to 450°C where a_{Mg} reaches 8 MPa/(at.%) ^{n_{SS}} .

Although Eq. 4-9 predicts well experimental results, it requires the identification of the solute strengthening parameters a_i and a_{ij} . A more fundamental approach consists in determining solute strengthening parameters from first principles calculations as proposed by Leyson *et al.* [147] or Uesugi and Higashi [148]. Following Leyson *et al.*, the yield strength of a multi-component alloy with n_s alloying elements writes [147]:

$$\sigma_{y,0.2}(T) = M \cdot \left\{ \sum_{i=1}^{n_s} (\tau_{i0})^{3/2} \right\}^{2/3} \cdot \left\{ 1 - \left[kT \left\{ \sum_{i=1}^{n_s} (\Delta E_i^b)^3 \right\}^{-1/3} \ln \left(\frac{\dot{\epsilon}_0^{in}}{\dot{\epsilon}^{in}} \right) \right]^{2/3} \right\} \quad \text{Eq. 4-13}$$

where M is Taylor's factor, k_b is Boltzmann's constant, $\dot{\epsilon}_0^{in}$ is a reference strain rate and τ_{i0} and ΔE_i^b are respectively the shear strength and characteristic energy barrier contributions of element i at zero Kelvin. The shear strength and energy barrier values predicted by Leyson *et al.* for Mn, Cr, Cu, Mg, Si and Fe in Al matrix are given in *Table 4-1* together with Suni's parameters a_i and a_{ij} at room temperature for relative comparison since the solute strengthening parameters of the two models are expected to vary in the same way according to the solute element.

	Mn	Cr	Cu	Mg	Si	Fe	Mg.Si
a_i and a_{ij} MPa/(at.%) ^{3/4}	59.9 ± 16.15	—	54.2 ± 8.1	24.0 ± 3.1	0.0	—	129.1 ± 8.8
$\tau_{i0} / X_i^{2/3}$ (MPa)	711	705	348	342	137	13.238	—
$\Delta E_i^b / X_i^{1/3}$ (eV)	7.53	6.65	4.10	4.06	2.58	28.8	—

Table 4-1 – Solute strengthening parameters a_i and a_{ij} at room temperature in Eq. 4-9 using $n_{SS} = 3/4$ [105]; Shear strength and energy barrier values at zero Kelvin in Eq. 4-13 [147].

The solutes given *Table 4-1* rank with increasing strengthening effect on an at.% basis as Mn > Cr > Cu > Mg > Si. Compared to these solute elements, little attention has been paid to Zn which has a low strengthening effect as shown in *Figure 4-1*.

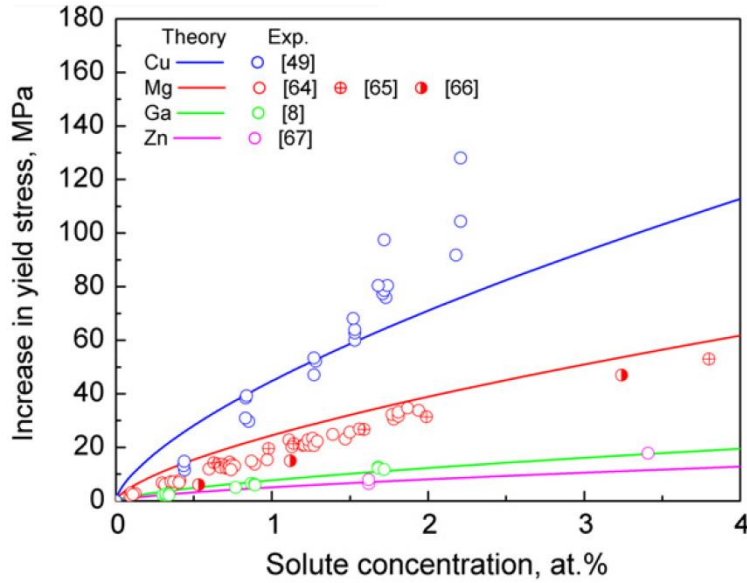


Figure 4-1 – Effect of solute concentration on yield stress for Al-Cu, Al-Mg, Al-Ga and Al-Zn alloys. References in this figure taken from Uesugi and Higashi [148] are given in their work.

The high strengthening effect of Cu and Mg and the low strengthening effect of Zn was to be expected considering the fact that Mg atoms are larger than Al at by 12%, Zn atoms are smaller by 2.8% and Cu atoms by 10.2% [149].

Contribution of precipitates to strengthening

Precipitation strengthening is obtained by the production of a dispersion of obstacles to dislocation motion. Several mechanisms have been proposed in the literature, involving particle shearing or particle by-passing. A dislocation with a line tension ($\Gamma = \beta\mu b^2$ where β is a parameter generally lower than the classical value of 1/2 [150]) moving towards a particle bends due to the intrinsic resistance force F_p of the precipitate (Figure 4-2).

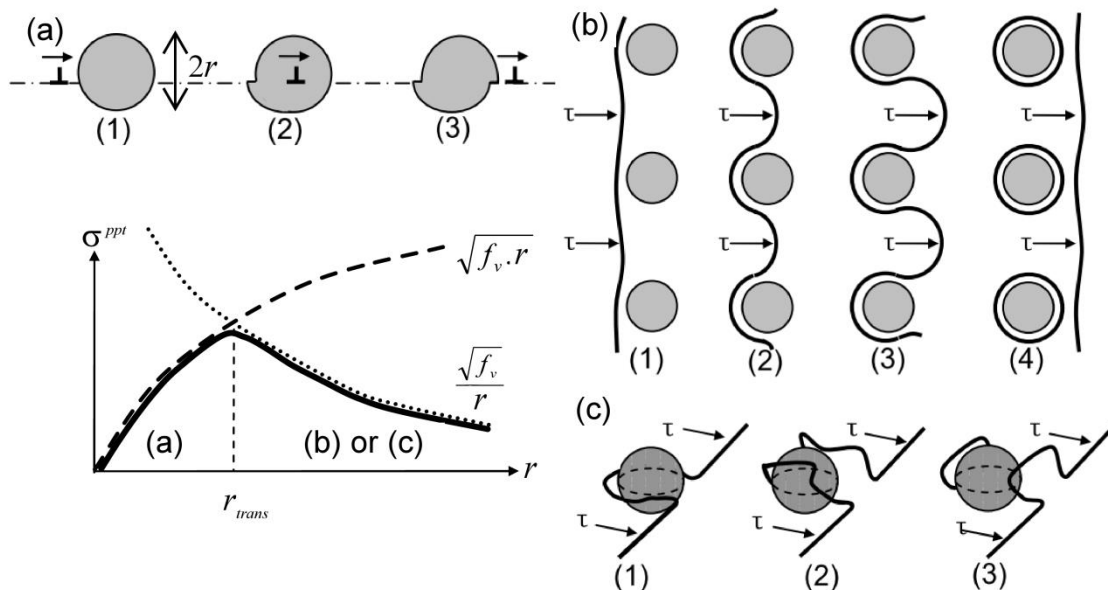


Figure 4-2 – Schematic of contribution of small (a) and large (b) and (c) precipitates to strengthening. Adapted from Fribourg [42].

Soft precipitates ($F_p \leq 2\Gamma$) are sheared by the dislocation as shown in *Figure 4-2-a*. Hard precipitates ($F_p > 2\Gamma$) are bypassed by the dislocation either by Orowan looping (see *Figure 4-2-b* where loops are stored around precipitates) or cross-slipⁱ (see *Figure 4-2-c* where a loop is stored in front of the precipitate). Soft precipitates are deformed which results in an increase of the precipitates/matrix interfacial energy. The greater strengthening effect is achieved by coherency strain hardening, where a dislocation interacts with the coherency strain field around a small coherent precipitate. The strengthening contribution of precipitates of radius r and volume fraction f_v is proportional to $(r f_v)^{1/2}$ for small precipitates and to $f_v^{1/2}/r$ for large ones as shown schematically in *Figure 4-2*. These two mechanisms showing a square root dependency on f_v , a peak strength occurs at a given precipitate size, r_{trans} independent of f_v . Assuming that the dislocation line moves through all the precipitates encountered in the slip plane, the stress at which the precipitates are overcome writes [20]:

$$\sigma^{ppt} = \frac{M\bar{F}}{b\bar{L}} = \frac{M}{b\bar{L}} \int_0^\infty F(r) f_{PSD}(r) dr \quad \text{Eq. 4-14}$$

where \bar{F} is the mean obstacle strength, \bar{L} is the average distance between precipitates, b is Burgers vector, M is Taylor's factor, $F(r)$ is the force necessary for the dislocation to overcome the precipitates of radius r and f_{PSD} defines the particle size distribution such that $f_{PSD}(r).dr$ is the probability that the size of a precipitate is between r and $r+dr$. While $F = 2\Gamma$ for large precipitates, Gerold [151] suggested for small precipitates that:

$$F(r) = k_s \mu b r \quad \text{Eq. 4-15}$$

where k_s is an adjustable parameter depending on the involved mechanism such as interface creation or coherency strain hardening. In his PhD work, Deschamps [152] suggested the value of 0.111, determined for η' precipitates in the ternary Al–6.1wt%Zn–2.35wt%Mg alloy, as an upper bound for k_s . For clusters and GPZ in this ternary, Deschamps and Brechet [20] used the value of $k_s = 0.07$ together with $M = 2$ and $\beta = 0.43$. In his PhD work, Godard [17] found the value of $k_s = 0.045$ for η' precipitates and the value of $k_s = 0.077$ for clusters and GPZ in AA7010. The effect of temperature on k_s was accounted for by Godard using a smooth transition from 0.077 below 100°C to 0.045 above 150°C.

The transition radius satisfies $k_s \mu b r_{trans} = 2\Gamma$, which gives $r_{trans} = 2\beta b/k_s$. Wang *et al.* [153] proposed the theoretical value $r_{trans} = 15\mu_{Al}b/\mu_{ppt}$ which gives 2.5 nm for Mg₂Si precipitates.

The onset of coarsening during artificial ageing was determined by SAXS measurements to estimate r_{trans} . In a recent paper, Fribourg *et al.* [82] found $r_{trans} = 3.3$ nm for artificially-aged AA7449 samples in agreement with the earlier findings by Guyot and Cottignies [150] of ca. 3 nm for Al-Zn-Mg-Cu alloys.

Different models have been proposed in the literature to estimate \bar{L} . Using Friedel's statistics, which gives good results for small and large precipitates, \bar{L} is given as [151]:

ⁱ Transfer of glide of a screw dislocation from one slip plane to another.

$$\bar{L} = \bar{r} \left(\frac{2\pi}{3f_v} \right)^{1/2} \quad \text{Eq. 4-16}$$

where \bar{r} is the average precipitates radius. For small precipitates ($< r_{trans}$), Eq. 4-14 becomes [20]:

$$\sigma^{ppt}(\bar{r} < r_{trans}) = \left(\frac{3}{4\pi\beta} \right)^{1/2} \frac{k_s^{3/2} M \mu}{b^{1/2}} (\bar{r}^{clusters} f_v^{cluster})^{1/2} \quad \text{Eq. 4-17}$$

For large precipitates ($> r_{trans}$), such as η in 7xxx alloys, Eq. 4-14 becomes [20]:

$$\sigma^{ppt}(\bar{r} > r_{trans}) = \left(\frac{6}{\pi} \right)^{1/2} \beta M \mu b \frac{(f_v^\eta)^{1/2}}{\bar{r}^\eta} \quad \text{Eq. 4-18}$$

In order to predict σ^{ppt} , most authors [19, 20, 140, 142, 154, 155] used a precipitate size distribution whose main effect is to allow a smooth transition between Eq. 4-17 and Eq. 4-18 at r_{trans} . This approach is computationally expensive but is justified for yield strength predictions during artificial-ageing where fine precipitates evolve into larger precipitates. Instead, Fribourg [82] used a simplified mean radius approach. This approach is computationally less expensive than the PSD approach but also less accurate, especially when \bar{r} of the precipitate size distribution is close to r_{trans} during artificial ageing. This is not an issue when \bar{r} is lower than r_{trans} , which is the case during coolings similar to those encountered during quenching as shown in the PhD work of P. Schloth [50] for AA7449 (see also section 3.1.3 for AA7040).

In physically-based models of yield strength, the effect of temperature has been determined from first principles of thermodynamics (see Eq. 4-13). However, many authors used empirical [17, 156-158] or phenomenological [159-162] laws whose parameters are identified against $\sigma_{y0.2}$ -values at different temperatures.

4.1.3. Temperature dependence of yield strength

In most alloys, yield strength decreases with increasing temperature as a result of thermally activated processes [110]. This is the case in heat-treatable AA as shown in *Figure 4-3* and *Figure 4-4*, where yield strength in annealed (O) and in artificially aged states increases significantly with decreasing temperature from 200°C to 30°C.

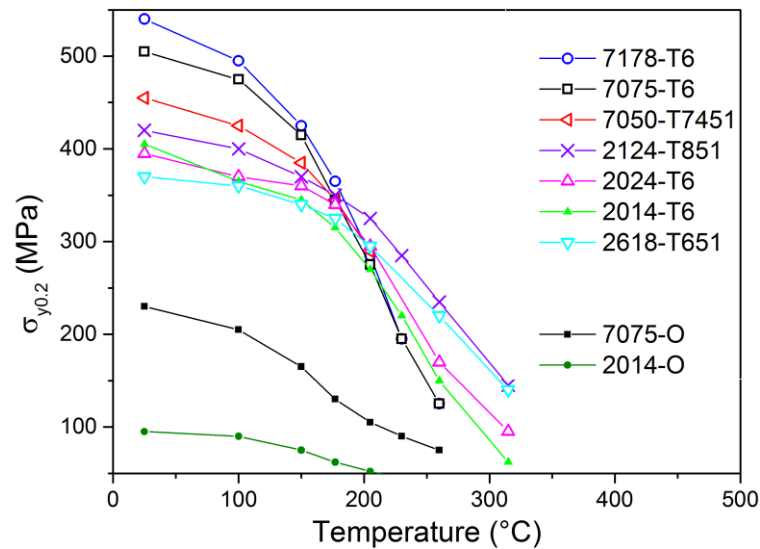


Figure 4-3 – Temperature dependence of yield strength of 2xxx and 7xxx alloys in annealed (O) and artificially aged states [163].

In Figure 4-3, yield strength values are obtained after heating to the desired temperature and 30 min holding time before mechanical load.

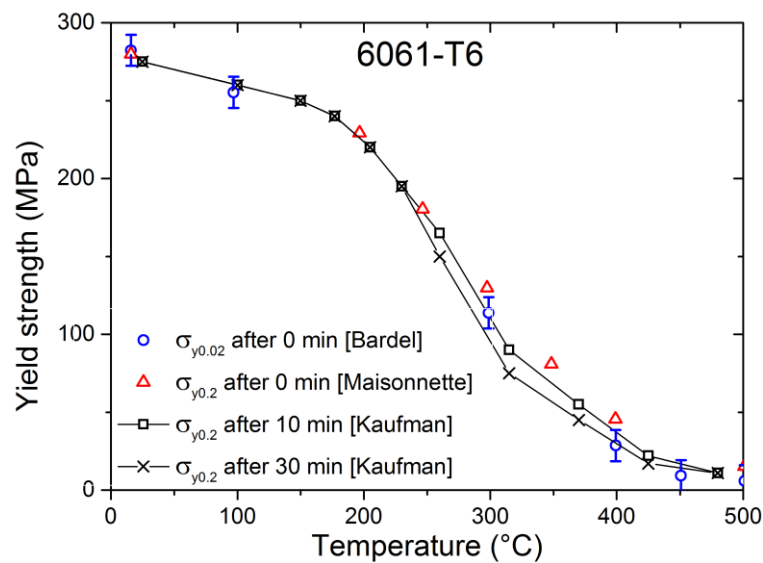


Figure 4-4 – Temperature dependence of yield strength of 6061 in T6 state. Bardel and Maisonnette: heating at 15 K/s and immediate mechanical load, a waiting time of 10 or 30 min before mechanical load was applied by Kaufman.

Figure 4-4 shows that the 30 min waiting time prior to mechanical load has little impact on yield strength at temperatures lower than 250°C. Like 2xxx and 7xxx alloys in Figure 4-3, the yield stress increase with decreasing temperature from 200°C to 30°C is high (ca. 50 MPa) in 6061-T6.

Unlike heat-treatable AA, non-heat-treatable AA in annealed state do not feature such increase of yield strength with decreasing temperature from 200°C to 30°C [17, 163, 164]. Instead, yield strength remains fairly constant up to ca. 200°C and starts to decrease as temperature is increased beyond 200°C. This seems to be also the case in heat-treatable AA in non-equilibrium solid solution as shown in Figure 4-5.

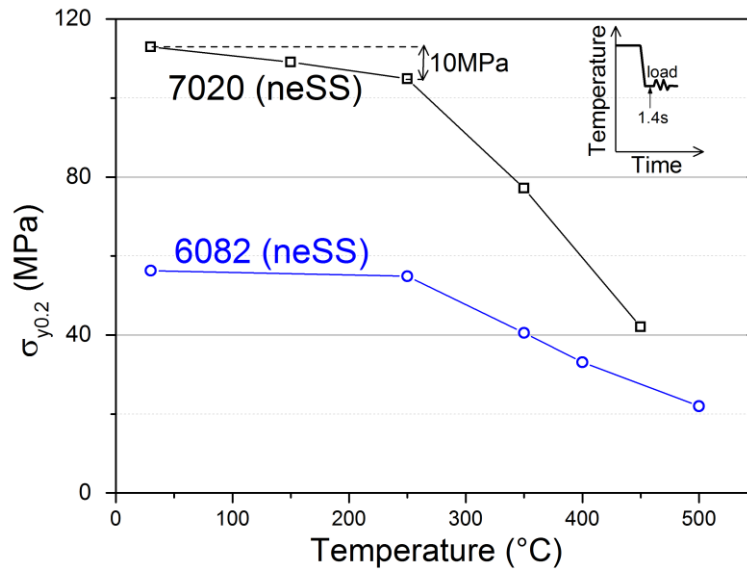


Figure 4-5 - Temperature dependence of yield strength of AA7020 and AA6082 in neSS [165]. Inset: compression loads were performed after IQ to the desired temperature and 1.4 seconds waiting time for temperature stabilisation.

In 2010, Keßler and Reich [165, 166] used a quenching and deformation dilatometer type Bähr DIL 805A/D to obtain neSS by interrupted quench (IQ). IQ measurements were performed at 300 K/min for AA7020 (high temperature critical cooling rate of ca. 180 K/min [73]) and 1000 K/min for 6082 (high temperature critical cooling rate of ca. 1000 K/min [72]). Compression was performed at 0.1 s^{-1} to avoid precipitation during loading.

Figure 4-5 shows that the yield strength decrease from 20°C to 250°C is less than 10%. This indicates that the contribution of solid solution to strengthening is little temperature dependant below 200°C. This is compatible with the theoretical work of Suzuki [136] who found that for closed-packed crystals, the yield strength due to dislocation locking by segregated solute atoms is relatively insensitive to temperature. However, such results are not well known. Indeed, literature on yield strength of heat-treatable AA in non-equilibrium solid solution is scarce because of experimental difficulties, such as temperature control and localisation of deformation outside of gauge length of specimens in neSS as pointed out by Bardel [138].

Back in the nineties, Godard *et al.* [7, 17, 22] perform IQ followed by tensile tests. They used a laboratory thermo-mechanical testing apparatus (Dithem) to determine the mechanical behaviour of AA7010 (Figure 4-6).

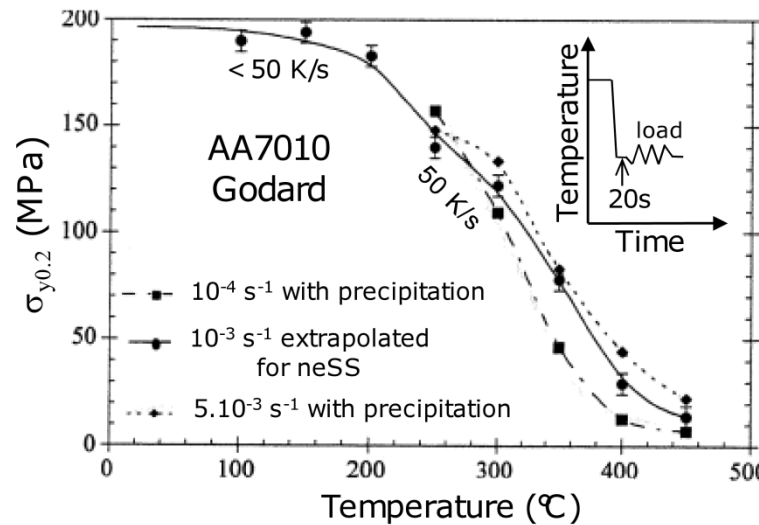


Figure 4-6 - Temperature dependence of yield strength of AA7010 with precipitation (dashed lines) and extrapolated for the neSS (solid line) [17]. Inset: tensile loads were performed after IQ to the desired temperature and 20 seconds waiting time.

In Figure 4-6, the plateau of yield strength below 200°C is misleading since the values were extrapolated using the evolution of Guinier radius determined by SAXS measurements [17]. The yield strength of AA7010 is higher than that of AA7020 in neSS (Figure 4-5). This can be explained by the different compositions: AA7010 contains more solute elements than AA7020. However, a yield strength of ca. 190 MPa below 200°C seems too high for a non-equilibrium solid solution.

4.1.4. Conclusion and limitation of previous works

From this literature survey, it appears that the contribution of solid solution and precipitation to strengthening are well described at room temperature. Indeed, most models predict yield strength at 20°C after perfect quenching followed by artificial ageing. The parameters of such models are not meant to be used for quenching simulations where the precipitation state is different from that after artificial ageing. For quenching simulations, the yield strength model parameters must be adjusted using high temperature yield strength values. The values available in the literature are usually not representative of quenching conditions since they are obtained after heating from room temperature to the desired temperature. Only a few authors performed interrupted quench-tests from the SHT temperature, i.e. from a solid solution at equilibrium without precipitates. Reich and Keßler determined the mechanical behaviour of AA6082 and AA7020 with and without (neSS) precipitates after continuous coolings at different cooling rates. This was possible thanks to the relatively low high temperature and low temperature critical cooling rates of these two alloys, together with a good temperature control in the apparatus. The mechanical properties of AA7020 were used for RS calculations using a phenomenological model with hardening parameters. Since the cooling rates during industrial quenching are not constant, a one-way coupling temperature→precipitation→stresses would be more accurate. For this, a yield strength

model could be calibrated using the valuable mechanical properties obtained by Reich and Keßler after continuous cooling.

In an attempt to determine the mechanical behaviour of AA7010 in neSS, Godard could not avoid precipitation hardening during quenching. Indeed, for alloys with elevated low temperature critical cooling rate, the characterisation of the neSS is limited by the achievable cooling rate. Godard announced a cooling rate of 50 K/s but could not maintain it at low temperature and performed the tensile loads after 20 seconds waiting time. The mechanical behaviour of AA7010 in neSS was then extrapolated from SAXS measurements, but the yield strength values seem then too high at low temperature.

From Reich's and Godard's works, it can be inferred that the characterisation of AA7449, AA7040 and AA2618 in neSS requires a good temperature control. Instead of continuous coolings which are not representative of industrial quenching, coolings at non-constant cooling rate similar to real coolings will be performed. The yield strengths will then be used to calibrate the yield strength model parameters valid for the range of coolings typical of industrial quenching conditions.

Based on the literature review on the available mechanical models for quenching simulations, an additive phenomenological equation is chosen in this work for all the FE simulations. The addition of yield strength, strain hardening and viscous stress is advantageous if precipitation mainly affects yield strength as assumed in this work. For the TM model (without precipitation), the yield strength is that of the non-equilibrium solid solution to be determined after fast quenches. For the TMG model (with precipitation from Gleeble tests), the yield strength will include precipitation but not explicitly. For the TMM model, a yield strength model considering only small particles will be used to take into account precipitation.

4.2. Thermo-mechanical testings in the Gleeble

The Gleeble 3500 machine at University of South Brittany is used to perform tensile-tests in different metallurgical states to characterise the mechanical behaviour of the three alloys. The aim is also to provide data to calibrate a yield strength model that will be used in a one-way coupling temperature→precipitation→stresses.

4.2.1. Gleeble thermo-mechanical simulator and sample configuration

The Gleeble machine is selected to carry out the thermo-mechanical tests because of its reliability in controlling temperature, jaw velocity and force. Specimens are held horizontally by water-cooled grips and heated via Joule effect. A closed-loop feedback control system enables precise control of the heat input based on the temperature monitored by the central thermocouple TC1 fixed at the specimen surface. The use of water-cooled grips provides a sufficiently high cooling rate for most applications but external water or gas quenching can also be applied to reach higher cooling rates. Hoop strain measurements are readily done by attaching a diametral extensometer that measures the reduction in area as the specimen is being tensioned. Diameter change and temperature are usually measured on the same plane, at the mid-length of the sample. Axial strains can also be measured using a longitudinal extensometer, provided a sufficiently isothermal gauge length exists.

Due to direct resistance heating and cooling from the water-cooled grips, an axial temperature gradient appears from the specimen mid-span to the ends with typically quadratic temperature profiles [167]. Usually the radial gradient is small and may be neglected except when specimen temperature is above 1000°C. The specimen geometry strongly affects the temperature distribution in the sample. Longer specimens reduce axial thermal gradient but longer free span always results in slower heating and cooling rates. In addition the material and geometry of the grips also affect cooling and thermal gradient. For instance, the use of stainless steel grips results in lower cooling rates and a lower thermal gradient than copper grips. With these considerations in mind, the optimal sample configuration (specimen geometry and grip choice) can be determined according to the specific thermal treatment conditions that are required.

When tensile test is considered, the axial thermal gradient inherent to the Gleeble specimens can be exploited to guarantee that the strength of the mid-span area is lower than that of the region located in the grips. Thus, almost no deformation occurs in the conductive part of the jaw system and cylindrical specimens without reduced diameter at the mid-length are used. However, when the strength of the material is almost identical in the full specimen length, it is desirable to reduce the mid-span of the specimens. In that case, the quadratic axial temperature profile together with a reduction in area at the mid-length of the specimen guarantees that the maximum strained region is at the specimen mid-span.

4.2.2. Requirements and setup for Gleeble tests

Thermal requirements

The thermal requirements come from metallurgical requirements.

The first metallurgical requirement is to obtain a solid solution at equilibrium in the gauge length while avoiding coarse precipitates outside the gauge lengthⁱ. To meet this requirement, the solutionising time in the Gleeble should not be too long, and the heating rate should be fast enough to limit precipitation during heating.

The second metallurgical requirement is to obtain a non-equilibrium solid solution after interrupted quench-tests at different temperatures in order to characterise it and calibrate the parameters corresponding to the solid solution contribution to strengthening. High cooling rates are thus required to prevent any precipitation phenomena during quench. Lower cooling rates are also required to be representative of quenching process but they are easier to obtain.

Furthermore, to guarantee a correct strain measurement, the axial thermal gradient in the specimen must be minimised to create a quasi-isothermal gauge length. High cooling rates and small axial thermal gradient being two contradictory thermal requirements, several specimen geometries and grips were tried to find the optimal sample configuration.

Mechanical requirements

The first mechanical requirement is to localise deformation in the gauge length in order to obtain reliable stress-strain curves. This is mainly achieved by the axial temperature profileⁱⁱ together with a possible reduction in area at mid-length of the specimen.

The second mechanical requirement is to be representative of what happens during quenching of industrial components. Thus, the loading conditions are defined to cover the equivalent inelastic strain-rates typical of cold-water quenched plates ($< 0.02 \text{ s}^{-1}$) and of boiling-water quenched forgings.

At high temperatures ($\geq 350^\circ\text{C}$), different strain-rates and pseudo-relaxations (blocked jaws) are to be imposed in order to characterise the strain-rate sensitivity (SRS).

At temperatures lower than 350°C , high strain-rates ($> 0.01 \text{ s}^{-1}$) are chosen to limit the effect of precipitation on yield strength in order to characterise the neSS. In addition, this effect of precipitation on yield strength is to be characterised through complementary tests with various waiting times before the beginning of the first load.

Experimental setup

Two different specimen geometries are used for Gleeble tests as shown in *Figure 4-7* (see appendix 7.4 for the dimensions).

ⁱ which could form during solutionising due to the quadratic axial temperature profile.

ⁱⁱ which depends on specimen length and grip material and geometry.

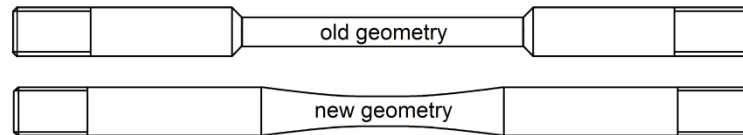


Figure 4-7 – Old and new specimen geometries used for thermo-mechanical tests.

These two geometries together with the use of copper grips allow obtaining cooling rates higher than 100 K/s above 300°C using compressed air, while minimising the axial thermal gradient during isothermal holdings. This is fast enough to avoid precipitation of the stable phases above 300°C. The “old geometry” was preferred at high temperatures ($\geq 400^\circ\text{C}$) because of the lower axial thermal gradient and the better positioning of the diametral extensometer. At intermediate temperature (100-350°C) this later geometry was found to be inadequate due to stress localisation outside the gauge length attributed to the formation of coarse precipitates during solutionising (see appendix 7.4). The “new geometry” was thus preferred since no localisation outside of gauge length was observed.

Before thermo-mechanical testings, unless otherwise stated, all tensile specimens are presolutionised in a furnace for at least 4 hours, quenched in cold-water and stored in a freezer at ca. -10°C to retard any precipitation. Gleeble specimens are heated at 30 K/s to the SHT temperature while the force is maintained near zero to allow free dilatation. This high heating rate together with a solutionising time of 3 min (unless otherwise stated) in the Gleeble are chosen to obtain a solid solution at equilibrium, i.e. without any precipitates. Indeed, SAXS experiments upon heating at 5-9 K/s of naturally aged AA7449 samples showed a complete dissolution of the precipitates when the samples reach the SHT temperature (see PhD work of P. Schloth [50]).

Three different cooling conditions from the SHT temperature are imposed in the Gleeble:

- i. Fast quenches in order to characterise the neSS. The fastest quenches are achieved by Water Quench (WQ) interrupted at either 20°C or 100°C . WQ interrupted at higher temperatures was too challenging. Hence, compressed air is used instead above 100°C . This results in lower cooling rates with a risk of precipitation at intermediate temperatures (150-250°C) during Air Quench (AQ).
- ii. Coolings similar to the ones of the surface during quenching (later called “surface cooling”) in order to take into account precipitation in a simple way.
- iii. Coolings similar to the ones achieved in the *in situ* SAXS experiment (later called “SAXS cooling”) in order to calibrate the parameter corresponding to the contribution of small precipitates to strengthening in the yield strength model.

These coolings performed at zero-force control are interrupted at desired temperatures where isothermal tensile loads are applied. The tests are performed at constant jaw displacement velocity instead of constant strain-rate to obtain a smoother extensometer signal. Force is measured using a 100 kN load cell.

During testing, the PC of the Gleeble machine records the evolution of the force, F , the displacement of the hydraulic cylinder (stroke), the extensometer signal and the temperatures TC1, TC2 and TC3ⁱ. The evolution of the specimen diameter d is calculated from the evolution of the diametral extensometer and the knowledge of the initial diameter d_i measured by a digital calliper before Gleeble test. The Cauchy axial stress σ_{zz} (also called true stress) and the logarithmic hoop strain $\varepsilon_{\theta\theta}$ (also called Log. strain or true strain) measured by the diametral extensometer (see appendix 7.4) are calculated by:

$$\sigma_{zz} = \frac{F}{\pi d^2 / 4} \text{ and } \varepsilon_{\theta\theta} = \ln \left[\frac{d}{d_0(T_{load})} \right] \quad \text{Eq. 4-19}$$

with $d_0(T_{load})$ the diameter at the begin of the load at temperature T_{load} . To limit noise, the force signal is filtered by Fourier transform.

Hoop strain $\varepsilon_{\theta\theta}$ measured by the diametral extensometer is transformed to axial strain ε_{zz} using (see appendix 7.4):

$$\varepsilon_{zz} = \frac{1-2\nu}{E} \sigma_{zz} - 2\varepsilon_{\theta\theta} \quad \text{Eq. 4-20}$$

where the Poisson's ratio ν is taken constant (0.33) and the Young's modulus E is temperature-dependent (see *Figure 7-3* in appendix 7.1). Eq. 4-20 is valid for a tensile test at constant temperature as performed experimentally.

4.2.3. Identification using SiDoLo

Equations of the model

In order to fit the experimental results, an elasto-viscoplastic constitutive model with additive hardening (Chaboche-type model) is chosen (see appendix 7.3). Assuming negligible kinematic hardening (see appendix 7.6.4), a uniaxial monotonic load at constant temperature is fully defined by:

$$\begin{aligned} \varepsilon_{zz} &= \varepsilon_{zz}^e + \varepsilon_{zz}^{in} \\ \varepsilon_{zz}^e &= \sigma_{zz} / E \\ \sigma_{zz} &= \sigma_y + H \cdot (p_{cum})^n + K \cdot (\dot{p})^m \text{ with } \dot{p} = \left| \dot{\varepsilon}_{zz}^{in} \right| \end{aligned} \quad \text{Eq. 4-21}$$

where the yield strength at 0% strain offset, σ_y , is assumed to be the only parameter which depends on precipitation and p_{cum} is defined in Eq. 4-1. Compared to the widely used multiplicative law with 3 parameters (Eq. 4-5), Eq. 4-21 with 5 temperature-dependent parameters (σ_y , H , n , K , m) is less present in the literature. Indeed, the parameters of Eq. 4-21 are more difficult to identify as pointed out by Lemaitre and Chaboche [127] and several sets of parameters that minimise the objective function might be found. The main advantage of the additive law is that the parameter σ_y has a

ⁱ TC2 and TC3 are symmetrically located at 5 mm from TC1 (see appendix 7.4)

physical meaning and can be used directly to calibrate a yield strength model that predicts the yield strength at 0% strain offset. In this work, the additive law is chosen in order to compare the identified parameters for AA7449, AA7040 and AA2618 to those of Godard for AA7010. Depending on the precipitation state, different values of σ_y are to be identified to feed the models used for FE quenching simulations as shown in *Table 4-2*.

FE simulations	Yield strength, σ_y
TM model “without precipitation”	$\sigma_y = \sigma_0$ of neSS (without precipitates), identified on tensile curves after WQ or obtained by extrapolation ($t \rightarrow t_{hard,0}$ or $t_{soft,0}$ in Eq. 4-22).
TMG model “with precipitation from Gleeble tests”	σ_y of a material with a precipitation state similar to that of the surface during quenching, identified on tensile curves after “surface cooling”.
TMM model “with precipitation: one-way coupling”	σ_y calculated by a yield strength model whose parameters are calibrated against σ_y values identified on tensile curves after “SAXS cooling”.

Table 4-2 – Yield strength values needed to feed the models used for three different FE simulations of quenching.

In order to fit the Gleeble tensile curves with different precipitation states at a given temperature, the yield stress, σ_y , is defined as the sum of a threshold stress, σ_0 , and two contributions which either increase or decrease the yield strength with time:

$$\sigma_y = \sigma_0 + \sigma_{hard} a_{hard} - \sigma_{soft} a_{soft} \quad \text{Eq. 4-22-a}$$

$$a_{hard}(t) = a_{hard,\infty} - (a_{hard,\infty} - a_{hard,0}) \exp\left(-(t - t_{hard,0}) / \tau_{hard}\right) \text{ with } t \geq t_{hard,0} \quad \text{Eq. 4-22-b}$$

$$a_{soft}(t) = a_{soft,\infty} - (a_{soft,\infty} - a_{soft,0}) \exp\left(-(t - t_{soft,0}) / \tau_{soft}\right) \text{ with } t \geq t_{soft,0} \quad \text{Eq. 4-22-c}$$

The use of the ageing variables a_{hard} and a_{soft} is inspired from the works of Barlas and Wisniewski [123, 168]. Hardening by fine precipitates is modelled by an amplitude, σ_{hard} , and an evolution law with a hardening variable a_{hard} which varies from $a_{hard,0}$ to $a_{hard,\infty}$. Similarly, the softening variable a_{soft} is used to fit experimental results exhibiting softening caused by coarse precipitates which decrease the contribution of solid solution to strengthening, static softening, dynamic particle coarsening, dynamic recovery or dynamic recrystallisation [118]. These softening mechanisms being difficult to dissociate [169], it is decided to use only one softening variable to try to fit softening. These simple equations to model the evolution of yield strength with time at constant temperature have no physical basis. They are mainly used to decouple the effects of precipitation and/or softening and strain-rate on yield strength, especially at high temperature. Indeed, precipitation is likely to occur during testing at low strain-rates and the dislocations introduced during testing are potential nucleation sites for precipitates.

The hardening variable is used to evidence the effect of precipitation on yield strength between 100°C and 300°C. More importantly, it provides an extrapolation procedure to determine the yield strength of non-equilibrium solid solutions, i.e. without precipitates.

Although Eq. 4-22 could be implemented in the FE simulations of quenching by using the additivity principle, this approach is not chosen in this work and none of the performed FE simulations of quenching uses Eq. 4-22. These equations are used to fit the Gleeble tensile curves with different precipitation states at a given temperature after rapid quench, with the following simplifications:

- precipitation either soften or harden the material at a given temperature, i.e. if $a_{soft,0} \neq 0$, $a_{hard,0} = 0$ and if $a_{hard,0} \neq 0$, $a_{soft,0} = 0$.
- $a_{soft,0} = 0$ for an initial time $t_{soft,0}$ taken when TC1 is equal to 400°C since SAXS results show that coarse precipitates start to form at ~400°C for AA7449 (Figure 3-1-a), ~350°C for AA7040 (Figure 3-3-a) and ~350°C for AA2618 (Figure 3-7).
- $a_{hard,0} = 0$ for an initial time $t_{hard,0}$ taken when TC1 is equal to 300°C since SAXS results show that fine hardening precipitates start to form at ~300°C for AA7449 (Figure 3-1-b), ~250°C for AA7040 (Figure 3-3-b) and ~300°C for AA2618 (Figure 3-7). This choice assumes that the yield strength at the testing temperature is not affected by the formation of coarse precipitates above 300°C during cooling in the Gleeble. This is justified by the low volume fractions of coarse precipitates (see chapter 3) during the coolings achieved in the Gleeble.
- $a_{soft,\infty} = 1$ and $a_{hard,\infty} = 1$, which assumes complete hardening or softening after an infinite time at a given temperature, in order to decrease to number of variables since the use of $a_{soft,\infty}$ and σ_{soft} to define the amplitude of softening for instance leads to an infinity of solutions.

Thus, with a_{hard} and a_{soft} varying between zero and unity, Eq. 4-22-a becomes:

$$\sigma_y = \sigma_0 + \sigma_{hard} \left[1 - \exp\left(-(t - t_{hard,0}) / \tau_{hard}\right) \right]$$

Eq. 4-23-a

with $\sigma_y(t_{hard,0}) = \sigma_0$ and $\lim_{t \rightarrow \infty}(\sigma_y) = \sigma_0 + \sigma_{hard}$

$$\sigma_y = \sigma_0 - \sigma_{soft} \left[1 - \exp\left(-(t - t_{soft,0}) / \tau_{soft}\right) \right]$$

Eq. 4-23-b

with $\sigma_y(t_{soft,0}) = \sigma_0$ and $\lim_{t \rightarrow \infty}(\sigma_y) = \sigma_0 - \sigma_{soft}$

Eq. 4-23-a is implemented in SiDoLo in order to perform fits with hardening variable (for temperatures ranging from 100°C to 300°C). Eq. 4-23-b is implemented in SiDoLo in order to perform fits with softening variable (for temperatures ranging from 350°C to 410°C).

Identification procedure

The nine temperature-dependent parameters (σ_0 , σ_{hard} , τ_{hard} , σ_{soft} , τ_{soft} , H , n , K , m) are identified by inverse method using a dedicated optimisation software (SiDoLo) developed by P. Pilvin [170]. At each test temperature, several tensile loads are used for the identification as detailed in appendix 7.3. SiDoLo simulates the ε_{zz} - time experimental loads and calculates the stresses corresponding to the current set of parameters. Among the parameters to identify, (σ_0 , H , n) are constrained to always decrease with increasing temperature and m is constrained to always increase with increasing temperature.

At high temperature ($\geq 400^\circ\text{C}$) where strain-hardening is negligible, H and n are set to low values. First, σ_{hard} and σ_{soft} are set to zero and the parameters to identify are (σ_0 , K , m). For these fits without ageing variable, more weight is given to short times (< 12 sec from the begin of isothermals) in order to be representative of what occurs during quenching. When these fits without ageing variable are good (for the entire time-window covered by the tensile loads), the identified parameters (σ_0 , K , m) are used for all the FE quenching simulations. When these fits are poor (for long times), a softening variable varying from zero to unity is used and the identified parameters are (σ_0 , σ_{soft} , τ_{soft} , K , m).

At room temperature ($\leq 35^\circ\text{C}$) where strain rate sensitivity (SRS) is negligible, K and m are set to low valuesⁱ, σ_{hard} and σ_{soft} are set to zero and the parameters to identify are (σ_0 , H , n). For these fits without ageing variable, more weight is given to low strains (< 1.4 %) representative of what occurs during quenching. The identified parameters (H , n) are used for all the FE quenching simulations. For tensile loads performed after water quench (WQ) in the Gleeble, the identified σ_0 is assumed to be the yield strength of the neSS, i.e. without precipitates. For tensile loads performed after coolings similar to the industrial ones (section 4.3.5), the identified σ_0 (of a material with precipitates) is used for the FE quenching simulations with TMG model (section 5.3.1).

At intermediate temperature ($100\text{-}265^\circ\text{C}$) where SRS is found to be negligible, K and m are set to low values, σ_{soft} is set to zero and the parameters to identify are (σ_0 , σ_{hard} , τ_{hard} , H , n). For these fits with hardening variable, more weight is given to short times (< 5 sec from the beginning of the isothermals) and low strains (< 1.4 %). The identified parameters (H , n) are used for all the FE quenching simulations and σ_0 is assumed to be the yield strength of the neSS, i.e. without precipitates.

Between 300°C and 350°C , σ_{hard} and σ_{soft} are first set to zero and the parameters to identify are (σ_0 , H , n , K , m). For these fits without ageing variable, more weight is given to short times (< 12 sec from the beginning of the isothermals). When these fits without ageing variable are good, the identified parameters (σ_0 , H , n , K , m) are used for all the FE quenching simulations. When these fits are poor, an ageing variable varying from zero to unity is used: the identified parameters are (σ_0 , σ_{hard} , τ_{hard} , H , n , K , m) at 300°C and (σ_0 , σ_{soft} , τ_{soft} , H , n , K , m) at 350°C . The identified parameters (H , n , K , m) are used for all the FE simulations and σ_0 is assumed to be the yield strength of the neSS, i.e. without precipitates.

Whether measured or extrapolated, the values of σ_0 determined for the neSS are used for the FE simulations with TM model (without precipitation). They are also used to calibrate the parameters of the solid solution contribution to strengthening (see section 4.3.6).

ⁱ not zero for numerical reasons

4.3. Results and discussion

In section 4.3.1, the fast interrupted quenches achieved in the Gleeble on AA7449, AA7040 and AA2618 are shown. The corresponding yield strength, in particular for non-equilibrium solid solutions are given in section 3.1.1. The tensile curves are then given in section 4.3.3 for AA7449 as an illustration, for the three alloys, of the viscous behaviour at high temperature and of the effect of precipitation on flow stress at intermediate temperatures. In section 4.3.4, the identified parameters of the constitutive law are given for the three alloys. In section 4.3.5, the coolings similar to the industrial ones are shown together with the corresponding mechanical behaviour. Using the relevant yield strength values obtained in the previous sections, the parameters of yield strength model to be used for the TMM model coupled with a precipitation model are determined in section 4.3.6. In the last section, the determination of the onset of accumulation of inelastic deformation is shown for AA7449.

4.3.1. Fast interrupted quenches on AA7449, AA7040 and AA2618

The fast quenches achieved in order to characterise the neSS of AA7449 are shown in *Figure 4-8*.

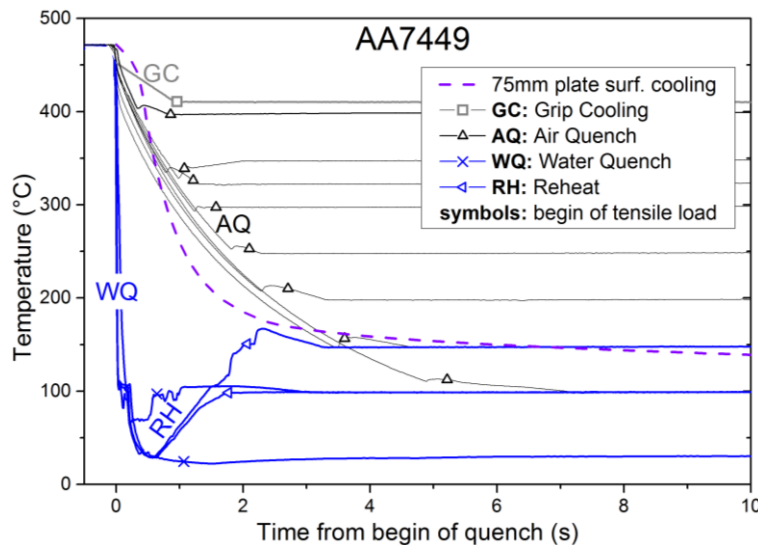


Figure 4-8 - Interrupted quenches achieved with AA7449 Gleeble specimens; temperature is measured by TC1 thermocouple.

The fastest quenches are achieved by WQ interrupted at either 25°C or 100°C. Since WQ interrupted at higher temperatures is too challenging due to high overshoots (not shown here), WQ to 25°C followed by a fast reheat (RH) to 150°C is performed to try to reach the neSS at 150°C. WQ to 20°C followed by a RH to 100°C is also performed. Air quench (AQ) enables interrupting the quench without significant over-undershoots, while the cooling rate above 300°C is high enough (> 100 K/s in *Figure 4-9*) to limit the formation of coarse precipitates by avoiding the nose of the iso-T6 hardness 95% C-curve of Robinson (*Figure 1-9-left*) determined by quench factor analysis based on Jominy tests.

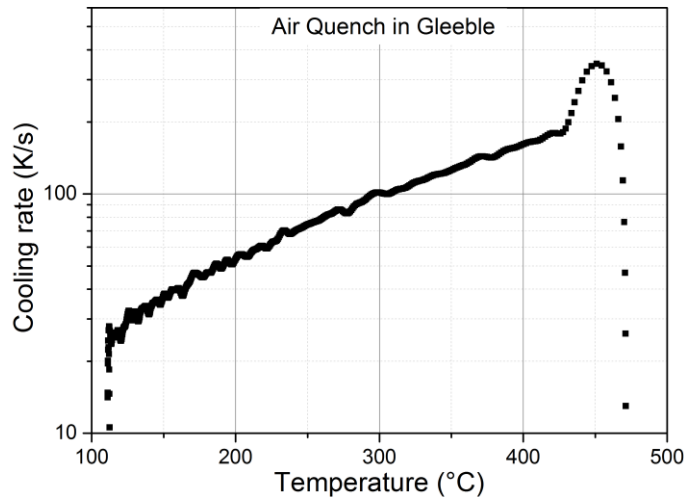


Figure 4-9 - Cooling rate achieved in new geometry specimen quenched by compressed air in the Gleeble.

Thus, it is expected that no or little amount of coarse precipitates form during AQ, which is confirmed by SAXS results in *Figure 3-1-a*. *Figure 4-8* also shows that the cooling down to 150°C of a 75 mm plate in surface is fairly close to the one obtained by AQ in the Gleeble. Therefore, the tensile loads performed immediately after AQ interrupted at 400°C, 350°C, 325°C, 300°C, 250°C, 200°C and 150°C are assumed to be representative of the surface mechanical behaviour. At 410°C, the relatively slow cooling rate achieved by Grip Cooling (GC), i.e. without additional air or water, is sufficient to avoid precipitation of η phase as confirmed by SAXS results in *Figure 3-1-a*.

The fast quenches achieved in order to characterise the neSS of AA7040 are shown in *Figure 4-10*.

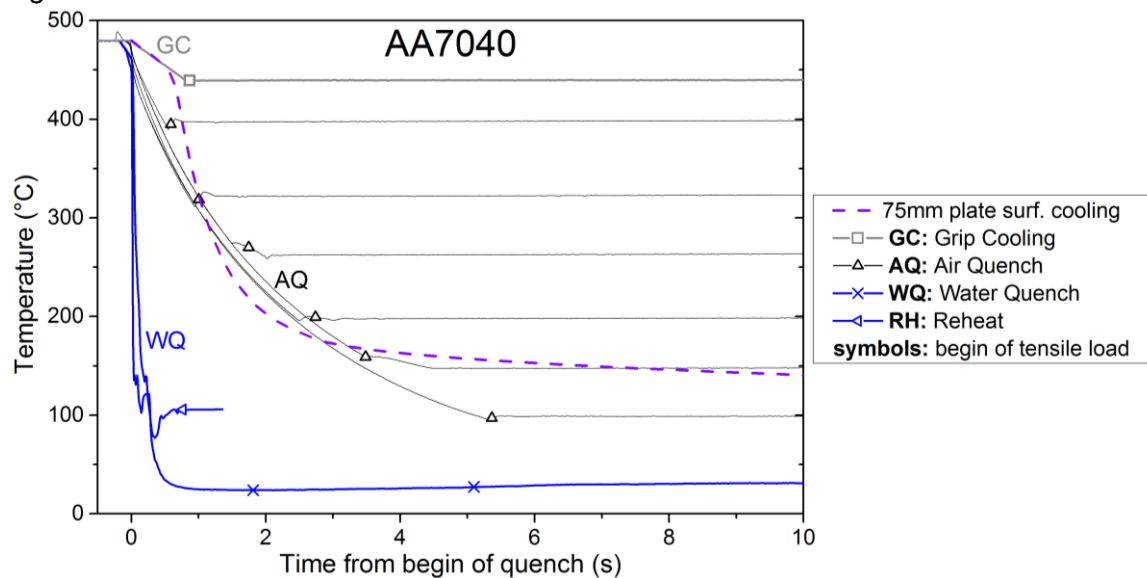


Figure 4-10 – Interrupted quenches achieved with AA7040 Gleeble specimens; temperature is measured by TC1 thermocouple.

The water quenches are interrupted either at 100°C or 20°C. The influence of waiting time is tested after WQ at 20°C with either 1 second or 4 seconds waiting time before tensile load. *Figure 4-10* also shows that the cooling down to 150°C of a 75 mm plate in surface is fairly close to the one obtained by AQ in the Gleeble (same cooling rate as in *Figure 4-9*). Therefore, the tensile loads performed immediately after AQ interrupted at 400°C, 325°C, 265°C, 200°C and 150°C are assumed to be representative of the surface mechanical behaviour for AA7040.

The interrupted quenches achieved in order to characterise the neSS of AA2618 are shown in *Figure 4-11*.

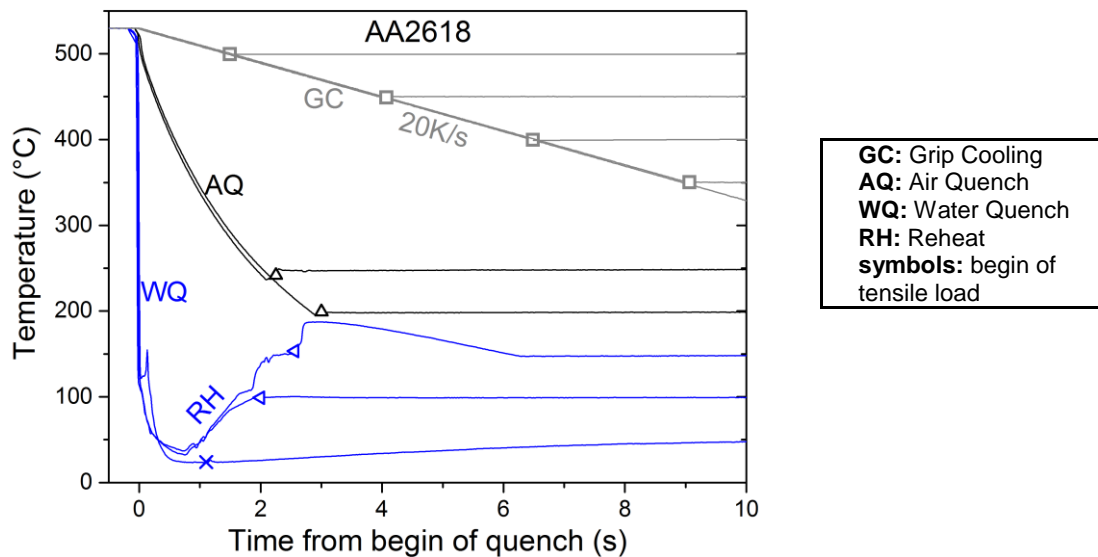


Figure 4-11 – Interrupted quenches achieved with AA2618 Gleeble specimens; temperature is measured by TC1 thermocouple.

In order to characterise the neSS of AA2618, AQ (same cooling rate as in *Figure 4-9*) are interrupted either at 250°C or 200°C and WQ at 35°C. The cooling rate of 20 K/s achieved by GC is chosen to limit precipitation of coarse precipitates at high temperature as expected by the DSC results in *Figure 3-8-a*. Although the volume fraction of coarse precipitates is expected to be low according to DSC, SAXS results in section 3.1.3 reveal the formation of large precipitatesⁱ at cooling rates higher than 70 K/s between 300°C and 450°C. As far as fine precipitates are concerned, they start to form at ca. 300°C even at high cooling rates (70 K/s) according to SAXS measurements in section 3.1.3. Therefore, fine precipitates are likely to form during AQ according to *Figure 4-9* and section 3.1.3.

ⁱ The calculated volume fraction, assuming spherical precipitates, is not reliable since scattering is anisotropic.

4.3.2. Evolution of yield strength

Tensile loads start at the desired temperature as soon as possible and are performed at relatively high strain-rates to limit precipitation during testing. The temperature evolution of the yield strength at 0.2% strain offset is given in *Figure 4-12* for AA7449.

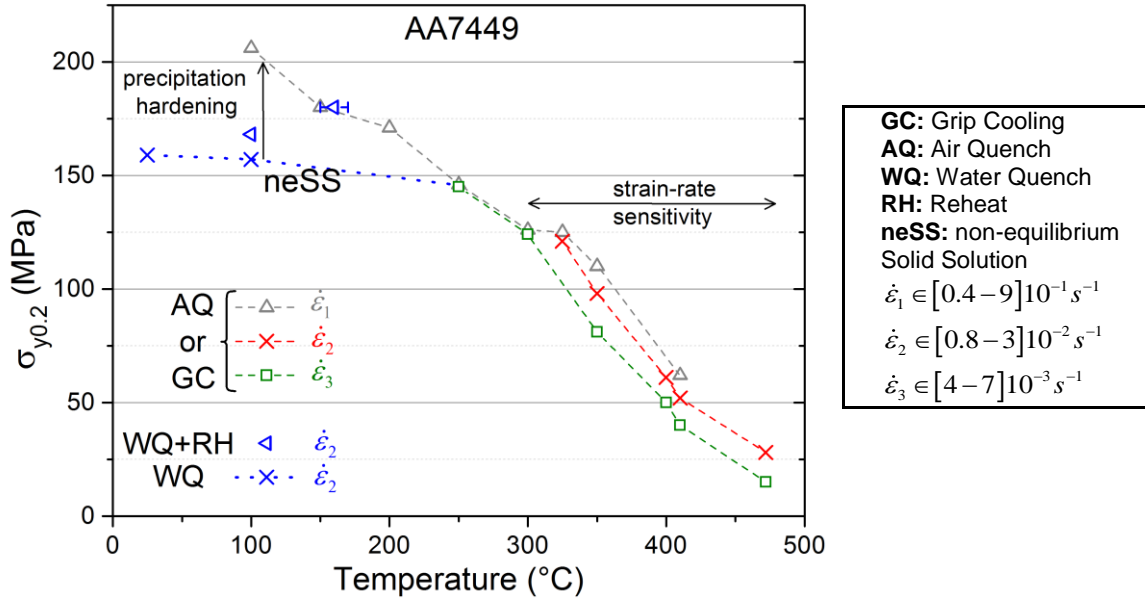


Figure 4-12 - Temperature dependence of yield strength of AA7449 obtained in the Gleeble at different strain-rates with various cooling conditions.

Due to experimental difficulties, the yield strength values at 100°C and 150°C after WQ +RH should be considered cautiously. However, they are consistent with each other and with the yield strength values at 25°C and 250°C: the values obtained after WQ+RH are higher than after WQ, which can be explained by precipitation hardening during RH. AQ is not fast enough at low temperatures (< 250°C) to avoid precipitation hardening.

While AA7449 exhibits a positive SRS between 350°C and the SHT temperature, yield strength is independent of strain-rate below ca. 300°C.

AA7449 in neSS shows a similar behaviour to that of AA7020 in neSS (*Figure 4-5*): the yield strength decrease from 25°C to 250°C is low (ca. 10%). The yield strength of AA7449 in neSS at 25°C is ca. 156 MPa (mean of 3 tests). This value is higher than that of AA7020 in neSS (*Figure 4-5*). This is explained by a higher solute content in AA7449 than in AA7020. Following the same argument, the yield strength of AA7449 in neSS at 25°C should be higher than that of AA7010 in neSS. This is not the case by taking the values of AA7010 by Godard extrapolated for the neSS (*Figure 4-6*). This means that this extrapolation using the evolution of the Guinier radius determined by SAXS measurements is questionable.

The temperature evolution of the yield strength is given in *Figure 4-13* for AA7040.

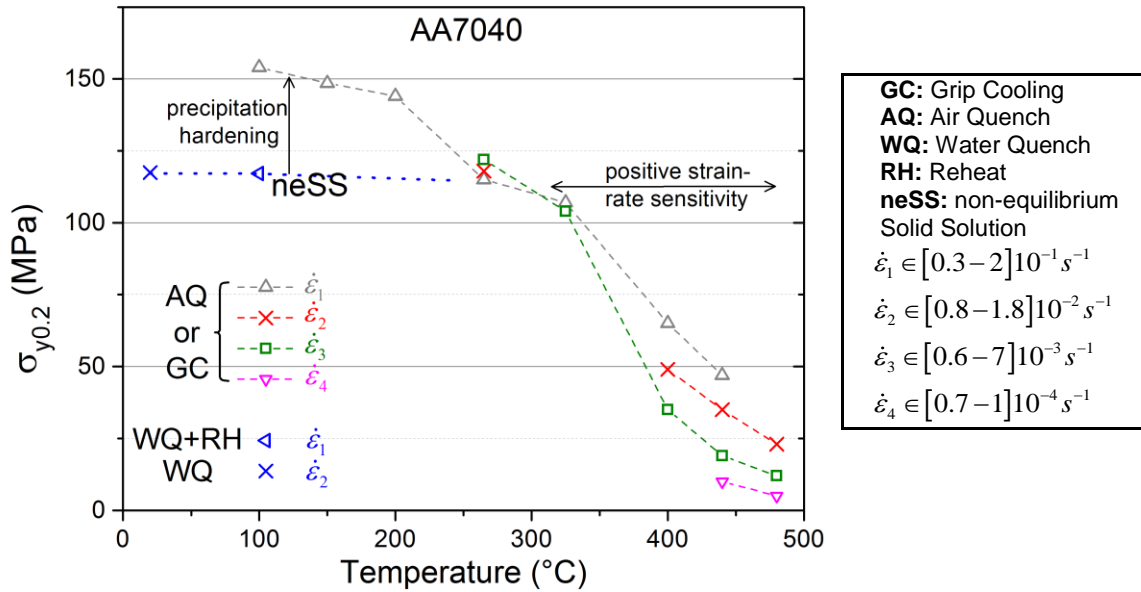


Figure 4-13 - Temperature dependence of yield strength of AA7040 obtained in the Gleeble at different strain-rates with various cooling conditions.

Although AA7040 is less quench-sensitive than AA7449, AQ is not fast enough at low temperature ($< 250^{\circ}\text{C}$) to avoid precipitation hardening. AA7040 exhibits a positive SRS at high temperature. SRS is assumed negligible below 200°C . At 265°C , it seems that AA7040 features a negative SRS in the strain-rate range $0.007\text{--}0.2\text{ s}^{-1}$, but the difference in stress is within the uncertainty.

The yield strength of AA7040 in neSS at 20°C is ca. 116 MPa (1 test performed) after 1 second waiting time and ca. 118 MPa (mean of 3 tests) after 4 seconds. The difference is within the measurement uncertainty ($\pm 5\text{ MPa}$). The yield strength value obtained after WQ interrupted at 100°C is ca. 117 MPa (mean of 3 tests). These values at 25°C and 100°C are slightly higher (5–7 MPa) than those of AA7020 because AA7040 contains more alloying elements. Again, a yield strength plateau is found at low temperature for the non-equilibrium solid solution.

The temperature evolution of the yield strength is given in *Figure 4-14* for AA2618.

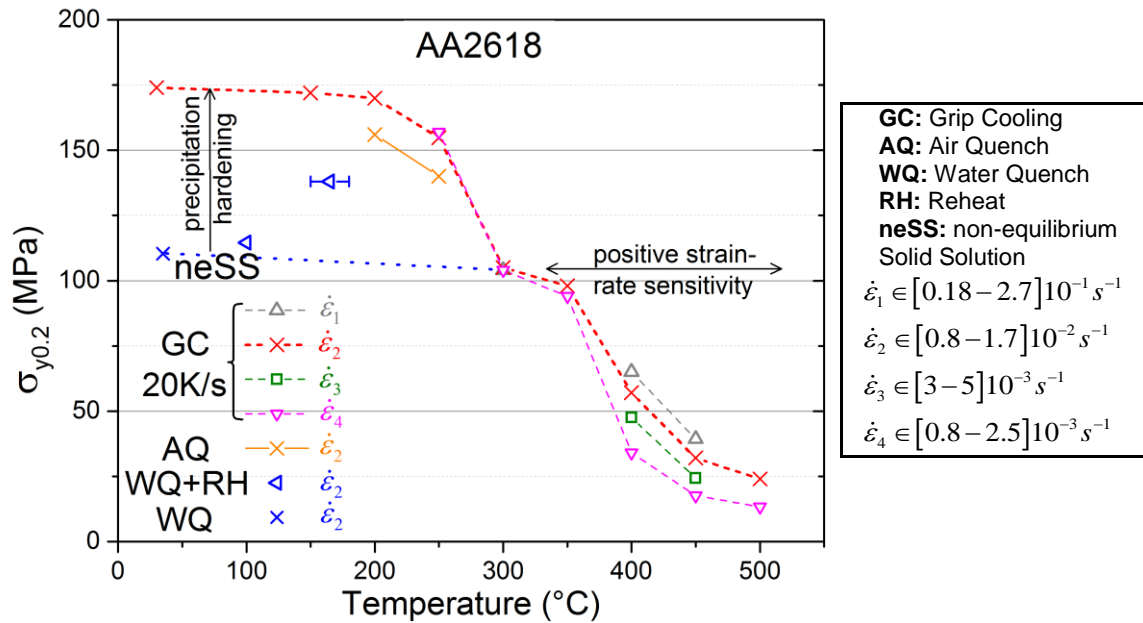


Figure 4-14 – Temperature dependence of yield strength of AA2618 obtained in the Gleeble at different strain-rates with various cooling conditions.

Figure 4-14 is very similar to *Figure 4-12* and *Figure 4-13*, except that the stress levels are different. The yield strength of AA2618 in neSS at 35°C is ca. 110 MPa (3 tests performed). This is lower than the yield strength values obtained at 100°C and 150°C after WQ+RHⁱ probably because of precipitation hardening during RH. The striking feature which makes *Figure 4-14* different from the others is the high yield strength value after AQ (> 50K/s) interrupted at either 250°C or 200°C. It seems that AQ is not fast enough to avoid precipitation hardening at 200°C and 250°C due to the formation of fine precipitates. GC at 20 K/s is definitely too slow to avoid precipitation hardening below 300°C. *Figure 4-14* shows that AA2618 exhibits a positive SRS at high temperature. It was checked that SRS is negligible at 150°C, 200°C and 250°C.

The yield strength values of the three alloys in neSS will be used in section 4.3.6 to adjust the parameters of the contribution of solid solution to strengthening.

4.3.3. Mechanical behaviour of AA7449

The tensile curves at the SHT temperature and after interrupted quenches are given exemplarily for AA7449 (see appendix 7.6 for AA7040 and appendix 7.7 AA2618). For the sake of brevity, the measured stress-strain curves are given together with the fits using SiDoLo which allow decoupling the effects of precipitation and/or softening and strain-rate on flow stress.

ⁱ These values should be taken carefully since they are each based on one test only

High temperature behaviour ($\geq 350^\circ\text{C}$)

At the SHT temperature, specimens are subjected to a succession of tensile loads at different strain-rates interrupted by a pseudo-relaxation (blocked jaws) during 90 seconds. The stress-strain curves measured in the Gleeble for AA7449 are given in *Figure 4-15* (a, b and c) together with the SiDoLo fit of the Gleeble measurements.

Two stress-strain curvesⁱ measured in a lamp furnaceⁱⁱ using a 100 kN load cellⁱⁱⁱ are given in *Figure 4-15 -d* for validation of the Gleeble measurements since the thermal gradients in the specimens are lower using a lamp furnace than using a Gleeble machine.

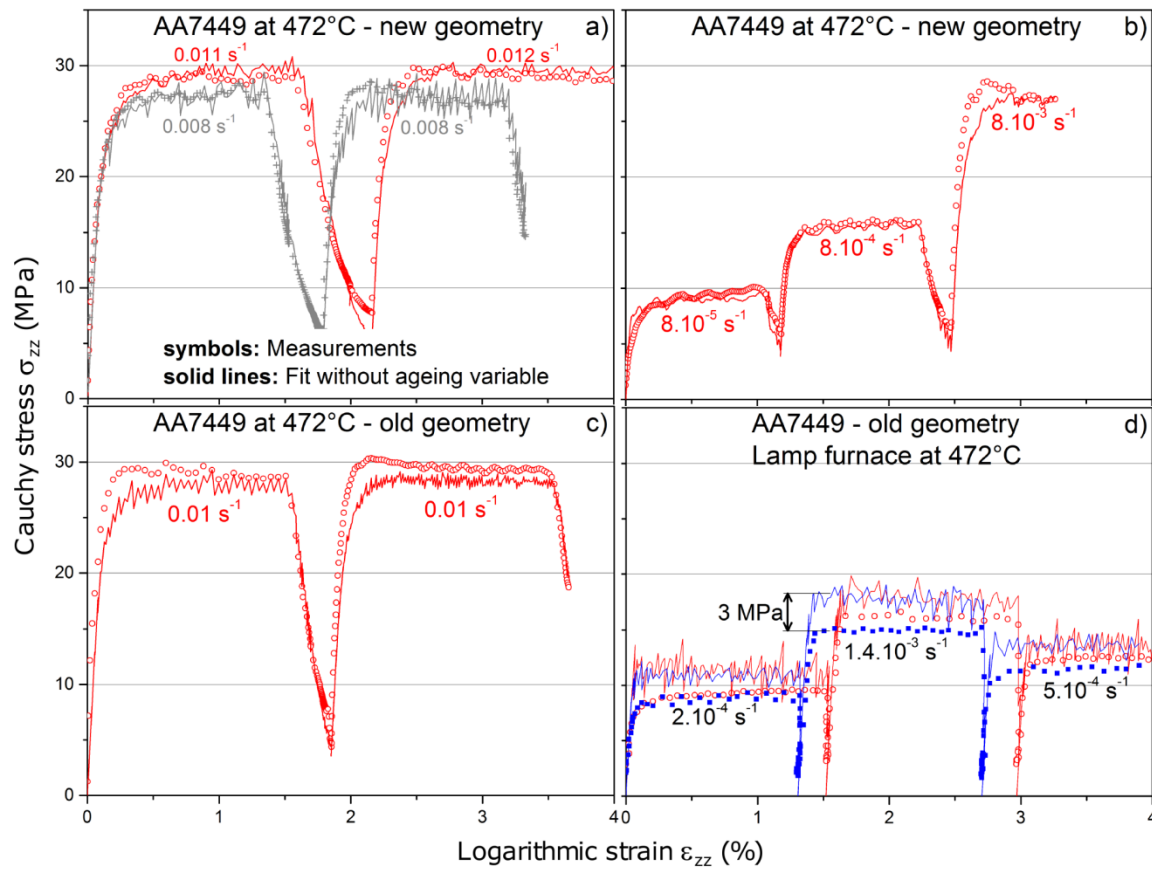


Figure 4-15 – Measured and fitted stress-strain curves for AA7449 at the SHT temperature obtained using the new specimen geometry in the Gleeble (a and b) and the old one in the Gleeble (c) and in a lamp furnace (d). All the specimens are taken from the quarter thickness of a 75 mm thick plate. The legend given in (a) applies to the four figures. $\sigma_0 = 0$ MPa, $H = 10^{-6}$ MPa, $n = 10^{-4}$, $K = 86.6$ MPa.s^{-m} and $m = 0.24$ for all the fits.

ⁱ not used for the identification of the parameters.

ⁱⁱ Research Inc. Clamshell Model 4068-12-10 lamp furnace driven by an Eurotherm 2604 PID temperature control unit.

ⁱⁱⁱ Servo hydraulic MFL UT System tensile testing machine controlled by an Instron Fast Track 8800 unit.

At the SHT temperature, AA7449 in *Figure 4-15* and AA7040 (appendix 7.6.1) exhibit a similar mechanical behaviour, with:

- i. a negligible strain hardening,
- ii. a high strain-rate sensitivity (the higher the strain-rate, the higher the flow stress) well captured by Norton's power law,
- iii. a high pseudo-relaxationⁱ in-between two stress plateaux, also well captured by Norton's power law,
- iv. no effect of precipitation: the stress reached on a plateau depends on strain-rate but not on time.

These four characteristics of the mechanical behaviour at the SHT temperature are similar to non-heat treatable aluminium alloys at high temperature.

In *Figure 4-15* the fit without ageing variable is good for both specimen geometries (± 2 MPa) which are therefore equivalent at the SHT temperature.

The fit of the Gleeble measurements slightly overestimates (2-3 MPa) the stresses measured in the lamp furnace (d). This difference may come from the longer solutionising time in the lamp furnace (ca. 120 min) compared to that in the Gleeble for the tests at SHT temperature (20 min).

The oscillations on the fits using SiDoLo are due to the fact that ε_{zz} - time experimental loads without smoothing are used in SiDoLo to calculate the flow stress.

Based on these results, an error of ± 3 MPa on the Gleeble stress-strain curves is attributed for AA7449 at the SHT temperature, to account for different specimen geometries and for different thermal conditions between Gleeble machine and lamp furnace.

For AA2618 above 400°C, and for test times lower than 500 seconds, the tensile tests after interrupted quench shown in appendix 7.6 exhibit the four characteristics described before.

Between 400°C and the SHT temperature, the same is also true for AA7449 and AA7040. Nevertheless, a slight softening can be observed during the first loads at ca. 0.01 s^{-1} for AA7449 at 410°C as shown in *Figure 4-16*.

ⁱ This is not pure relaxation since flow stress decreases while visco-plastic deformation keeps increasing during the holding period.

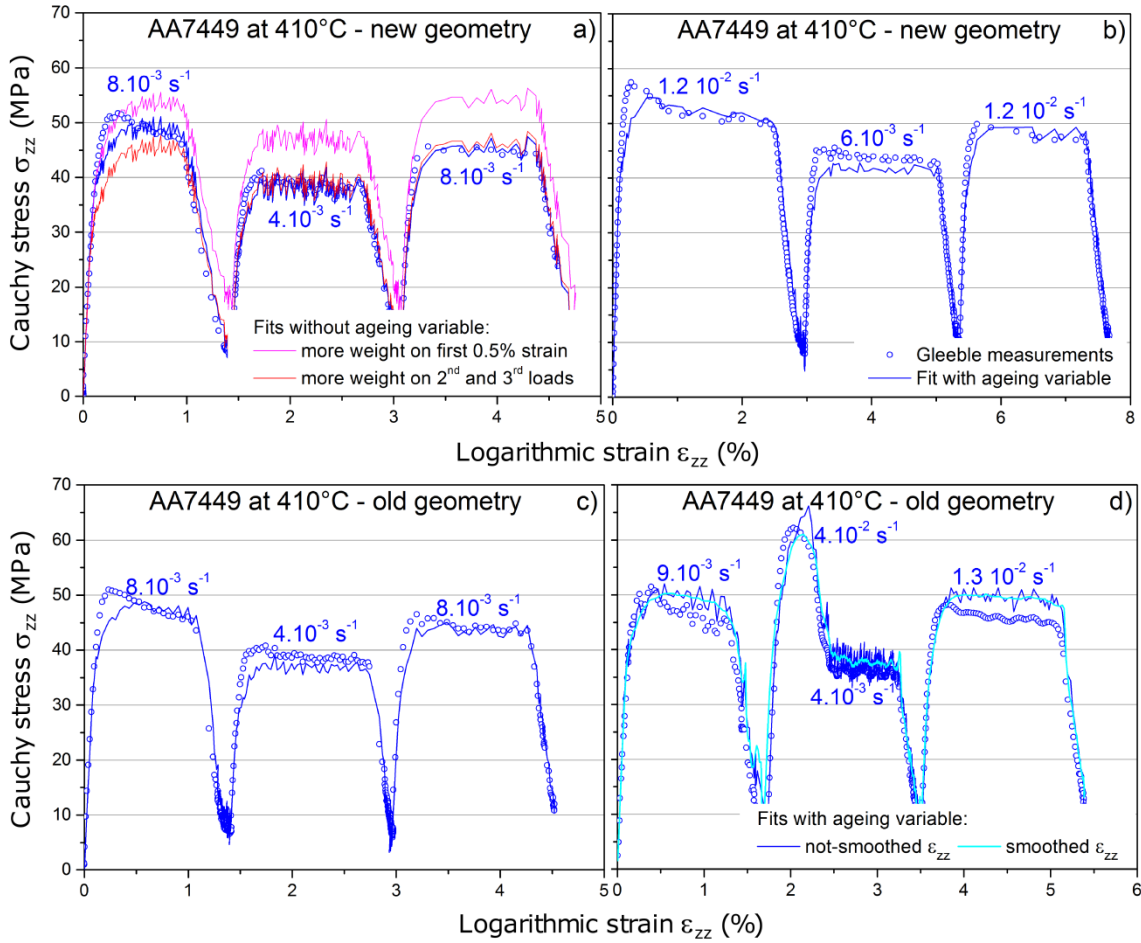


Figure 4-16 – Measured and fitted stress-strain curves for AA7449 at 410°C obtained using the new specimen geometry (a and b) and the old one (c and d). The legend given in b) applies to the four figures. $H = 10^{-6}$ MPa, $n = 10^{-4}$, $K = 135$ MPa.s^{-m} and $m = 0.23$ for all the fits.

During the first load of each test at ca. 0.01 s⁻¹, the flow stress decreases as deformation increases. This softening behaviour was also reported by Godard *et al.* on AA7010 at 300°C and on AA5182 at 350°C and 400°C (10^{-3} s⁻¹) [22], by Zhang *et al.* on AA1050, AA5182 and AA7075 at 400°C [169] and by Jin *et al.* on AA7150 between 300°C and 450°C [118].

Since the four tests in Figure 4-16 are performed with slightly different imposed mechanical loads and with two different specimen geometries, the fits by SiDoLo are useful for a better comparison since they integrate the experimental ε_{zz} - time loads and thus account for different strain-rates. Although the oscillations on the fits can be lowered by smoothing the ε_{zz} - time experimental loads used for stress calculation in SiDoLo (see Figure 4-16-d), it is chosen to work with the raw curves.

Two fits without ageing variable are given in Figure 4-16-a. The fit with more weight on small strains ($< 0.5\%$), with $\sigma_0 = 8.0$ MPa, fits well the beginning of the curve but overestimates stresses at larger strains. The fit with more weight on the 2nd and 3rd loads, with $\sigma_0 = 0$ MPa, fits well the 2nd and 3rd loads but underestimates stresses at small strains. One way to better fit the first load is to use an ageing (softening) variable to describe dynamic-softening.

The agreement between the Gleeble measurements and the fits with softening variable ($\sigma_0 = 8.0$ MPa, $\sigma_{soft} = 8.9$ MPa and $\tau_{soft} = 2.2$ sec) is good for all four tests (± 4 MPa). This means that the two specimen geometries (old and new) are equivalent at 410°C.

In order to provide an initial guess of (K, m) for the inverse method in SiDoLo, a first estimation of these parameters was made beforehand by taking the average stress on each plateau with its corresponding strain-rate as shown in *Figure 4-17*.

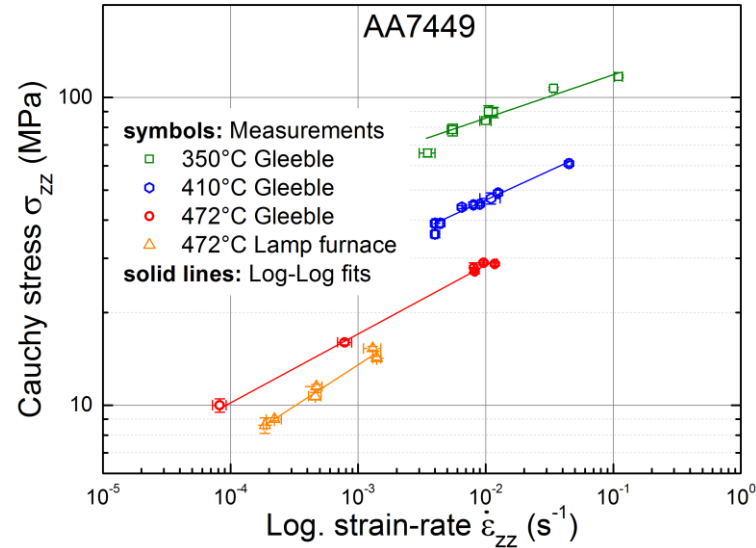


Figure 4-17 – Plot of initial estimation of (K, m) at 350°C, 410°C and 472°C for AA7449 provided to SiDoLo.

Taking $\sigma_0 = 0$ MPa and $H = 0$ MPa in Eq. 4-21, K and m are found easily by linear regression after taking the decimal logarithm of Eq. 4-21:

$$\log(\sigma_{zz}) = \log(K) + m \cdot \log(\dot{\epsilon}_{zz}^m) \quad \text{Eq. 4-24}$$

The results of the linear regression are given in *Table 4-3*.

AA7449	K (MPa.s ^{-m})	m	$N = 1/m$	R^2
472°C Gleeble	79 ± 1	0.22 ± 0.01	4.5	0.99
Lamp furnace	89 ± 1	0.27 ± 0.02	3.7	0.97
410°C Gleeble	110 ± 1	0.19 ± 0.01	5.3	0.96
350°C Gleeble	164 ± 1	0.14 ± 0.02	7.1	0.92

Table 4-3 – Results of the linear regression for AA7449 at 410°C and 472°C.

At temperatures close to the melting temperatureⁱ, T_m , (ca. 565°C for AA7449) the viscous stress is limited by the ultimate strength which becomes very low. This explains the lower value of K at 472°C compared to 410°C and 350°C in *Table 4-3*.

Tensile tests after interrupted quench-tests at 350°C show that flow stress is time-dependant as shown in *Figure 4-18* for AA7449.

ⁱ mean value of the solidus and liquidus temperatures

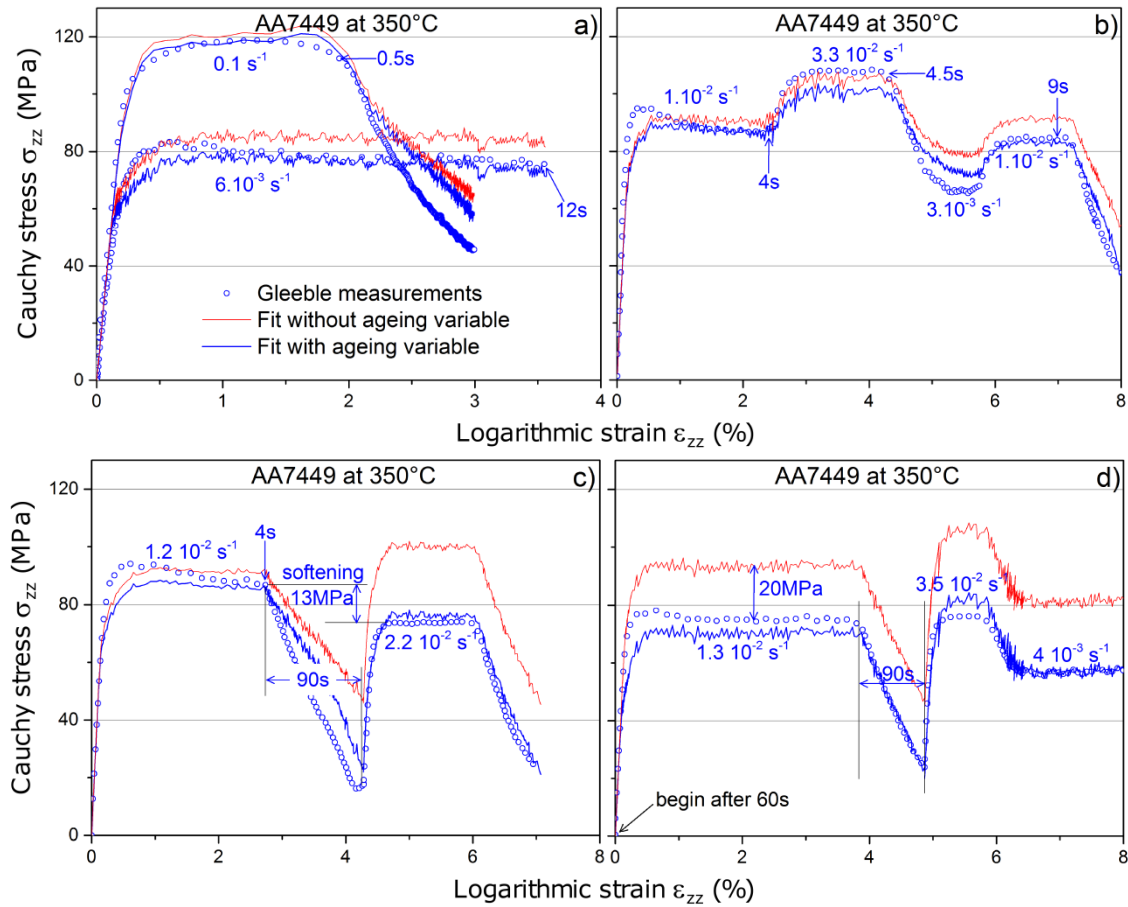


Figure 4-18 - Measured and fitted stress-strain curves for AA7449 at 350°C obtained using the new specimen geometry. The legend given in a) applies to the four figures. For all the fits, $\sigma_0 = 13$ MPa, $H = 7$ MPa, $n = 0.1$, $K = 145$ MPa.s^{-m} and $m = 0.15$. For the fits with ageing variable, $\sigma_{soft} = 24.3$ MPa and $\tau_{soft} = 21$ sec.

The mechanical behaviour of AA7449 at 350°C is similar to the one at 410°C with a high SRS while strain-hardening is still negligible. Again, during the first loads at ca. 0.01 s⁻¹, the flow stress decreases with increasing strain. This can be due to dynamic-softening or softening by formation of coarse precipitates. In order to see the influence of precipitation on flow stress, time values are given in Figure 4-18. The agreement between the Gleeble measurements and the SiDoLo fits without ageing variable is:

- reasonable for short timesⁱ (≤ 12 sec) in the tests in (a) and (b) and for the first load in (c),
- poor for long times (> 60 sec) in the test in (d) and for the second load after 90 seconds of pseudo-relaxation in (c).

The fit without ageing variable overestimates stresses for times higher than 60 seconds. This is attributed to the formation of coarse precipitates which decrease the solute content and therefore lead to softening and/or to static softening, dynamic particles coarsening, dynamic recovery or dynamic recrystallisation. The use of an ageing (softening) variable gives a better fit for long times. It is based on Eq. 4-23 with an initial

ⁱ from the beginning of the isothermal

time, $t_{soft,0}$, taken when TC1 is equal to 400°C as explained in section 4.2.3. The use of an initial time $t_{soft,0}$ instead of the more rigorous concept of equivalent time increments used in the additivity principle is justified by the high cooling rates between 400°C and 350°C during air quench in the Gleeble (> 100 K/s). This identification strategy for softening is also used for AA2618 at 350°C (see appendix 7.7.2).

Behaviour at $T < 350^{\circ}\text{C}$

Stress-strain curves and stress evolutions for AA7449 after quenches interrupted either at 325°C, 300°C or 250°C are presented in *Figure 4-19* together with the SiDoLo fits.

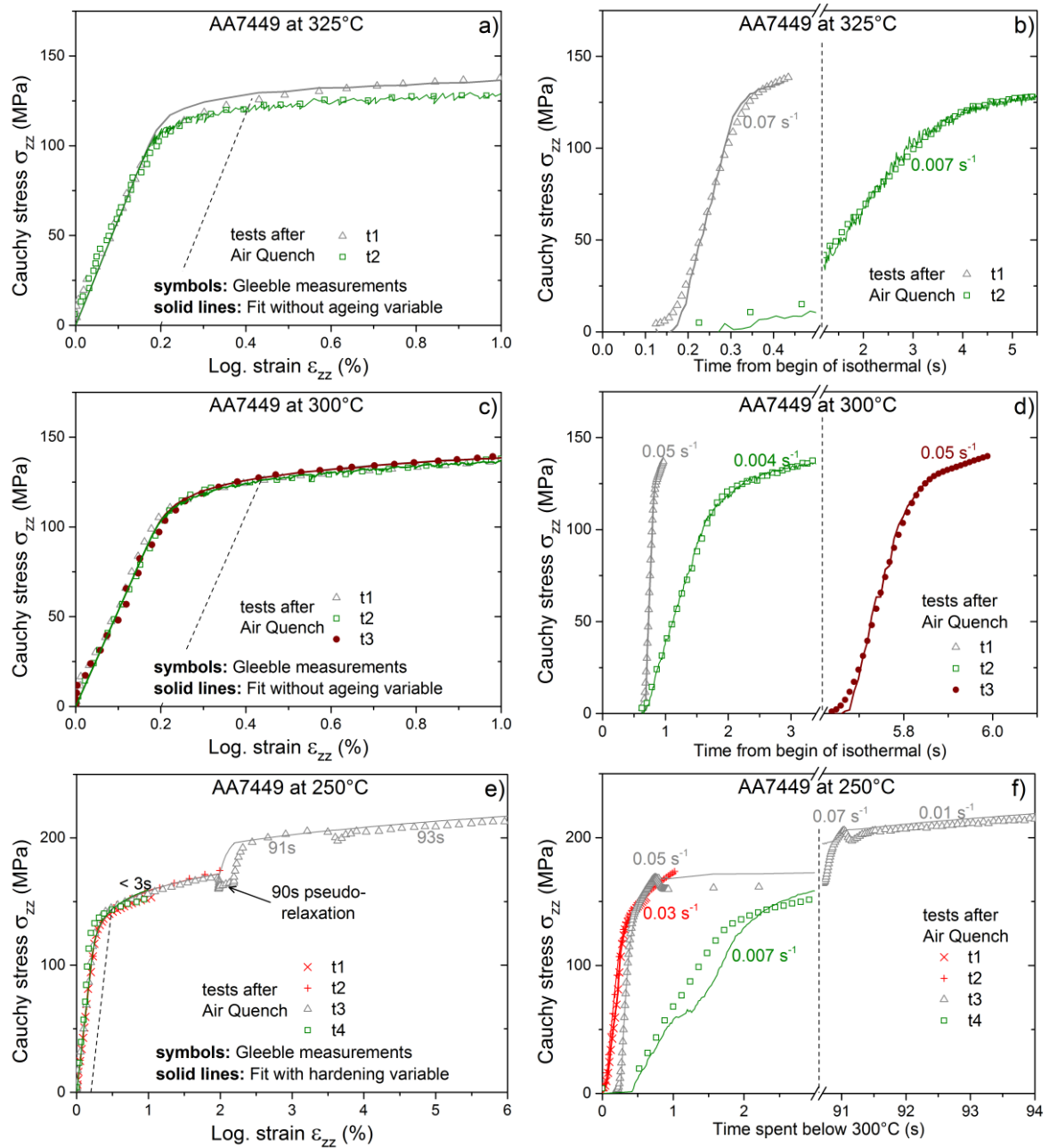


Figure 4-19 – Measured and fitted stress-strain curves (left) and corresponding strain evolutions (right) for AA7449 at 325°C, 300°C and 250°C using the new specimen geometry.

At 325°C (Figure 4-19-a and b), two tests at different strain-rates are performed to determine the SRS of AA7449. During test “t2” at 0.007 s⁻¹, the yield strength is reached after ca. 4 seconds at 325°C, i.e. without softening according to the results at 350°C (Figure 4-18). The fact that the yield strength at 0.007 s⁻¹ is lower than that at 0.07 s⁻¹ is therefore attributed to a positive SRS at 325°C.

Similar tests are performed at 300°C (Figure 4-19-c and d) where *a fortiori* no softening occurs during “t2” at 0.004 s⁻¹. In order to check that precipitation hardening is negligible during “t2”, the test “t3” is performed with 5.6 seconds waiting time at 300°C before loading. The fact that the stress-strain curves of “t1” and “t3” are almost superimposed shows that the hardening kinetics at 300°C is rather slow and that SRS is almost negligible at 300°C.

Similar tests are performed at 250°C (Figure 4-19-e and f) to check that SRS is also negligible. Here, the fit is performed using a hardening variable to decouple the effects of precipitation and strain-rate on yield strength. Additionally, a strain-rate jump is performed after the 90 seconds pseudo-relaxation of test “t3”. From Figure 4-19-e and f, it is concluded that AA7449 is not strain-rate sensitive at 250°C. Below 250°C where SRS is assumed to be negligible, tensile loads are performed at high strain-rate (≥ 0.01 s⁻¹) to limit the effect of precipitation on yield strength during loading.

The effect of time on flow stress at 200°C is shown in Figure 4-20.

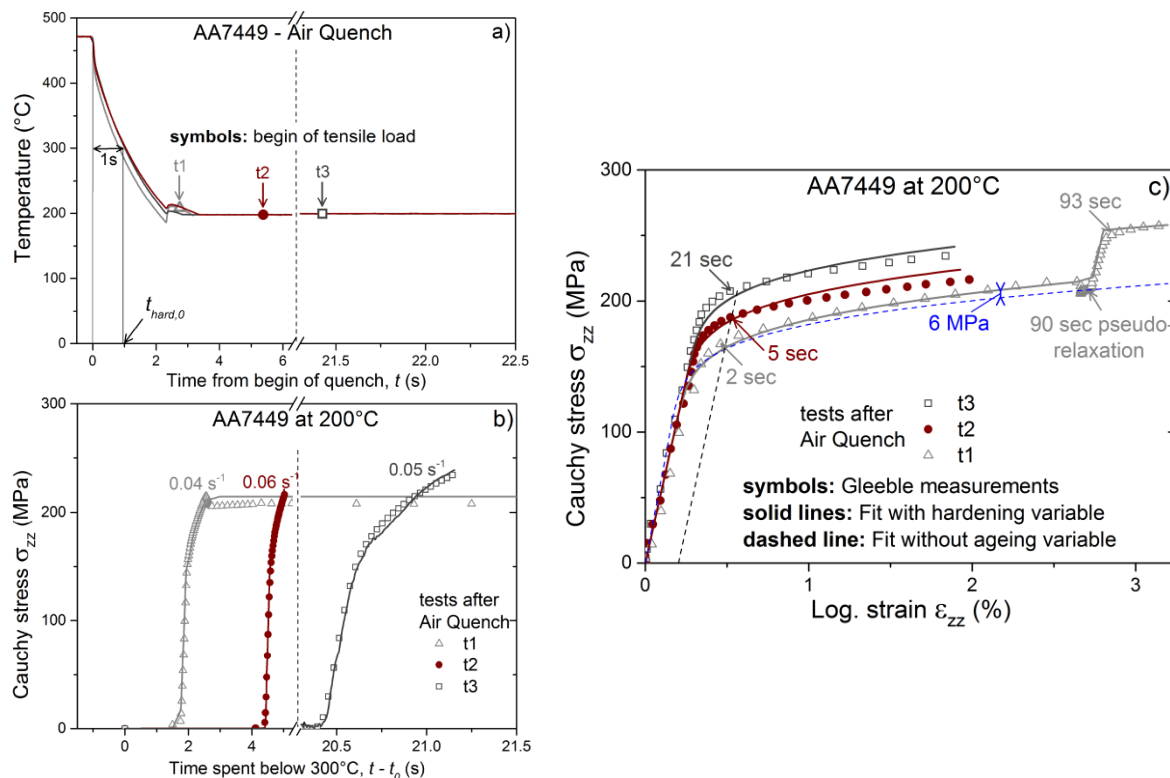


Figure 4-20 – Interrupted air quench at 200°C: temperature evolution (a) in Gleeble specimens (new geometry) subjected to tensile loads (b) ; measured and fitted stress-strain curves (c).

Three specimens are subjected to an air quench interrupted at 200°C followed by tensile load. One test “t1” is performed right after AQ to characterise the neSS. The other tests “t2” and “t3” are performed after different holding times before tensile load in order to characterise the effect of precipitation on flow stress. *Figure 4-20-c* shows that the flow stress of AA7449 at 200°C depends on both strain and time due to strain-hardening and strengthening by precipitation respectively.

The use of a hardening variable in the constitutive equation provides a good fit of the three stress-strain curves. This fit with hardening variable is useful to:

- Check that the strain-rate chosen to avoid/limit precipitation during the tensile loads is high enough. This is shown by the fit without ageing variable, which gives a stress-strain curve deviating only slightly from the measurements (6 MPa difference at 2.2 % deformation).
- Check that strain-hardening is little affected by the holding time before tensile load, i.e. by precipitation as assumed in the model.
- Validate/calibrate a physically-based yield strength model (section 4.3.6).

It is based on Eq. 4-23 with an initial time, $t_{hard,0}$, taken when TC1 is equal to 300°C (*Figure 4-20-a*) as explained in section 4.2.3.

Again, the use of $t_{hard,0}$ instead of the more rigorous concept of equivalent time increments used in the additivity principle is justified by the high cooling rates during AQ in the Gleeble machine between 300°C and 200°C (between 100 K/s and 50 K/s respectively).

As introduced in section 4.2.3, it is decided to identify only σ_{hard} by setting $a_{hard,\infty}$ to unityⁱ. This identification strategy for hardening is also used for AA7449 at 150°C and 100°C (*Figure 4-21*) and for AA7040 (appendix 7.6) and AA2618 (appendix 7.7).

ⁱ The other strategy consisting in setting σ_{hard} according to the as-quenched and peak-aged values ($\sigma_{hard} = \sigma_{hard,PA} - \sigma_{hard,AQ}$) and identifying $a_{hard,\infty}$ is not chosen since peak-aged states are obtained after several hours, which is far beyond the time window of the interrupted quench-tests.

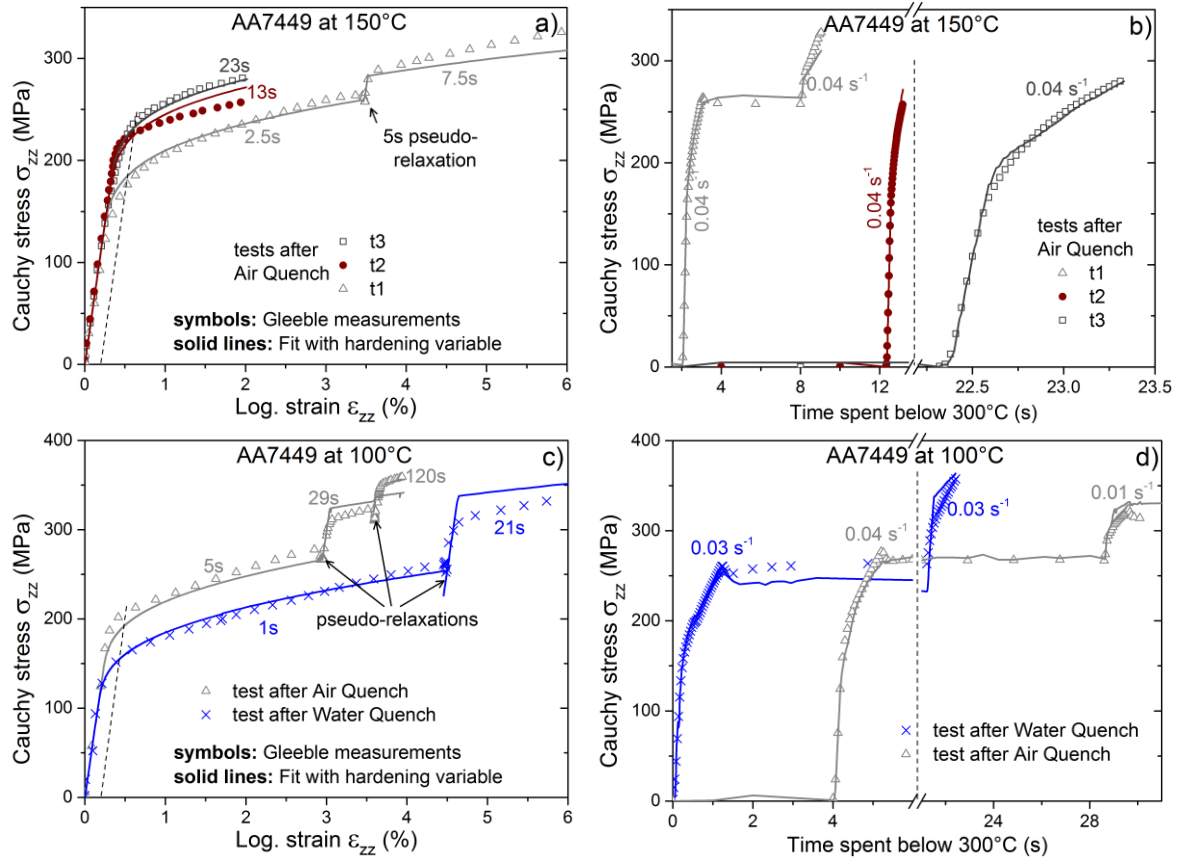


Figure 4-21 – Measured and fitted stress-strain curves (left) and corresponding strain evolutions (right) for AA7449 at 150°C and 100°C using the new specimen geometry.

The fits at 100°C and 150°C are good for short times (< 3 seconds spent below 300°C) since more weight is given to them in the objective function. For longer times, the fit is fair with some discrepancies which may come from the arbitrary use of the exponential law without physical-basis and the possible effect of precipitation on work hardening (that is ignored throughout this study). The tensile curves of AA7449 at room temperature after water quench are given in appendix 7.4 where the uncertainty on strain is discussed.

4.3.4. Identification of model parameters

As previously explained, the tensile loads performed after the interrupted quenches presented in Figure 4-8 for AA7449, Figure 4-10 for AA7040 and Figure 4-11 for AA2618 are used to identify the parameters in Eq. 4-21 and Eq. 4-23 for the three alloys.

4. Thermo-mechanical behaviour

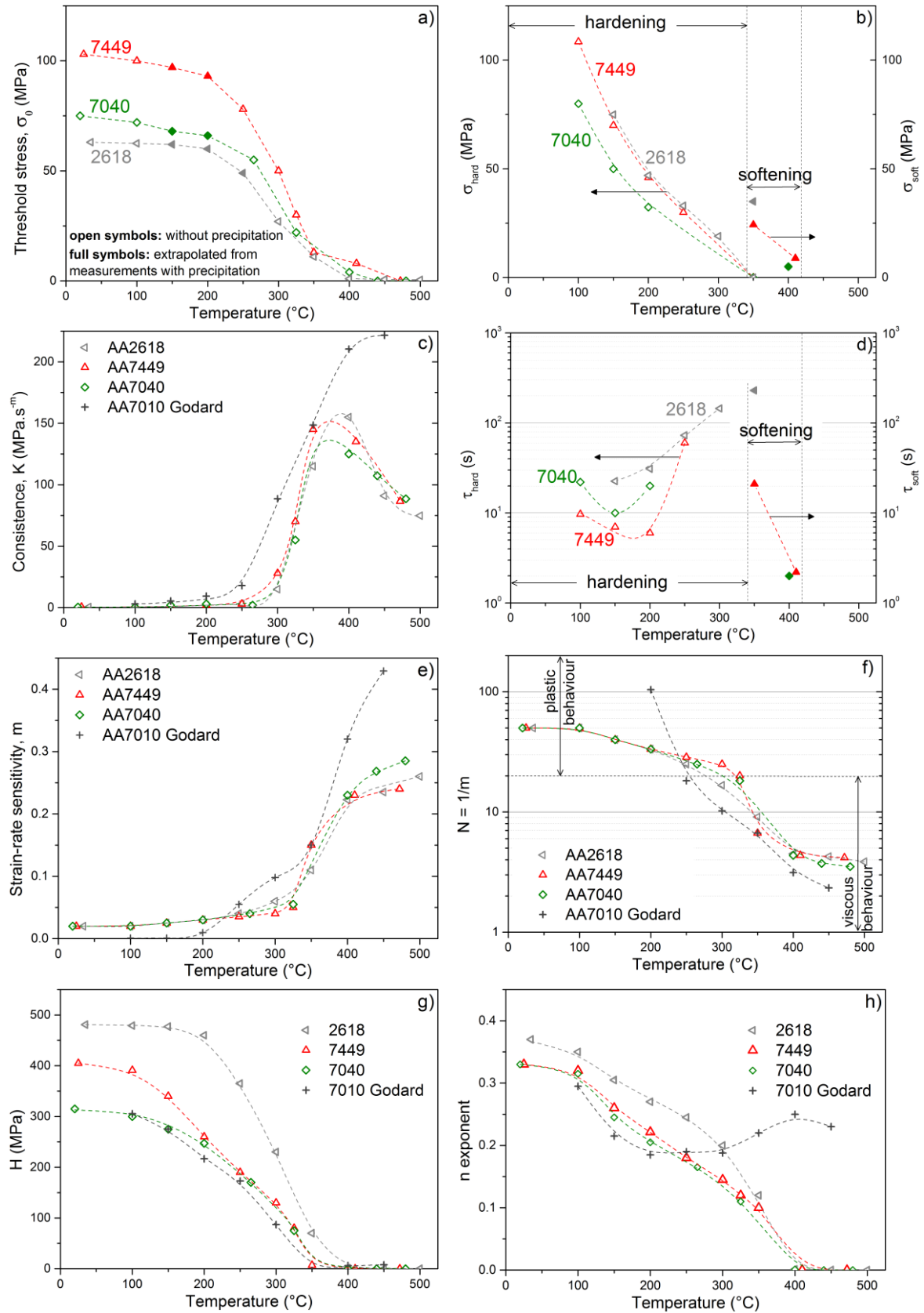


Figure 4-22 – Identified parameters of Eq. 4-21 and Eq. 4-23 for AA7449, AA7040 and AA2618. Parameters for AA7010 by Godard are given for comparison. Dashed lines are guide for the eye.

In *Figure 4-22-a*, the σ_0 -Temperature curves exhibit a plateau at low temperature ($< 200^\circ\text{C}$). The value of the plateaux can be explained by the different compositions of the three alloys: the higher the solute elements content, the higher the σ_0 value. This threshold stress decreases considerably from ca. 250°C to 350°C and is set close to zero at high temperature ($\geq 400^\circ\text{C}$), as also considered by Godard on AA7010ⁱ.

The parameters related to the ageing variables used to fit the curves with hardening or softening are given in *Figure 4-22-b* and *d*. σ_{hard} decreases with increasing temperature and is set to zero at 350°C where no sign of precipitation hardening can be observed. The hardening amplitude is higher for AA7449 than for AA7040, possibly due to the higher solute content in AA7449 than in AA7040. This could also explain the shorter characteristic time τ_{hard} for AA7449 compared to AA7040. Furthermore, a C-shape reminiscent of TTP-diagrams can be recognised on the τ_{hard} curves in *Figure 4-22-d*.

The K -Temperature curves obtained for AA7449, AA7040 and AA2618 have a bell-shape typically encountered for metallic alloys [123, 127]. This is explained by low K values at low temperature ($< 250^\circ\text{C}$ in *Figure 4-22-c*) where SRS is small but also low K values at high temperature (above the temperatures tested in this work) close to T_m where the viscous stress is limited by the ultimate strength which becomes small. Magnin *et al.* [107] found $K = 30 \text{ MPa.s}^{-m}$ ($m \sim 0.2$) at the solidus temperature and $K = 3 \text{ MPa.s}^{-m}$ ($m \sim 0.5$) at T_m for Al-4.5wt.%Cu alloy. The strain-rate sensitivity, m , is set to low values below 300°C and increases rapidly at higher temperatures (*Figure 4-22-e*). The inverse of m , $N = 1/m$, being more often used in the literature, is shown in *Figure 4-22-f*. N is higher than 20 at low temperature (plastic behaviour) and decreases with increasing temperature. For AA7449, AA7040 and AA2618, the N values obtained between 350°C and 500°C vary between 8 and 3 respectively, which is typical of dislocation creep [110]. For a better comparison of the viscous parameters K and N , it is useful to normalise the temperature by the melting temperature and to plot them as a function of the homologous temperature as shown in *Figure 4-23*.

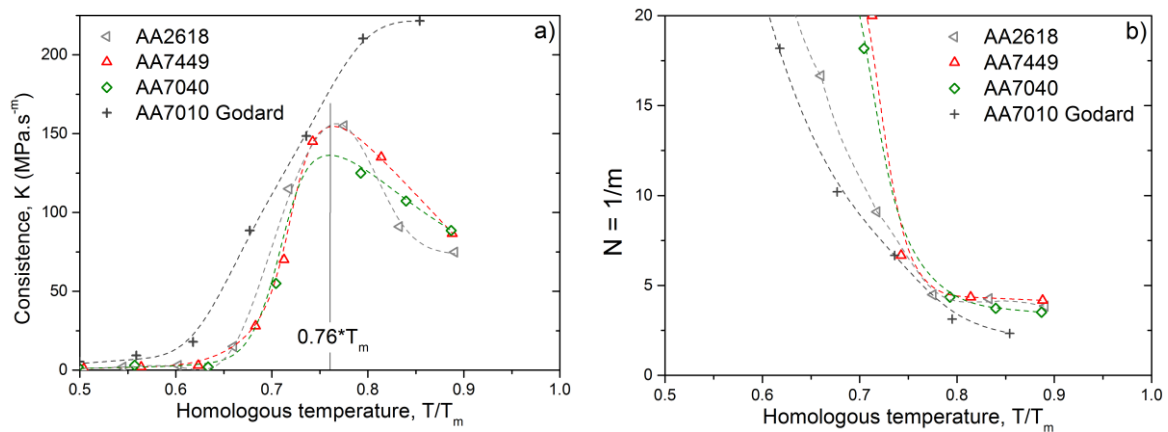


Figure 4-23 – Temperature dependence of parameters K (a) and $N = 1/m$ (b) of Norton's power law. Dashed lines are guide for the eye.

ⁱ the σ_0 values of Godard for AA7010 are not given in *Figure 4-22-a* since they are too high to correspond to the neSS without precipitates.

While the consistence always increases with increasing temperature in Godard's work on AA7010, K increases up to ca. $0.76 \cdot T_m$ (635-660 K) in this work on AA7449, AA7040 and AA2618 and decreases when approaching T_m . The maximum of the curve was found to be at ca. $0.57 \cdot T_m$ in the work of Wisniewski on a Cu-Cr-Zr alloy [168] and at ca. $0.63 \cdot T_m$ in the work of Le on AISI 316L stainless steel [125]. This indicates that AA7449, AA7040 and AA2618 have a high consistence when temperature increases. The (K, m) values obtained by Godard for AA7010 above 350°C are higher than those obtained in this work, and yet AA7010 has a chemical composition very close to that of AA7040. To understand the differences between AA7010 and AA7040 parameters in *Figure 4-22-c and e*, it was tried to constrain K to always increase with increasing temperature as this is the case for AA7010 (see appendix 7.6.1 where it is concluded that the parameters of AA7010 from Godard at high temperature ($\geq 400^\circ\text{C}$) should be used carefully for strain-rates higher than 0.005 s^{-1} not used for the identification).

The strain-hardening parameters H and n are highest at low temperature due to maximum dislocation storage and decrease with increasing temperature due to dislocation annihilation. At high temperature ($\geq 400^\circ\text{C}$) where H is set close to zero (*Figure 4-22-g*), n is also set close to zeroⁱ in accordance with Magnin's results [107]. This choice is different from that of Godard for AA7010. While n is almost identical for AA7040 and AA7449, H is higher for AA7449 than for AA7040. This can be explained by the effect of solute content [105, 106] which is higher in AA7449 than in AA7040. Strain-hardening is higher in AA2618 than in the three other alloys.

4.3.5. Behaviour after coolings similar to the industrial ones

Tensile tests after plate surface coolings

In order to obtain a precipitation state similar to that of the surface during quenching, specimens are cooled down with a temperature history as close as possible to the surface coolings. The coolings are interrupted either at 100°C, 40°C or 25°C where isothermal tensile loads are applied. The imposed temperature cycles are given in *Figure 4-24-a and b* together with the cooling rates above 150°C. The corresponding stress-strain curves are shown in symbols in *Figure 4-24-c and d*.

ⁱ n is meaningless when H is close to zero

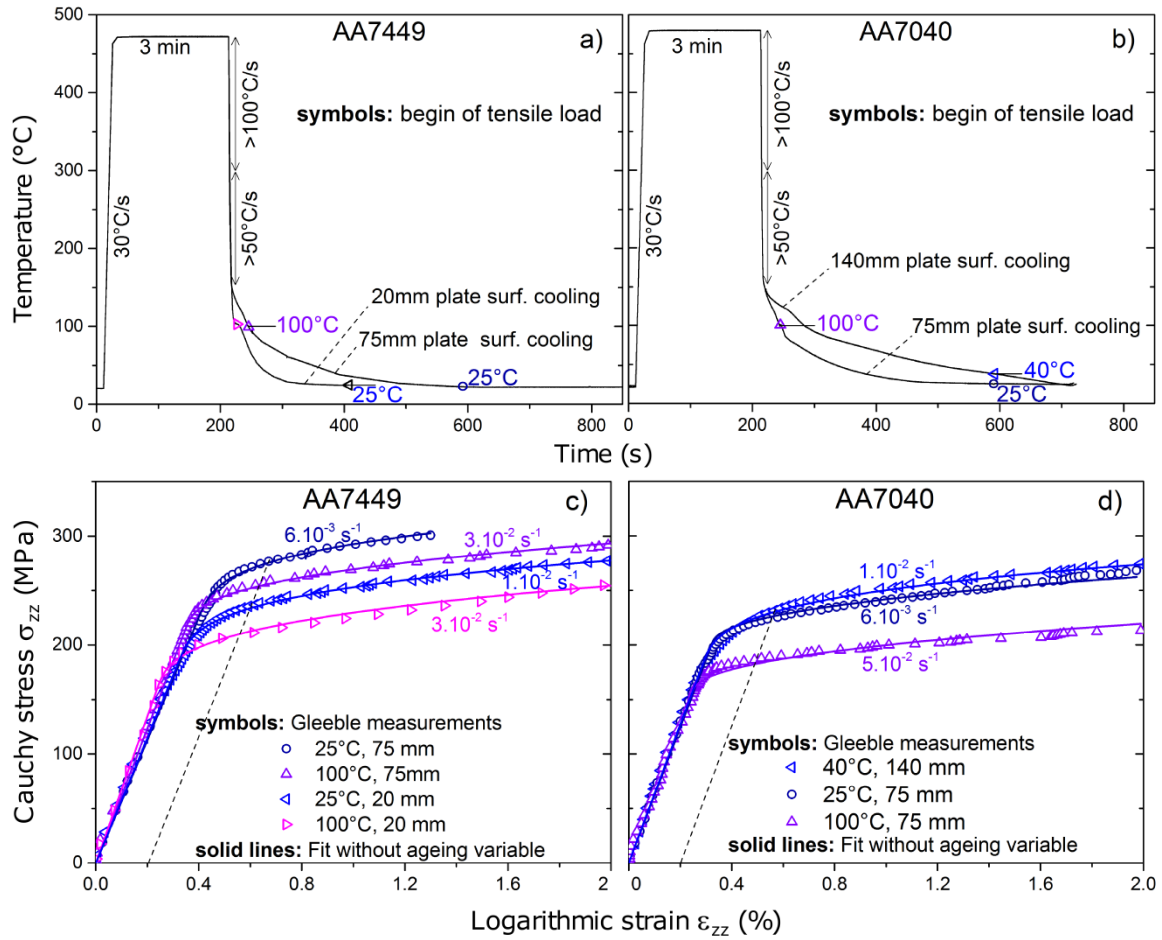


Figure 4-24 – Surface coolings (top) imposed in Gleeble specimens subjected to tensile loads (bottom) where the measurements (symbols) are fitted using Eq. 4-21 (solid lines).

The strength increase from 100°C to 25°C is attributed to the formation of hardening clusters at low temperature as observed by *in situ* SAXS during cooling of AA7449 in the recent paper of Schloth *et al.* [10]. Clusters were also revealed at temperatures below 250°C by *in situ* SAXS experiments performed on AA7040 at similar cooling rates to the ones encountered during quenching of thick plates (Figure 3-1-b).

Figure 4-24 illustrates also the influence of cooling path on yield strength: for instance, yield strengths at 25°C and at 100°C for AA7449 (Figure 4-24-c) are higher after a cooling similar to that of a 75 mm thick plate in surface than after a cooling similar to the one of a 20 mm thick plate in surface. For a given cooling path, the flow stress in AA7449 is higher than in AA7040 since it contains more alloying elements available for strengthening by solid solution and precipitation. The tensile curves feature strain hardening, which is nevertheless little affected by the cooling paths as assumed in the model. Therefore, H and n are set to the values given in Figure 4-22-g and h for the inverse method performed to identify σ_y in Eq. 4-21.

The identified σ_y values at 25°C, 40°C and 100°C after plate surface cooling are given in Figure 4-25 together with the σ_y values at higher temperature after air quenchⁱ.

ⁱ Above 150°C, AQ and plate surface coolings are almost superimposed.

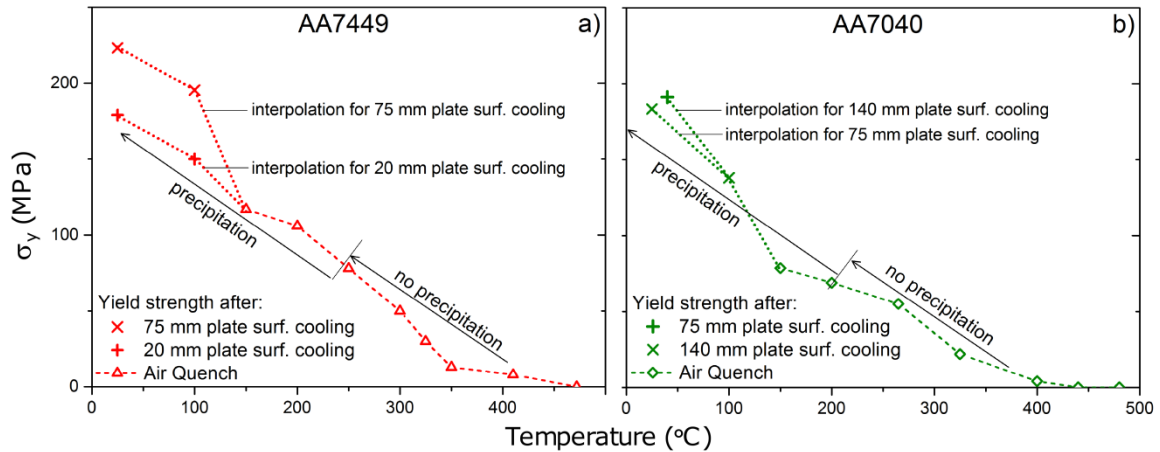


Figure 4-25 – Temperature dependence of σ_y parameter in Eq. 4-21 for AA7449 (a) and AA7040 (b) after plate surface coolings. Interrupted lines are linear interpolation used for the TMG model.

The parameter σ_y in Figure 4-25 and (H , n , K , m) in Figure 4-22 will be used in Eq. 4-21 for FE quenching simulations with TMG model. In this model, precipitation is taken into account indirectly through σ_y which has been identified on tensile curves with precipitation. The results of this TMG model are shown in section 5.3.1.

Tensile tests after SAXS coolings

The coolings achieved in the *in situ* SAXS experiments (see section 3.1.3) are reproduced in the Gleeble in order to associate a yield strength value to the quantities (Guinier radius and precipitate volume fraction) determined by SAXS.

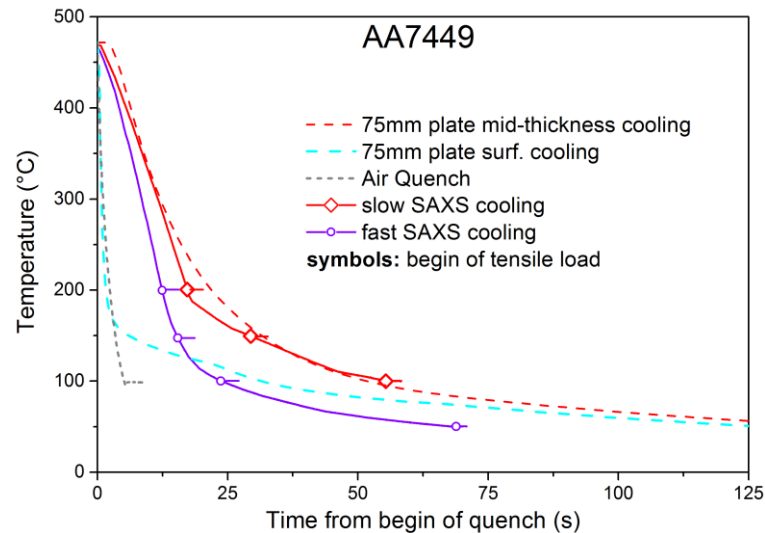


Figure 4-26 – Slow and fast coolings (solid lines) from *in situ* SAXS experiment on AA7449, reproduced in the Gleeble. Other cooling curves in dashed lines are also shown as an indication.

For AA7449, two *in situ* SAXS coolings are reproduced in the Gleeble (Figure 4-26). While the slow cooling is close to the cooling at mid-thickness (center) of a 75 mm plate, the fast cooling corresponds approximately to the cooling at quarter thickness. The

coolings are interrupted either at 200°C, 150°C, 100°C or 50°C where isothermal tensile loads are applied.

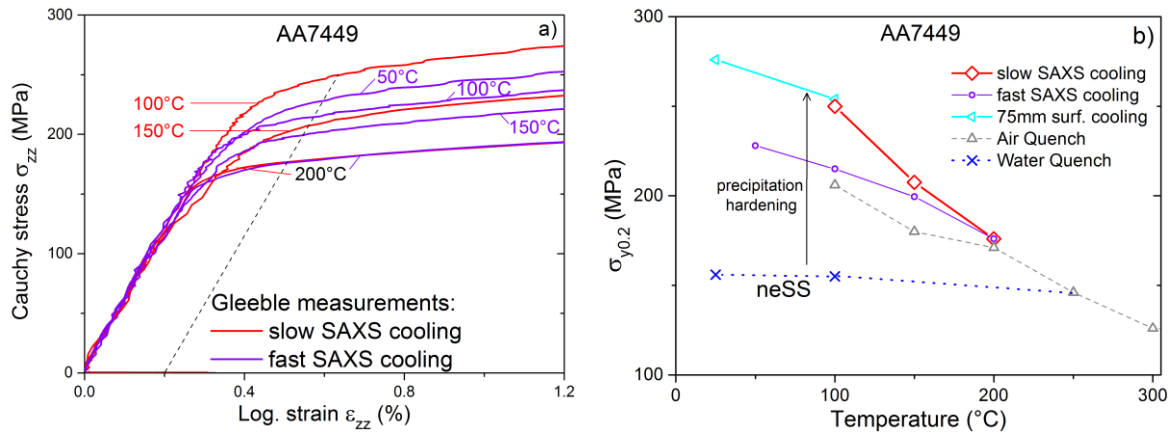


Figure 4-27 – Measured tensile curves after SAXS coolings reproduced in the Gleeble for AA7449 (a) and corresponding temperature dependence of yield strength (b) together with yield strength obtained after water quench, air quench and 75 mm plate surface cooling.

Again, strain hardening is little affected by the cooling paths (Figure 4-27-a). For a given cooling, yield strength increases upon cooling due to the combined effect of temperature decrease and precipitation. The yield strength obtained after slow and fast SAXS cooling is almost identical to the one obtained after air quench interrupted at 200°C (Figure 4-27-b). This indicates that for these different cooling conditions, precipitation of coarse precipitates above 200°C does not induce much hardening.

At 100°C, the yield strength obtained after slow SAXS cooling is:

- significantly higher than that after fast SAXS cooling,
- almost equal to that after cooling of a 75 mm plate in surface.

This might come from the time spent between 150°C and 100°C: less than 8 seconds for fast SAXS cooling but ca. 25 seconds for both slow SAXS cooling and 75 mm plate surface cooling.

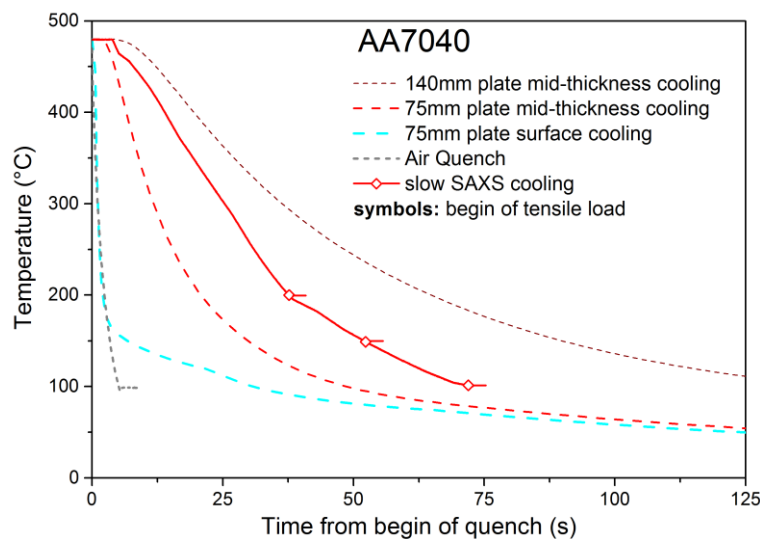


Figure 4-28 – Slow cooling (solid line) from in situ SAXS experiment on AA7040, reproduced in the Gleeble. Other cooling curves in dashed lines are also shown as an indication.

For AA7040, only one slow SAXS cooling is reproduced in the Gleeble (*Figure 4-28*). This cooling condition is intermediate between 75 mm and 140 mm plates mid-thickness coolings. It is interrupted either at 200°C, 150°C or 100°C where isothermal tensile loads are applied.

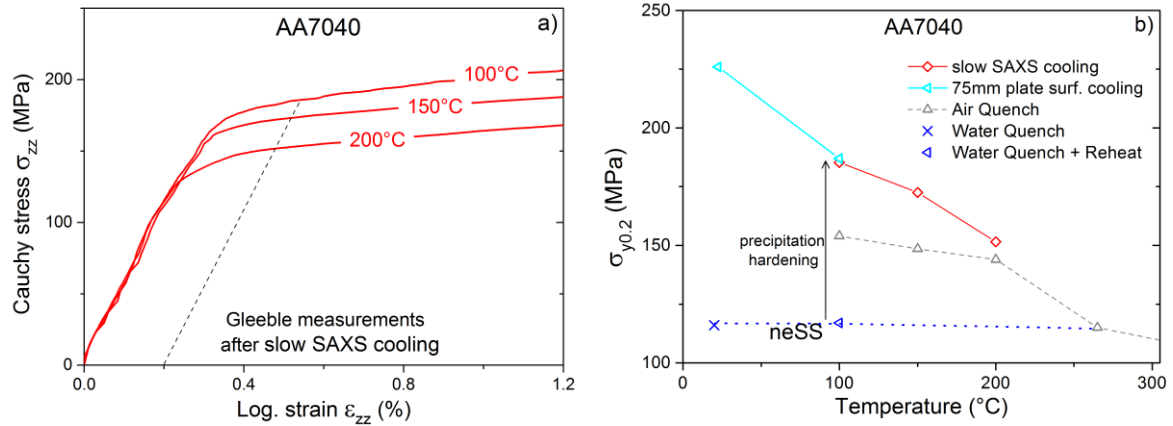


Figure 4-29 – Measured tensile curves after SAXS cooling reproduced in the Gleeble for AA7040 (a) and corresponding temperature dependence of yield strength (b) together with yield strength obtained after water quench (+reheat), air quench and 75 mm plate surface cooling.

After slow cooling typical of thick plates, the mechanical behaviour of AA7040 is qualitatively similar to that of AA7449. AA7040 features strain hardening little affected by the cooling paths (*Figure 4-29-a*). The yield strength at 200°C obtained after slow SAXS cooling is only slightly higher to the one obtained after air quench interrupted at 200°C (*Figure 4-29-b*). This indicates that for these two coolings, precipitation of coarse precipitates above 200°C does not induce much hardening.

At 100°C, the yield strength obtained after slow SAXS cooling is:

- significantly higher than that after air quench,
- almost equal to that after the cooling of a 75mm plate in surface.

This might come from the time spent between 150°C and 100°C: less than 3 seconds for air quench but 20 seconds for both slow SAXS cooling and 25 seconds for 75 mm plate surface cooling. The $\sigma_{y0.2}$ values obtained after SAXS coolings given in *Figure 4-27-b* and *Figure 4-29-a* are used to calibrate the contribution of shearable precipitates in the yield strength model (see next section).

4.3.6. Identification of the parameters of the yield strength model

The identified parameters of Eq. 4-21 and Eq. 4-23 are firstly interpolated to determine the yield strength evolution of neSS, i.e. without precipitates, that will be used in the TM model (without precipitation).

Then for TMM model, the approach of Leyson and the approach of Suni are used to determine the contribution of solid solution to strengthening. When available, the parameters found in the literature are used in the equations presented in section 4.1.2 to calculate the yield strength of neSS. In order to fit the measured yield strength values, the parameters are adjusted when necessary and the missing parameters are adjusted by hand.

For the contribution of precipitates to strengthening, the radius and volume fraction of small precipitates measured by SAXS are used together with the corresponding yield strength values measured in the Gleeble in order to determine the single adjustable parameter k_s (Eq. 4-15 and Eq. 4-17).

Contribution of solid solution to strengthening

The contribution of solid solution to strengthening is to be calibrated against the measured yield strength at 0.2% strain offset, $\sigma_{y0.2}$. The measured $\sigma_{y0.2}$ values of AA7449 and AA7040 in neSS are given in *Figure 4-30*, together with the $\sigma_{y0.2}$ -Temperature curves predicted by the physically-based model of Leyson *et al.* [147] (Eq. 4-13). The $\sigma_{y0.2}$ values calculated using Eq. 4-21 and Eq. 4-23 with $t \rightarrow t_{hard,0}$ or $t_{soft,0}$, together with the identified parameters in *Figure 4-22*, are also shown (solid lines) for comparison.

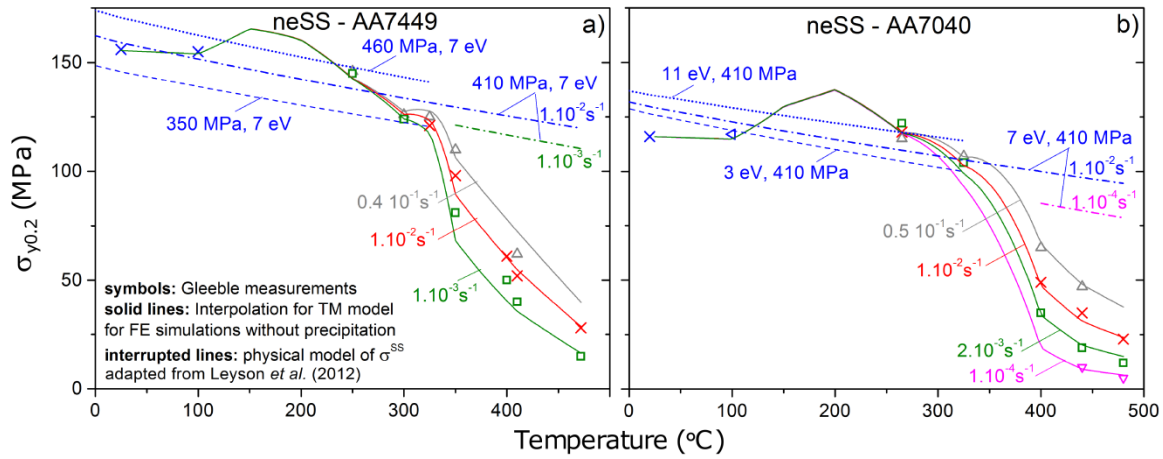


Figure 4-30 – Temperature dependence of yield strength of AA7449 (a) and AA7040 (b) in neSS. The legend given in (a) also applies to (b).

Firstly, it is checked in *Figure 4-30* that the solid lines are close to the measured $\sigma_{y0.2}$ values (symbols). This shows the quality of the identified parameters in *Figure 4-22* to predict reasonably well the yield strength at 0.2% strain offset. The solid lines are obtained using a linear interpolation of the parameters (σ_0 , H , n , K , m) between two temperatures. The linear interpolation for (σ_0 , H , n , m) is justified by the smooth monotonic evolution of these parameters with temperature. Due to the bell-shape of K and the low number of points to define the bell in *Figure 4-22-c*, a non-linear interpolation of K would be preferable. However, *Figure 4-30* shows that the linear interpolation also chosen for K provides acceptable $\sigma_{y0.2}$ values (solid lines). These curves feature a “bump” between 100°C and ca. 250°C where no $\sigma_{y0.2}$ value of neSS could be measured. The relatively high $\sigma_{y0.2}$ values at 150°C and 200°C may come from the extrapolation procedure ($t \rightarrow t_{hard,0}$ or $t_{soft,0}$ in Eq. 4-22) used to obtain σ_0 of neSS (without precipitates). If this is the case, the “bump” is not physical and should be ruled out by using a linear interpolation of $\sigma_{y0.2}$ between 100°C and 250°C for instance. However, a bell-shape of the $\sigma_{y0.2}$ -Temperature curve can be physically explained by Dynamic Strain Ageing which can lead to a negative SRS at low temperature for strain-rates where the mobility of solute atoms and dislocations is comparable [171]. This could explain the $\sigma_{y0.2}$ values at 265°C

for AA7040 in *Figure 4-30-b*, which seem to increase with decreasing strain-rate. However, further tests would be necessary between 100°C and 250°C to check for possible Dynamic Strain Ageing. For the FE simulations without precipitation, the parameters (σ_0 , H , n , K , m) that give the bell-shape $\sigma_{y0.2}$ -Temperature curves in *Figure 4-30* are chosen. This choice to keep the “bump” has almost no consequence on the calculated RS profiles since deformation between 150°C and 250°C is almost only elastic at the surface of water-quenched plates.

Secondly, the $\sigma_{y0.2}$ values predicted by the physically-based model of Leyson *et al.* [147] (interrupted lines) are compared to the measurements for AA7449 and AA7040ⁱ. These predicted values are obtained by adjusting the parameters related to Zn which was not studied in the work of Leyson *et al.* The sensibility of the yield strength parameter $\tau_{Zn0} / X_{Zn}^{2/3}$ for a given energy barrier parameter $\Delta E_{Zn}^b / X_{Zn}^{1/3}$ set to 7 eV is shown in *Figure 4-30-a*: the higher the yield strength parameter, the higher the amplitude and slope in absolute value of the $\sigma_{y0.2}$ -Temperature curve. The sensibility of the energy barrier parameter for a given parameter $\tau_{Zn0} / X_{Zn}^{2/3}$ set to 410 MPa is shown *Figure 4-30-b*: the higher the energy barrier parameter, the higher the amplitude and the lower the slope in absolute value of the $\sigma_{y0.2}$ -Temperature curve. Below ca. 325°C, a relatively good agreement between measurements and calculations is found using the values of 410 MPa for $\tau_{Zn0} / X_{Zn}^{2/3}$ and 7 eV for $\Delta E_{Zn}^b / X_{Zn}^{1/3}$, together with the other values given in the work of Leyson *et al.* for Mg, Cr, Si, Cu, Mn and Fe. The yield strength parameter of 410 MPa for Zn determined in this work is lower than that of Mn, which is in agreement with the literature (see section 4.1.2). However, it should be lower than that of Cu and that of Mg (known to contribute more than Zn to strengthening as shown in *Figure 4-1*), which is not the case. The predictions above 325°C highly overestimate the measurements. This can be attributed to the too high energy barrier (ca. 316 kJ/mol for AA7449 and ca. 292 kJ/mol for AA7040) calculated by using the parameters $\Delta E_i^b / X_i^{1/3}$ given in *Table 4-1* and 7 eV for Zn.

Despite its strong physical basis and its ability to predict reasonably well $\sigma_{y0.2}$ values of AA7449 and AA7040 in neSS below 325°C, the model of Leyson *et al.* is not chosen in this work due to the high discrepancy above 325°C and the poor agreement for AA2618. The model of Suni *et al.* is used instead.

The room temperature experimental $\sigma_{y0.2}$ values of AA2618, AA7449 and AA7040 in neSS are used together with the values of Al-Mg, Al-Cu and Al-Mn binaries to adjust the parameters a_i in Eq. 4-9. This is achieved by minimising the room means square between calculated and experimental yield strengths. *Figure 4-31-a* shows the good agreement between measured and calculated values using the parameters given in *Figure 4-31-b* (optimised parameters).

ⁱ The comparison for AA2618 is not given since the predicted $\sigma_{y0.2}$ values are ca. 30 MPa lower than the measured ones below 300°C.

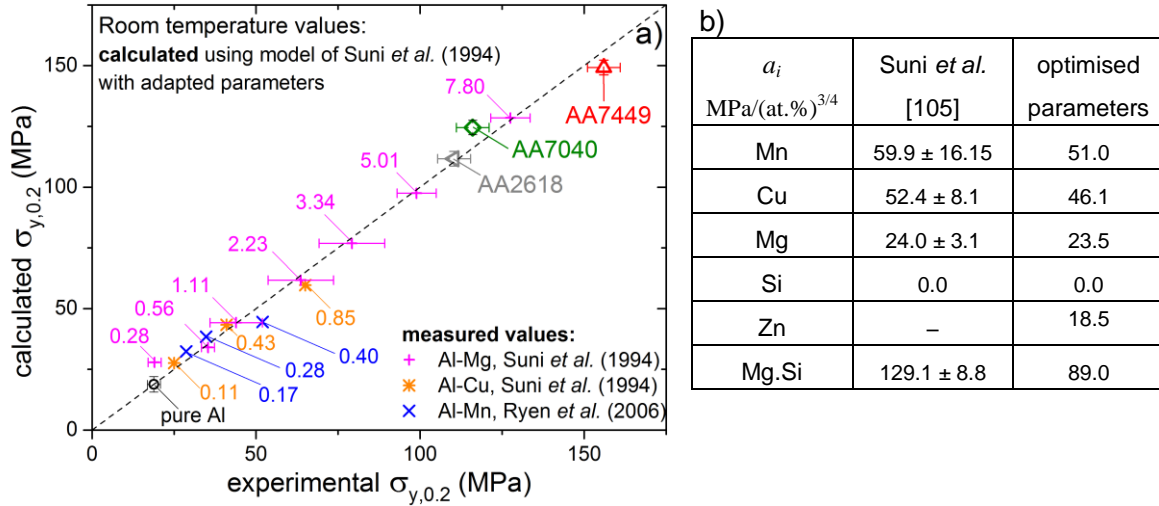


Figure 4-31 – Calculated vs. experimental $\sigma_{y,0.2}$ values for three binaries with various compositions indicated by the numbers (in at.%) [105, 146] and for AA2618, AA7449 and AA7040 (a); corresponding a_i values adjusted in this work together with original values of Suni *et al.* $n_{SS} = 3/4$.

The root mean square between calculated and experimental yield strength is ca. 16.7 MPa, which is close to the value obtained by Suni *et al.*. The vertical error bars for AA2618, AA7449 and AA7040 account for the composition uncertainty. The uncertainty on the experimental yield strength is indicated by the horizontal error bars. The parameters a_{Mn} , a_{Cu} and a_{Mg} adjusted in this work are within the statistical fitting error of Suni *et al.* given in Figure 4-31-b. a_{Zn} determined after optimisation is significantly lower than a_{Cu} and a_{Mn} , which is in agreement with the literature [17], but seems too high according to Figure 4-1. Due to the limited number of aluminium alloys containing Si and Zn used in this work to adjust $a_{Mg.Si}$ and a_{Zn} , the obtained values should be considered cautiously if they are to be used for other alloys. The evolution of $\sigma_{y,0.2}$ with temperature is described using the empirical relationship [157]:

$$\sigma_{y,0.2}^{calc,neSS}(T) = \left\{ \sigma_{y,0.2}^{pure}(20^\circ C) + \sigma_{y,0.2}^{SS}(20^\circ C) \right\} \cdot f(T)$$

$$\text{with } f(T) = \left\{ 1 + \left(\frac{Z^*}{Z(T)} \right)^{m_2} \right\}^{-1} \quad \text{Eq. 4-25}$$

where $\sigma_{y,0.2}^{pure}(20^\circ C) = 18.8$ MPa [105] and $\sigma_{y,0.2}^{SS}(20^\circ C)$ is the yield strength calculated using Eq. 4-9, together with the parameters given in Figure 4-31-b.

Z^* and m_2 are constants to determine and Z is the Zener-Hollomon parameter given in Eq. 4-4 with Q_{HW} a parameter to determine.

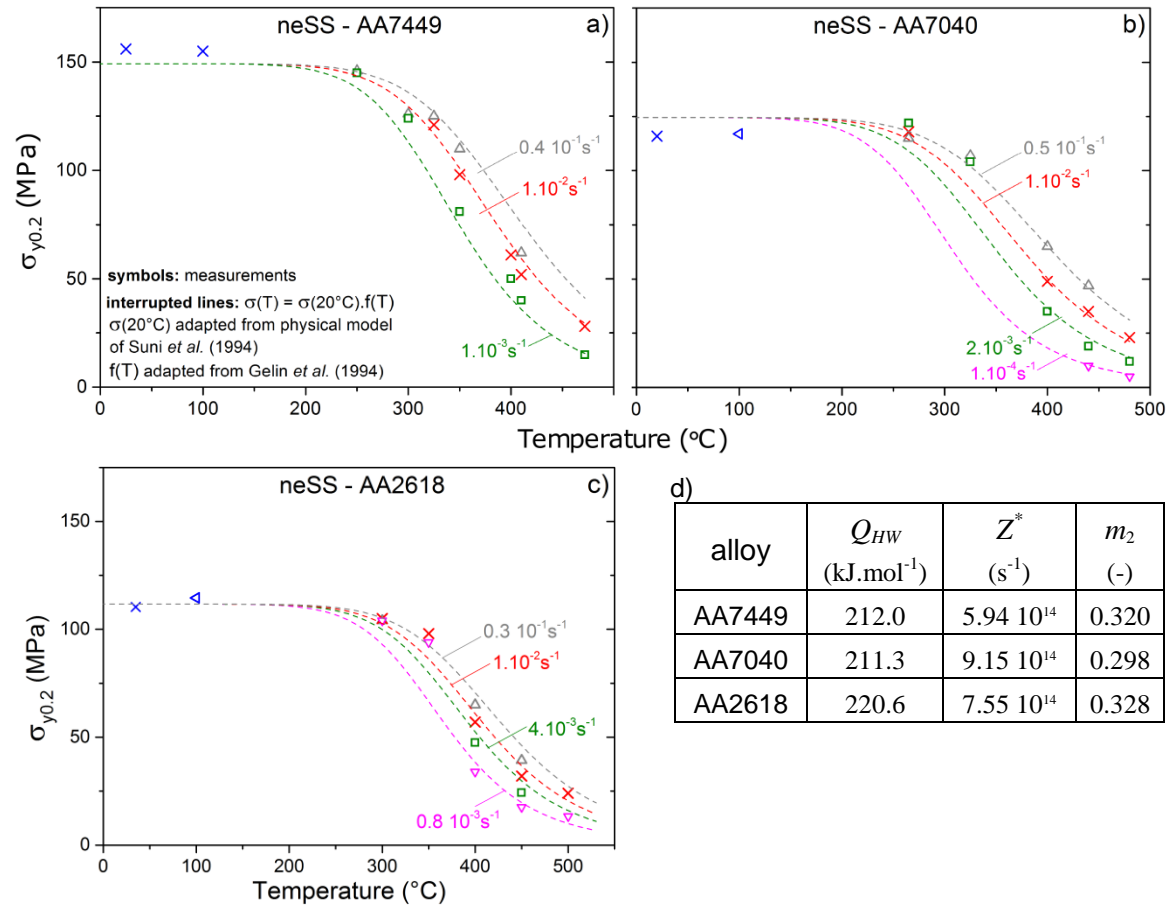


Figure 4-32 – Temperature dependence of experimental and fitted neSS $\sigma_{y0.2}$ values of AA7449 (a), AA7040 (b) and AA2618 (c); corresponding values of the parameters in Eq. 4-25. The legend in (a) applies to (b) and (c).

Although SRS at 350°C is overestimated by the fit using Eq. 4-25 for AA7040 and AA2618, the overall agreement between the measurements and their fit is relatively good for the three alloys as shown in Figure 4-32. The parameters Q_{HW} found for the three alloys are close to the values of the solution-treated AA7012 (200-230 kJ/mol) [120] and AA7150 (229.75 kJ/mol) [118] and the as-quenched AA7050 (256.6 kJ/mol) [121]. Cavaliere [172] found the much lower value of 161 kJ/mol for AA2618 that might be due to the different testing conditions (water quench to room temperature followed by heating at 3 K/s to the testing temperature). Since no Dynamic Strain Ageing is considered in the model the curves don't exhibit the bell-shape appearing in Figure 4-30.

Contribution of precipitates to strengthening during quenching

Figure 4-27-b and Figure 4-29-b provide a first estimate of the contribution of precipitates to strengthening after coolings similar to the industrial ones. Subtracting the yield strength of the neSS to that obtained after SAXS cooling gives a stress increment due to precipitates in the order of ca. 100 MPa.

The contribution of large precipitates to strengthening given by Eq. 4-18 can be estimated using an average radius of 25 nm and an average volume fraction of 0.05% for η representative of as-quenched (and natural aged) thick 7xxx plates [50]. This gives

a stress increment due to large η precipitates of ca. 8 MPa using $M = 2$, $\beta = 0.43$ and $\mu = 27$ GPa. This contribution is low compared to the ca. 100 MPa stress increment due to all the precipitates. Therefore, the contribution of large precipitates through Eq. 4-18 will be neglected in this work and only Eq. 4-17 describing the contribution of small precipitates to strengthening will be used. Furthermore, the fact that the mean precipitate radius \bar{r} is lower than r_{trans} (~ 3 nm for 7xxx alloys [82, 150]) during coolings similar to the industrial ones [10] justifies the use of a mean radius approach in this work.

Instead of adjusting the three parameters M , β and k_s in Eq. 4-17, the values $M = 2$ and $\beta = 0.43$ by Deschamps *et al.* are taken and the only adjustable parameter is k_s . The measured yield strength at 0.2% strain offset obtained after SAXS coolings reproduced in the Gleeble (*Figure 4-27-b* and *Figure 4-29-b*) are used for the calibration, together with the corresponding size and volume fraction of precipitates measured by SAXS.

Using Eq. 4-8 with $\sigma_{y0.2}^{LF} + \sigma_{y0.2}^{GB} = \sigma_{y0.2}^{pure}$ and Eq. 4-17, k_s writes:

$$k_s(T) = \left(\frac{4\pi\beta}{3} \right)^{1/3} \left\{ \frac{\sigma_{y0.2}^{exp}(T) - \sigma_{y0.2}^{calc,neSS}(T)}{M\mu(T) \cdot (\bar{r}^{cluster} f_v^{cluster} / b)^{1/2}} \right\}^{2/3} \quad \text{Eq. 4-26}$$

where the experimental values $\sigma_{y0.2}^{exp}(T)$ are given in *Figure 4-27-b* and *Figure 4-29-b*, and $\sigma_{y0.2}^{calc,neSS}(T)$ is calculated using Eq. 4-25. This requires the calculation of the concentration of elements i in the matrix appearing in Eq. 4-9 by using solute balance:

$$X_i(T) = \frac{X_i^0 - f_v^\eta(T) \cdot X_i^\eta - f_v^{cluster}(T) \cdot X_i^{cluster}}{1 - f_v^\eta(T) - f_v^{cluster}(T)} \quad (\text{in at.}\%) \quad \text{Eq. 4-27}$$

where f_v^η and $f_v^{cluster}$ are the volume fractions measured by *in situ* SAXS, X_i^η and $X_i^{cluster}$ are the concentrations of elements i in the phase η and in the clusters respectively (taken from Schloth *et al.* [10]) and X_i^0 is the nominal concentration of elements i in the alloy. Using Eq. 4-9 and Eq. 4-27 gives after SAXS coolings a maximal decrease of yield strength by solid solution of 3 MPa due to solute depletion by large η precipitates which is small compared to the ca. 50 MPa due to solute depletion by small precipitates. This is due to the fact that f_v^η is much lower than $f_v^{cluster}$ during SAXS coolings. Thus, solute depletion by large η precipitates is neglected and Eq. 4-27 becomes:

$$X_i(T) = \frac{X_i^0 - f_v^{cluster}(T) \cdot X_i^{cluster}}{1 - f_v^{cluster}(T)} \quad (\text{in at.}\%) \quad \text{Eq. 4-28}$$

The calculated values of k_s are given in *Figure 4-33-a* and the parameters used for the calculations in *Figure 4-33-b*.

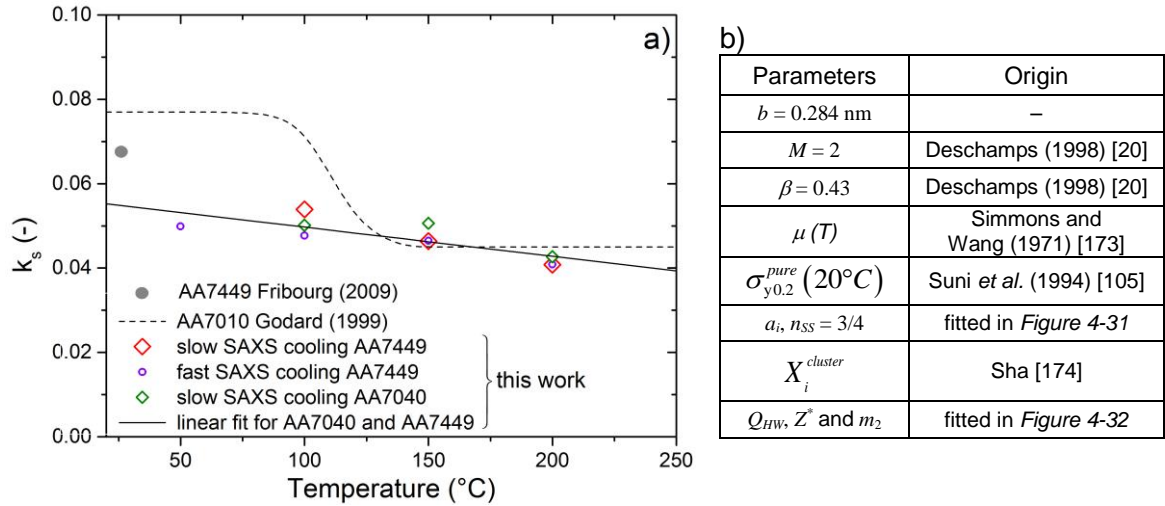


Figure 4-33 – k_s values found in the literature for AA7449 and AA7010 and calculated in this work for AA7449 and AA7040 after SAXS coolings (a); parameters used for the calculations (b).

The k_s values found in this work are close to the values of Godard above 125°C but significantly lower than the values of Godard and Fribourg at lower temperatures. This could be due to fact that the radii obtained by SAXS for AA7449 are slightly overestimated as explained in section 3.1.3 or due to the mean radius approach used instead of the PSD. A linear fit of the k_s values obtained in this work, shown in Figure 4-33-a, is used for implementation of the yield strength model:

$$k_s(20 \leq T < 250^\circ C) = 5.665 \cdot 10^{-2} - 6.934 \cdot 10^{-5} T \quad \text{Eq. 4-29}$$

This description of $k_s(T)$ provides an acceptable overall agreement between experimental and calculated $\sigma_{y,0.2}$ values as shown in Figure 4-34.

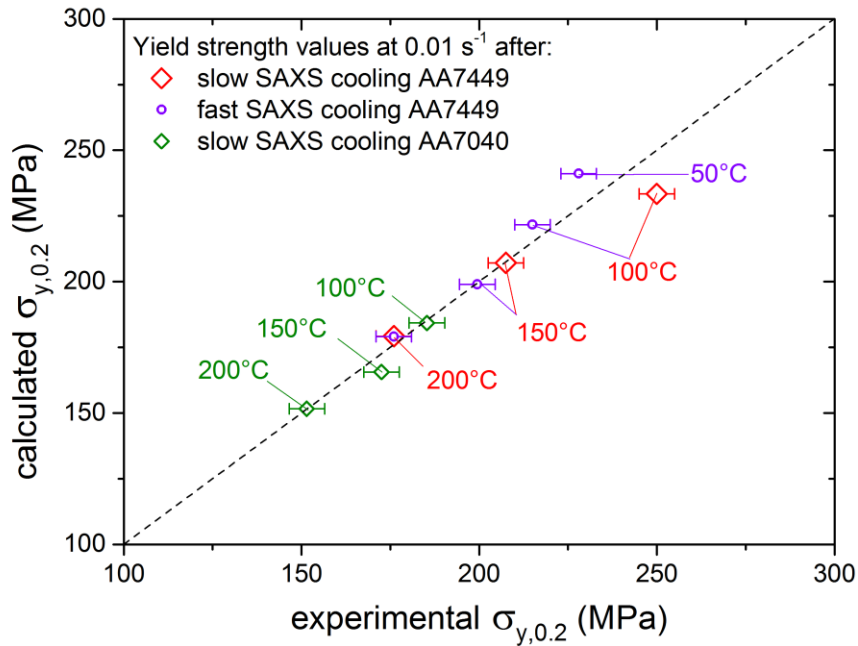


Figure 4-34 – Calculated vs. experimental $\sigma_{y,0.2}$ values for AA7449 and AA7040 after different cooling conditions using Eq. 4-29 for $k_s(T)$ together with the parameters given in Figure 4-33-b.

Here, it should be noted that only the k_s values below 150°C are important for RS calculations in water-quenched thick plates since deformation is mostly elastic between 150°C and 250°C. Finally, the parameters of the calibrated yield strength model used for FE simulations with precipitation using a TMM model are summarised in *Table 4-4*.

Parameter	Significance	Value	Origin
b	Burgers vector	0.284 nm	–
μ	Matrix shear modulus	Temperature dependent	Simmons and Wang (1971) [173]
M	Taylor's factor	2	Deschamps (1998) [20]
β	Dislocation line tension parameter	0.43	Deschamps (1998) [20]
k_s	Parameter for strengthening by small precipitates	$5.665 \cdot 10^{-2} - 6.934 \cdot 10^{-5} \cdot T(^{\circ}\text{C})$	fitted in <i>Figure 4-33</i>
a_i, a_{ij}	Solute strengthening parameters	Solute dependent	fitted in <i>Figure 4-31</i>
n_{ss}	Solute exponent	0.75	Suni <i>et al.</i> (1994) [105]
$\sigma_{y0.2}^{pure}(20^{\circ}\text{C})$	Yield strength of pure aluminium	18.8 MPa	Suni <i>et al.</i> (1994) [105]
Q_{HW}, Z^* and m_2	Parameters of Eq. 4-25	Alloy dependent	fitted in <i>Figure 4-32</i>
R	Gas constant	$8.314 \text{ J}\cdot\text{mol}^{-1}\cdot\text{K}^{-1}$	–

Table 4-4 – Parameters of the yield strength model.

These parameters are introduced into the yield strength model, which finally writes:

$$\sigma_{y0.2}^{\text{model}}(T, \dot{\epsilon}^{in}, X_i, \bar{r}^{cluster}, f_v^{cluster}) = \left\{ \sigma_{y0.2}^{pure} + \sigma_{y0.2}^{SS} \right\} \cdot \left\{ 1 + \left[\frac{Z^*}{\dot{\epsilon}^{in}} \exp\left(\frac{-Q_{HW}}{RT}\right) \right]^{m_2} \right\}^{-1} + \sigma^{ppt}$$

$$\sigma_{y0.2}^{SS}(X_i) = \left\{ \sum_i (a_i^{1/n_{ss}} X_i) + a_{MgSi}^{1/n_{ss}} X_{Mg} X_{Si} \right\}^{n_{ss}} \quad i = \{Zn, Mg, Cu, Mn\} \quad \text{Eq. 4-30}$$

$$\sigma^{ppt}(T, \bar{r}^{cluster}, f_v^{cluster}) = \left(\frac{3}{4\pi\beta} \right)^{1/2} \frac{[k_s(T)]^{3/2} M \mu(T)}{b^{1/2}} (\bar{r}^{cluster} \cdot f_v^{cluster})^{1/2}$$

where X_i , $\bar{r}^{cluster}$ and $f_v^{cluster}$ are outputs of a precipitation model.

Before applying the calibrated yield strength model to coolings different from the SAXS coolings used for its calibration, it has to be checked that the use of $\bar{r}^{cluster}$ and $f_v^{cluster}$ predicted by the precipitation modelⁱ for the SAXS coolings instead of $r^{cluster}$ and $f_v^{cluster}$ measured by SAXS gives also good $\sigma_{y0.2}$ predictions. This is the case as shown in *Figure 4-35* where the overall agreement between experimental $\sigma_{y0.2}$ values and the predicted values by the yield strength model is good.

ⁱ calibrated in the PhD work of P. Schloth for the small precipitates forming below ca. 160-180°C.

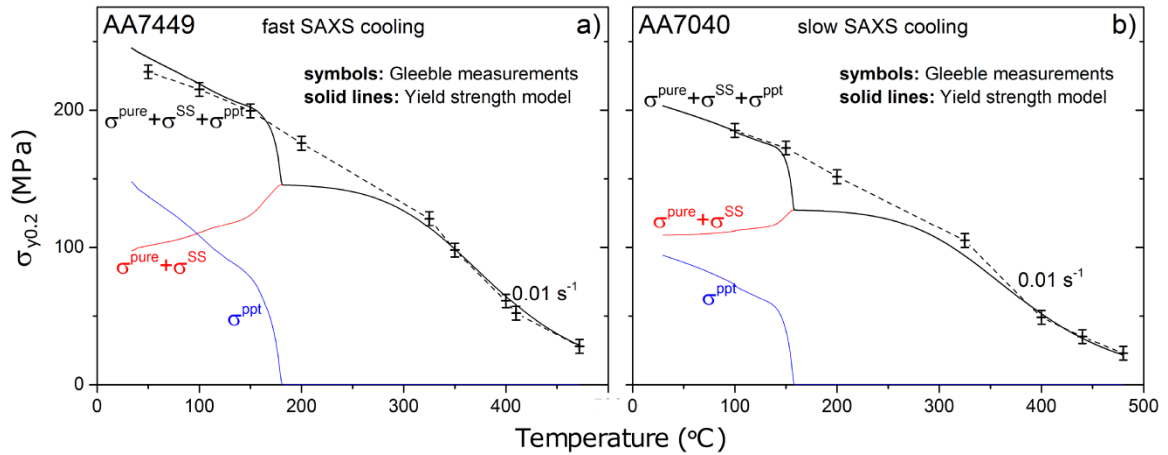


Figure 4-35 – $\sigma_{y0.2}$ values obtained experimentally (Gleeble measurements after SAXS coolings) and predicted by the calibrated yield strength model coupled to the precipitation model for AA7449 (a) and AA7040 (b). Interpolation of measurements in dashed lines are guide for the eye.

At high temperature ($> 300^{\circ}\text{C}$), the yield strength model fits almost perfectly the measurements as expected by the good calibration (see Figure 4-32).

At low temperature ($< 160^{\circ}\text{C}$) where the formation of clusters is taken into account in the precipitation model, the agreement between measured and predicted yield strength is good. This means that the precipitation model is well calibrated, i.e. predicts good $\bar{r}^{cluster}$ and $f_v^{cluster}$ values.

At intermediate temperature ($200\text{--}270^{\circ}\text{C}$) where possible precipitation of η' is not considered in the precipitation model, the predicted yield strength is lower than the measured one. This is explained by the fact that precipitation of η' takes place in the measurements but is ignored in the precipitation model above ca. $160\text{--}180^{\circ}\text{C}$. This simplification in the precipitation model leads to $\sigma_{y0.2}$ -Temperature curves which are not realistic at ca. $160\text{--}180^{\circ}\text{C}$. However, this has no consequence on RS calculations in water-quenched thick plates since deformation is mostly elastic between 150°C and 250°C .

In order to assess the predictability of the calibrated yield strength model for coolings different from those used for its calibration, the interrupted quenches achieved in the Gleeble machine are imposed in the precipitation model. This is shown exemplarily for AA7449 after AQ interrupted at 150°C in Figure 4-36 and in appendix 7.9 for other cooling conditions and for AA7040.

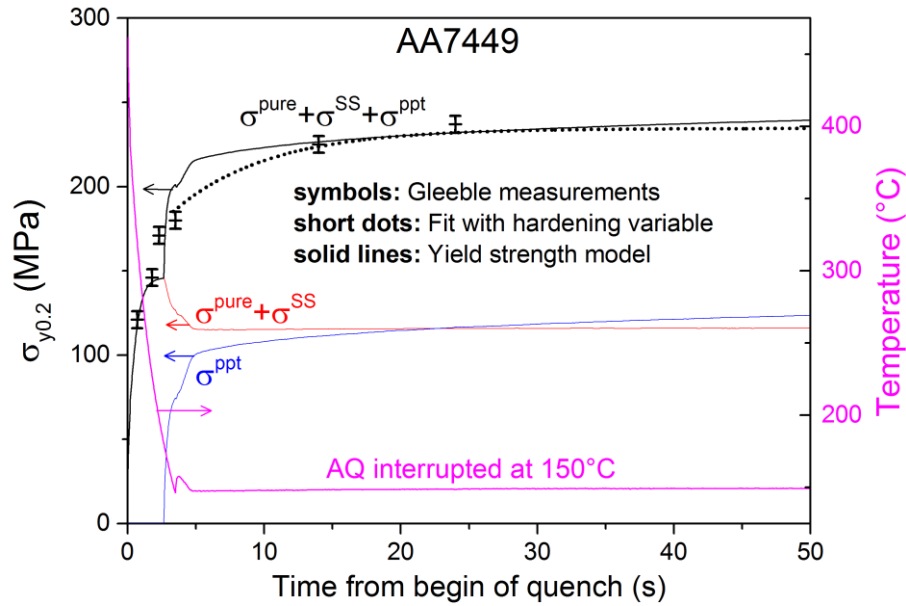


Figure 4-36 – Evolution of $\sigma_{y0.2}$ values obtained experimentally (Gleeble measurements after AQ interrupted at 150°C), predicted using the fit with hardening variable (Eq. 4-21 and Eq. 4-23 with parameters identified in Figure 4-21-a and b) and predicted using the calibrated yield strength model.

During AQ, yield strength increases rapidly from the SHT temperature to 200°C because of thermal effect. Below 200°C, yield strength increases because of the formation of small precipitates whose strengthening contribution (~100 MPa) is greater than their softening effect on the solid solution (~40 MPa) due to solute depletion in the matrix. The $\sigma_{y0.2}$ values predicted by the calibrated yield strength model compare very well with the experimental values. The agreement between $\sigma_{y0.2}$ of yield strength model and $\sigma_{y0.2}$ using the fit with hardening variable (exponential law in Eq. 4-23) is good except between 5 and 10 seconds where the yield strength increase predicted by the yield strength model is faster than the exponential one.

4.3.7. Determination of onset of accumulation of inelastic deformation

In order to determine T_{cum} defined in section 4.1.1, tensile tests at either 300°C, 325°C or 350°C are followed by a load at 45°C as suggested by Alankar and Wells [122]. The imposed coolings are shown in *Figure 4-37* for AA7449.

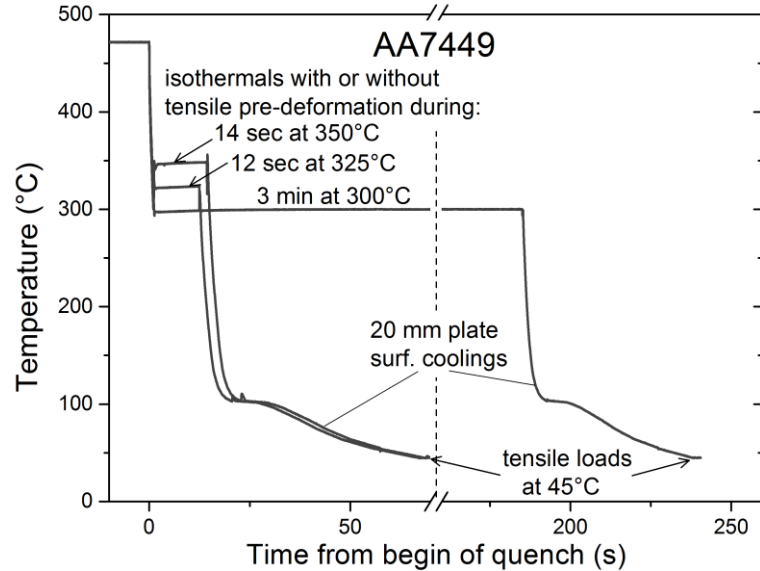
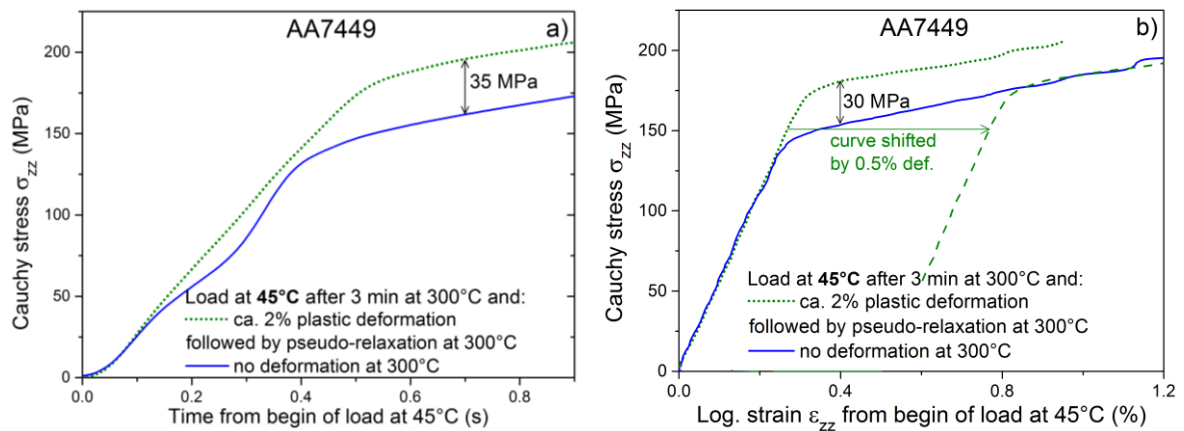
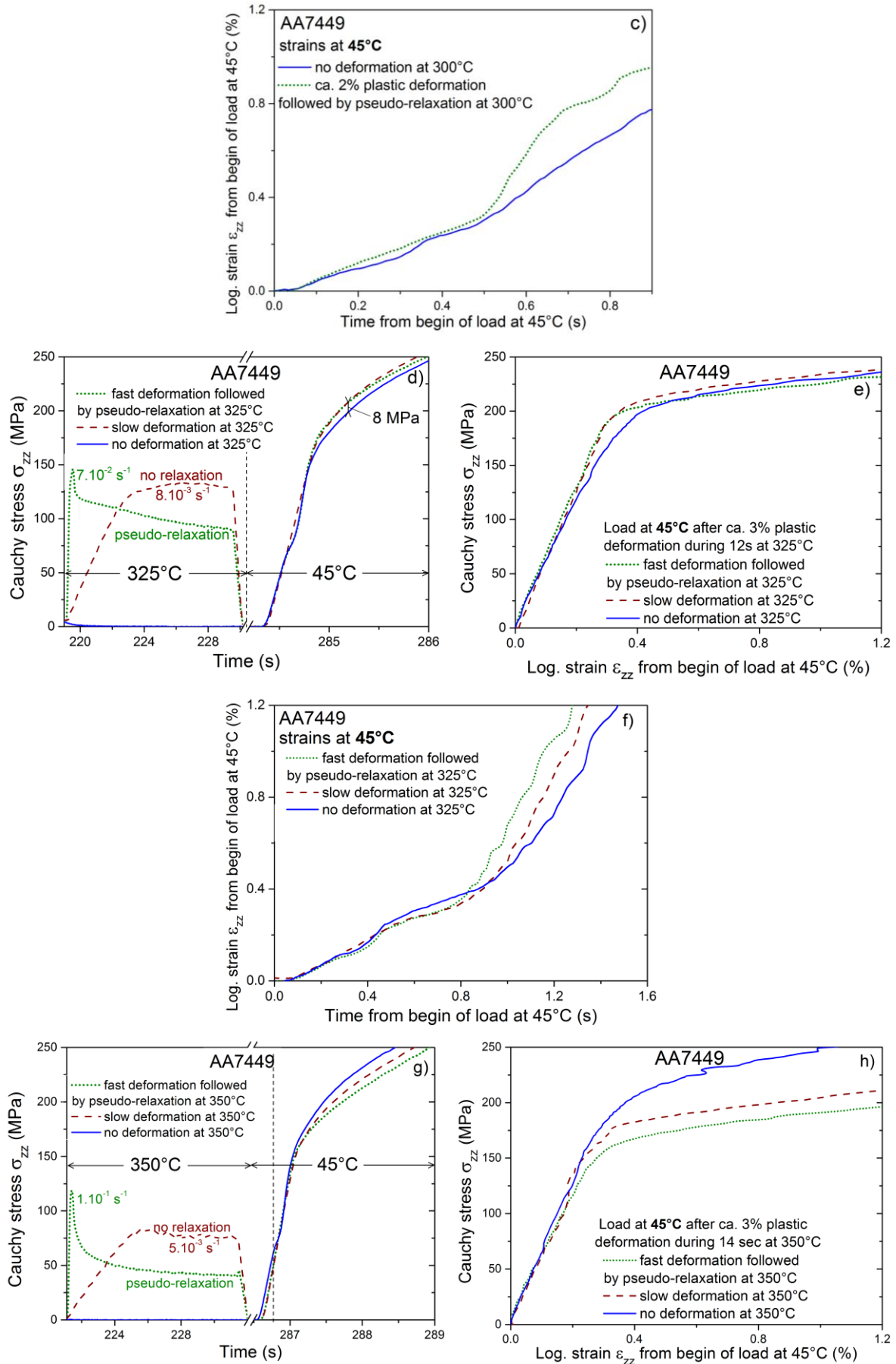


Figure 4-37 – Coolings imposed in AA7449 new geometry Gleeble specimens subjected to tensile load at 45°C with or without pre-deformation at 300°C, 325°C and 350°C.

For each of the three cooling conditions shown *Figure 4-37*, AA7449 Gleeble specimens from identical sampling are subjected to an air quench interrupted by an isothermal holding during which different mechanical loads are imposed. The isothermal holding is followed by a cooling similar to that of a 20 mm plate surface interrupted at 45°C where a tensile load is performed. Similar thermo-mechanical loadings are performed on AA7040 and AA2618 (see appendixes 7.6.3 and 7.7.4 respectively). The measured stresses and strains are given in *Figure 4-38* for AA7449 and in appendix 7.6.3 for AA7040 and 7.7.4 for AA2618.



4. Thermo-mechanical behaviour



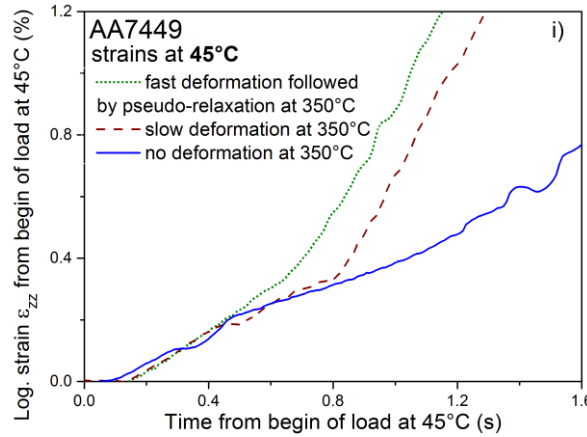


Figure 4-38 – Stress response of AA7449 subjected to loading at 45°C with or without pre-deformation at 300°C (a), (b) and (c), 325°C (d), (e) and (f) and 350°C (g), (h) and (i).

When pre-deformation is performed at a temperature lower than T_{cum} , the load curve at low temperature depends on this pre-deformation: the higher the pre-deformation, the higher the stress. This is the case at 300°C in Figure 4-38-a where the load curve at 45°C depends on pre-deformation at 300°C. This can also be seen in the stress-strain curves in Figure 4-38-b which should always be associated with the corresponding strain-time curves because of the strain uncertainties discussed in appendix 7.4. One fourth of the ca. 2% plastic deformation reached at 300°C is accumulated at 45°C as shown by the stress-strain curve shifted by 0.5% deformation.

Figure 4-38-d to f shows that the influence of pre-deformation at 325°C on the load curve at 45°C is low. Indeed, the stress-time curves at 45°C after pre-deformation at 325°C are only 8 MPa higher than the curve at 45°C after no deformation at 325°C (Figure 4-38-d). The corresponding stress-strain curves at 45°C are almost superimposed (Figure 4-38-e). Figure 4-38-g to i has similar features that at 325°C, except that the stress-time curve at 45°C after no deformation at 350°C is higher than the curves at 45°C after pre-deformation at 350°C. This indicates that plastic deformation at 350°C does not accumulate at 45°C. The fact that the stress-time curve at 45°C is higher without pre-deformation than with pre-deformation at 350°C is counter-intuitive. One possible explanation is that precipitation kinetics at 350°C is faster in case of pre-deformation at 350°C. Indeed, the presence of dislocations due to the plastic deformation tends to accelerate precipitate growth via pipe diffusion [18]. Thus, after 14 seconds at 350°C, solute depletion and thereby softening would be greater with pre-deformation than without pre-deformation at 350°C.

Similar experiments performed at 400°C for AA7449 and AA7040 showed no accumulation of inelastic deformation at that temperature.

From these experiments, unless otherwise stated, the value of 325°C has been chosen for T_{cum} in all the FE models of quenching for the three alloys. This means that all the plastic deformation occurring below 325°C is accumulated in the model. This choice leads to a slight overestimation of p_{cum} since only a small amount of the plastic deformation at 300°C is accumulated at 45°C as shown in Figure 4-38-b.

4.4. Summary of chapter 4

The interrupted quench-tests achieved on AA7449, AA7040 and AA2618 were used to determine their thermo-mechanical behaviour at different temperatures. The Gleeble has proved to be an appropriate tool to achieve complex cooling paths in order to obtain desired metallurgical states and characterise the corresponding behaviour.

In details, the following conclusions are drawn:

- The yield strength at 0.2% strain offset of AA7449, AA7040 and AA2618 in neSS shows a plateau below ca. 250°C. These values – necessary to establish the TM model ignoring precipitation – have been used to adjust the solute strengthening parameters required for the TMM model coupled with a precipitation model.
- The effect of holding time at constant temperature on yield strength reveals precipitation hardening at low temperature and softening at high temperature. These phenomena were evidenced by either a hardening or a softening variable in a yield strength modelling equation. The hardening variable used between 100°C and 300°C provided an extrapolation procedure to determine the yield strength of non-equilibrium solid solutions, i.e. without precipitates. The softening variable was used between 350°C and 410°C to decouple the effects of precipitation and/or softening and strain-rate on yield strength. Neither the softening nor the hardening variables will be used in the FE simulations of quenching (chapter 5).
- It has been checked that precipitation mainly affects yield strength for small strains as assumed in the models.
- Tensile tests after surface coolings have been performed to feed a TMG model.
- Tensile tests after SAXS coolings have been performed to adjust the only adjustable parameter for strengthening by small precipitates.
- The predictability of the calibrated yield strength model has been verified for coolings different from those used for its calibration.
- The effect of plastic strain recovery at high temperature has been evidenced. For the three alloys, it has been found that inelastic deformation is not “remembered” above 325°C – a required parameter for all the FE quenching simulations.
- Moreover, it has been checked for AA7040 (appendix 7.6.4) that the Bauschinger effect can be neglected in the case of RS generation during quenching.

The FE quenching simulations without precipitation model (TM and TMG models) will be based on the parameters defined in the following constitutive equations:

- $\sigma_{zz} = \sigma_0 + H.(p_{cum})^n + K.(\dot{p})^m$ for the TM model with (σ_0, H, n, K, m) given in *Figure 4-22* and applied through the whole thickness,
- $\sigma_{zz} = \sigma_y + H.(p_{cum})^n + K.(\dot{p})^m$ for the TMG model with (H, n, K, m) given in *Figure 4-22* and σ_y (also applied through the whole thickness) given in *Figure 4-25* for AA7449 and AA7040 and in *Figure 5-4* for AA2618.

5. RS predictions by finite element simulations

The heat transfer coefficients and the parameters of the mechanical behaviour law identified in part 2.2 and in part 4.3 respectively are used in this chapter to feed the FE simulations of quenching (presented in part 5.1) to calculate RS in thick plates and forgings. The results of FE quenching simulations achieved with the TM model (ignoring precipitation) using the parameters identified for non-equilibrium solid solution of the three alloys are given in part 5.2.

FE quenching simulations accounting for precipitation are given in part 5.3. Firstly, it is shown that the TMG model (simple but realistic thermo-mechanical model including precipitation without precipitation model) gives satisfactorily results (section 5.3.1). Secondly, RS results are given in 5.3.2 using the more sophisticated approach (TMM model) based on the yield strength model calibrated in section 4.3.6 coupled with the precipitation model introduced in part 3.1.

For the sake of brevity, the measured RS profiles presented in chapter 2 are given together with the results of FE simulations.

Finally, the TMM model is applied to a thicker (140 mm) AA7449 plate for which no RS measurements are done since such thick AA7449 plates are not industrially produced yet.

5.1. Thermo-mechanical models of quenching

5.1.1. Cold-water quenching of thick plates

The vertical quenching in cold water of AA7449 and AA7040 thick plates is simulated using a thermo-mechanical model similar to the one used by Jeanmart and Bouvaist [3] and implemented in the commercial FE code Abaqus 6.10. Compared to a 3D modelⁱ (*Figure 5-1-left*), this pseudo-2D model, assuming that the plate is infiniteⁱⁱ, is chosen for its simplicity. It consists of one row of axisymmetric elements through the plate thickness as shown in *Figure 5-1-right*. A FILM subroutine in Abaqus is used to define the heat flux q imposed at the plate surface (face between nodes #100 and #200). Zero flux is imposed on the other free surfaces. At plate mid-thickness, node #1 is fixed. The displacement along x of nodes #102 to #200 is set equal to that of node #101. This boundary condition is used to guarantee that the right free surface remains vertical during quenching (no twisting).

ⁱ used in preliminary FE quenching simulations (not shown in this work).

ⁱⁱ Although the plates are thick, they are considered as thin plates because in the experiments the plate extent (width and length) is large enough compared to the thickness.

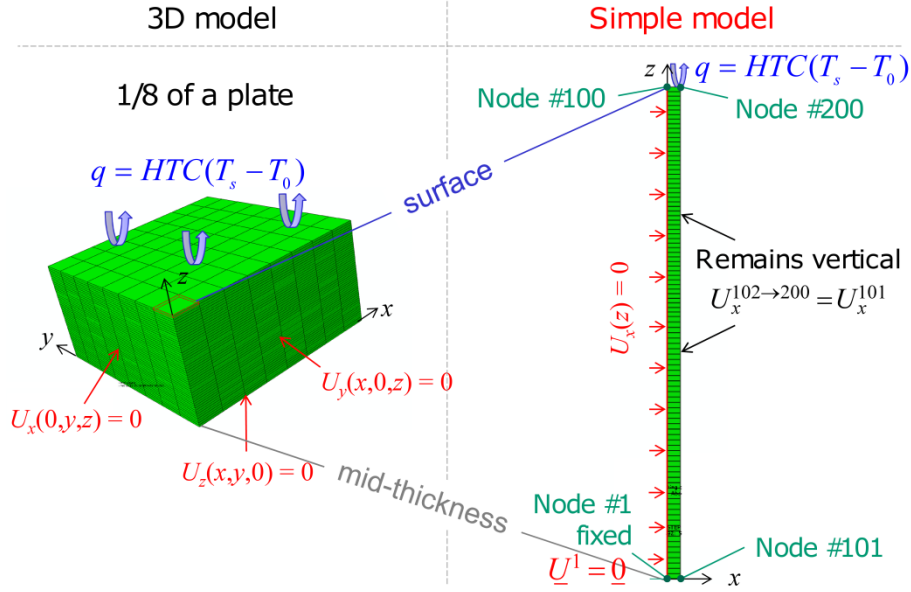


Figure 5-1 – 3D model (left) and corresponding pseudo-2D model used in this work (right).

The model features (mesh, element type and time increment) are discussed in the Abaqus benchmarks manual [175] where the numerical solution for constant HTC and thermal diffusivity together with an elastic, perfectly plastic material, with a temperature-dependent yield stress is compared to the semi-analytic solution given by Landau *et al.* [176]. In this model, temperature distribution is 1-D through the plate, i.e. $T = T(z, t)$ where z is the short transverse direction.

In this work, a non-linear heat transfer analysis is performed using the temperature-dependent thermal diffusivity provided by Constellium for AA7040 and AA7449 in neSS (see appendix 7.1). Surface heat flux is modelled with a Cauchy boundary condition using a global temperature-dependent heat transfer coefficient determined by Yu and Robinson [56] in the frame of the European project COMPACT (see section 2.2.2). The temperature field is recorded in the Abaqus results file during the heat transfer analysis. This temperature-time history is then used as input to the thermal-stress analysis. The temperature-dependant coefficient of thermal expansion (CTE) provided by Constellium is used to calculate thermal strainsⁱ and stresses induced by temperature gradients. Stress and strain components are 2-D in the plane (plane stress):

$$\sigma_{zz}(z) = 0 ; \sigma_{zx} = \sigma_{zy} = 0 \text{ and } \sigma_{zx} = \sigma_{zy} = 0 \quad \text{Eq. 5-1}$$

where x and y are the in-plane directions and z is the short transverse direction. Assuming no twisting, one has:

$$\sigma_{xy} = 0 \text{ and } \varepsilon_{xy} = 0 \quad \text{Eq. 5-2}$$

As verified experimentally on 75 mm thick AA7449 plates by neutron diffraction and by layer removal, x and y directions are equivalent:

$$\sigma_{xx} = \sigma_{yy} \text{ and } \varepsilon_{xx} = \varepsilon_{yy} \quad \text{Eq. 5-3}$$

ⁱ contribute only to dilatational, not shear strain

Therefore, only one stress component will be shown in the plates for which one also has:

$$|\sigma_{xx}| = \bar{\sigma} \quad \text{Eq. 5-4}$$

where $\bar{\sigma}$ is the von Mises equivalent stress. The stress and strain tensors write:

$$\underline{\sigma} = \begin{pmatrix} \sigma_{xx} & 0 & 0 \\ 0 & \sigma_{xx} & 0 \\ 0 & 0 & 0 \end{pmatrix} \text{ and } \underline{\varepsilon} = \begin{pmatrix} \varepsilon_{xx} & 0 & 0 \\ 0 & \varepsilon_{xx} & 0 \\ 0 & 0 & \varepsilon_{zz} \end{pmatrix} \quad \text{Eq. 5-5}$$

The thermal-stress analysis consists in finding $\varepsilon_{xx}(z,t)$ by substituting $T(z,t)$ into the strain compatibility equations. Then, $\sigma_{xx}(z,t)$ is found by using constitutive equations and force and moment balance through the (traction free) plate [4]:

$$\int_{-e}^{+e} \sigma_{zz}(z,t) dz = 0 \text{ and } \int_{-e}^{+e} z \cdot \sigma_{zz}(z,t) dz = 0 \quad \text{Eq. 5-6}$$

where e is the half thickness. Application examples of this solution procedure are found in the literature for simple constitutive equations [4, 177].

In this work, elastic behaviour and plastic flow are defined using the 3D Chaboche-type model implemented in an Abaqus user subroutineⁱ:

$$\begin{aligned} f &= J(\underline{\sigma}) - \sigma_y - H \cdot (p_{cum})^n \\ f < 0 &\Rightarrow \underline{\sigma} = \lambda_e \text{Tr}(\underline{\varepsilon}^e) \underline{I} + 2\mu_e \underline{\varepsilon}^e \quad \text{elastic behaviour} \\ f = 0 \text{ and } \dot{f} = 0 &\Rightarrow \dot{\underline{\varepsilon}}^{in} = \left\langle \frac{f(\underline{\sigma})}{K} \right\rangle^{1/m} \frac{\partial f}{\partial \underline{\sigma}} \quad \text{plastic flow} \end{aligned} \quad \text{Eq. 5-7}$$

where f is the scalar yield function and J is defined from the second invariant to be homogeneous to a stress (see appendix 7.3).

The temperature-dependent parameters (H , n , K , m) are interpolated linearly as a function of temperature. Moreover, since they are considered independent of precipitation, they are considered as uniform material properties (applied through the whole thickness) and the same values are used for the three models (TM, TMG and TMM). At high temperature, the same σ_y values are also applied through the whole thickness for the three models since the volume fraction of η phase formed during cold-water quench is low. In other words, σ_y is considered little affected by precipitation at high temperature. This is justified by the short time spent at high temperature during quenching. The three models differ only from σ_y at low temperature as shown in *Figure 5-2*, where the low temperature σ_y values used for the TMM model are not shown for clarity.

ⁱ It was checked that the implementation in UHARD and CREEP subroutines gives the same results. UHARD was chosen.

5. RS predictions by finite element simulations

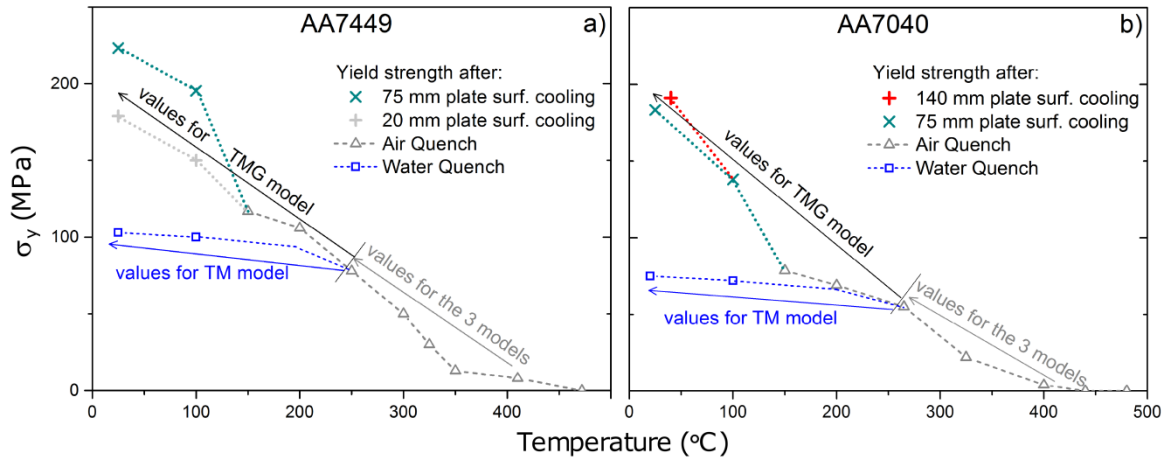


Figure 5-2 – σ_y parameters used for the FE quenching simulations of AA7449 (a) and AA7040 (b) plates using either the TM model or the TMG model.

In Figure 5-2, the different σ_y parameters used at low temperature are:

- $\sigma_y = \sigma_0$ of neSS (without precipitates) given in Figure 4-22-a for the TM model,
- σ_y after “surface coolings” in Figure 4-25 for the TMG model.

For the TM and TMG models, the same parameter $\sigma_y(T)$ is applied through the whole thickness and interpolated linearly as a function of temperature. This is a simplification for the TMG model because σ_y should be also dependent on the distance to the plate surface since precipitation varies with cooling paths.

For the TMM model, $\sigma_y(T)$ is dependent on the distance to the plate surface through $\sigma_{y0.2}^{model}$, the yield strength predicted by the yield strength model using Eq. 4-30:

$$\sigma_y = \sigma_{y0.2}^{model} - H \cdot (0.002)^n \text{ if } T < 150^\circ\text{C and } \sigma_y \text{ of TMG model if } T \geq 150^\circ\text{C} \quad \text{Eq. 5-8}$$

The use of Eq. 5-8 for the TMM model means that the yield strength model is only applied below 150°C and not above in order to have a smooth flow stress at 160-180°C which would not be the case with the yield strength model applied above 150°C (see for instance Figure 4-35).

The value of 325°C has been chosen for T_{cum} for AA7449 and AA7040 in all the FE models of quenching to account for plastic strain recovery at high temperature. If this is ignored (T_{cum} set to the SHT temperature), it was calculated that RS in a 75 mm thick AA7449 plate (not shown here) are overestimated by up to 15% at plate mid-thickness, compared to the case where $T_{cum} = 325^\circ\text{C}$.

5.1.2. Boiling-water quenching of forgings

The quenching in boiling water of AA2618 forgings (small and large) is simulated using axisymmetric models. The meshes are made of quadratic quadrilateral elements (DCAX8) of about 3 mm × 3 mm in size as shown in *Figure 5-3*.

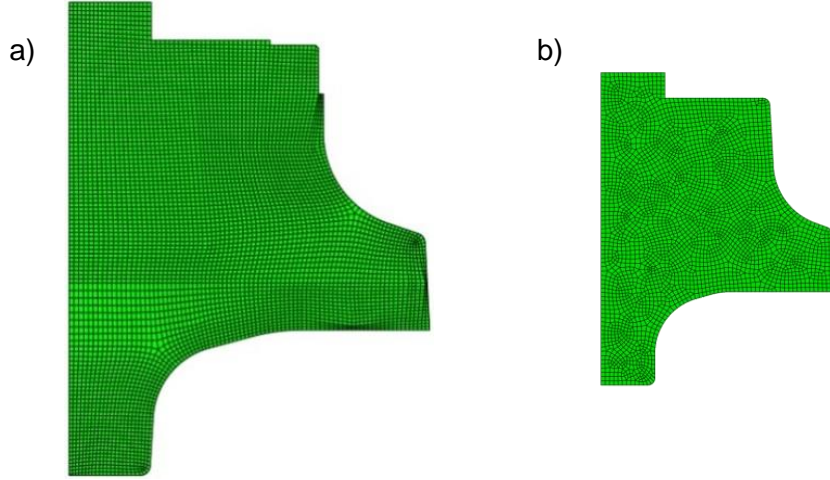


Figure 5-3 – Axisymmetric models of large (a) and small (b) AA2618 forgings.

As for the thick plate modelling, an uncoupled heat transfer and subsequent thermal-stress analysis is preferred because a preliminary study showed that it is faster and takes less memory than a coupled analysis where deformation and temperature are solved together. The non-linear heat transfer analysis is performed using the temperature-dependent thermal diffusivity provided by ABB Turbo Systems for AA2618 (see appendix 7.1). For each forging, 6 surfaces are defined to apply six different temperature-dependent HTC's (see section 2.2.2). The temperature field is recorded in the Abaqus results file during the heat transfer analysis. This file is then used as input to the thermal-stress analysis.

In this model, the stress tensor in cylindrical coordinates writes:

$$\underline{\sigma} = \begin{pmatrix} \sigma_{rr} & \sigma_{rz} & 0 \\ \sigma_{zr} & \sigma_{zz} & 0 \\ 0 & 0 & \sigma_{\theta\theta} \end{pmatrix} \quad \text{Eq. 5-9}$$

where r , θ and z are the radial, hoop and axial directions respectively. Along the forging axis, radial σ_{rr} and hoop $\sigma_{\theta\theta}$ components are equal. Shear components $\sigma_{rz} = \sigma_{zr}$ are small but different from zero due to the forging shape.

As explained in section 2.4.4, the residual elastic strain components calculated in the FE quenching simulations will be used instead of the residual stress components for the comparison with measurements.

The Chaboche-type model given in Eq. 5-7 is also implemented using a UHARD subroutine in Abaqus. The temperature-dependant parameters (H , n , K , m) for AA2618 are taken from *Figure 4-22* for both TM and TMG models. These two models differ only from σ_y at low temperature as shown in *Figure 5-4*.

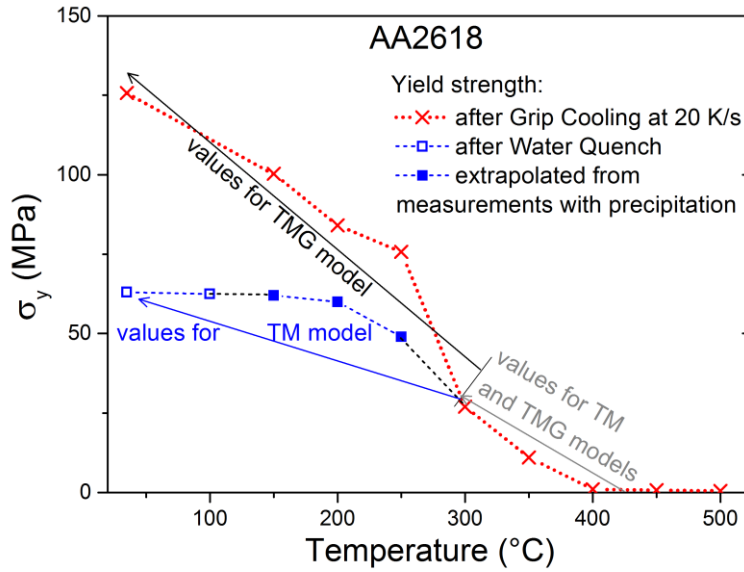


Figure 5-4 – σ_y parameters used for the FE quenching simulations of AA2618 forgings.

In Figure 5-4, the different σ_y parameters used at low temperature are:

- $\sigma_y = \sigma_0$ of neSS (without precipitates) given in Figure 4-22-a for the TM model,
- σ_y after grip cooling at 20 K/s for the TMG model.

The same parameter $\sigma_y(T)$ is applied through the whole forging and interpolated linearly as a function of temperature. This is a simplification for the TMG model because σ_y should be also dependent on the position in the forging since precipitation varies with cooling paths. Unless otherwise stated, the value of 325°C has been chosen for T_{cum} (see appendix 7.7.4) in all the FE models of quenching for AA2618. The implementation of the TMM model for FE quenching simulations of forgings is left as a perspective of this work.

5.2. RS predictions using the TM model without precipitation

5.2.1. As-quenched thick plates

The calculated cooling curves at surface and mid-thickness are given in Figure 5-5.

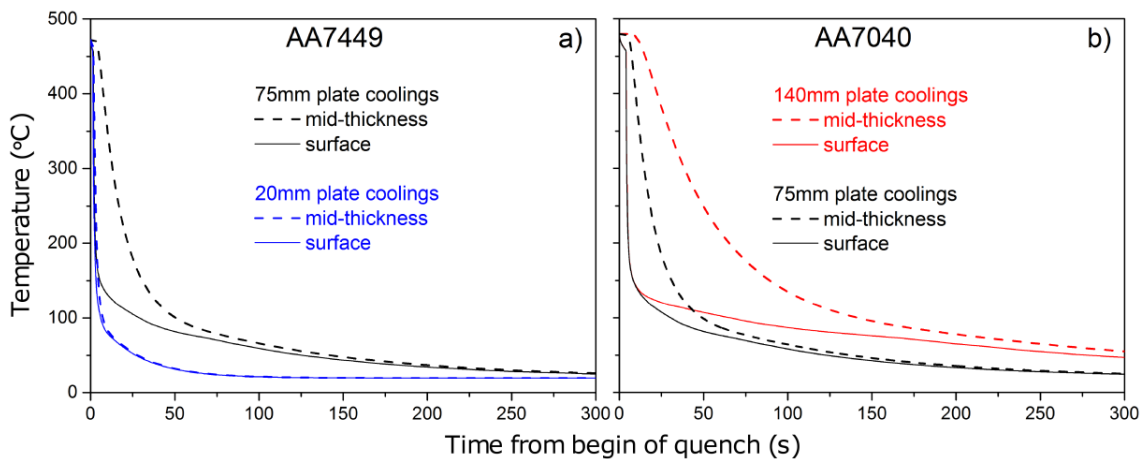


Figure 5-5 – Calculated cooling curves in AA7449 (a) and AA7040 (b) plates.

The thicker the plate, the larger the temperature difference between mid-thickness and surface, but also the longer the cooling time to reach 20°C through the thickness. Surface cooling of 75 mm and 140 mm plates is fast from the SHT temperature to ca. 150°C but slow below this temperature where precipitation hardening has time to occur. Precipitation hardening leads to higher RS as long as there is a significant temperature difference between mid-thickness and surface. The RS profiles obtained with the TM model are given in *Figure 5-6*, together with the measured as-quenched RS.

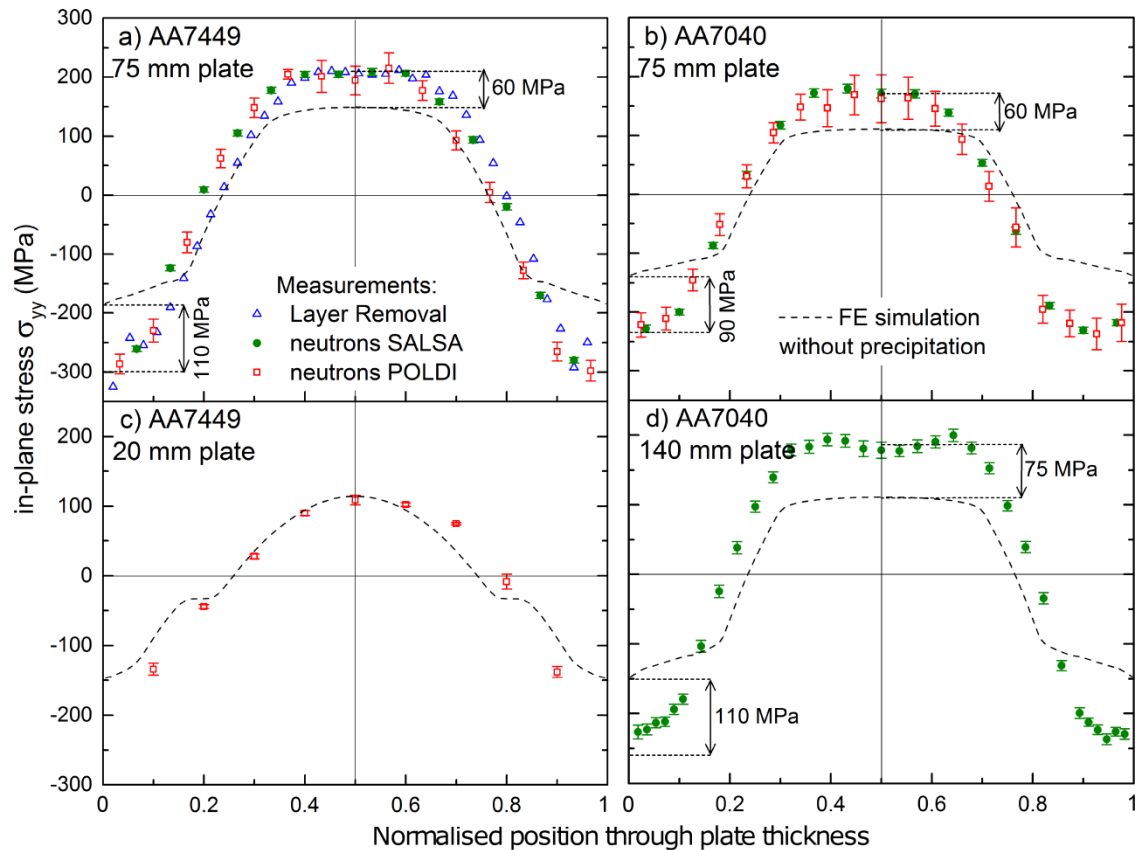


Figure 5-6 – Measured RS and simulated RS ignoring precipitation in 75 mm thick AA7449 (a), 75 mm thick AA7040 (b), 20 mm thick AA7449 (c) and 140 mm thick AA7040 (d) plates. The legends of measurements and simulations are given in (a) and (b) respectively.

Except for the 20 mm thick plate, the simulation without precipitation underestimates surface RS because the flow stress in the simulation without precipitation is lower than the real flow stress at the surface. The RS at mid-thickness are also underestimated because the compressive stresses are balanced by tensile stresses through thickness. In the 20 mm thick AA7449 plate (*Figure 5-6-c*), the RS at mid-thickness predicted without precipitation compare well with the measurements. Indeed, the cooling of the 20 mm plate is so fast that precipitation hardening is limited.

These results show that that a model taking into account precipitation is necessary for reasonable RS predictions in plates thicker than 20 mm.

5.2.2. As-quenched forgings

The calculated cooling rates at the surface and center of forgings are given in *Figure 5-7*.

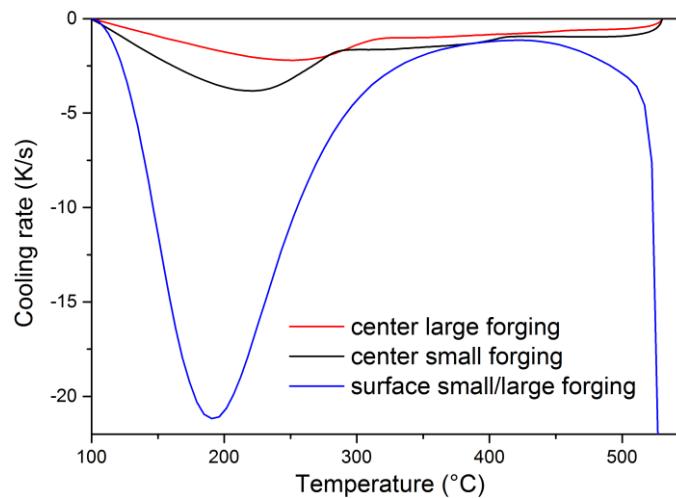


Figure 5-7 – Calculated surface and center cooling rates in forgings.

Above 300°C, the fastest cooling rates in the two forgings are always lower than 5K/sⁱ. This is lower than the high temperature critical cooling rate of AA2618 (~17K/s according to section 3.3.2), meaning that the *S* phase forms during cooling. However, the volume fraction of *S* phase at the center of the two forgings is expected to be low according to DSC measurement upon cooling at ca. 1.17 K/s. Ignoring high temperature precipitation is therefore justified for RS calculations in the small and large forgings. This simplification may be too simplistic for very large forgings with cooling rates lower than 1 K/s.

For the sake of brevity and for the reasons explained in part 2.4, the comparison between measurements and simulations will be done on residual elastic strains (residual stresses are shown in appendix 7.10) for the forgings. Nevertheless, simulated as-quenched residual stresses are shown in the form of coloured maps in *Figure 5-8* for the small forging and in *Figure 5-9* for the large forging.

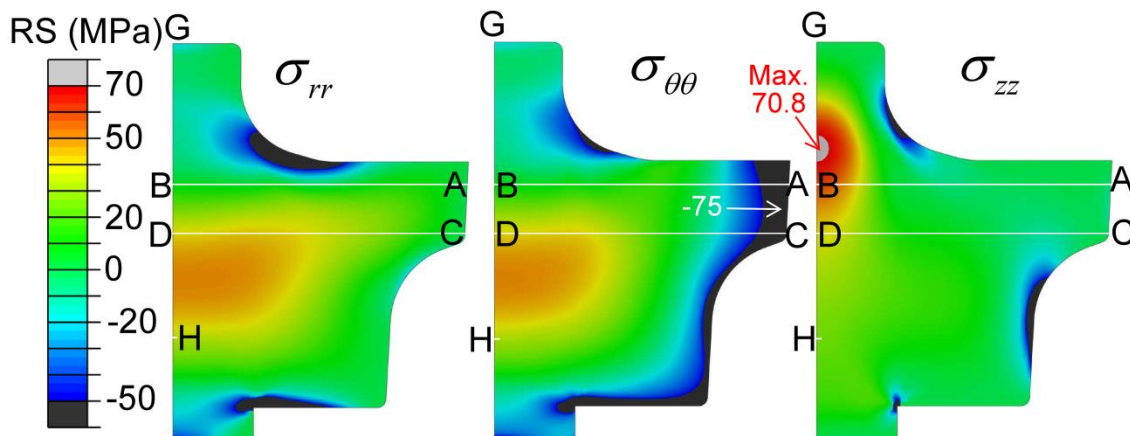


Figure 5-8 – Residual stress components predicted by the TM model (ignoring precipitation) in small forging. For clarity, RS higher than 70 MPa are in grey and RS lower than -50 MPa in black.

ⁱ except at surface close to the SHT temperature.

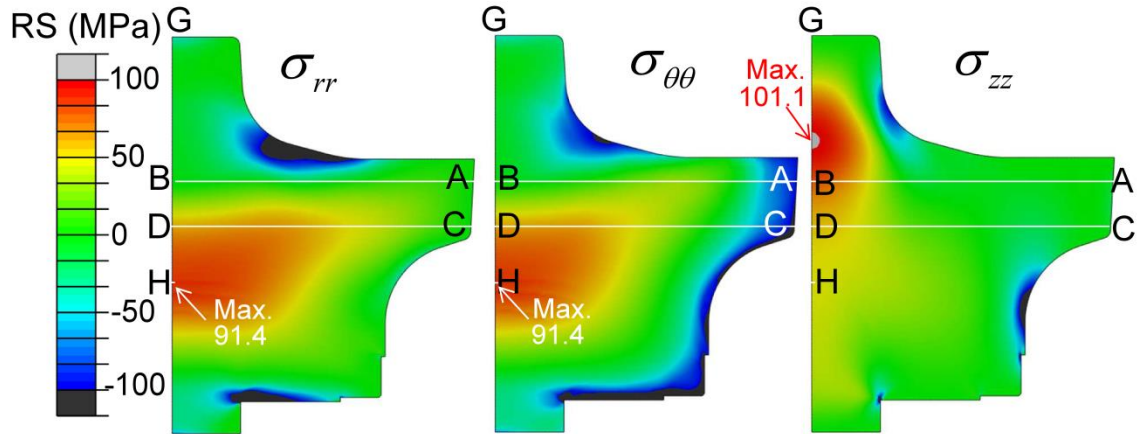


Figure 5-9 – Residual stresses predicted by the TM model (without precipitation) in large forging. For clarity, RS higher than 100 MPa are in grey and RS lower than -100 MPa in black.

As expected by the measurements (see section 2.4.4), the forgings are in a bi-axial compression state close to the surfaces and in a tri-axial tension state at the center (around B, D and H). The maximal tensile residual stress is found close to B for the axial component as indicated in *Figure 5-8* and *Figure 5-9*.

In the small forging, the corresponding value of 70.8 MPa predicted by the simulation overestimates by ca. 10 MPa the experimental value of $\sim 58 \pm 7$ MPa given in section 2.4.4. The comparison between experimental and simulated residual stresses is not further detailed since residual elastic strains should be compared instead. Nevertheless, the fact that the simulations overestimate the measurements means that the TM model (without precipitation) could be used by the industrial for a pessimistic (overestimated tensile stresses) estimation of residual stresses in the small forging.

In the large forging, the maximum tensile stress of 101.1 MPa predicted by the simulation is ca. 10 MPa lower than the experimental value of $\sim 113 \pm 15$ MPa given in section 2.4.4.

The residual strain profiles obtained with the simulation without precipitation are given in *Figure 5-10* for the two as-quenched forgings together with the measured residual strains.

5. RS predictions by finite element simulations

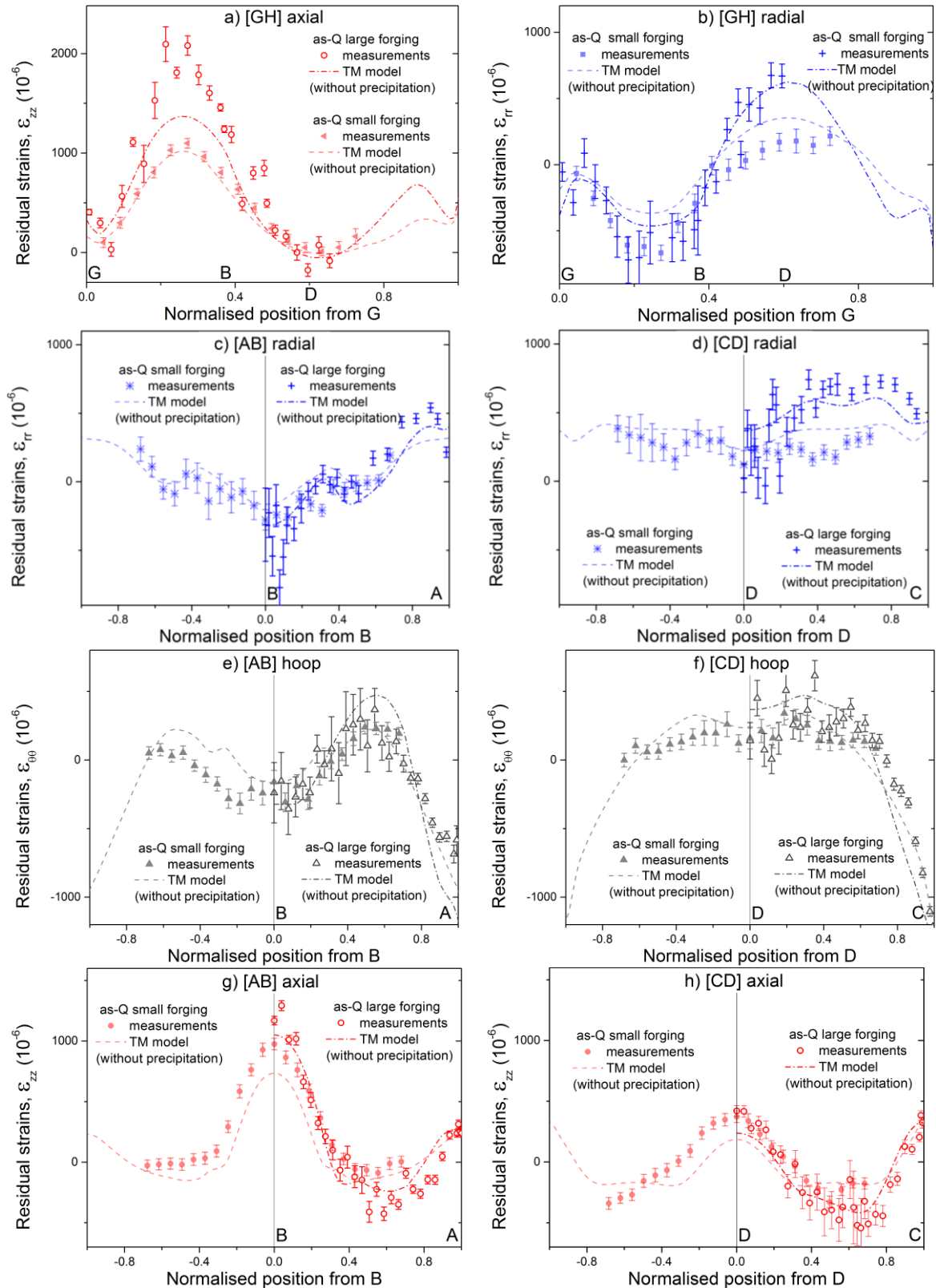


Figure 5-10 - Comparison between measured residual strain components and simulated ones using the TM model (ignoring precipitation) in as-quenched small and large forgings.

Qualitatively, the shape of the measured residual strain profiles in the two as-quenched forgings is well reproduced by the simulations. This indicates the quality of the calculated

thermal field evolution in the two forgings to simulate the industrial quench, especially in the small forging for which the HTCs identified for the large forging have been applied. Quantitatively, the overall agreement between measurements and simulations is good. In details, along the forging axis [GH], the agreement between measured and simulated (TM model) residual strains is:

- Excellent for ε_{zz} (Figure 5-10-a) and good for ε_{rr} (Figure 5-10-b) in the small forging.
- Fair for ε_{zz} (Figure 5-10-a) and good for ε_{rr} (Figure 5-10-b) in the large forging. Here, the fact that the simulation largely underestimates ε_{zz} at ca. 0.2-0.3 from G (Figure 5-10-a) is attributed to precipitation hardening not taken into account in the TM model. Therefore, a FE quenching simulation with precipitation is necessary for the large forging.

Along the radius and diameter of the large and small forgings respectively (Figure 5-10-c, e and g for [AB] and Figure 5-10-d, f and h for [CD]), the agreement between measured and simulated (FE model 1) residual strains is:

- Excellent for ε_{rr} (Figure 5-10-c and d) in both forgings. However, this excellent agreement is not guaranteed for the large forging because of the large error bars in the measurements around the center (close to B and D).
- Good for $\varepsilon_{\theta\theta}$ (Figure 5-10-e and f) in both forgings with the same remark as before for the large forging.
- Relatively good for ε_{zz} (Figure 5-10-g and h) in both forgings where the simulations slightly underestimates residual strains around the center.

Although residual strain measurements close to the surface of the small forging are lacking, it seems that a FE quenching simulation with precipitation is not absolutely necessary for this forging.

The agreement between measured and simulated residual elastic strains looks also good for the large forging. However, the error bars in the measurements around the center are high. Furthermore, precipitation hardening during quenching of the large forging is suspected to cause the discrepancy evidenced for ε_{zz} at ca. 0.2-0.3 from G (Figure 5-10-a). This will be check in the next part with FE quenching simulations of forgings taking into account precipitation in a simple way (TMG model).

5.3. RS predictions with precipitation

5.3.1. Taking into account precipitation without precipitation model

As-quenched thick plates

For the four cases (different alloys and thicknesses) treated with the TMG model (accounting for precipitation in a simple way from Gleeble tests), the evolution at plate surface of the internal stress σ_{xx} during quench is shown in *Figure 5-11* together with the accumulated equivalent plastic strain p_{cum} and the in-plane inelastic strain component ε_{xx}^{in} .

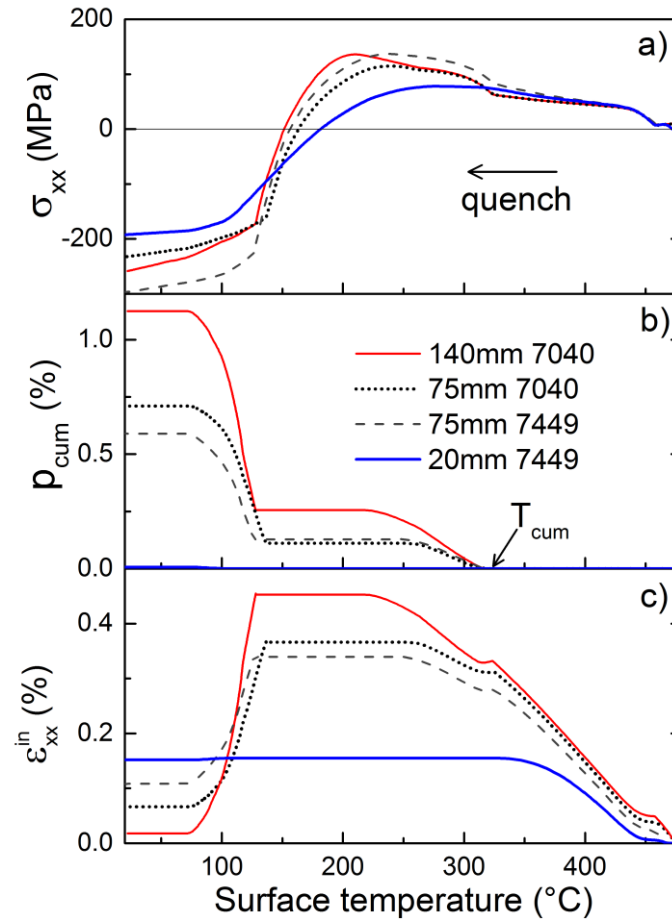


Figure 5-11 – Calculated evolution at plate surface using $T_{cum} = 325^{\circ}\text{C}$ of in-plane component of internal stress (a), accumulated equivalent plastic strain (b) and in-plane component of inelastic strain (c). The legend is given in (b).

The plate surface goes from tensile to compressive stresses (*Figure 5-11-a*) during quench. Surface inelastic strain occurs almost immediately after the begin of quench (*Figure 5-11-c*). For the 75 mm and the 140 mm plates, *Figure 5-11-b* shows that p_{cum} begins to increase at T_{cum} when the surface is still in tension. Then it stops increasing until the surface internal stress reaches again the flow stress (in compression) at about 130°C. Plastic deformation occurs until the temperature reaches 75°C. At the end of quenching, below ca. 75°C, deformation is elastic again due to an increase of the yield stress (*Figure 5-11-b* and *c*).

For the 20 mm thick plate, plastic deformation is much lower than for higher thicknesses. This is due to a much lower temperature difference between mid-thickness and surface. At the surface, the final value of p_{cum} after quenching depends strongly on the plate thickness because the thermal behaviour strongly depends on the plate thickness. For plates between 20 mm and 140 mm, the core, in turns, deforms elastically at low temperature (not shown here).

As mentioned in section 3.1.1, the choice of 325°C for T_{cum} could result in a slight overestimation of p_{cum} leading to a stress overestimation. To check this point, T_{cum} was varied from 325 to 250°C in the simulations. This resulted in σ_{xx} differences lower than 2% at surface and mid-thickness, meaning that an accurate determination of T_{cum} is not mandatory. As presented in section 3.1.1, a final value of 325°C was chosen for the simulations. The RS profiles obtained using the TMG model are given in *Figure 5-12* together with the simulation ignoring precipitation (TM model). RS measurements in both alloys are also shown.

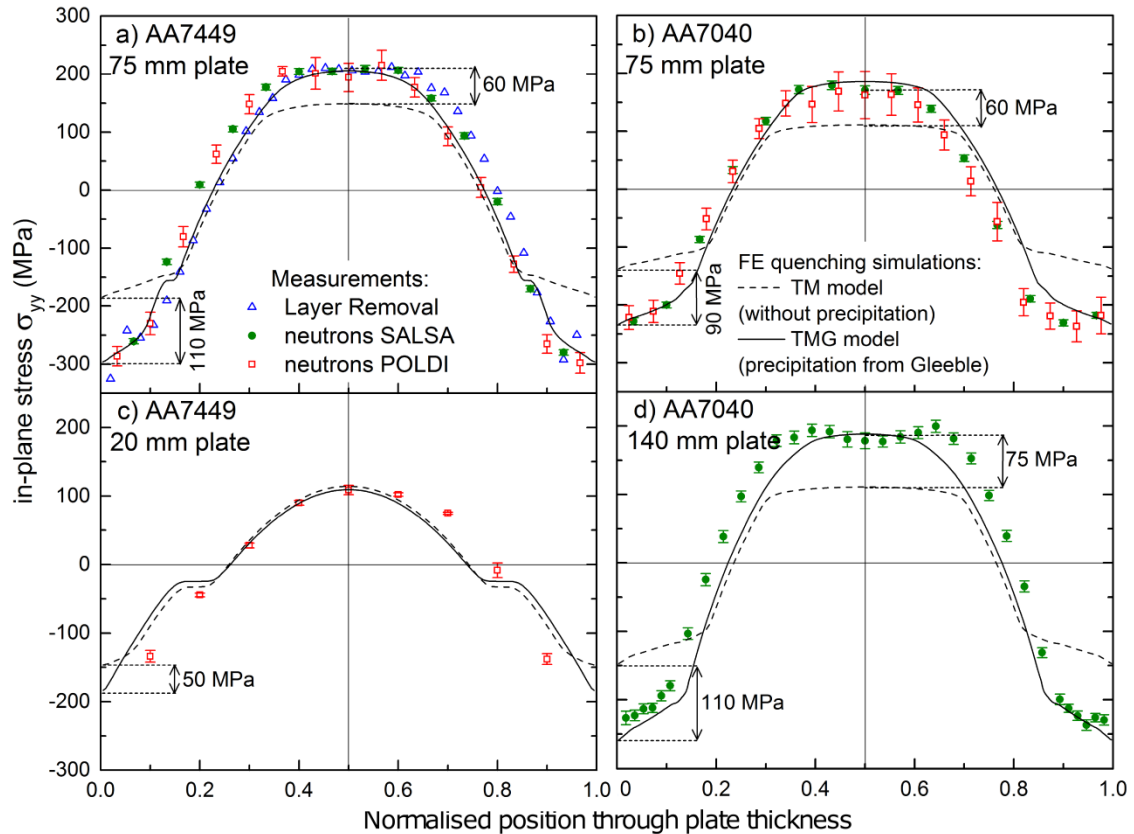


Figure 5-12 – Comparison between measured RS and calculated RS in a) 75 mm thick 7449 plate, b) 75 mm thick 7040 plate, c) 20 mm thick 7449 plate and d) 140 mm thick 7040 plate. The legend of the measurements is given in a) and the legend of the simulations in b).

The TMG model predicts very accurately the RS profile in the 75 mm thick plates (solid lines in *Figure 5-12-a* and *b*). A sensibility analysis on the model parameters (not shown here) showed that σ_y is the most sensitive parameter as expected by the large

differences between RS predicted by the TM model and the TMG model in *Figure 5-12*, which differ only from σ_y at low temperature.

For the 140 mm thick AA7040 plate (*Figure 5-12-d*), the TMG model predicts well the RS at surface and satisfactorily at mid-thickness.

In the 20 mm thick AA7449 plate (*Figure 5-12-c*), the RS at mid-thickness predicted with or without precipitation compare well with the measurements. Indeed, the cooling of the 20 mm plate (*Figure 5-5-a*) is so fast that precipitation hardening is limited. However, it is not negligible as revealed by the 50 MPa difference between simulations with and without precipitation at the surface. Robinson *et al.* [2] measured ca. 180 MPa compressive stress at the surface of a 16 mm thick AA7010 block. As AA7449 contains more alloying elements than AA7010, surface RS in compression should be higher than 180 MPa in a 20 mm thick AA7449 plate. This is in accordance with the 200 MPa compressive stresses predicted by the simulation with precipitation. Surface measurements by X-ray diffraction would be necessary to verify this value and to check the presence of the shoulder predicted by the model at quarter thickness.

For a given alloy, the higher the plate thickness, the higher the surface RS in as-quenched temper. This is in agreement with the results of Robinson *et al.* [2] for cold-water-quenched AA7010 blocks. The RS underestimation by the TM model (without precipitation) increases with increasing thickness. Thus, as plate thickness increases, a model with precipitation becomes necessary to predict reasonably well the RS profile.

The good agreement between the TMG model and the measurements shows the relevance of this model based on tensile tests after coolings similar to the surface during quenching. But it means that a few Gleeble tensile tests should be performed for each plate thickness and each alloy one would like to model. These interrupted Gleeble tests are:

- for each alloy, one tensile test at SHT temperature and a few tensile tests after rapid cooling between SHT temperature and 200°C,
- for each alloy and plate thickness, two tensile tests at lower temperature (e.g. 25°C and 100°C) after a cooling similar to that of the surface during quenching.

This method decreases the number of Gleeble tests compared to the traditional approach based on a yield strength model depending on precipitation. However, the latter approach remains necessary for modelling complex parts with different thicknesses or plates with a full range of thicknesses with the same physically-based model.

As-quenched forgings

The as-quenched residual strain profile along the axis in the two forgings obtained using the TMG model are given in *Figure 5-13* together with the simulation without precipitation (TM model). Residual strain measurements are also shown.

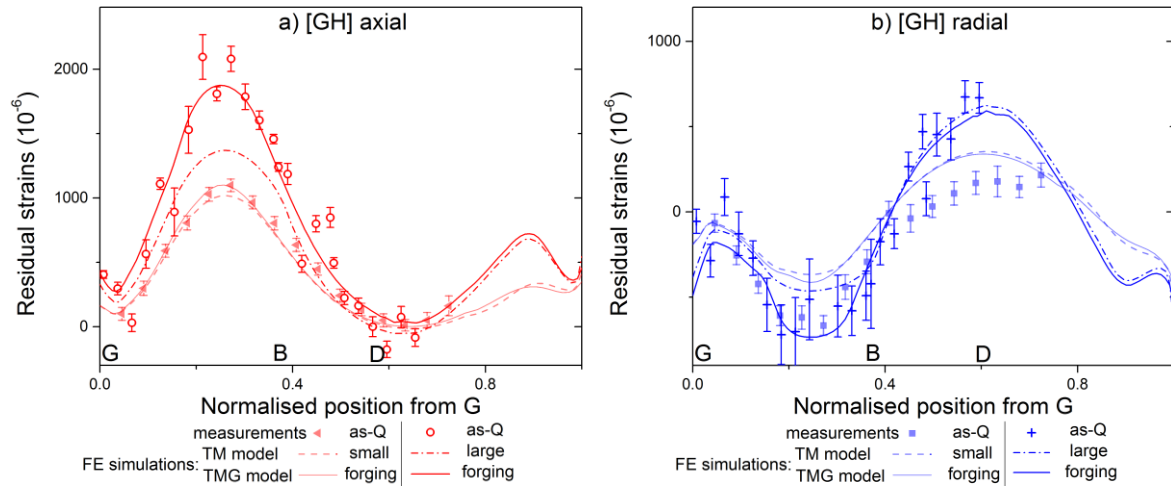


Figure 5-13 – Comparison between measured residual strains and simulated ones using the TM model (ignoring precipitation) and the TMG model in as-quenched small and large forgings.

In the small as-quenched forging, residual strains predicted by the TMG model (with precipitation) based on Gleeble interrupted quench-tests at 20 K/s are almost identical to those predicted without precipitation (TM model). This suggests that the effect of precipitation is small for this forging size.

In the large as-quenched forging, the two models give similar strain values except in the region where tensile stresses are maximal between G and B. There, the simulation without precipitation (TM model) underestimates measurements. The agreement in terms of residual strains is improved using a TMG model based on Gleeble interrupted quench-tests at 20 K/s, meaning that precipitation hardening during cooling has to be taken into account to predict reasonably well residual strains and stresses.

The difference in terms of residual stresses between the TM model and the TMG model is shown in Figure 5-14 for the small forging and in Figure 5-15 for the large forging. In these difference plots, the regions in green indicate that both models predict the same RS (at ± 2 MPa and ± 5 MPa in the small and large forgings respectively). The regions in dark blue and red indicate that the RS predicted by the TMG model are higher in absolute than those predicted by the TM model.

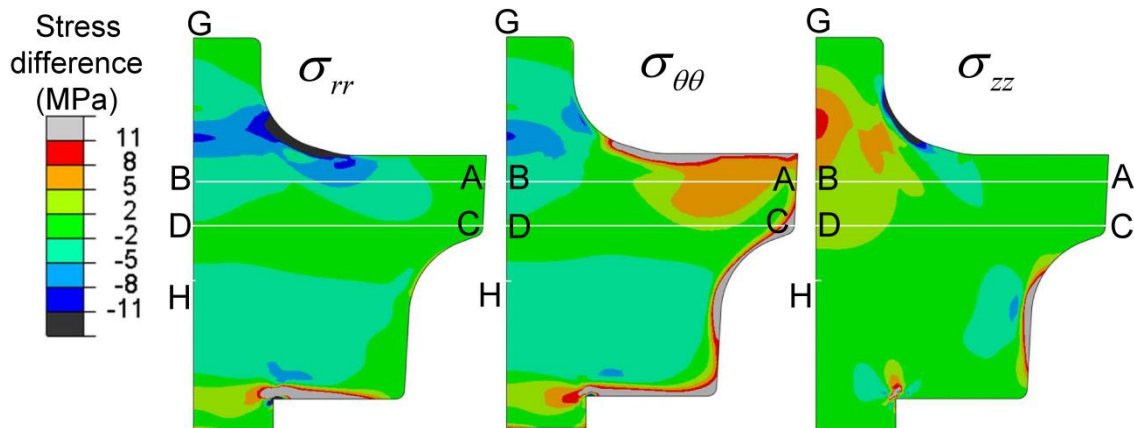


Figure 5-14 – Subtraction of stresses in small forging predicted by the TM model (ignoring precipitation) to those predicted by the TMG model.

In the small forging, the RS predicted by both models mainly differ in the region between B and G, where the stress components predicted by the TMG model are up to ca. 11 MPa higher in absolute value than those predicted by the TM model.

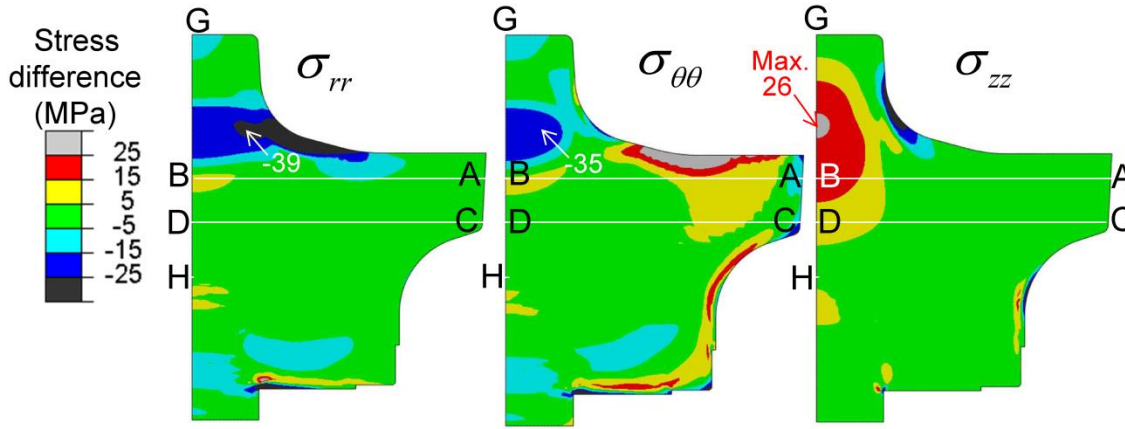


Figure 5-15 – Subtraction of stresses in large forging predicted by the TM model (ignoring precipitation) to those predicted by the TMG model.

In the large forging (Figure 5-15), the stress components predicted by the TMG model are up to ca. 40 MPa higher in absolute value than those predicted by the TM model.

The RS profiles along [GH] are given in appendix 7.10 for the large forging, together with the RS profiles along [AB] and [CD] where the differences between both models are low.

5.3.2. Taking into account precipitation with a precipitation model: TMM model with one-way coupling

The framework for one-way coupling is implemented in Abaqus for quenching of plates of different thicknesses. It is applied to AA7449 plates but not to AA7040 plates due to the limitations presented in appendix 7.9.

Principle of implementation in Abaqus

The cooling curves calculated at different positions in the plate thickness (3 positions for the 20 mm plate and 10 positions for the 75 mm plate) are imposed in the precipitation model calibrated for GP(I) zones forming below 184°C (see section 3.4.1). For each cooling curve, the precipitation model gives as output the evolution of the average precipitate radius and the volume fraction as well as the matrix chemical composition (X_{Zn} , X_{Cu} , X_{Mg}). These values are read by Abaqus and stored in five user fields. At each time step, these fields are interpolated linearly in-between two positions (Gauss points) to get these values through the whole plate thickness.

Instead of using only a few positions in the plate thickness, it would be more accurate to refine the mesh and impose the cooling curve for each node in the precipitation model to obtain the accurate precipitation state at every position. However, this would be expensive in terms of memory allocation and computational time. Therefore, only a few positions are used for precipitation model calculations.

For the TMM model, $\sigma_y(T)$ is dependent on the distance to the plate surface through $\sigma_{y0.2}^{model}$, the yield strength predicted by the yield strength model using Eq. 4-30:

$$\sigma_y = \sigma_{y0.2}^{model} - H \cdot (0.002)^n \text{ if } T < 150^\circ\text{C and } \sigma_y \text{ of TMG model if } T \geq 150^\circ\text{C}$$

This means that the yield strength model is only applied below 150°C and not above in order to have a smooth flow stress at 160-180°C which would not be the case with the yield strength model applied above 150°C (see for instance *Figure 4-36*).

Results

The RS profiles calculated in 75 mm thick AA7449 plate by the TMM and TMG models are given in *Figure 5-16*. RS measurements in rolling (L) and transverse long (TL) directions are also shown.

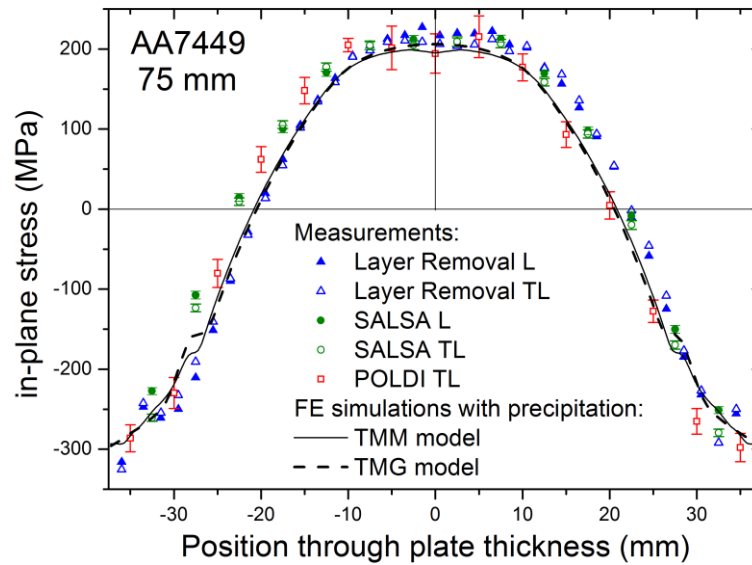


Figure 5-16 – Comparison between measured RS in 75 mm thick AA7449 plate and calculated ones by the TMM and TMG models. $T_{cum} = 325^\circ\text{C}$ for the FE simulations.

As expected by the good agreement between experimental $\sigma_{y0.2}$ values and the predicted values by the yield strength model after the cooling of a 75 mm AA7449 plate in surface (see *Figure 7-36-a* in appendix 7.9), surface RS predicted by the two FE simulations are identical. Furthermore, the shape of the RS profiles is almost identical for the two models as expected by mechanical equilibrium. The TMM model slightly underestimates tensile RS at mid-thickness compared to the TMG model. This difference is balanced at ca. 10 mm from the surface where the RS profile features a slight shoulder. This stress underestimation at mid-thickness comes from the lower yield strength at mid-thickness calculated by the TMM model compared to the one used in the TMG model as shown in *Figure 5-17*.

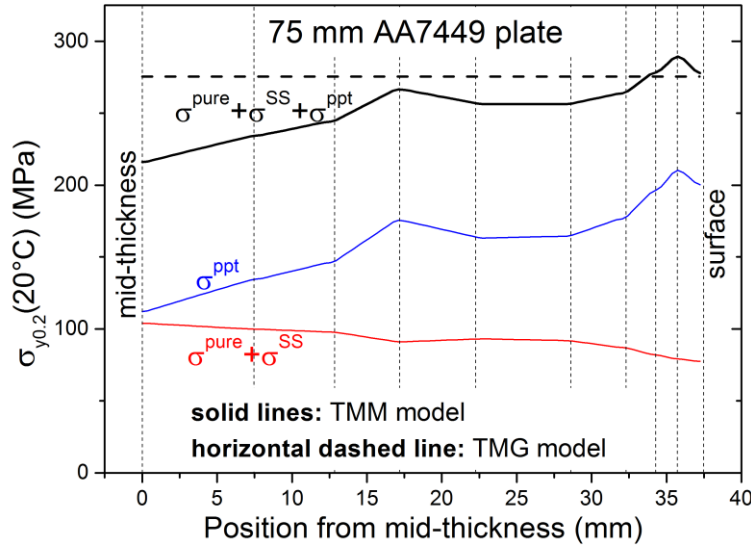


Figure 5-17 – Comparison between yield strength distributions at 20°C after cold-water quenching of a 75 mm thick 7449 plate calculated by the TMM model and used in the TMG model. Vertical lines: position at which $(\bar{r}^{cluster}, f_v^{cluster}, X_{Zn}, X_{Cu}, X_{Mg})$ are imposed and in-between which linear interpolation of these 5 fields is done.

In Figure 5-17, the yield strength at 0.2% used in the TMG model (calculated by adding $H(0.002)^n$ to σ_y given in Figure 4-25-a) is constant through the whole thickness since the same parameters (σ_y, H, n) are applied everywhere.

In the TMM model, the yield strength at 0.2% (calculated using Eq. 4-30) given in Figure 5-17 depends on position since the simulated average radius and volume fraction of clusters and matrix chemical composition are position dependent. As expected, the surface yield strength at 0.2% predicted by the TMM model is equal to that used in the TMG model. The yield strength at 0.2% predicted by the TMM model decreases from surface to mid-thickness (except close to surface and at quarter-thickness due to the imposed macrosegregation profile). This is due to the predicted contribution of precipitates to strengthening also shown in Figure 5-17. It should be noted that the evolution of the yield strength at 0.2% and its contributions predicted by the TMM model are not exactly linear in-between two vertical lines because linear interpolation in-between two vertical lines is performed on $(\bar{r}^{cluster}, f_v^{cluster}, X_{Zn}, X_{Cu}, X_{Mg})$ and not on the resulting yield strength.

It is interesting to realise that the two FE models with precipitation only differ from each other by the yield strength at 0.2% and not by strain hardening as shown in Figure 5-18-a and b.

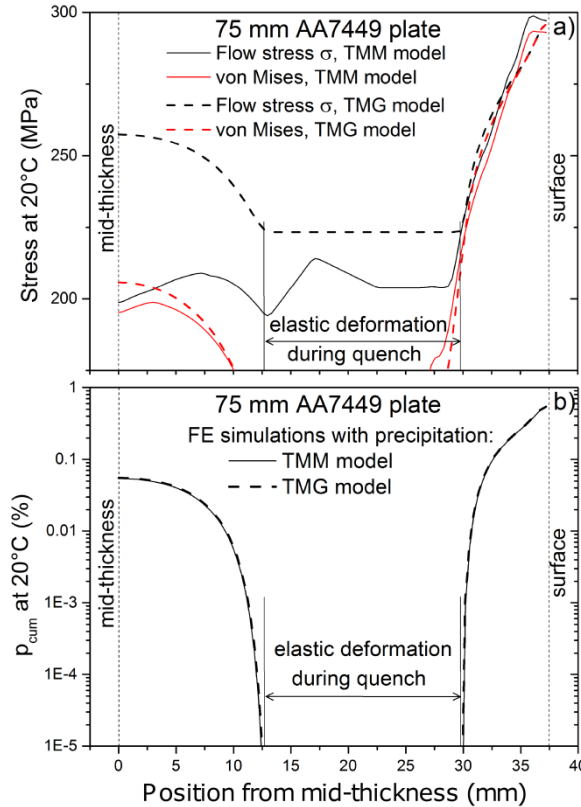


Figure 5-18 – Comparison between flow stress and von Mises stress profiles in 75 mm thick AA7449 plate calculated by the TMM and TMG models (a) and corresponding p_{cum} profiles using $T_{cum} = 325^{\circ}\text{C}$ (b).

Figure 5-18-a shows that at the end of quenching, the von Mises stress is strictly inferior to the flow stress through the whole thickness for the TMM model (solid lines). This means that deformation is elastic at the end of quenching, even at the surface. For the TMG model, however, the surface yields at the end of quenching as shown by the von Mises stress equal to the flow stress (dashed lines). Nevertheless, Figure 5-18-b shows that the equivalent inelastic deformation, p_{cum} predicted by the two models is identical. The RS profiles in 20 mm thick AA7449 plate calculated by the TMM and TMG models are given in Figure 5-19 together with RS measurements in TL direction.

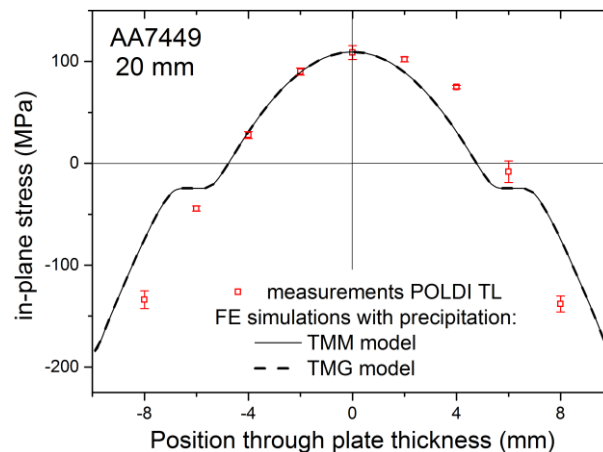


Figure 5-19 – Comparison between measured RS in 20 mm thick AA7449 plate and calculated ones by the TMM and TMG models. $T_{cum} = 325^{\circ}\text{C}$ for the FE simulations.

The two models with precipitation predict identical RS profiles in the as-quenched 20 mm thick AA7449 plate. This was to be expected due to the very low p_{cum} value during quenching as shown in *Figure 5-11*.

For the 20 mm and 75 mm thicknesses, the agreement between measurements and simulations with precipitation is excellent, thus validating both models.

5.3.3. Application of the TMM model to thicker AA7449 plates

Unlike the TMG model which is not purely predictive since it requires a few tensile tests for each alloy and plate thickness, the TMM model can be applied to any desired thickness, even those which are not industrially produced such as 140 mm for AA7449 plates. This is shown exemplarily in *Figure 5-20* where the as-quenched RS predicted with the TMM model for 75 mm and 140 mm thick AA7449 plates are compared.

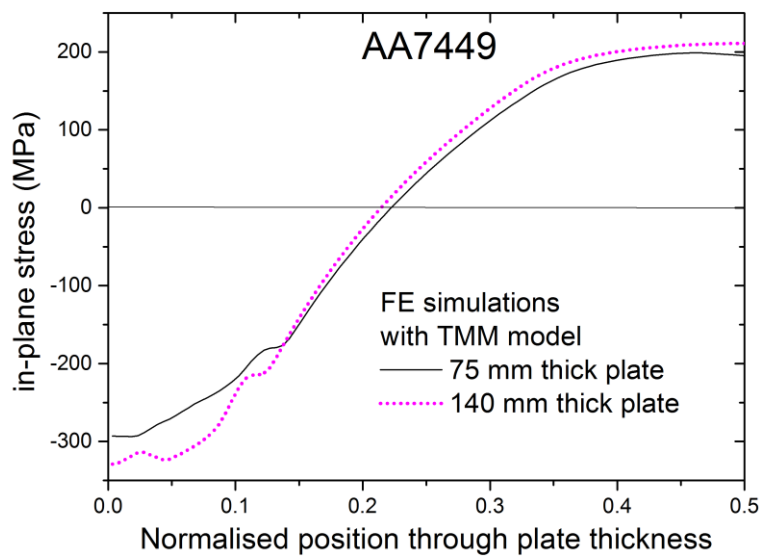


Figure 5-20 – Comparison between as-quenched RS in 70 mm and 140 mm thick AA7449 plates predicted by the TMM model using $T_{cum} = 325^{\circ}\text{C}$.

The as-quenched residual stresses predicted by the TMM model are higher in absolute value in the 140 mm thick AA7449 plate than in the 75 mm one. Indeed, due to longer cooling times, the simulated average precipitate radius and volume fraction of GP(I) zones are higher in the 140 mm thick AA7449 plate than in the 75 mm one. Here, it should be kept in mind that softening by precipitation of coarse precipitates during quenching is not considered. This simplification might result in slightly overestimated RS at mid-thickness of the 140 mm thick plate.

5.4. Summary of chapter 5

For cold-water quenched plates, finite element simulations of quenching showed that:

- In the as-quenched 20 mm thick AA7449 plate, the RS at mid-thickness predicted with or without precipitation taken into account compare well with the measurements. Indeed, the cooling of the 20 mm plate is so fast that precipitation hardening is limited. However, it is not negligible as revealed by the 50 MPa difference between simulations with and without precipitation at the surface.
- In plates thicker than 20 mm, precipitation has to be taken into account since the RS underestimation by the TM model increases with increasing thickness. Thus, as plate thickness increases, a model with precipitation becomes necessary to predict reasonably well the RS profile.

Two models were used to account for precipitation in heat treatable aluminium plates:

- A Thermo-Metallurgical-Mechanical model taking into account precipitation using a precipitation model in a one-way coupling temperature→precipitation→stresses (TMM model).
- A Thermo-Mechanical model taken into account precipitation in a simple-way using a few Gleeble interrupted quench-tests (TMG model),

In the TMM model, the yield strength is position dependent through the precipitation and yield strength models. In the TM and TMG models, the yield strength parameter is considered constant through the thickness and interpolated linearly as a function of temperature.

The TMG and TMM models predict identical RS profiles in the as-quenched 20 mm thick AA7449 plate. In the as-quenched 75 mm thick AA7449 plate, very little differences were found between the RS profiles predicted by these two models. For these two thicknesses, the agreement between measurements and simulations is excellent, thus validating both models.

For the TMG model, this shows the relevance of a model based on tensile tests after surface coolings similar to the industrial ones. Indeed, the TMG model provided also an excellent agreement between measurements and simulations in the as-quenched 75 mm and 140 mm thick AA7040 plates.

For the TMM model, this shows the quality of the calibration of the precipitation and yield strength models. Indeed, the calibration was done on SAXS coolings slightly different from surface coolings.

Compared to the TMM model, the TMG model:

- does not require a precipitation model. Therefore, the characterisation of precipitation kinetics to calibrate the precipitation model is not needed,
- decreases considerably the number of Gleeble tests,
- is easier to implement in a FE code especially for complex geometries,
- is less expensive in terms of computational time and memory.

However, the major drawback of the TMG model is that it is not fully predictive. Indeed, it requires a few tensile tests for each alloy and plate thickness. Therefore, the physically-based TMM model remains necessary for modelling complex parts with different thicknesses or plates with a full range of thicknesses without achieving specific Gleeble tests for each thickness.

The TMM model was applied to a thicker (140 mm) AA7449 plate for which no RS measurements are done since such thick AA7449 plates are not industrially produced yet. The predicted surface and mid-thickness as-quenched residual stresses are slightly higher in absolute value than those in the 75 mm AA7449 plate. This is consistent with the trend observed for AA7040 plates for which measurements in 75 mm and 140 mm plates were performed.

For boiling-water quenched AA2618 forgings, finite element simulations of quenching showed that:

- In the small AA2618 forging, the residual strains predicted without precipitation compare well with the measurements. Almost identical residual strains were predicted by a TMG model based on Gleeble interrupted quench-tests at 20 K/s, suggesting that the effect of precipitation is small for this forging.
- In the large AA2618 forging, the residual strains predicted without precipitation compare well with the measurements except in the region where tensile stresses are maximal. There, the simulation without precipitation underestimates residual strains. The agreement was improved using a TMG model based on Gleeble interrupted quench-tests at a cooling rate of 20 K/s, meaning that precipitation hardening during cooling has to be taken into account to predict reasonably well residual strains and stresses.

As mentioned for the plates, a TMG model is not fully predictive. For the forgings, a TMG model based on Gleeble interrupted quench-tests at 20 K/s was used. This means that the effect on RS of large precipitates forming during quenching was ignored since it was found in chapter 3 that the high critical cooling rate of *S* phase in AA2618 is ~17 K/s. For the investigated forgings, the relatively good agreement between the measurements and results of the TMG model based on Gleeble interrupted quench-tests at 20 K/s indicates that high temperature precipitation can indeed be neglected. However, this might not be the case for larger forgings with slower coolings. Further work is required to determine the forging size above which high temperature precipitation of *S* phase will significantly affect RS. This could be done by means of:

- a TMG model based on Gleeble interrupted quench-tests at low cooling rate (e.g. 2 K/s).
- a TMM model based on a precipitation model involving at least two phases *S* and *S'*. For this, the calibration at high temperature ($\geq 250^{\circ}\text{C}$) performed in section 3.4.2 should be completed at lower temperatures.

6. Conclusion and perspectives

6.1. Conclusion

The objective of this work was to develop a comprehensive model of quenching including precipitation effects for understanding the development of RS in thick heat treatable aluminium components, knowing their history.

Although the two industrial contexts share the same physical equations (heat and moment balance), they differ in many ways due to:

- different geometries. The simplifications for plates are not valid for forgings. Thus, while only one stress component was needed for large plates (rolling and transverse long directions were found to be equivalent), three stress components were required for forgings. This explains the higher stress uncertainties of neutron diffraction measurements (limitation) in forgings compared to the plates. The determination of the heat transfer coefficients was also more challenging in the forgings.
- different quenchant temperatures. 20°C water quenching of plates induces higher residual stresses than 100°C water quenching of forgings.
- different alloys. AA7449 is much more quench-sensitive than AA7040 and AA2618. This led to the use of specific methods to characterise precipitation. Furthermore, while the η precipitates can be considered as spherical, the S precipitates are not spherical (limitation for the precipitation model).

Due to these challenges, research efforts were mainly put on the experimental investigation by making use of the available techniques, namely:

- three different large scale neutron diffraction facilities for as-quenched residual stress measurements. This, together with a destructive technique gave confidence in the residual strains and stresses measurements.
- a Gleeble machine for *in situ* resistivity measurements and thermo-mechanical interrupted quench-tests.

Three models were developed in this work:

- a TM model (ignoring precipitation) using parameters identified for non-equilibrium solid solution of the three alloys,
- a TMM model where a yield strength model is coupled with a precipitation model,
- a TMG model that is a simple but realistic thermo-mechanical model including precipitation without precipitation model.

The pioneering characterisation of precipitation during cooling by *in situ* SAXS measurements performed by P. Schloth in the frame of this CCMX project was used to build a physically-based thermo-metallurgical-mechanical model (TMM model) using a precipitation model and a yield strength model. The calibration of the precipitation model

was performed by P. Schloth using an extensive characterisation work and this model was applied in the present work.

In order to provide reasonable residual stress predictions independently of the outcome of the work of P. Schloth, an alternative was proposed in this thesis. It does not require any precipitation model. The precipitation-dependent flow stress during quenching is determined *in situ* by Gleeble interrupted quench-tests performed after surface coolings representative of the industrial ones in thick components and is introduced into a thermo-mechanical model, the so-called TMG model.

For relatively thin products (20 mm thick plate and small forging), none of these models with precipitation is required since a thermo-metallurgical model ignoring precipitation gives residual stresses in excellent agreement with measurements. One can only note a limited hardening phenomenon at the surface of 20 mm thick plate which is predicted by TMG and TMM models and not by TM model, but which is difficult to confirm experimentally.

For thicker products, it was found that precipitation must be taken into account for reasonable residual stress predictions. The advantages and drawbacks of either model were discussed.

The TMM model gives an excellent agreement between measurements and simulations provided that the precipitation model is well calibrated. This physically-based model is necessary for modelling complex parts with different thicknesses. Nevertheless, a lot of effort has to be dedicated to the characterisation and modelling of the precipitation of metastable non-stoichiometric phases and GP zones during quenching. This tedious work is not needed for the TMG model which requires only a few interrupted quench-tests while giving an excellent agreement between measurements and simulations for all the investigated components. In particular, it is verified that the two models taking into account precipitation give identical residual stress profiles in thick AA7449 plates

For both industrial cases, the main finding of this work is that hardening precipitation by small precipitates increases as-quenched residual stresses in thick components.

Throughout this work, the Gleeble has proved to be an appropriate tool to achieve complex cooling paths in order to obtain desired metallurgical states and characterise the corresponding behaviour. The fundamental results obtained in this work and necessary for quenching simulations are:

- The yield strength at 0.2% strain offset of AA7449, AA7040 and AA2618 in non-equilibrium solid solution shows a plateau below ca. 250°C. The measured values – necessary for a TM model – have been used to adjust the solute strengthening parameters required for a TMM model coupled with a precipitation model.
- It has been checked that precipitation mainly affects yield strength for small strains as assumed in the models.

- The effect of plastic strain recovery at high temperature has been evidenced. For the three alloys, it has been found that inelastic deformation is not “remembered” above ca. 325°C, a required parameter for all the FE quenching simulations.
- It has been verified for AA7040 that the Bauschinger effect can be neglected in the case of RS generation during quenching.

6.2. Perspectives

From this work, the following scientific perspectives are drawn:

- Surface measurements by X-ray diffraction would improve the spatial resolution of residual stress measurements close to the surface in high compression.
- The precipitation model should be improved to account for non-spherical precipitates and quenched-induced vacancies (through a specific module).
- The exact chemical composition of clusters is needed to improve the predictions of the precipitation model.
- The original methodology used for the identification of the precipitation model parameters should be improved by comparing both the experimental and calculated radius and volume fraction of precipitates. Furthermore, it could be applied to non-isothermal experiments such as *in situ* SAXS coolings.

The blocked-jaw experiments (constrained cooling) could be used instead of the interrupted quench-tests to retrieve the thermo-mechanical behaviour with a few tests only. Nevertheless, this last hypothesis needs to be carefully checked.

From an industrial point of view, the following perspectives are suggested:

- Further work is required to determine the forging/plate size above which high temperature precipitation will significantly affect residual stresses.
- A sensibility analysis on the TMG model parameters should be performed to determine the temperature domains where thermo-mechanical properties need to be accurate.
- The quenching step could be optimised (choice of the quenchant and of the amount of pre-machining before heat treatment) to master residual stresses.
- The determination of heat transfer coefficients could be optimised (position and number of thermocouples) for more complex (pre-machined) geometries.
- The as-quenched residual stresses can be used to simulate further processing steps such as stretching, machining and in-service.

7. Appendixes

7.1. Properties of 2618, 7040 and 7449 alloys

The thermo-physical properties provided by the industrials are used for the simulations. The properties given by Constellium are calculated by the Prophase software [178] for a supersaturated solid solution. The properties given by ABB Turbo Systems come from internal measurements. The heat equation is solved using the thermal diffusivity given in *Figure 7-1*.

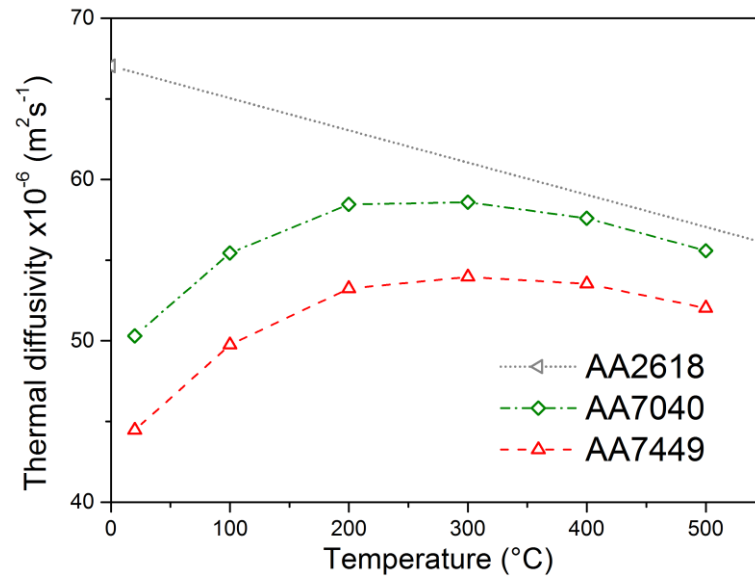


Figure 7-1 – Thermal diffusivity as a function of temperature for AA2618, AA7040 and AA7449.

The coefficients of thermal expansion (CTE) provided by the industrials are used to calculate thermal strains which are compared to those obtained using Gleeble measurements in *Figure 7-2*.

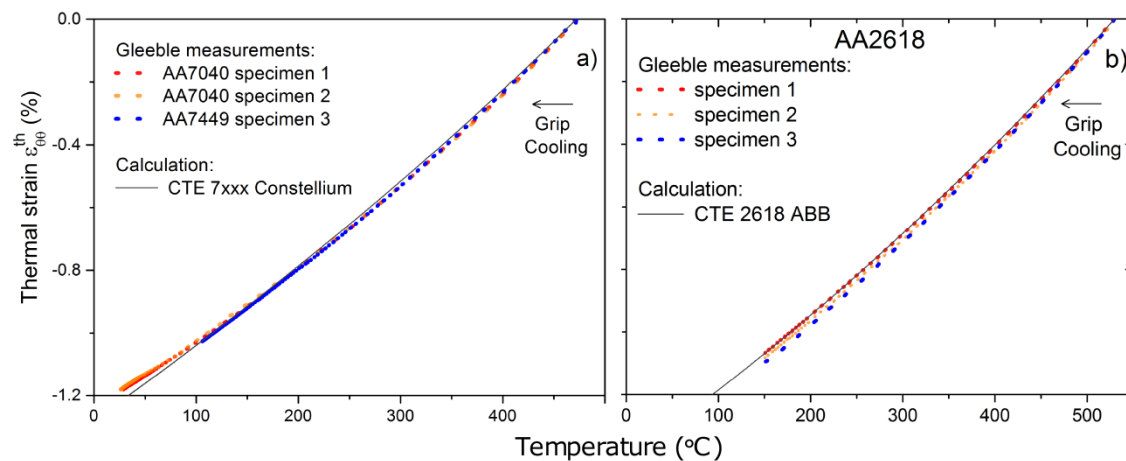


Figure 7-2 – Measured and calculated thermal strain evolution during grip cooling of 7xxx (a) and AA2618 (b) Gleeble specimens at zero force control.

In order to be close to reality (i.e. to represent the quench of a component), the Gleeble measurements consist in cooling the specimen by the grips from the SHT temperature at zero force control (free contraction). The hoop strains measured by the diametral extensometer compares very well with the calculations.

The evolution of the Young's modulus with temperature provided by the industrials is given in Figure 7-3 together with results of the literature.

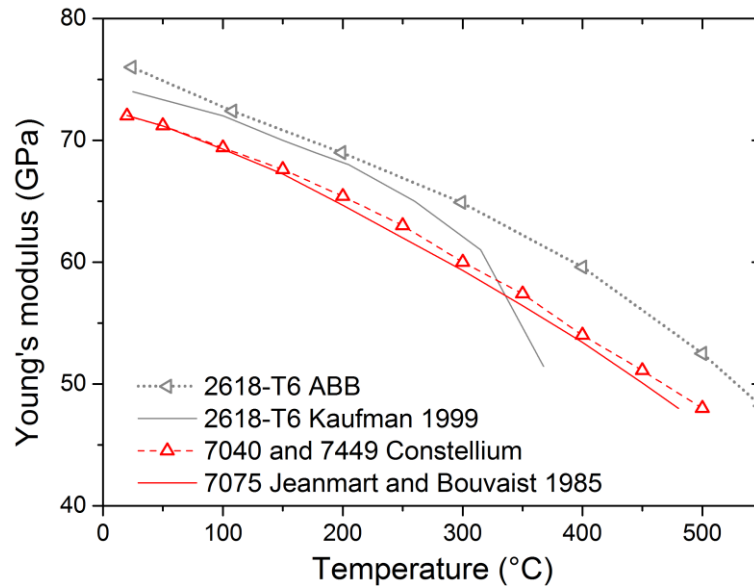


Figure 7-3 – Young's modulus versus temperature for AA2618 in T6 state and for three 7xxx alloys.

The Young's modulus used for AA7040 and AA7449 is close to that of AA7075 determined by Jeanmart and Bouvaist [3] using vibration tests. The Young's modulus used for AA2618 (dynamic modulus) is slightly higher than the one found in the literature below 300°C. At higher temperatures, the values by Kaufman (static modulus) are much lower than the values provided by ABB Turbo Systems due to the different measurement method (static versus dynamic).

7.2. Choice of NGV for RS measurements by ND

Selected diffraction peaks recorded at SALSA are given in *Figure 7-4* and *Figure 7-5* in order to understand the differences in the errors bars representing the statistical uncertainty on peak position.

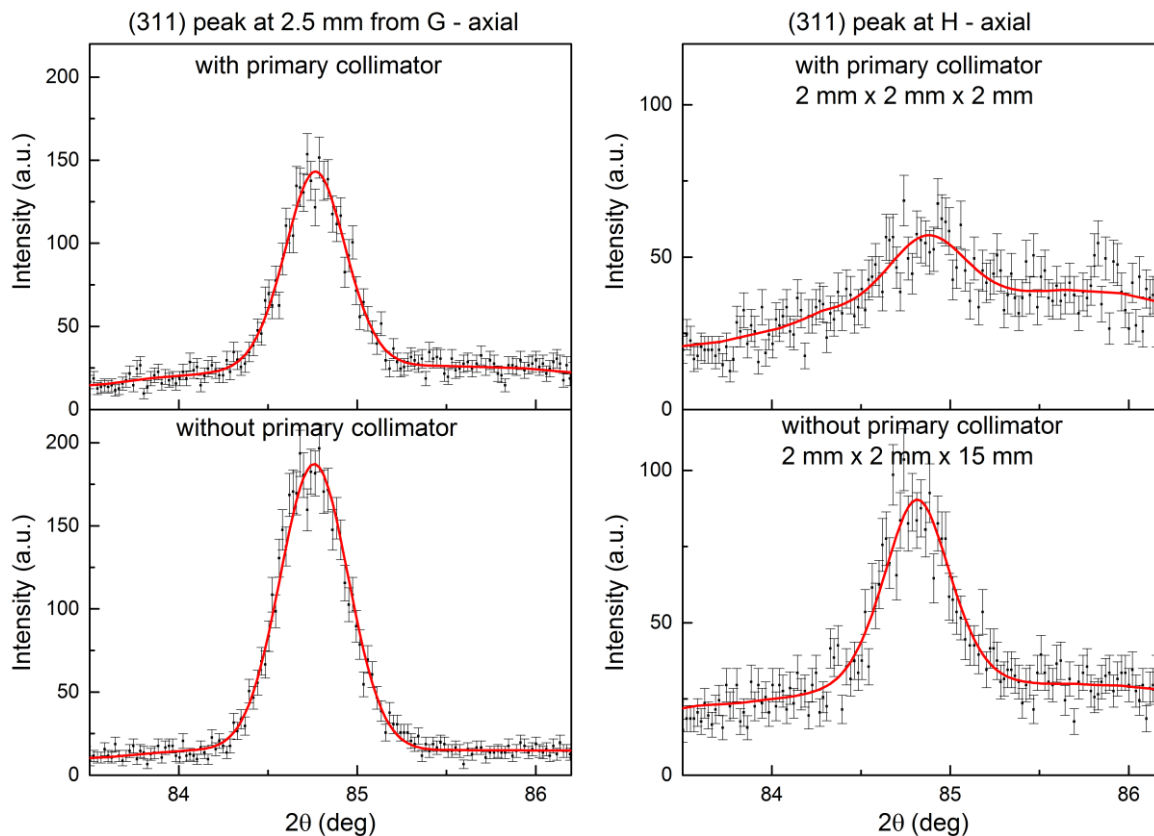


Figure 7-4 - Diffraction peaks at SALSA in axial configuration at 2.5mm from G (left) and at H (right) with (top) and without (bottom) primary collimator. Solid lines are fits using pseudo-Voigt function with quadratic baseline.

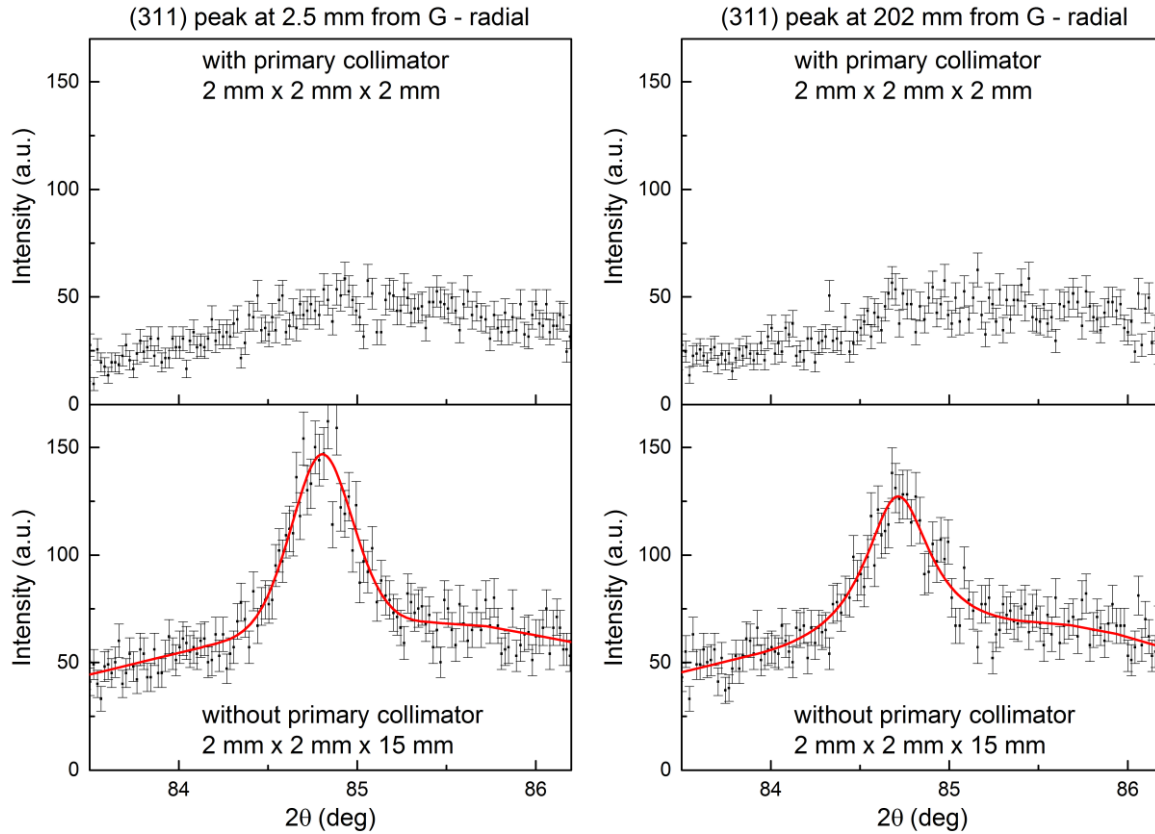


Figure 7-5 - Diffraction peaks in radial configuration at 2.5mm from G (left) and at 202 mm from G (right) with (top) and without (bottom) primary collimator.

These diffraction peaks show that the signal-to-noise ratio is lower with a primary collimator than without. Indeed, the primary collimator improves the gauge volume definition but at the cost of the measurement statistics. Hence, without primary collimator, the quality of the peak fit is better especially for long beam paths with high attenuation (e.g. peak at H in). As expected by geometrical considerationsⁱ, the signal-to-noise ratio is lower in the radial configuration than in the axial one, especially with a primary collimator where the (311) peak cannot be distinguished from the background. Thus, it is necessary to work without primary collimator in the radial configuration, as chosen in the final experimental setup.

ⁱ In the radial configuration, the beam path is longer than in the axial configuration.

7.3. Principle of parameter identification by SiDoLo

Model formulation with additive hardening and ageing variables

An elasto-viscoplastic constitutive model with additive hardening (Chaboche-type model) is chosen. This model slightly differs from its original form by the definition of the accumulated plastic strain and by the use of two additional internal variables for ageing. The equations are given in *Table 7-1*.

Uniaxial tensile tests (SiDoLo fits of Gleeble measurements)	Tridimensional loads (Abaqus calculations)	
$\varepsilon = \varepsilon^e + \varepsilon^{in}$	$\underline{\varepsilon} = \underline{\varepsilon}^e + \underline{\varepsilon}^{in}$	Eq. 7-1
$\sigma = E\varepsilon^e$	$\underline{\sigma} = \lambda_e \text{Tr}(\underline{\varepsilon}^e) \underline{I} + 2\mu_e \underline{\varepsilon}^e$	Eq. 7-2
$f = \sigma - X - (\sigma_y + R)$	$f = \sqrt{3/2 (\underline{s} - \underline{X}) : (\underline{s} - \underline{X})} - (\sigma_y + R)$ $\Leftrightarrow f = J(\underline{\sigma} - \underline{X}) - \sigma_y - R$	Eq. 7-3
$R = H.(p_{cum})^n$ with $p_{cum} = \begin{cases} \int \dot{p} \, dt & \text{when } T < T_{cum} \\ 0 & \text{when } T > T_{cum} \end{cases}$		Eq. 7-4
$\dot{p} = \dot{\varepsilon}^{in} $	$\dot{p} = \sqrt{\frac{2}{3} \dot{\underline{\varepsilon}}^{in} : \dot{\underline{\varepsilon}}^{in}}$	Eq. 7-5
$\dot{\varepsilon}^{in} = \left\langle \frac{f}{K} \right\rangle^{1/m} \text{sign}(\sigma - X)$	$\dot{\underline{\varepsilon}}^{in} = \left\langle \frac{f(\underline{\sigma})}{K} \right\rangle^{1/m} \frac{\partial f}{\partial \underline{\sigma}}$	Eq. 7-6
$\sigma_y = \sigma_0 + \sigma_{hard} a_{hard} - \sigma_{soft} a_{soft}$ with $\sigma_{hard} > 0$ and $\sigma_{soft} > 0$		Eq. 7-7
$\dot{a}_{hard} = \frac{a_{hard,\infty} - a_{hard}}{\tau_{hard}}$ with $a_{hard}(t_{hard,0}) = a_{hard,0}$ $\dot{a}_{soft} = \frac{a_{soft,\infty} - a_{soft}}{\tau_{soft}}$ with $a_{soft}(t_{soft,0}) = a_{soft,0}$		Eq. 7-8

Table 7-1 – Equations of the model used for uniaxial tensile tests and tridimensional loads.

In a small deformation framework, Eq. 7-1 assumes that the total strain ε is partitioned into an elastic ε^e part and an inelastic ε^{in} part. The elastic part of the strain is related to the stress σ by Hooke's law (Eq. 7-2). Stress and strain are tensors in the 3D case.

The model is characterised by a yield function f , which depends on the stress, the yield strength σ_y and the hardening variables R and X . The onset of plasticity is governed by the scalar yield condition $f = 0$. In 3D, the kinematic hardening variable X becomes a deviatoric tensor. The expression given in Eq. 7-3-right corresponds to the von Mises criterion, where \underline{s} is the deviatoric stress tensor (obtained by removing the hydrostatic pressure from the stress tensor) and J is calculated from the second invariant J_2 to be homogeneous to a stress. In the expression of f , the deviatoric stress tensor is chosen

instead of the stress tensor since plastic flow is generally observed to be independent of hydrostatic pressure for metals.

The scalar R is the isotropic hardening variable which corresponds to the size of the elastic domain. It is related to the accumulated inelastic strain, p_{cum} , for instance by the power law given in Eq. 7-4 (Ramberg-Osgood's model with two material parameters, H and n). The rate of p being defined by the absolute value of the inelastic strain-rate (Eq. 7-5-left), \dot{p} and $\dot{\varepsilon}^{in}$ are identical for monotonic loads. In our model, the parameter T is used to take into account the fact that high temperature strain has no influence on later low temperature mechanical behaviour. Above T_{cum} , the equivalent inelastic strain has no influence on the flow strength. Below T_{cum} , the equivalent inelastic strain has a full effect on the flow strength.

The inelastic (viscoplastic) strain-rate, $\dot{\varepsilon}^{in}$, is defined using a Norton-type law with two viscosity parameters, K and m (Eq. 7-6).

Eventually, the yield strength is defined as the sum of a threshold stress, σ_0 (yield strength without precipitates) and two contributions of precipitates which either increase or decrease the yield strength with time as shown in Eq. 7-7.

In this work, kinematic hardening is neglected, thus, we have: $X = 0$. As a result, an uniaxial load at constant temperature is fully defined by:

$$\begin{aligned}\varepsilon &= \varepsilon^e + \varepsilon^{in} \\ \varepsilon^e &= \sigma / E \\ \sigma &= \sigma_y + H \cdot (p_{cum})^n + K \cdot (\dot{p})^m\end{aligned}\tag{Eq. 7-9}$$

with:

$$\begin{aligned}\sigma_y &= \sigma_0 + \sigma_{hard} a_{hard} - \sigma_{soft} a_{soft} \\ a_{hard}(t) &= a_{hard,\infty} - (a_{hard,\infty} - a_{hard,0}) \exp(-(t - t_{hard,0}) / \tau_{hard}) \text{ with } t \geq t_0 \\ a_{soft}(t) &= a_{soft,\infty} - (a_{soft,\infty} - a_{soft,0}) \exp(-(t - t_{soft,0}) / \tau_{soft}) \text{ with } t \geq t_0\end{aligned}\tag{Eq. 7-10}$$

Identification procedure using SiDoLo

For a given temperature, the identification problem consists in determining the set of model parameters \underline{A} which minimises the objective function:

$$G(\underline{A}) = \sum_{i=1}^{n_t} G_i(\underline{A}) \text{ with } G_i(\underline{A}) = \frac{1}{M_i} \sum_{j=1}^{M_i} \left(\frac{\sigma_{i,j}^{sim} - \sigma_{i,j}^{exp}}{\hat{\sigma}_{i,j}} \right)^2\tag{Eq. 7-11}$$

where n_t is the number of tests at the given temperature, M_i is the number of measurement points of the i^{th} test, σ is the tensile axial stress calculated using Eq. 4-20 and $\hat{\sigma}$ the error associated with the stress measurement. The superscripts *sim* and *exp* indicate the simulation and experimental data respectively. The model defined by Eq. 7-9 and Eq. 7-10 involves ten material parameters to identify by inverse method:

$$\underline{A} = \{E, \sigma_0, H, n, K, m, \sigma_{hard}, \tau_{hard}, \sigma_{soft}, \tau_{soft}\} \quad \text{Eq. 7-12}$$

For each one of the n_t tests at the given temperature, the SiDoLo software [170] simulates the ε_{zz} -time experimental load and calculates the stresses $\sigma_{i,j}^{sim}$ corresponding to the current set of model parameters. Therefore, the observable (measurable) variables introduced in SiDoLo are:

$$\underline{Z}^{exp} = \{t, \varepsilon_{zz}, \sigma_{zz}^{exp}\} \quad \text{Eq. 7-13}$$

The variables to integrate (numerical integration by Runge-Kutta methods with adaptative stepsize control) are:

$$\underline{Y} = \{\varepsilon^{vp}, p_{cum}, a_{hard}, a_{soft}\} \quad \text{Eq. 7-14}$$

A differential model is used for which $Z(t)$ requires the resolution of a system of two first order differential equations:

$$\begin{cases} \dot{\underline{Y}} = \underline{F}(\underline{Z}^{exp}, \underline{Y}; \underline{A}) \text{ with } \underline{Y}(t_0) = \underline{Y}_0 \\ \underline{Z} = \underline{G}(\underline{Y}; \underline{A}) \end{cases} \quad \text{Eq. 7-15}$$

The non-linear optimisation problem is solved by SiDoLo using an algorithm combining two gradient-based methods: a steepest descent method at the initial stages of the optimisation followed by the Levenberg-Marquardt method to accelerate convergence. This optimisation algorithm is widely used but may be stuck into a local minimum [159]. Since the evolution law of the material parameters with temperature is *a priori* unknown, the identification is performed independently at each temperature using several tensile tests. This identification is not unique due to the large number of parameters. Therefore, it is checked that the evolution of the parameters with temperature is not chaotic. If this is the case, the constraints (lower and upper bounds) are changed to avoid unexpected solutions. In the FE simulations, the Young's modulus provided by the industrials is used instead of the one identified on the elastic part of the Gleeble stress-strain curves which is not determined accurately enough.

7.4. Gleeble specimen geometries

Choice of geometries

Two different specimen geometries are used for Gleeble tests as shown in *Figure 7-6*.

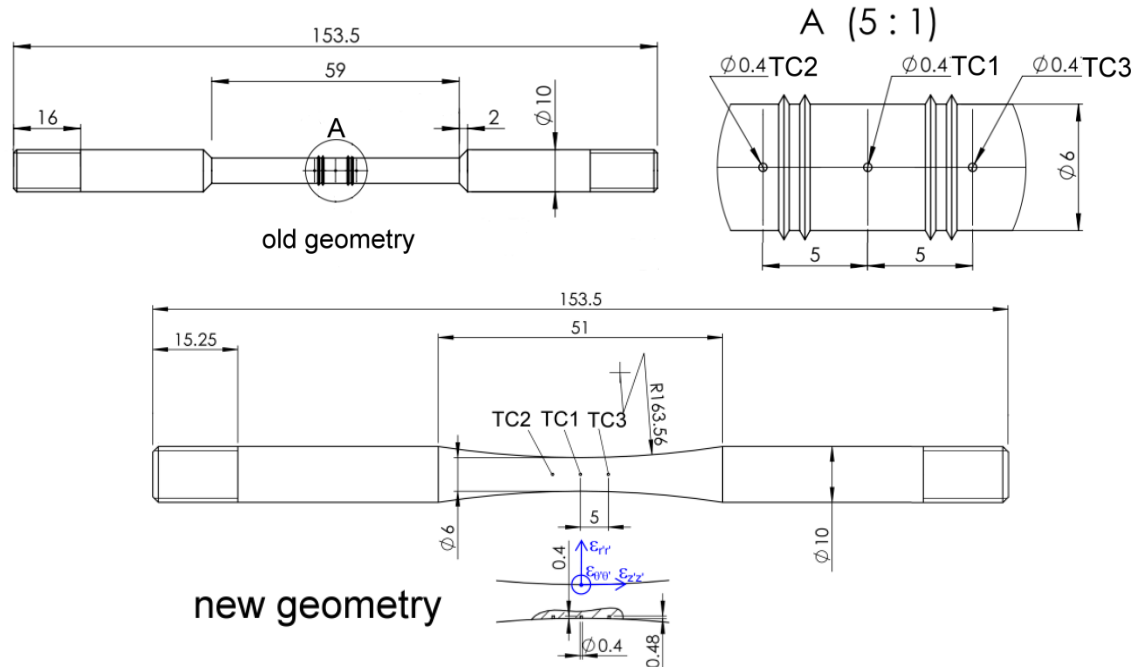


Figure 7-6 – Specimen geometries used for tensile tests in the Gleeble machine (dimensions in millimeters).

Specimens are equipped with three type-K thermocouples fixed to the specimen surface and protected by alumina tubes. Due to the inherent axial thermal gradient, temperature is maximal at specimen mid-span (i.e. at position of TC1). Therefore, ignoring possible precipitation, yield strength is minimal at the specimen mid-span where strains and stresses are localised. If precipitates form in the specimen, yield strength is still minimal at the specimen mid-span provided that precipitation hardens or softens the material uniformly. However, it can happen that precipitation softens more the material outside the gauge length than at the mid-span. This can lead to stress localisation outside the gauge length, especially for the “old geometry” which was used first – as its name suggests – until this undesirable case was encountered. This “old geometry”, initially designed for axial strain measurementsⁱ, was found to be inadequate at intermediate temperatures (100-350°C) due to deformation out of the gauge length attributed to the formation of coarse precipitates during solutionising in the Gleeble. The “new geometry” is thus used at intermediate temperatures to overcome this issue: the reduced diameter ensures strain localisation at the specimen mid-span.

ⁱ The grooves on each side of TC1 for the “old geometry” were designed for an axial extensometer which turned out to underestimate strains compared to a radial extensometer due to the axial thermal gradient.

Stresses and strains in Gleeble specimen geometries

A diametral extensometer is used for the two specimen geometries tested in the Gleeble. It is placed at the specimen mid-span where the cross section is minimal as shown in *Figure 7-7-c*. According to the small deformation theory, the radial, ε_{rr} , hoop, $\varepsilon_{\theta\theta}$, and axial, ε_{zz} , strains in cylindrical coordinates write:

$$\varepsilon_{rr}(r) = \frac{\partial U_r}{\partial r}, \quad \varepsilon_{\theta\theta}(r) = \frac{U_r}{r} \quad \text{and} \quad \varepsilon_{zz}(z) = \frac{\partial U_z}{\partial z} \quad \text{with} \quad \underline{U}(\mathbf{P}) = U_r(r) \cdot \underline{e}_r + U_z(z) \cdot \underline{e}_z \quad \text{Eq. 7-16}$$

where $\underline{U}(\mathbf{P})$ is the displacement field at point $\mathbf{P}(r, z)$. For an isotropic material of radius R_{cyl} , the diametral extensometer measures the ratio $\Delta R_{cyl}/R_{cyl}$, where ΔR_{cyl} is the radial displacement at the specimen surface. Replacing r by R_{cyl} in the expression of $\varepsilon_{\theta\theta}$ in Eq. 7-16 gives:

$$\varepsilon_{\theta\theta}(R_{cyl}) = \frac{\Delta R_{cyl}}{R_{cyl}} \quad \text{Eq. 7-17}$$

Eq. 7-17 means that the diametral extensometer measures the hoop strain component at the specimen surface ($r = R_{cyl}$). If deformation is homogeneous in the measured cross section, the diametral extensometer also measures the radial strain component:

$$U_r(r) = A \cdot r \quad \text{with} \quad A = cst \Rightarrow \varepsilon_{rr} = \varepsilon_{\theta\theta} = A = \varepsilon_{\theta\theta}(R_{cyl}) \quad \text{Eq. 7-18}$$

At constant temperature where thermal strain equals zero, the total deformation ε is the sum of the elastic ε^e and inelastic ε^{in} deformations:

$$\varepsilon = \varepsilon^e + \varepsilon^{in} \quad \text{Eq. 7-19}$$

Using Hooke's law ($\sigma_{zz} = E\varepsilon_{zz}^e = -E\varepsilon_{\theta\theta}^e / \nu$) and assuming incompressibility of plastic deformation ($\varepsilon_{\theta\theta}^{in} = -\frac{1}{2} \varepsilon_{zz}^{in}$), one has:

$$\varepsilon_{zz}^{in} = -2(\varepsilon_{\theta\theta} + \nu \cdot \sigma_{zz} / E) \quad \text{Eq. 7-20}$$

Hence, hoop strains measured by the diametral extensometer are transformed to axial strains using:

$$\varepsilon_{zz} = \frac{1-2\nu}{E} \sigma_{zz} - 2\varepsilon_{\theta\theta} \quad \text{Eq. 7-21}$$

Eq. 7-21, which assumes uniform temperature in the central cross section, is valid for a tensile test at constant temperature as performed experimentally.

In order to compare the stress and strain fields in both specimen geometries, the tensile test at 20°C of AA7040 specimens is simulated using an axisymmetric mechanical model implemented in the commercial FE code ABAQUS 6.10. Due to symmetry, only one-half of the specimens is modelled. The material properties of AA7040 at 20°C after water quench in the Gleeble are considered uniform in the simulation. The same displacement velocity is imposed at the specimen end for both geometries as shown in *Figure 7-7*.

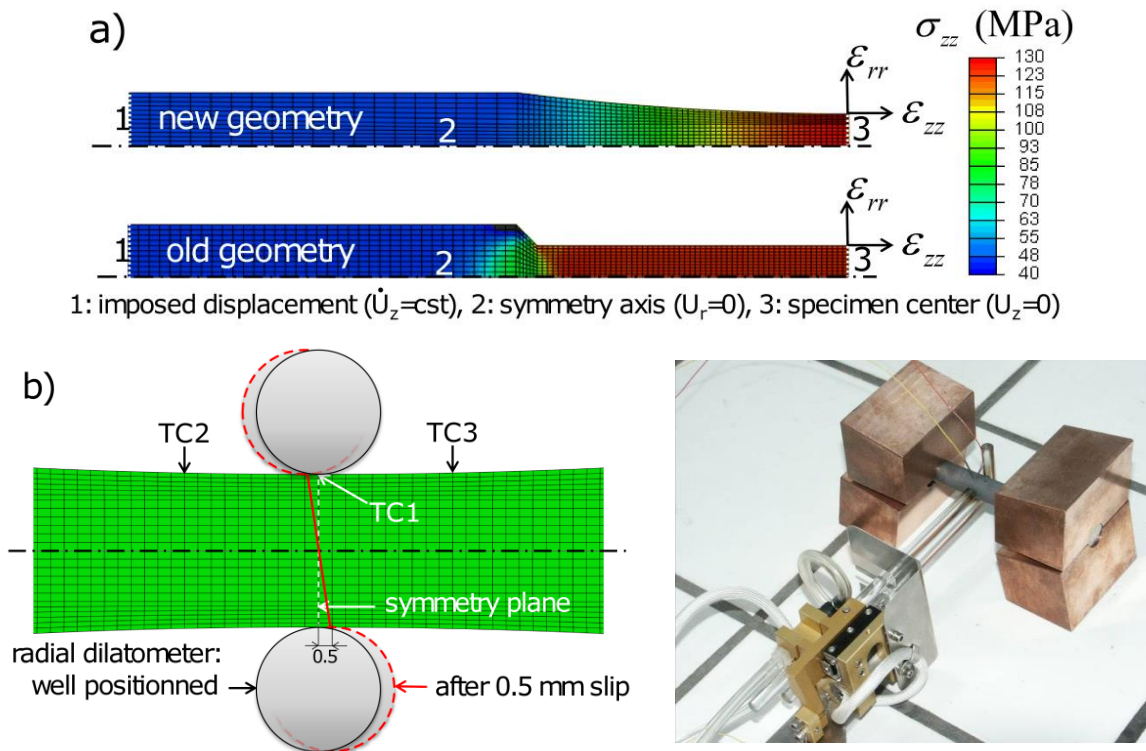
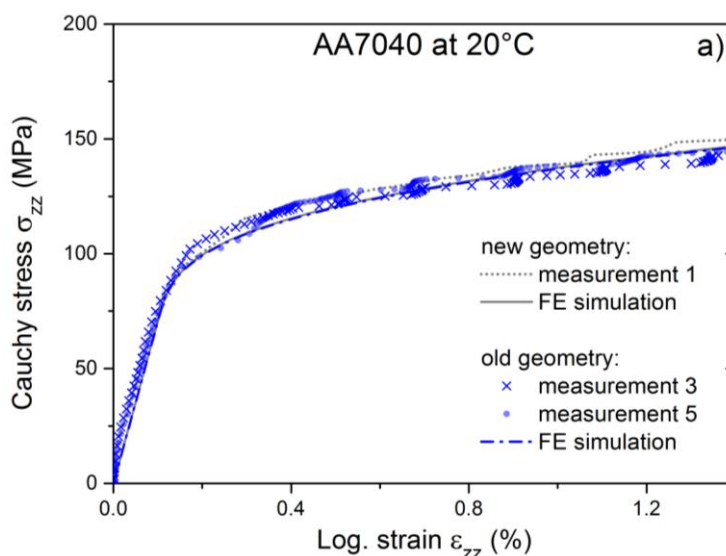


Figure 7-7 – FE simulation of tensile test at 20°C for the two specimen geometries (a); schematic of the diametral extensometer position at the specimen mid-span (b) and picture of diametral extensometer (c).

As expected by the different geometries, the axial stress calculated in the “new geometry” is localised at the specimen mid-span, which is not the case in the “old geometry”. The simulated stress-strain curves are identical for both geometries as shown in Figure 7-8-a. The Gleeble measurements used for the parameter identification of AA7040 at 20°C are also shown in this figure. The fact that the stress-strain curves are superimposed means that both geometries can be used to determine the mechanical behaviour of AA7040 in neSS at 20°C.



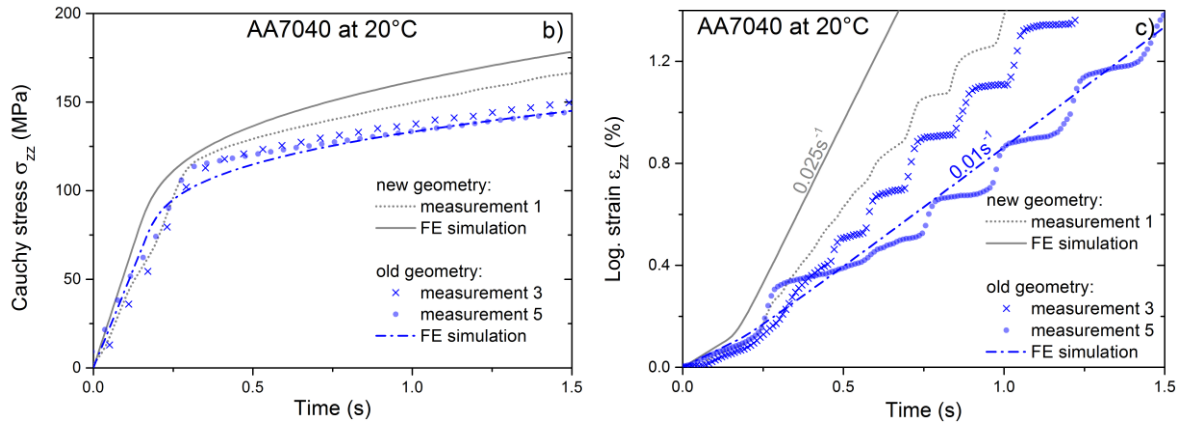


Figure 7-8 – Simulated and measured stresses and strains during tensile test at 20°C performed immediately after water quench in the Gleeble for AA7040. ϵ_{zz} is calculated from $\epsilon_{\theta\theta}$ using Eq. 7-21.

Figure 7-8-b shows that the measured stress-time curve of the “new geometry” is higher than that of the “old geometry”. This is confirmed by the simulation and is explained by stress localisation at the mid-span of the “new geometry” specimen. This also explains the higher strains at position of TC1 in the new geometry compared to the old one. Figure 7-8-c shows that, for a given geometry, the measured ϵ_{zz} – time curves deviate from each other. The possible reasons for this deviation are:

- the difficulty to place the extensometer perpendicularly to the specimen,
- the possible extensometer slip (especially with air or water quench),
- the relatively short gauge length where temperature is uniform (especially at high temperature),
- the possible localisation of deformation outside the gauge length (especially at intermediate temperatures for the old geometry).

Figure 7-7-b shows that if the diametral extensometer slips, the specimen diameter is overestimated and the strains are hence underestimated. The effect of poor extensometer positioning on strain can be quantified by the simulation as shown in Figure 7-9.

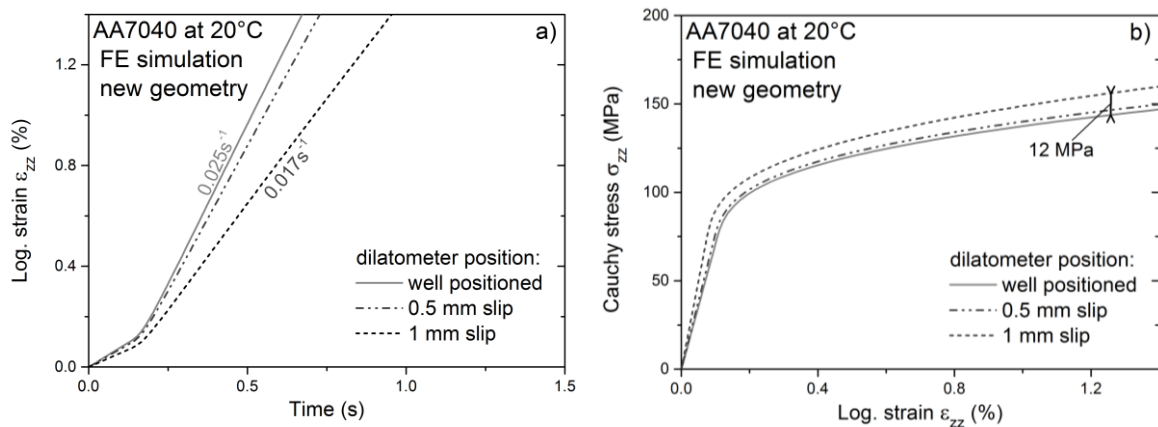
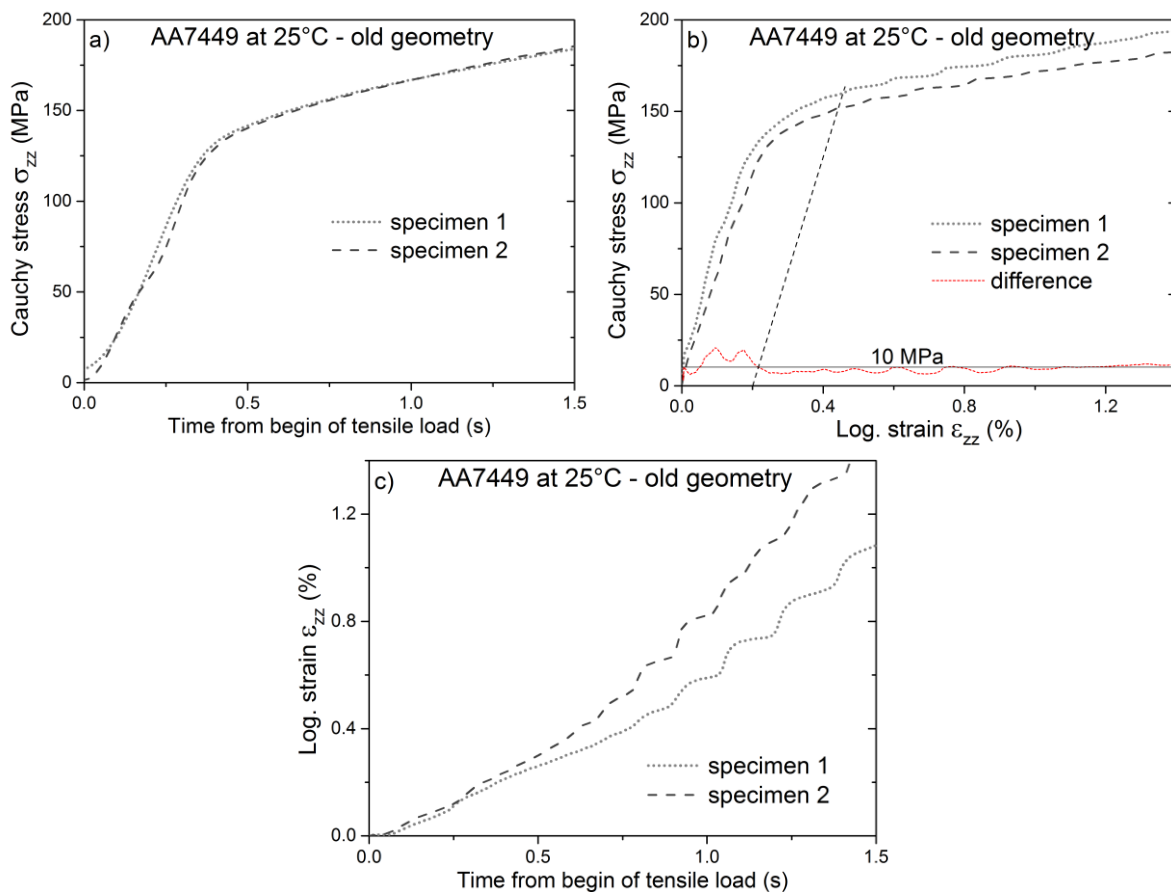


Figure 7-9 – Effect of poor diametral extensometer positioning on strain (a) and stress-strain curve (b) simulated for the new geometry specimen at 20°C.

While a 0.5 mm slip of the diametral extensometer as shown schematically in *Figure 7-7-b* has almost no effect on the strain and stress-strain curve, a 1 mm slip leads to significant lower strains (*Figure 7-9-a*) resulting in a stress-strain curve ca. 12 MPa higher than without extensometer slip (*Figure 7-9-b*). Although it is experimentally possible to detect an extensometer slip by a discontinuity in the signal, it is difficult to quantify the amount of slip. Therefore, several tests are duplicated (same programming) in order to estimate the error on the stress-strain curve due the statistical uncertainty on strain.

Experimental uncertainty on stresses and strains

In order to determine the statistical uncertainty on the measured stresses and strains, old and new geometry specimens from identical sampling were subjected to the same thermo-mechanical load for the three alloys. The imposed thermo-mechanical load consists in a water quench in the Gleeble immediately followed by a tensile load (jaw displacement of 1.1 mm in 2 seconds) at low temperature ($\leq 35^\circ\text{C}$). The results are given in *Figure 7-10* for the three alloys.



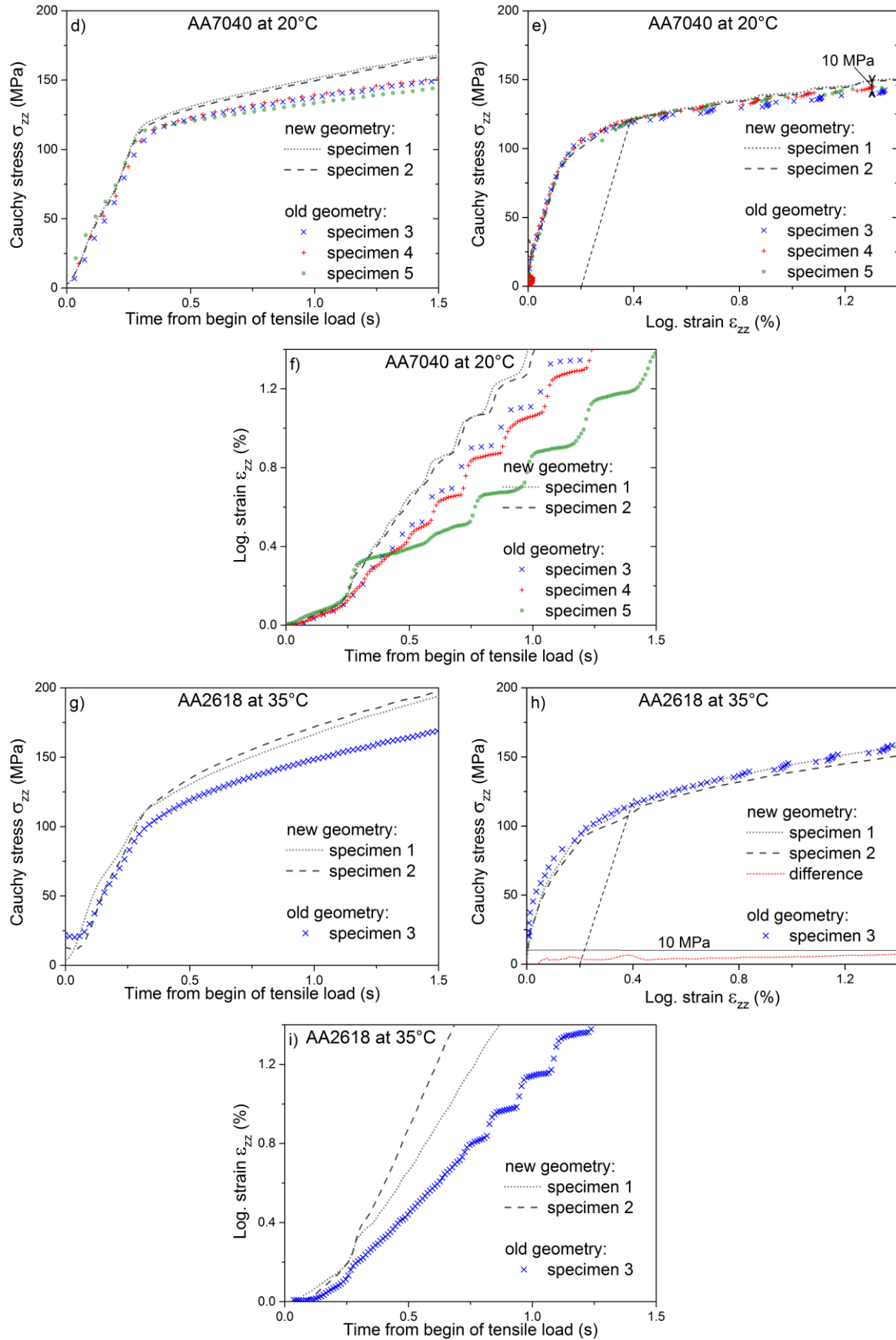
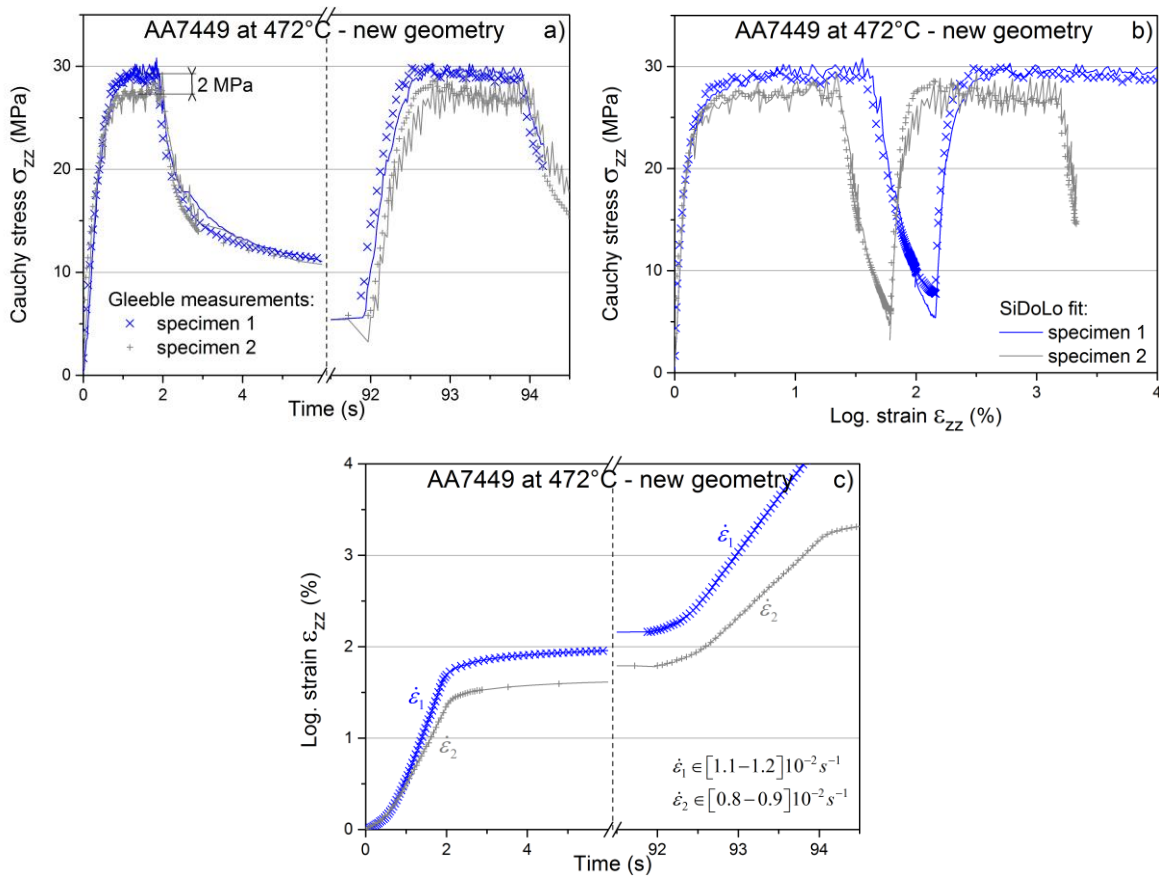


Figure 7-10 – Measured stresses and strains during tensile tests performed immediately after water quench in the Gleeble for AA7449 (a, b, c), AA7040 (d, e, f) and AA2618 (g, h, i).

In each alloy, for a given specimen geometry, the $\sigma_{zz} - time$ curves are almost superimposed as shown in (a), (d) and (g). This means that the stress uncertaintyⁱ is low and can be neglected.

Nevertheless, although strain-rate sensitivity is negligible at room temperature, the $\sigma_{zz} - \varepsilon_{zz}$ curves, are not exactly superimposed as shown in (b), (e) and (h). This is due to the fact that the $\varepsilon_{zz} - time$ curvesⁱⁱ deviate from each other as shown in (c), (f) and (i). This deviation begins after ca. 0.2% deformation, i.e. after the elastic deformation, and increases with increasing strain. This is a source of uncertainty on the $\sigma_{zz} - \varepsilon_{zz}$ curves. This effect is relatively low (e.g. < 10 MPa at ca. 150 MPa, i.e. < 7% in *Figure 7-10-e*). Hence, an error of ± 5 MPa on the stress-strain curves is attributed at low temperature for the three alloys due to the statistical uncertainty on strain.

A similar analysis for AA7449 and AA7040 at high temperature is partially shown in *Figure 7-11* where the SiDoLo fits (solid lines) are superimposed to the measurements (symbols) in order to decouple the effects of strain-rate and possible softening on flow stress.



ⁱ Due to uncertainty on the force measured by the load cell (100 kN with a class of accuracy of 0.02)

ⁱⁱ The strain jumps observed only at low temperature are attributed to Portevin – Le Chatelier effect, associated with an interaction between mobile dislocations and solute atoms called dynamic ageing, observable by oscillations on the stress-strain curves.

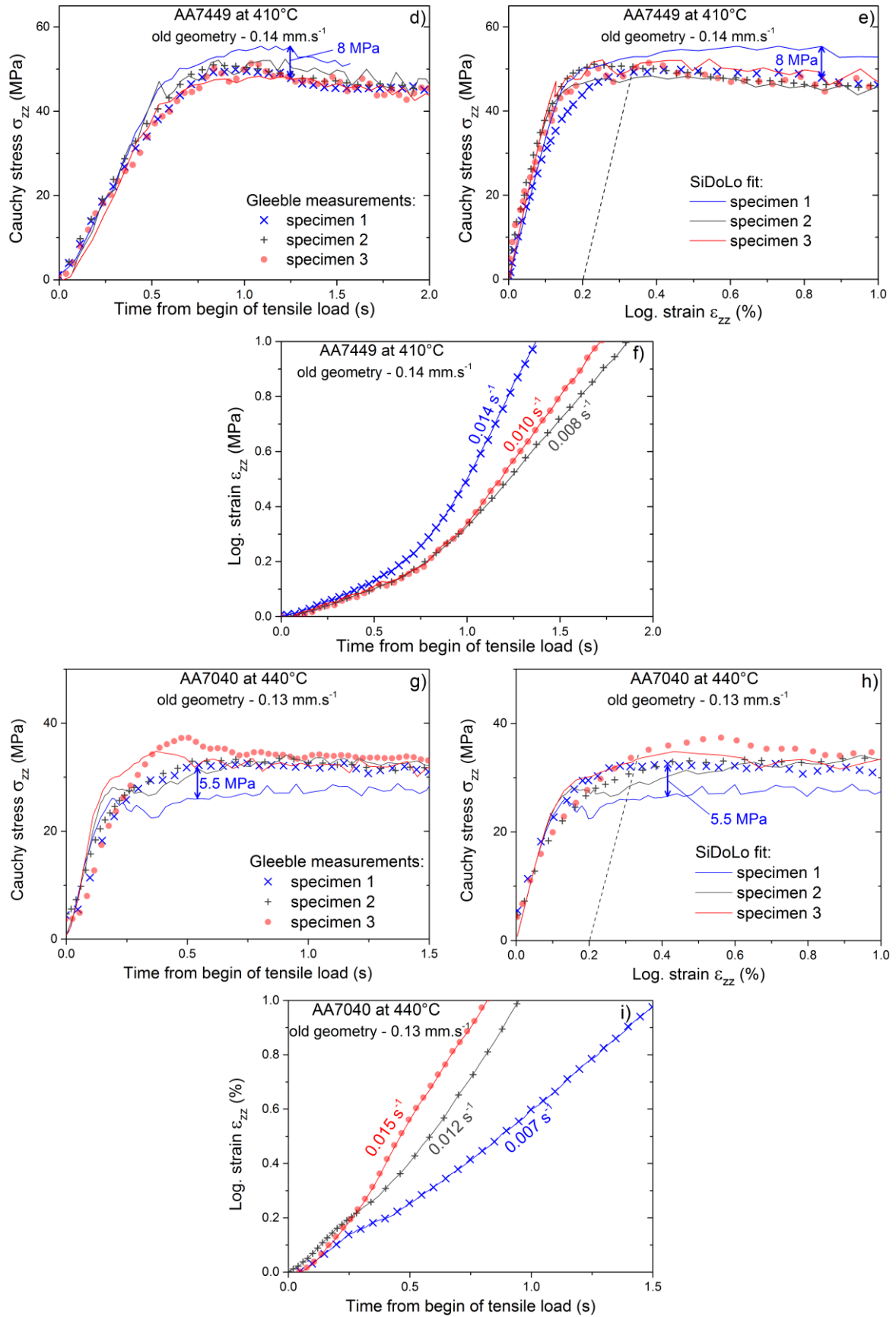


Figure 7-11 – Measured and fitted stresses and strains during tensile tests performed in the Gleeble for AA7449 at 472°C (a, b, c) and 410°C (d, e, f) and for AA7040 at 440°C (g, h, i).

At high temperature where strain hardening is low, the uncertainty on strain leads to a horizontal shift of the $\sigma_{zz} - \varepsilon_{zz}$ curve as shown in *Figure 7-11-b* for AA7449 at 472°C. The different stress plateaux are explained by the different flow stresses (*Figure 7-11-a*) due to the slightly different strain-rates (*Figure 7-11-c*) together with the high strain-rate sensitivity of AA7449 at the SHT temperature. The fit using SiDoLo (explained in appendix 7.3), which simulates the $\varepsilon_{zz} - \text{time}$ curve, is excellent for both specimens. This means that the error on stress-strain curve at 472°C for AA7449 due to the statistical uncertainty on strain and strain-rate is negligible.

For AA7449 at 410°C and AA7040 at 440°C, strain measurements are less reproducible with experimental strain-rates differing from up to a factor 2 for a given mechanical load. *Figure 7-11-e* and *h* show that the strain-rate effect on stress-strain curves is not logical as revealed by the SiDoLo fit which over or underestimates the measured stress. In these two cases, the high uncertainties on experimental strains lead to errors on the stress-strain curves of ca. ± 4 MPa.

A similar analysis was performed for the three alloys at the different testing temperatures. The analysis was restricted to low strain values encountered during quenching. The results are summarised in *Table 7-2*.

Temperature (°C)	AA7449	AA7040	AA2618
≤ 35 after WQ	± 5 MPa	± 5 MPa	± 5 MPa
100 after AQ	± 2.5 MPa	± 3.5 MPa	–
150 after AQ or GC	± 7.5 MPa	± 5 MPa	± 3 MPa
250-265 after AQ	± 2 MPa	± 6 MPa	–
325 after AQ	–	± 2.5 MPa	–
350 after AQ	± 8 MPa	–	–
410-440 after AQ or GC	± 4 MPa	± 4 MPa	± 4 MPa

Table 7-2 – Maximal errors on Gleeble stress-strain curves ($\varepsilon_{zz} < 1.4\%$) due to statistical uncertainties on strain and strain-rate. WQ: Water Quench; AQ: Air Quench; GC: Grip Cooling. ‘–’ indicates that only one test was performed.

The average uncertainty on stress due to strain measurement errors is then considered as ± 5 MPa with a maximum of ± 8 MPa.

7.5. Influence of presolutionising and sampling on flow stress

AA2618 specimens cut in different forgings

Tensile specimens were cut at different positions (surface and center) and orientations (axial, radial and hoop) in different forgings (small, large and very large) to check that mechanical properties are isotropic, uniform within a forging and independent of the forging size. The influence of sampling was checked at 150°C and 250°C (*Figure 7-12*) where preliminary tensile tests without presolutionising are shown together with test with presolutionising.

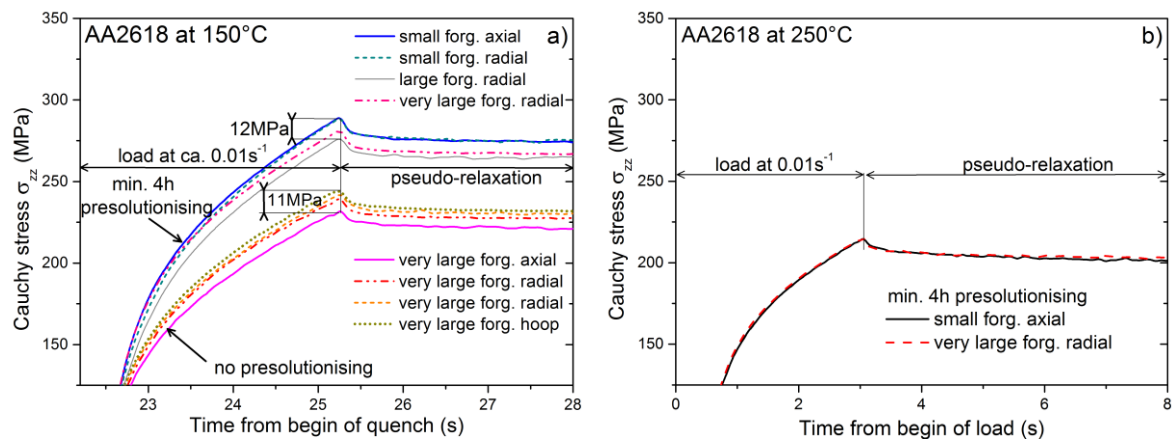


Figure 7-12 – Stress evolution after grip cooling at 20K/s showing the influence of presolutionising and sampling in AA2618 at 150°C (a) and 250°C (b).

Figure 7-12-a shows two groups of stress curves: the specimens presolutionised (min. 4 hour) in furnace exhibit a higher stress than the not presolutionised ones. This is due to the initial microstructure of the forgings received in annealed state, i.e. containing coarse precipitates formed during slow cooling. Without presolutionising, these precipitates are not dissolved during solutionising in the Gleeble (< 10 min). It was found that 4 hours presolutionising in oven was necessary to completely dissolve coarse precipitates. Consequently, except the four tests without presolutionising shown in *Figure 7-12*, all tests on AA2618 were performed with presolutionising (min. 4 hours). *Figure 7-12-b* shows no difference between the two samplings at 250°C.

For each of the two groups of stress curves (with or without presolutionising), *Figure 7-12-a* also shows that different samplings give the same stresses within ca. 12 MPa at 150°C. Hence, an error of ± 6 MPa on the stress-strain curves was attributed at 150°C for AA2618 due to different sampling.

A presolutionising time of at least 4 hours was chosen for AA2618. Specimens were sampled from the large and very large forgings.

AA7449 specimens cut in a 75 mm thick plate

Tensile specimens were cut at different positions (surface, quarter and core) and orientations (rolling and transverse long directions) in an AA7449 hot-rolled 75 mm thick plate. Before thermo-mechanical testings, specimens are presolutionised in a furnace for at least 4 hours, quenched in cold-water and stored in a freezer at ca. -10°C to retard any precipitation.

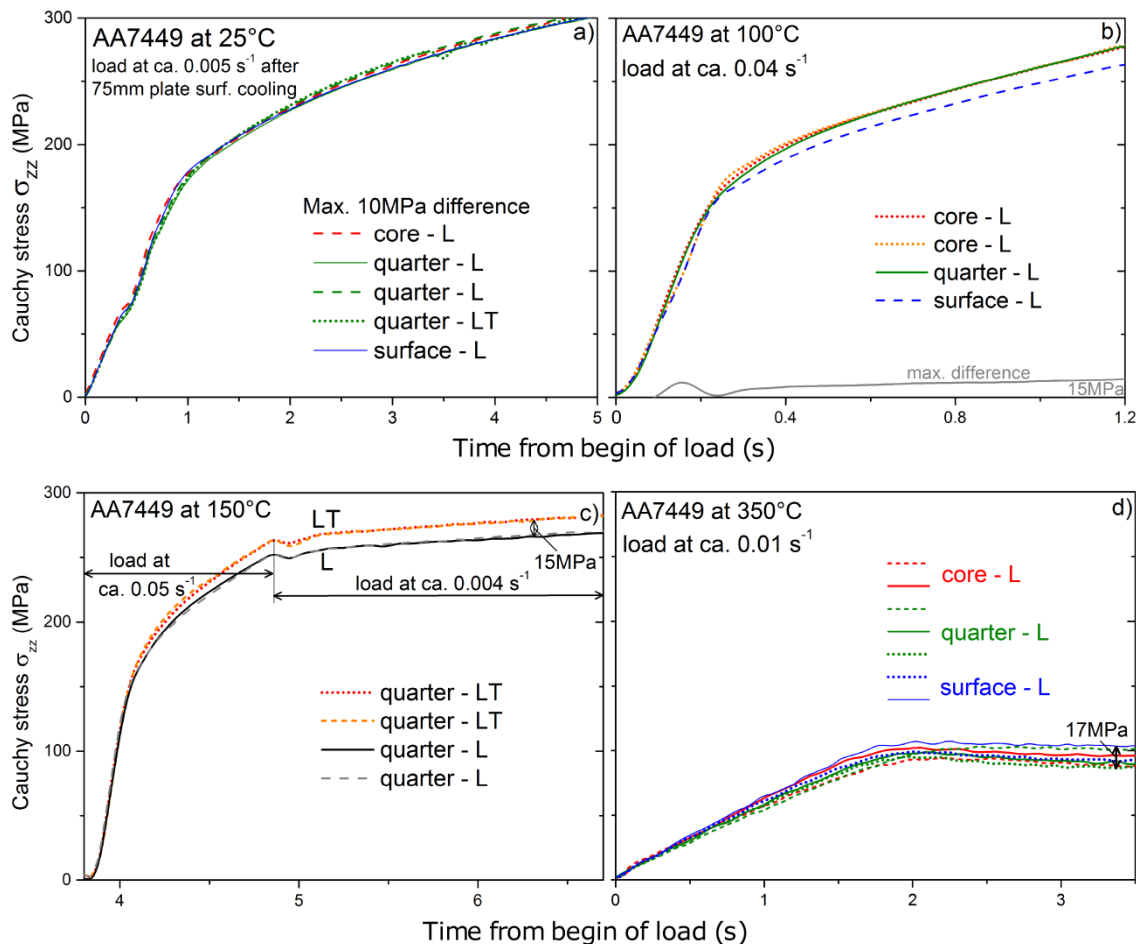


Figure 7-13 - Stress evolution in AA7449 specimens subjected to different thermo-mechanical conditions (after air quench unless otherwise state), showing the influence of sampling position and direction in the plate thickness. L: rolling direction; LT: transverse long direction.

At 25°C after a plate surface cooling, the influence of sampling position and direction on stress is low with only 10 MPa ($\sim 4\%$) difference as shown in Figure 7-13-a. At 100°C after air quench, core and quarter samplings give identical stresses up to 15 MPa ($\sim 6\%$) higher than for surface sampling (only one test) as shown in Figure 7-13-b. At 150°C after air quench, stress is higher (up to 15 MPa) for the transverse long than for the rolling sampling direction as shown in Figure 7-13-c with a good reproducibility. At 350°C after air quench, the three sampling positions give stresses within 17 MPa ($\sim 15\%$) but without clear trend between the different positions.

The influence of sampling was not checked for AA7040 with all specimens cut from quarter thickness in the rolling direction of 75 mm thick AA7040 plates.

7.6. Gleeble results for AA7040

7.6.1. AA7040 at $T \geq 400^\circ\text{C}$

K unconstrained

At the SHT temperature, specimens are subjected to a succession of tensile loads at different strain-rates interrupted by a pseudo-relaxation (blocked jaws). The stress-strain curves measured in the Gleeble for AA7040 are given in *Figure 7-14-a* and *b* together with the SiDoLo fit of the measurements. Tensile tests after interrupted quench-tests at 440°C and 400°C are shown in *Figure 7-14-c* and *d*.

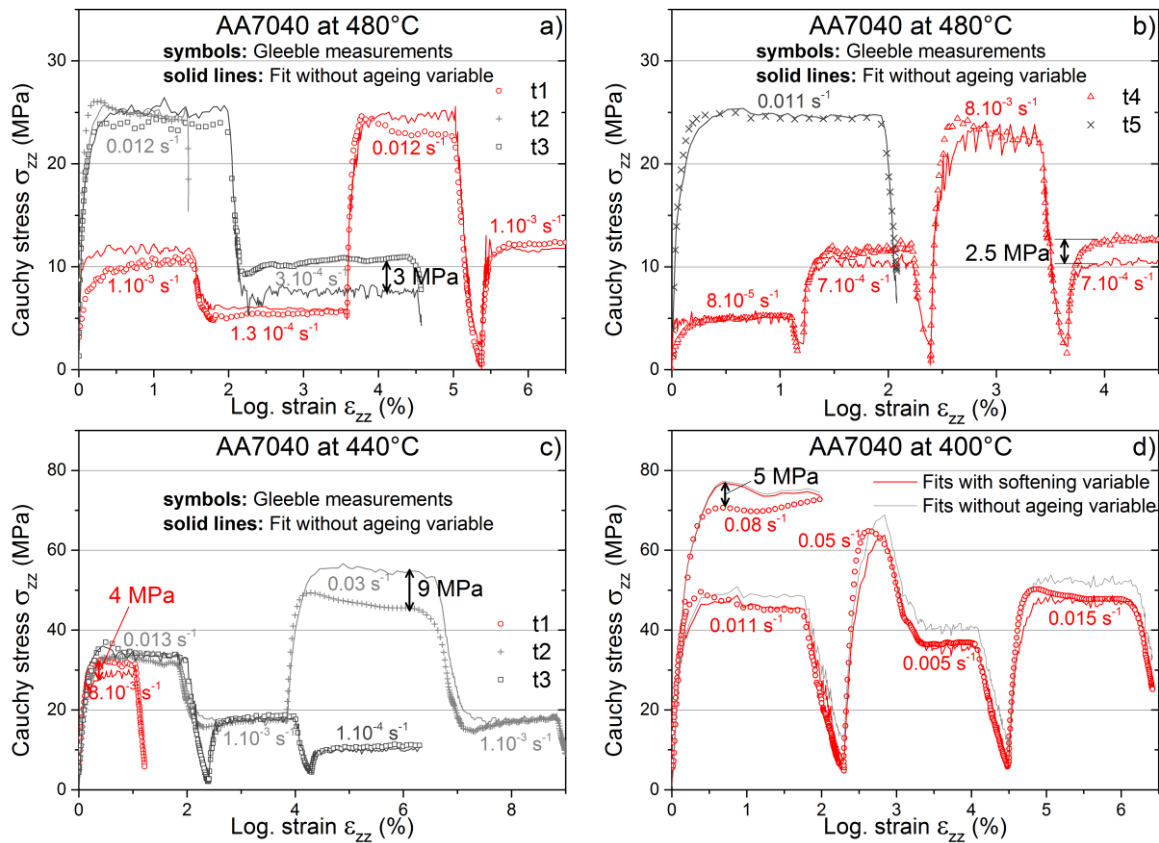


Figure 7-14 – Measured and fitted stress-strain curves for AA7040 at 480°C (a and b), 440°C (c) and 400°C (d) using the old specimen geometry.

Above 400°C , AA7040 features all the characteristics described in section 4.3.1 for AA7449 at the SHT temperature. At 480°C (*Figure 7-14-a* and *b*), the fit without ageing variable with $\sigma_0 = 0$ MPa, $H = 10^{-4}$ MPa, $n = 10^{-4}$, $K = 88.58$ MPa.s $^{-m}$ and $m = 0.285$ is good with a difference with measurements less than 3 MPa.

At 440°C (*Figure 7-14-c*), the fit with $\sigma_0 = 0$ MPa, $H = 10^{-4}$ MPa, $n = 10^{-4}$, $K = 107.32$ MPa.s $^{-m}$ and $m = 0.268$ is good except for test “t1” (max. 4 MPa difference) and for load 3 of test “t2” (max. 9 MPa difference). The discrepancy for load 3 at 0.03 s $^{-1}$ of test “t2” is not important for RS calculations since the equivalent plastic strain-rate is lower than 0.015 s $^{-1}$ in water-quenched plates with thicknesses lower than 140 mm.

At 400°C (Figure 7-14-d), the fits without ageing variable ($\sigma_0 = 4$ MPa, $H = 0.03$ MPa, $n = 10^{-3}$, $K = 125.0$ MPa.s^{-m} and $m = 0.23$) with more weight on small strains (< 0.5 %) at 0.011 s⁻¹ overestimate stresses at high strains due to softening. The fits with softening variable ($\sigma_0 = 4$ MPa, $\sigma_{soft} = 5$ MPa and $\tau_{soft} = 2$ sec) improve the agreement with Gleeble measurements at 400°C. Based on the results of Figure 7-14, a global error of ± 4 MPa on the Gleeble stress-strain curves is attributed for AA7040 at $T \geq 400^\circ\text{C}$.

The initial guess of (K, m) for the inverse method in SiDoLo was made beforehand by taking the average stress on each plateau with its corresponding strain-rate as shown in Figure 7-15.

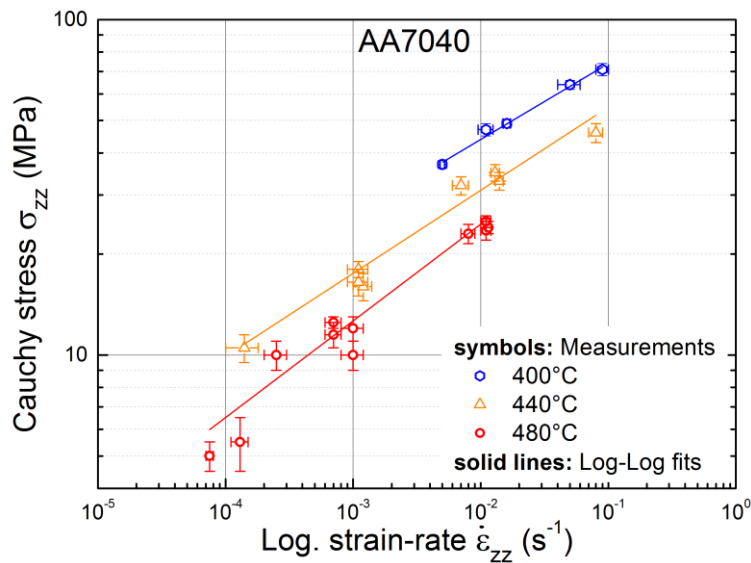


Figure 7-15 – Plot for initial estimation of (K, m) at 400°C, 440°C and 480°C for AA7040 provided to SiDoLo.

The results of the linear regression are given in Table 7-4.

AA7040	K (MPa.s ^{-m})	m	$N=1/m$	R^2
480°C	88 ± 1	0.28 ± 0.02	3.6	0.96
440°C	95 ± 1	0.25 ± 0.02	4.0	0.96
400°C	126 ± 1	0.23 ± 0.01	4.4	0.99

Table 7-3 – Results of the linear regression for AA7040 at 400°C, 440°C and 480°C.

At temperatures close to the melting temperature (ca. 576°C for AA7040), the viscous stress is limited by the ultimate strength which becomes very low. This explains the lower value of K at 480°C compared to 440°C and 400°C in Table 7-3 and the bell-shape of the K -Temperature curve of AA7040 as shown in Figure 4-23-a.

K constrained to increase with increasing temperature

As mentioned in section 4.3.4, it was tried for AA7040 to constrain K to always increase with increasing temperature as this is the case for AA7010. The identified parameters are shown in Figure 7-16.

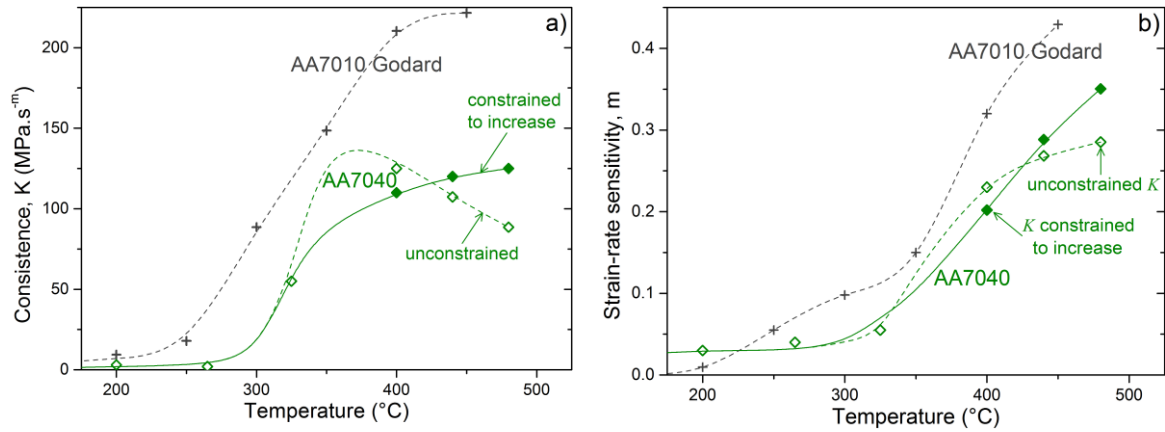


Figure 7-16 – Temperature dependence of parameters K (a) and m (b) for AA7010 from Godard and for AA7040 with constrained and unconstrained K . Lines are guide for the eye.

The measured stress-strain curves for AA7040 at 480°C are given in Figure 7-20 together with the SiDoLo fit using the parameters obtained with K constrained to increase (full symbols in Figure 7-16).

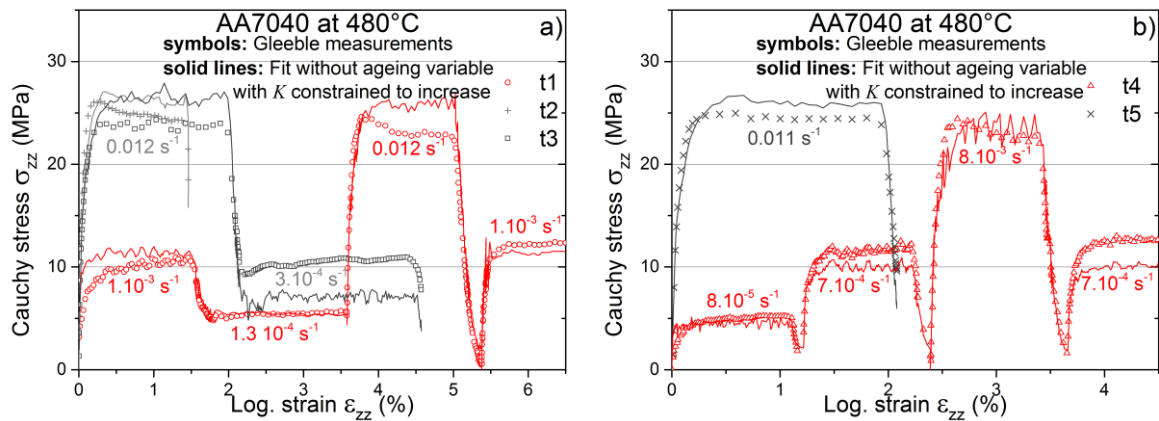


Figure 7-17 – Measured stress-strain curves for AA7040 at 480°C together with fitted curves using (K, m) in full symbols in Figure 7-16.

Although K used for the SiDoLo fits in Figure 7-20 was constrained to increase with increasing temperature, the agreement between Gleeble measurements and fits is as good as in Figure 7-14-a and b (unconstrained K). This means that the two sets of parameters (K, m) for AA7040 at 480°C shown in Figure 7-16 provide an equally satisfactorily fit of the measurements. The solution of the identification procedure is therefore not unique at 480°C.

At 440°C, the fit using (K, m) in full symbols in Figure 7-16 is also as good as in Figure 7-14-c except for the load at 0.03 s⁻¹ where the fit in Figure 7-18-a is worse.

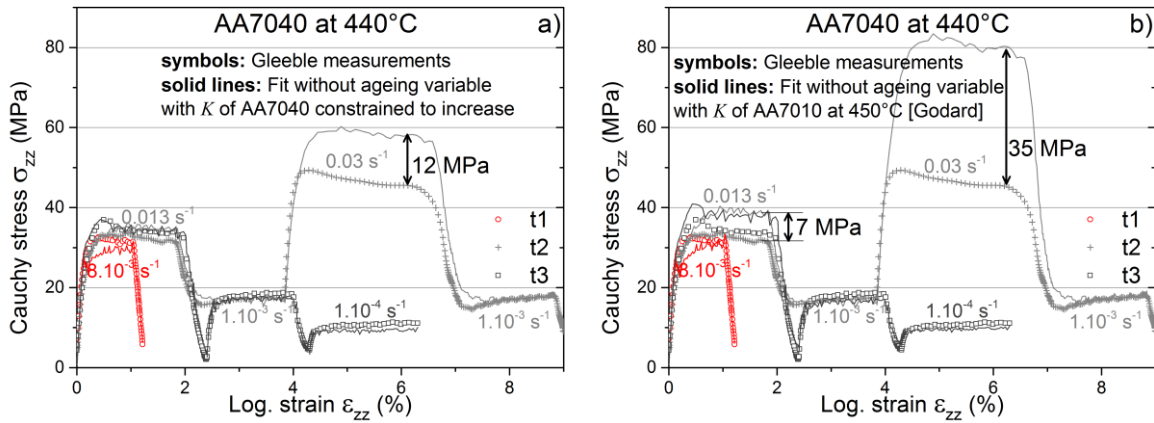


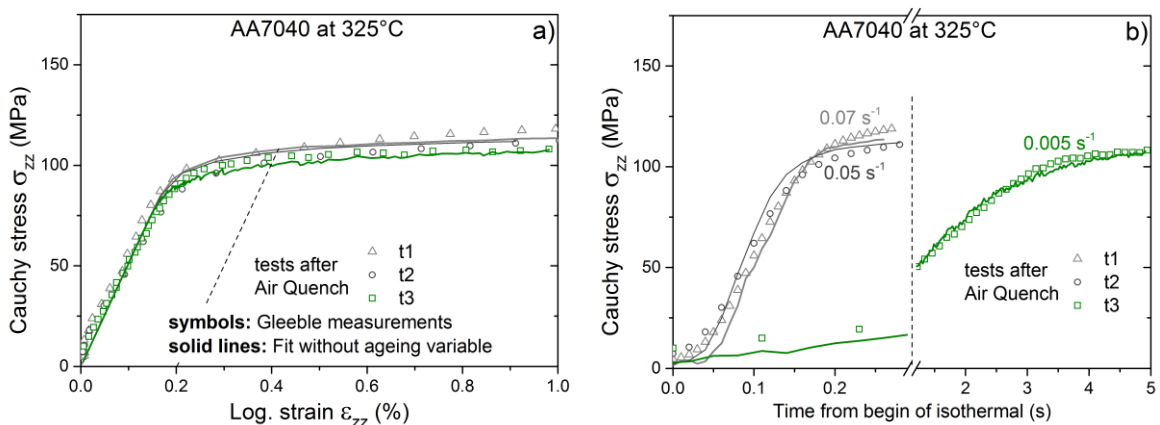
Figure 7-18 – Measured stress-strain curves for AA7040 at 440°C together with fitted curves using (K, m) in full symbols in Figure 7-16 (a) and using (σ_0, H, n, K, m) of AA7010 at 450°C (b).

Figure 7-18-b shows that the agreement between measurements at 440°C and fit using (σ_0, H, n, K, m) of AA7010 at 450°C is good at low strain-rates ($< 0.01 \text{ s}^{-1}$) but becomes poor as the strain-rate increases. Here, it should be mentioned that the parameters of AA7010 from Godard were identified using tensile loads at max. 0.005 s^{-1} . This means that the parameters of AA7010 from Godard at high temperature ($\geq 400^\circ\text{C}$) should be used carefully for strain-rates higher than 0.005 s^{-1} . Indeed, the predicted flow stress seems too high in these conditions.

As a conclusion, when K of AA7040 is constrained to increase with increasing temperature (full symbols in Figure 7-16-a), the increase of m with increasing temperature is more pronounced (Figure 7-16-b). However, the (K, m) parameters of AA7010 from Godard remain higher than those for AA7040.

7.6.2. AA7040 at $T < 350^\circ\text{C}$

Stress-strain curves and stress evolutions for AA7040 after quenches interrupted either at 325°C , 265°C , 200°C , 150°C or 100°C are presented in Figure 7-19 together with the SiDoLo fits.



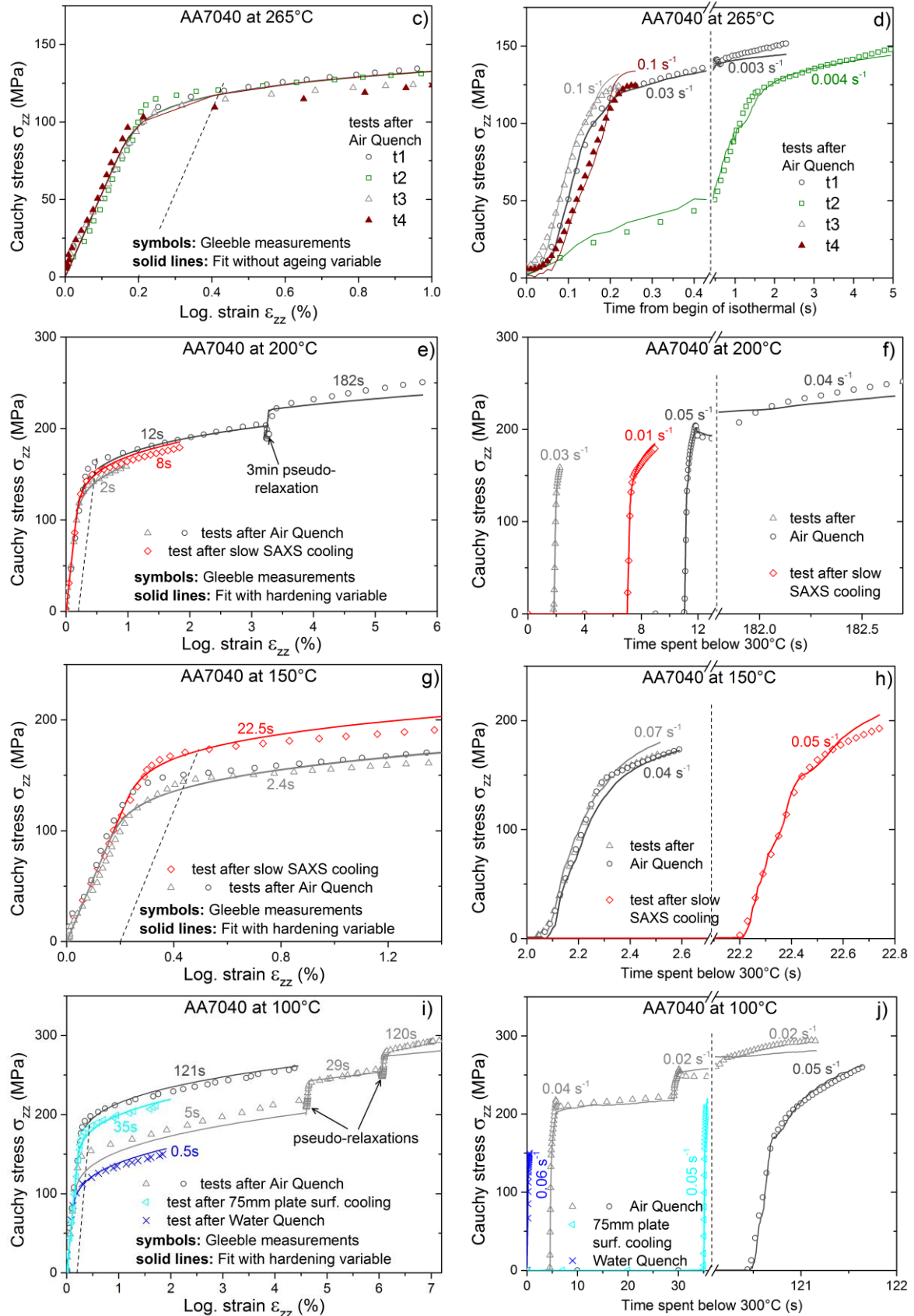


Figure 7-19 – Measured and fitted stress-strain curves (left) and corresponding strain evolutions (right) for AA7040 using the new specimen geometry.

At 325°C, AA7040 features a non-negligible strain-rate sensitivity as shown in *Figure 7-19-a* and *b*. The identified parameters of the fit without ageing variable for AA7040 at 325°C are $\sigma_0 = 22.0$ MPa, $H = 75.0$ MPa, $n = 0.11$, $K = 55.0$ MPa.s^{-m} and $m = 0.055$.

At 265°C, the four tests shown in *Figure 7-19-c* and *d* indicate that the yield strength of AA7040 increases slightly with decreasing strain-rate. This can be explained either by hardening precipitation during the test at low strain-rate or by a negative strain-rate-sensitivity for strain-rates ranging from 0.004 s⁻¹ to 0.1 s⁻¹. The difference in yield strength being within the error of measurement (± 10 MPa), the strain-rate parameters are imposed to low values ($K = 2$ MPa.s^{-m} and $m = 0.04$) at 265°C, thus neglecting strain-rate effects. The parameters of the fit without ageing variable for AA7040 at 265°C are $\sigma_0 = 55.0$ MPa, $H = 170.0$ MPa and $n = 0.165$.

Below 265°C where AA7040 is assumed to be not strain-rate sensitive, tensile loads are performed at high strain-rate (≥ 0.01 s⁻¹) in order to limit the effect of precipitation on yield strength during loading. In addition, the waiting time before the beginning of the first load is varied in order to characterise the effect of precipitation on yield strength. Here, the fit is performed using a hardening variable with the same choices as for AA7449, i.e. with an initial time in Eq. 4-23, τ_{hard} , taken when TC1 is equal to 300°C and thus with $a_{hard}(T=300^\circ\text{C}) = a_{hard,0} = 0$ and $a_{hard,\infty} = 1$. As for AA7449, the fits at 100°C, 150°C and 200°C for AA7040 are good for short times (< 3 seconds spent below 300°C) and some discrepancies appear at longer times for the same reasons as for AA7449. The tensile curves of AA7040 at room temperature after water quench are given in appendix 7.4.

7.6.3. AA7040 determination of T_{cum}

In order to determine T_{cum} defined in section 4.1.1, tensile tests at either 200°C or 325°C are followed by a load at 45°C. The imposed coolings are shown in *Figure 7-20* for AA7040.

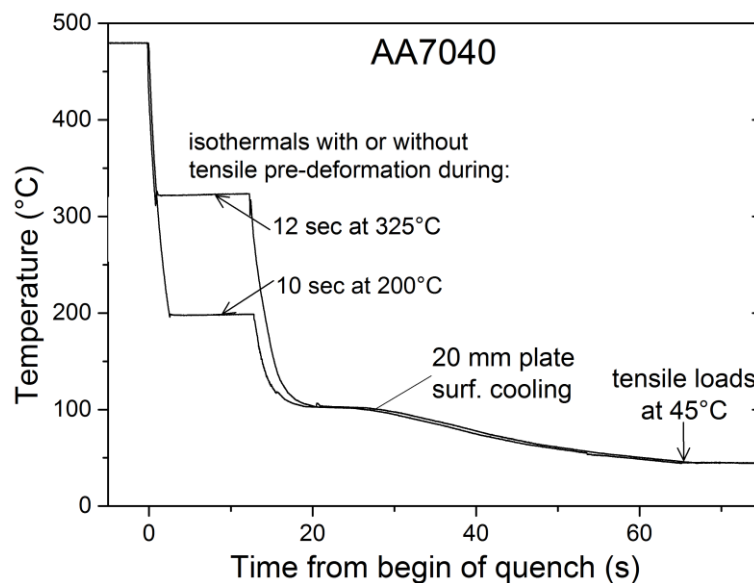


Figure 7-20 – Coolings imposed in AA7040 new geometry Gleeble specimens subjected to tensile load at 45°C with or without pre-deformation at 200°C and 325°C.

For the two cooling conditions shown *Figure 7-20*, AA7040 Gleeble specimens from identical sampling are subjected to an air quench interrupted by an isothermal holding during which different mechanical loads are imposed. The isothermal holding is followed by a cooling similar to that of a 20 mm plate surface interrupted at 45°C where a tensile load is performed. The measured stresses and strains are given in *Figure 4-21* and for pre-deformation at 200°C and 325°C respectively.

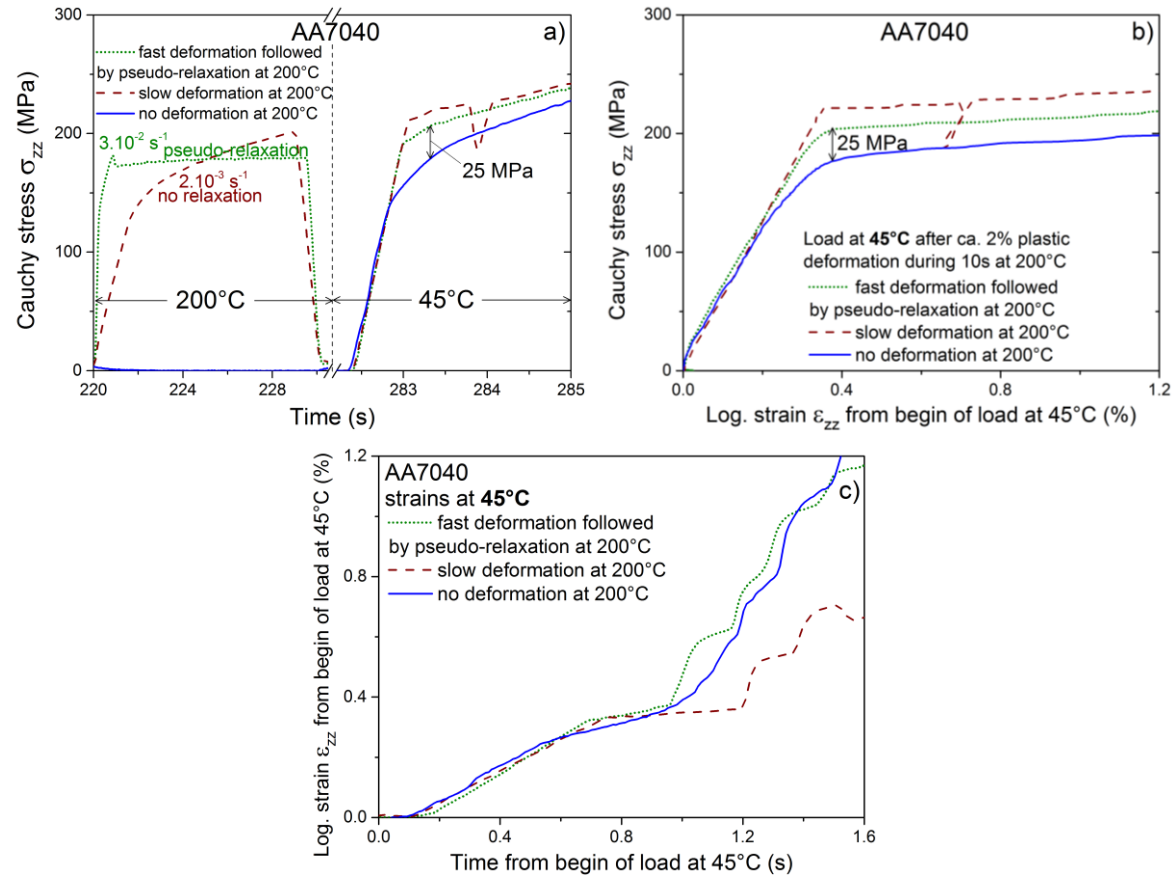


Figure 7-21 - Stress response of AA7040 specimens subjected to loading at 45°C with or without pre-deformation at 200°C.

When pre-deformation is performed at a temperature lower than T_{cum} , the load curve at low temperature depends on this pre-deformation: the higher the pre-deformation, the higher the stress. This is the case in *Figure 4-21-a* where the load curve at 45°C depends on pre-deformation at 200°C. This can also be seen in the stress-strain curves in *Figure 4-21-b* which should always be associated with the corresponding strain-time curves (*Figure 4-21-c*) because of the strain uncertainties discussed in appendix 7.4.

Figure 7-22 shows that the influence of pre-deformation at 325°C on the load curve at 45°C is low.

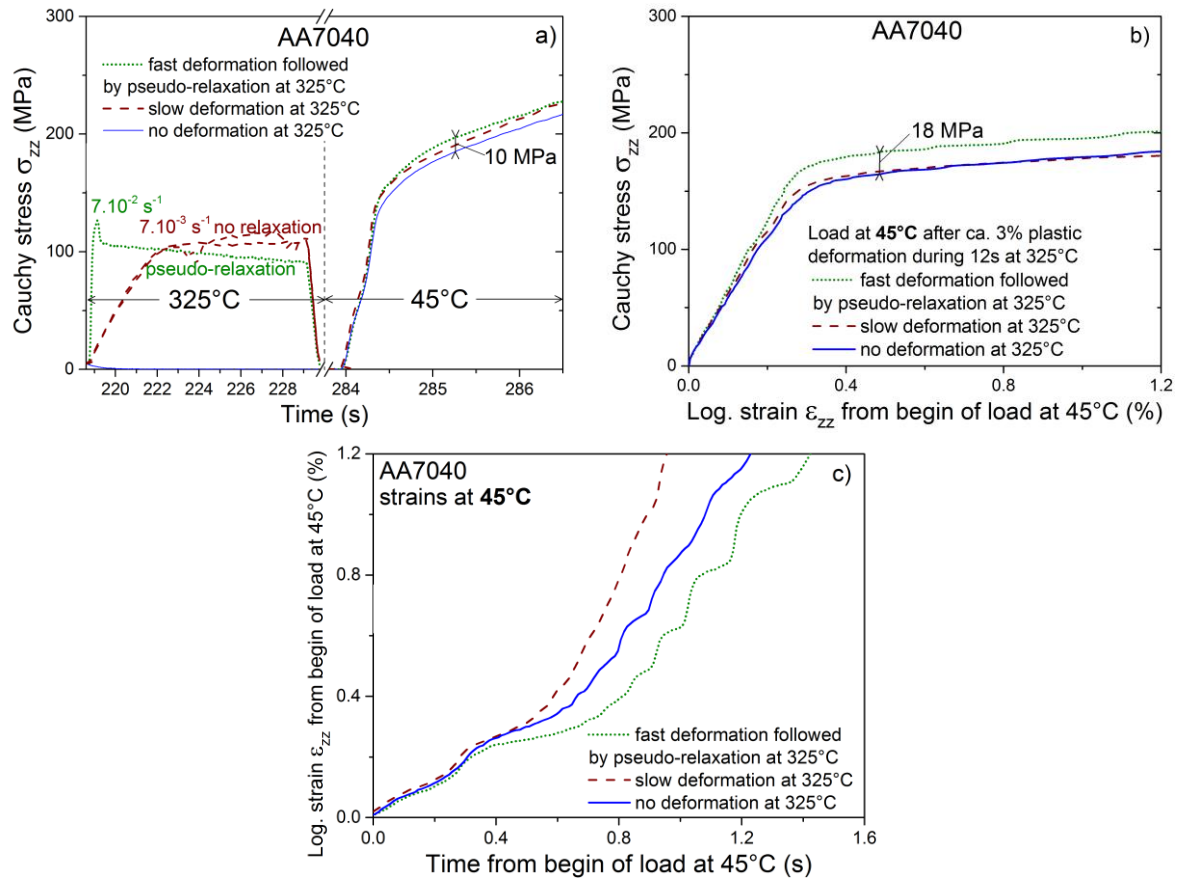


Figure 7-22 - Stress response of AA7040 specimens subjected to loading at 45°C with or without pre-deformation at 325°C.

The stress-time curves at 45°C after pre-deformation at 325°C are only 10 MPa higher than the curve at 45°C after no deformation at 325°C (Figure 7-22-a). The corresponding stress-strain curves at 45°C are almost superimposed (Figure 7-22-b) except for the curve after fast deformation followed by pseudo-relaxation at 325°C. This curve should be considered cautiously since the strain evolution in Figure 7-22-c seems too slow compared to the results for AA7449 after fast deformation followed by pseudo-relaxation at 325°C.

From these experiments, the value of 325°C has been chosen for T_{cum} in all the FE models of quenching for AA7040.

7.6.4. Effect of non-monotonic load on RS for AA7040 – Bauschinger effect

In order to evaluate the effect of non-monotonic load on RS, pre-deformation tensile tests at 265°C were followed by a load at 50°C either in tension or in compression as shown in *Figure 7-23* for AA7040.

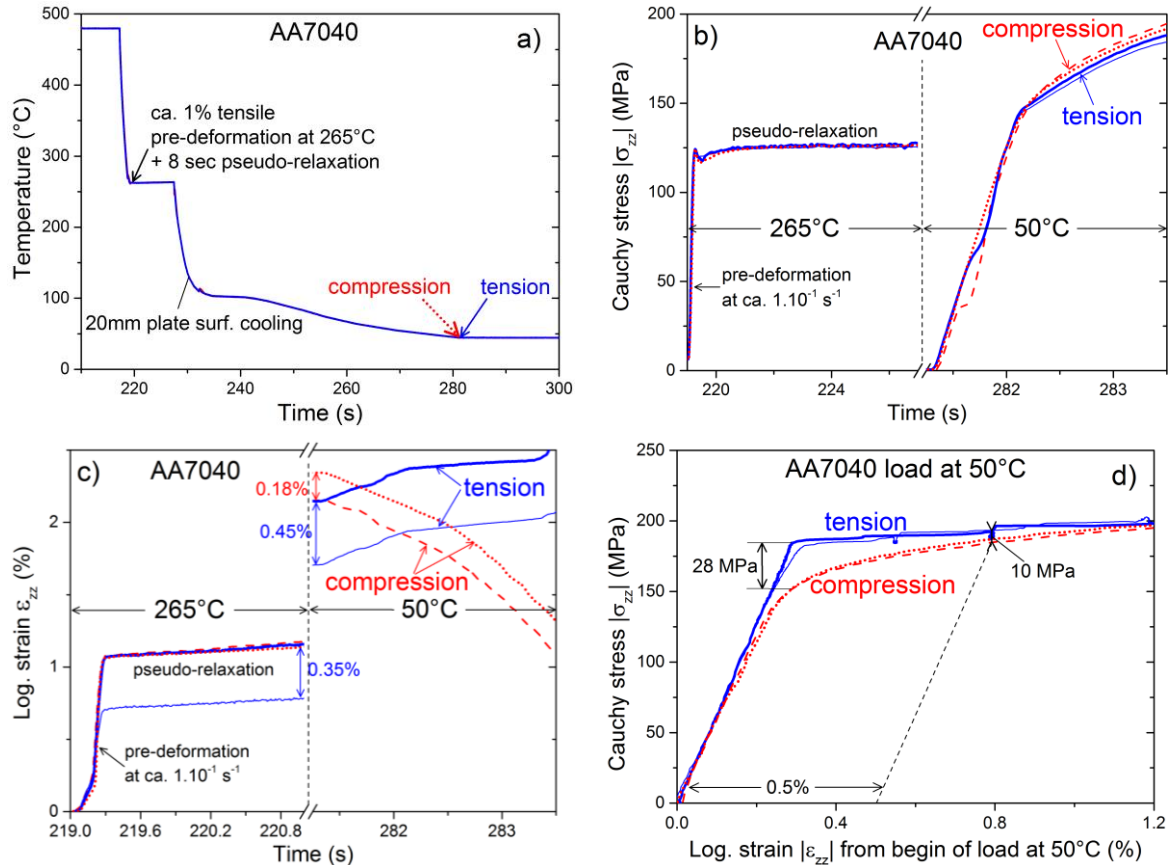


Figure 7-23 – Cooling imposed in Gleeble specimens (a) subjected to tensile load at 265°C followed by tension or compression at 50°C; corresponding stress (b) and strain (c) evolutions; Bauschinger stress-strain curves at 50°C (d). Four curves are shown since each testing is duplicated.

This thermo-mechanical testing with the compression step is a simplified attempt to represent what happens at the plate surface during quenching, namely tension at high temperature followed by compression at low temperature.

Both specimens experience the same thermal cycle (*Figure 7-23-a*), so that the effect of precipitation on flow stress is the same. In the presence of kinematic hardening, the load curve after tensile pre-straining is higher in tension than in compression. This is not the case in *Figure 7-23-b* where the stress-time curves at 50°C are ca. 10 MPa higher in compression than in tension. Due to the strain uncertainties discussed in appendix 7.4, the corresponding strain-time curves in *Figure 7-23-c* are not reproducible. The differences between two duplicated tests are lower in compression than in tension. Duplication of each test shows nevertheless that these different strain evolutions at 50°C are reproducible in relative value, i.e. after vertical shift of the strain-time curves at 50°C

in *Figure 7-23-c*. Considering these vertical shifts, the corresponding Bauschinger stress-strain curves at 50°C are then given in *Figure 7-23-d*.

The stress-strain curves show that the yield strength in compression is 28 MPa lower than in tension. *Figure 7-23-d* indicates thus that the Bauschinger effect exists for AA7040 in under-aged state at low plastic strains. The difference between flow stress in tension and in compression decreases with increasing plastic strain at 50°C. At 0.5% plastic strain – value corresponding to the amount of equivalent accumulated inelastic strain below 265°C at the surface of a 75 mm plate – the difference is only ca. 10 MPa. At 0.9% plastic strain – value corresponding to the equivalent accumulated inelastic strain at the surface of a 140 mm plate – there is no difference between flow stress in tension and flow stress in compression. The error of measurement being ± 8 MPa, the Bauschinger effect can be considered negligible for plates thicker than 70 mm quenched in cold water.

This justifies the assumption of isotropic hardening in Eq. 4-21. For the 20 mm plate, the Bauschinger effect can also be neglected because of the lower tensile plastic strain occurring at high temperature compared to that for higher thicknesses.

7.7. Gleeble results for AA2618

7.7.1. AA2618 at $T \geq 400^\circ\text{C}$

Tensile tests on AA2618 after interrupted quench-tests at 500°C , 450°C and 400°C are shown in *Figure 7-24*.

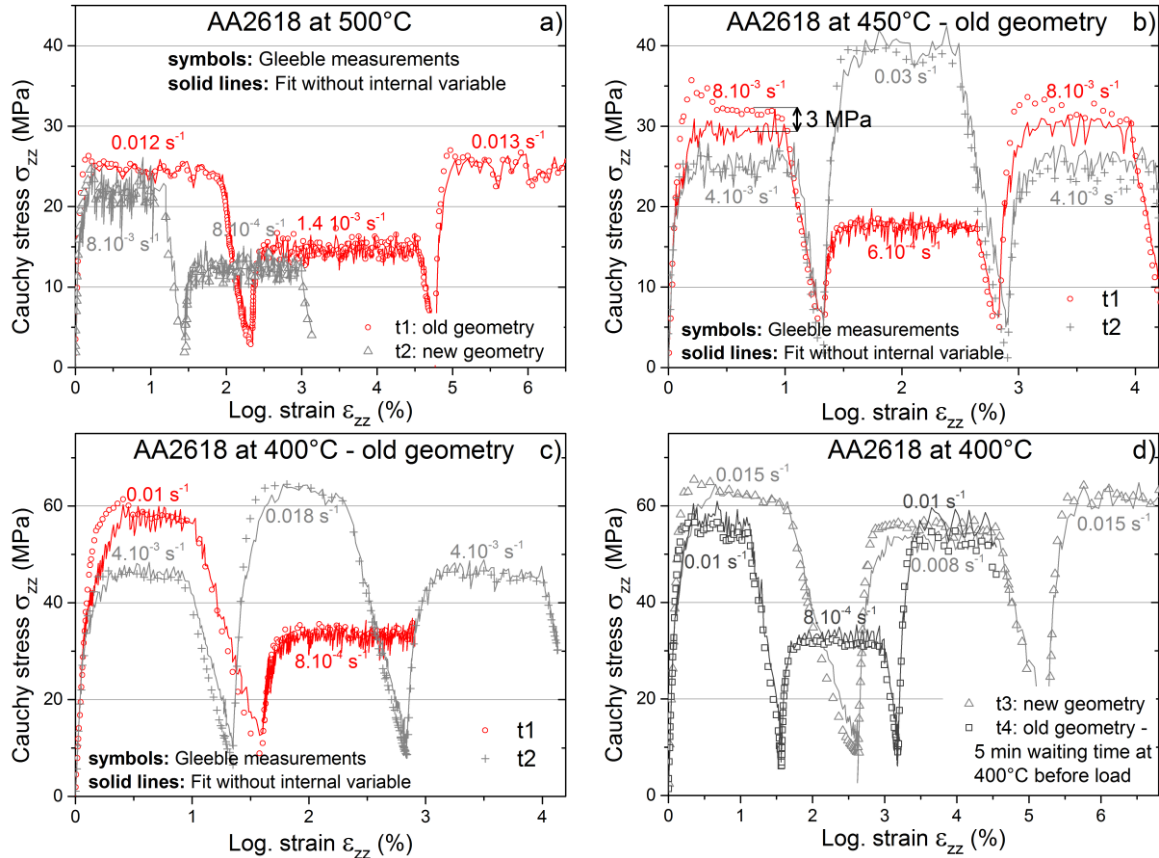


Figure 7-24 – Measured and fitted stress-strain curves for AA2618 at 500°C (a), 450°C (b) and 400°C (c and d).

Above 400°C , AA2618 features all the characteristics described in section 4.3.1 for AA7449 at the SHT temperature. In *Figure 7-24-a*, the fit without internal variable with $\sigma_0 = 0.5 \text{ MPa}$, $H = 10^{-4} \text{ MPa}$, $n = 10^{-4}$, $K = 74.86 \text{ MPa.s}^{-m}$ and $m = 0.26$ is excellent for the two geometries which are therefore equivalent at 500°C for AA2618.

At 450°C in *Figure 7-24-b*, the fit with $\sigma_0 = 0.7 \text{ MPa}$, $H = 0.0015 \text{ MPa}$, $n = 10^{-4}$, $K = 91.0 \text{ MPa.s}^{-m}$ and $m = 0.235$ is good except for loads 1 and 3 of test “t1” for which the fit slightly underestimates the measurements (ca. 3 MPa difference).

Measurements at 400°C and corresponding fits ($\sigma_0 = 1.0 \text{ MPa}$, $H = 0.01 \text{ MPa}$, $n = 10^{-3}$, $K = 155.0 \text{ MPa.s}^{-m}$ and $m = 0.223$) show that the two geometries are equivalent and that the stress reached on a plateau does not depend on time spent before load. Indeed, the 5 min waiting time before loading in test “t4” have no effect on stress (*Figure 7-24-d*). Based on the results of *Figure 7-24*, an error of $\pm 4 \text{ MPa}$ on the Gleeble stress-strain curves is attributed for AA2618 at $T \geq 400^\circ\text{C}$.

The initial guess of (K, m) for the inverse method was made beforehand by taking the average stress on each plateau with its corresponding strain-rate as shown in *Figure 7-25*.

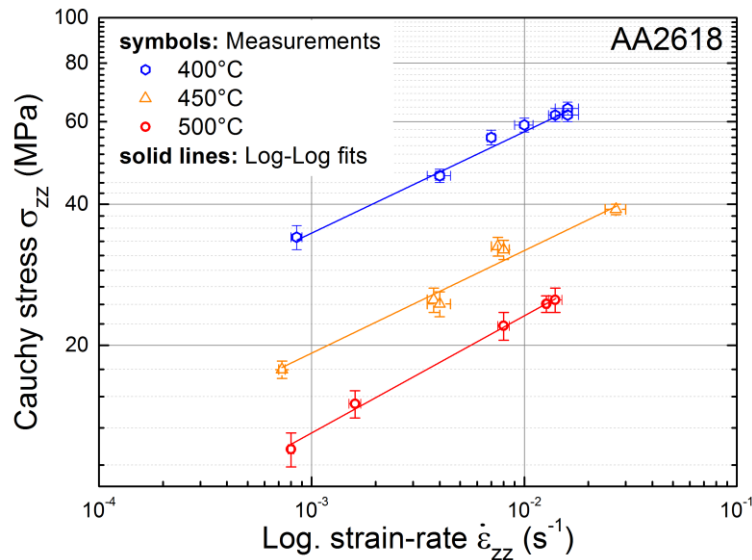


Figure 7-25 – Plot of initial estimation of (K, m) at 400°C, 450°C and 500°C for AA2618 provided to SiDoLo.

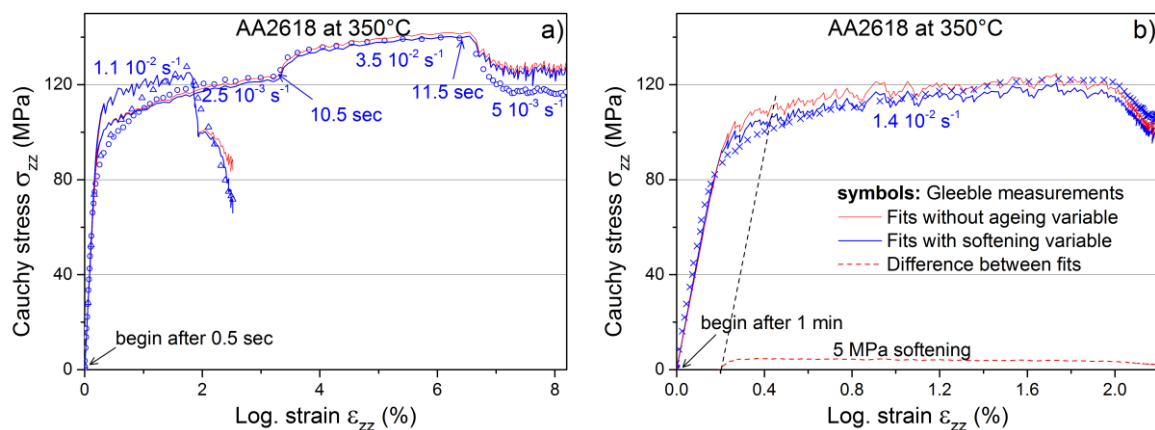
The results of the linear regression are given in *Table 7-4*.

AA2618	K (MPa.s ^{-m})	m	$N=1/m$	R^2
500°C	73 ± 1	0.25 ± 0.01	4.0	0.99
450°C	88 ± 1	0.22 ± 0.02	4.5	0.97
400°C	161 ± 1	0.22 ± 0.01	4.5	0.98

Table 7-4 – Results of the linear regression for AA2618 at 400°C, 450°C and 500°C.

At temperatures close to the melting temperature (ca. 595°C for AA2618), as for AA7449 and AA7040, the viscous stress is limited by the ultimate strength which becomes very low. This explains the lower value of K at 500°C compared to 450°C and 400°C in *Table 7-4* and the bell-shape of the K -Temperature curve of AA2618 shown in *Figure 4-23-a*.

7.7.2. AA2618 at 350°C



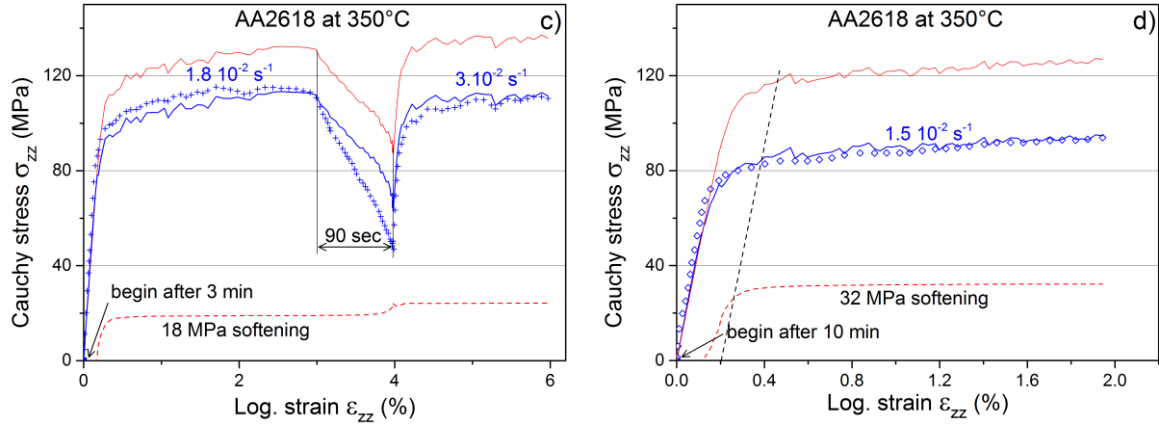
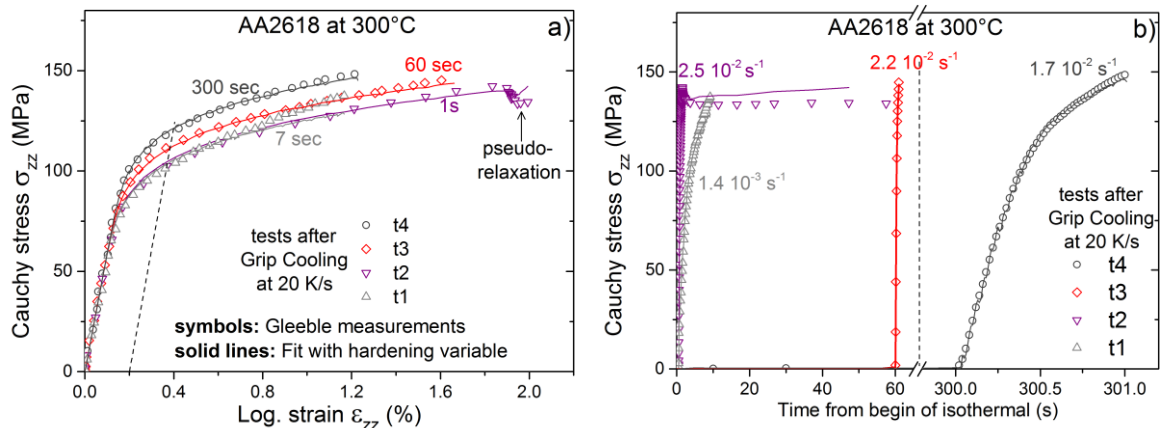


Figure 7-26 – Measured and fitted stress-strain curves for AA2618 at 350°C obtained using the new specimen geometry. The legend given in b) applies to the four figures. The legend given in a) applies to the four figures. For all the fits, $\sigma_0 = 11$ MPa, $H = 70$ MPa, $n = 0.12$, $K = 115$ MPa.s^{-m} and $m = 0.11$. For the fits with ageing variable, $\sigma_{soft} = 35$ MPa and $\tau_{soft} = 230$ sec.

At 350°C, AA2618 features a relatively high SRS together with some strain-hardening. The fit without ageing variable is reasonable for relatively short times (≤ 70 sec) in the tests in Figure 7-26-a and b, but it overestimates stresses for times higher than 3 minutes in Figure 7-26-c and d. The use of an ageing variable gives better fits for long times. The fits with ageing (softening) variable are based on Eq. 4-23 with an initial time, $t_{soft,0}$, taken when TC1 is equal to 400°C as explained in section 4.2.3.

7.7.3. AA2618 at T < 350°C

Stress-strain curves and stress evolutions for AA2618 after quenches interrupted either at 300°C, 250°C, 200°C, 150°C, 100°C or 35°C are presented in Figure 7-27 together with the SiDoLo fits.



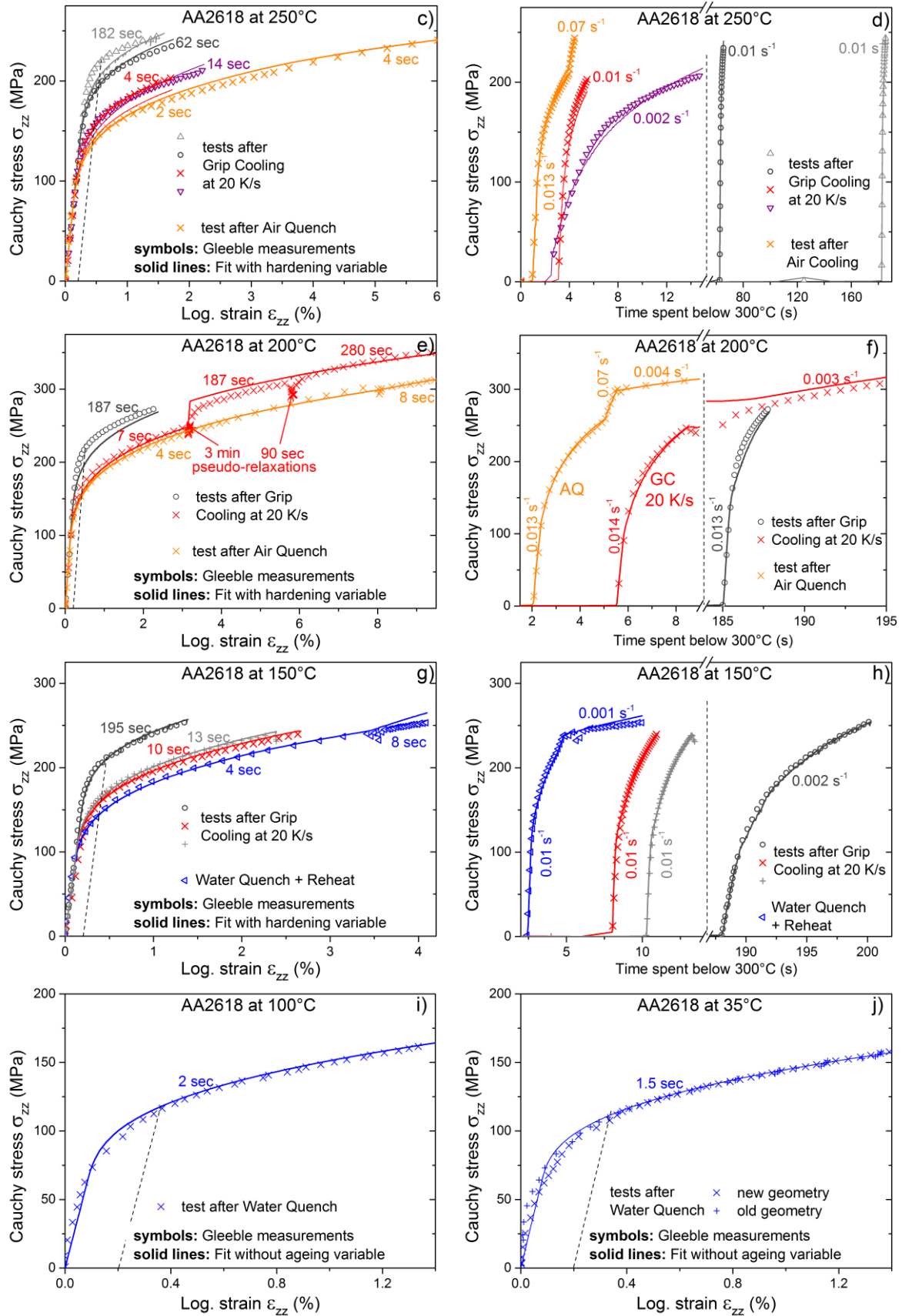


Figure 7-27 – Measured and fitted stress-strain curves for AA2618.

At 300°C, the SRS becomes negligible for AA2618 as shown in *Figure 7-27-a and b*. At 250°C and 200°C, the SRS is also negligible as shown *Figure 7-27-c to f* by the strain-rate jumps performed during the tests after AQ. At 200°C, a small but non-negligible stress decrease is observed during the pseudo-relaxations. This relaxation cannot be fitted as low values for K and m are chosen. This choice has no consequence on FE simulations of quenching due to the fast cooling rate at 200°C in the BWQ forgings. At 150°C, the strain-rate jump performed during the test after WQ+RH shows that SRS is negligible.

In *Figure 7-27*, the fits with hardening variable are good for short times (< 4 seconds spent below 300°C) since more weight is given to them in the identification. At 300°C and 150°C, they are also good for long times with a strain-hardening independent of precipitation. At 200°C and 250°C, however, some discrepancy between measurements and fits can be explained by a slight decrease of strain-hardening with precipitation. The tensile curves of AA2618 at 35°C after water quench are given in appendix 7.4 where the uncertainty on strain is discussed.

7.7.4. AA2618 determination of T_{cum}

In order to determine T_{cum} defined in section 4.1.1, tensile tests at either 300°C or 350°C are followed by a load at 65°C. The imposed coolings are shown in *Figure 7-28* for AA2618.

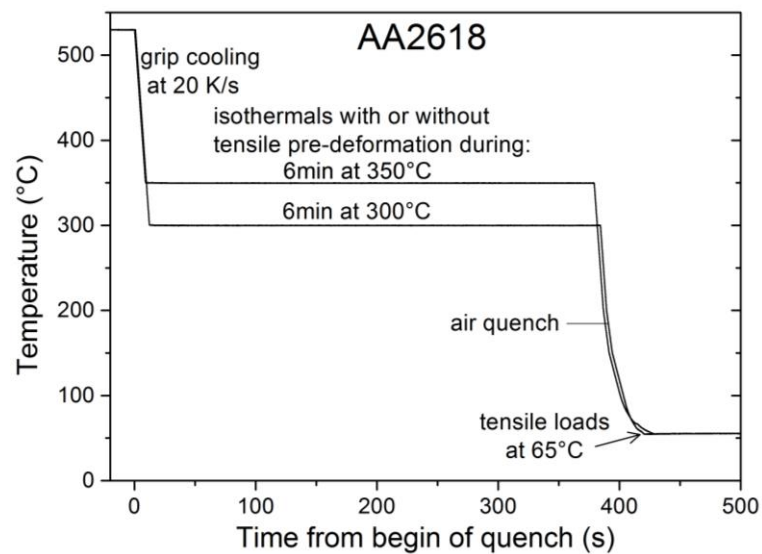


Figure 7-28 – Coolings imposed in AA2618 new geometry Gleeble specimens subjected to tensile load at 65°C with or without pre-deformation at 300°C and 350°C.

For the two cooling conditions shown *Figure 7-28*, AA2618 Gleeble specimens from identical sampling are subjected to an air quench interrupted by an isothermal holding during which different mechanical loads are imposed. The isothermal holding is followed by air quench interrupted at 65°C where a tensile load is performed. The obtained stresses and strains are given in *Figure 7-29*.

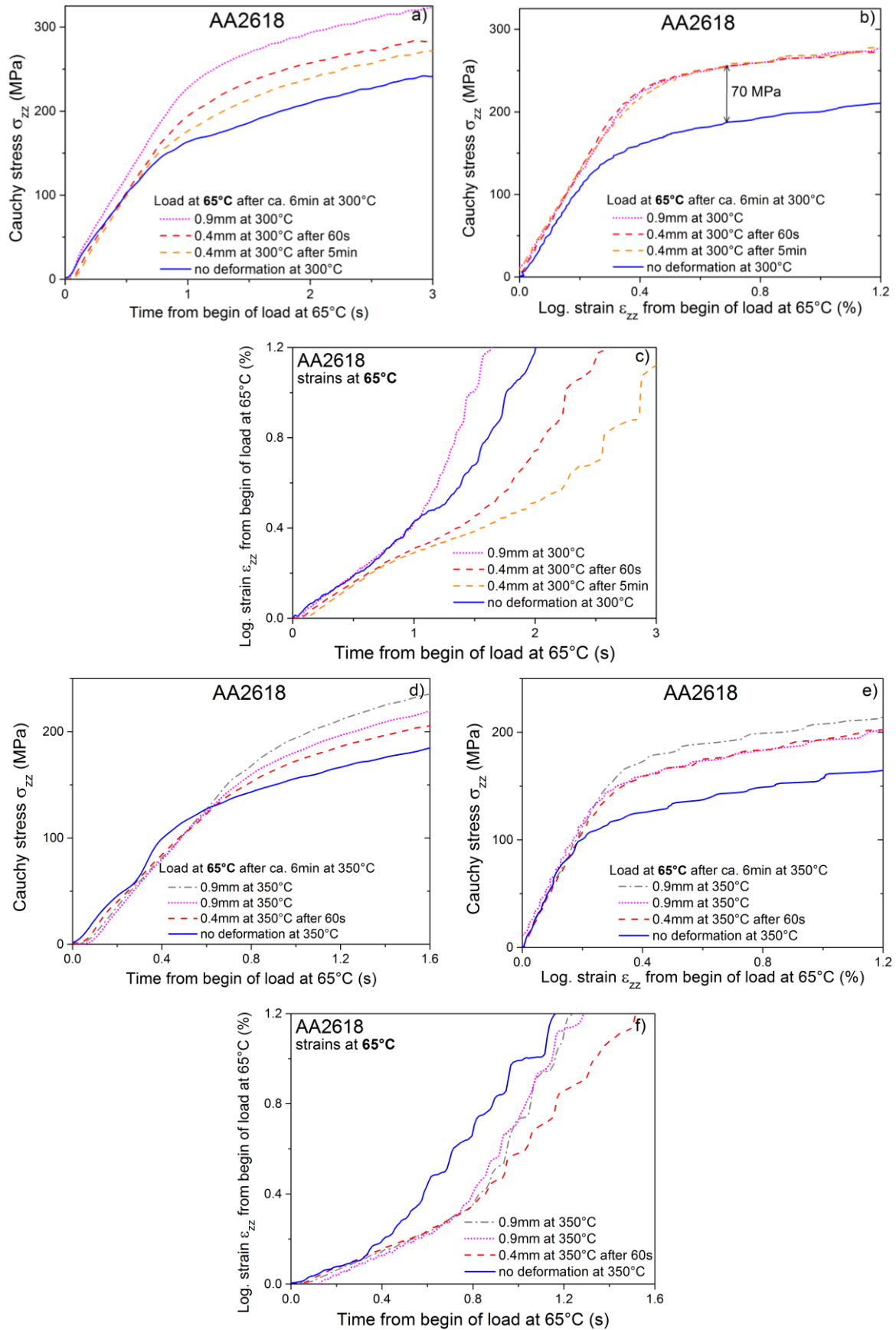


Figure 7-29 – Stress response of AA2618 subjected to loading at 65°C with or without pre-deformation at 300°C (a), (b) and (c) and 350°C (d), (e) and (f).

When pre-deformation is performed at a temperature lower than T_{cum} , the load curve at low temperature depends on this pre-deformation: the higher the pre-deformation, the higher the stress. This is the case at 300°C in *Figure 7-29-a* where the load curve at 65°C depends on pre-deformation at 300°C. This can also be seen in the stress-strain curves in *Figure 7-29-b* which should always be associated with the corresponding strain-time curves because of the strain uncertainties discussed in appendix 7.4.

Figure 7-29-bottom shows that the influence of pre-deformation at 350°C on the load curve at 65°C is low if one compares the curves at 65°C after 0.4mm and 0.9mm pre-deformation at 350°C. However, this is not the case if one compares with the stress-strain curve at 65°C without pre-deformation at 350°C. This curve seems too low and the stress evolution in *Figure 7-29-d* indicates that this test without pre-deformation at 350°C is dubious and should be duplicated.

Since these measurements for AA2618 do not provide an accurate value of T_{cum} but a temperature interval [300-400°C], several FE quenching simulations were run for the large forging using the TMG model with different values of T_{cum} .

The difference in terms of residual stresses between the TMG model with $T_{cum} = 350^\circ\text{C}$ and the TMG model with $T_{cum} = 325^\circ\text{C}$ is shown in *Figure 7-30* for the large forging. In these difference plots, the regions in green indicate that both models predict the same RS at ± 2 MPa. The regions in light grey and in black indicate that the RS predicted with $T_{cum} = 350^\circ\text{C}$ are more than 11 MPa higher in absolute than those predicted with $T_{cum} = 325^\circ\text{C}$.

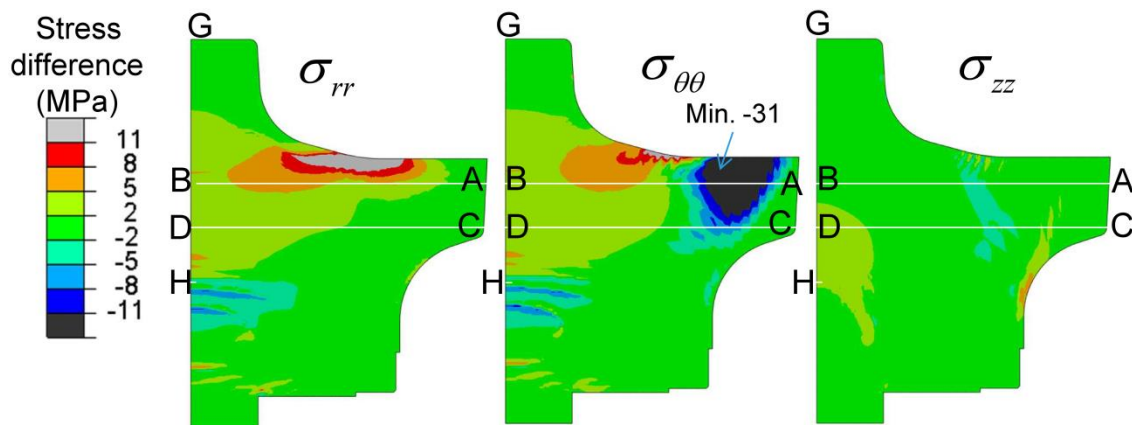


Figure 7-30 – Subtraction of stresses in large forging predicted by the TMG model with $T_{cum} = 325^\circ\text{C}$ to those predicted by the TMG model with $T_{cum} = 350^\circ\text{C}$.

The RS predicted using 325°C or 350°C for T_{cum} are very close except in the region close to A where the compressive hoop stress predicted with $T_{cum} = 350^\circ\text{C}$ is up to 31 MPa higher in absolute value than with $T_{cum} = 325^\circ\text{C}$.

These differences are increased when ignoring plastic strain recovery ($T_{cum} = 530^\circ\text{C}$) as shown in *Figure 7-31*.

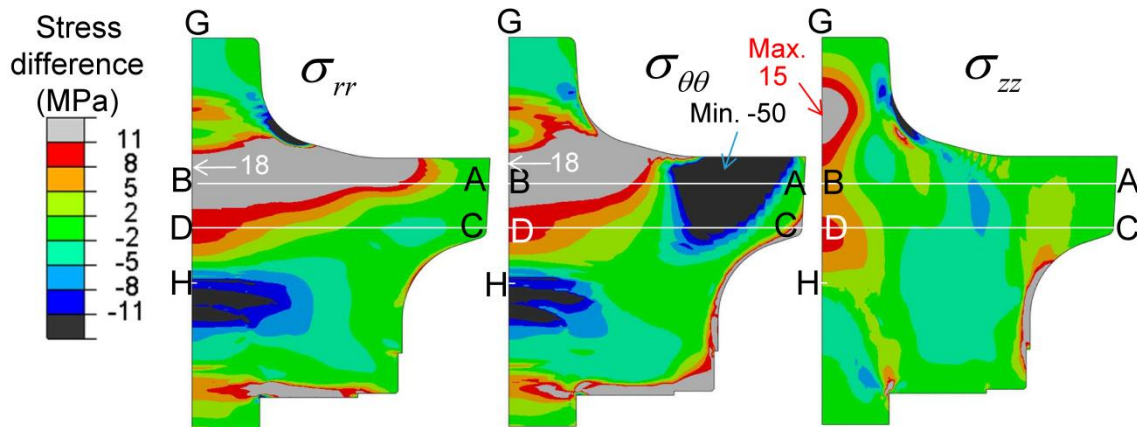


Figure 7-31 – Subtraction of stresses in large forging predicted by the TMG model with $T_{cum} = 325^{\circ}\text{C}$ to those predicted by the TMG model ignoring plastic strain recovery ($T_{cum} = 530^{\circ}\text{C}$).

The RS predicted using $T_{cum} = 530^{\circ}\text{C}$ are much higher in absolute value than those predicted using $T_{cum} = 325^{\circ}\text{C}$.

From these simulations, the value of 325°C has been chosen for T_{cum} in all the FE quenching simulations of AA2618 forgings.

7.8. Application of isothermal model to non-isothermal testing

One way to implement Eq. 4-21 in a FE code is to tabulate the parameters given in *Figure 7-32* at the different testing temperatures. In a thermo-mechanical model of quenching, these parameters are interpolated as a function of temperature. Here, an experiment is proposed to verify that a linear interpolation of the parameters determined in section 6.3.5 can be used to simulate non-isothermal testing. In other words, the mechanical model calibrated using tensile loads at constant temperature is applied to a non-isothermal tensile load. This experiment consists in cooling a specimen in the Gleeble, while the jaws are blocked as shown in *Figure 7-32*.

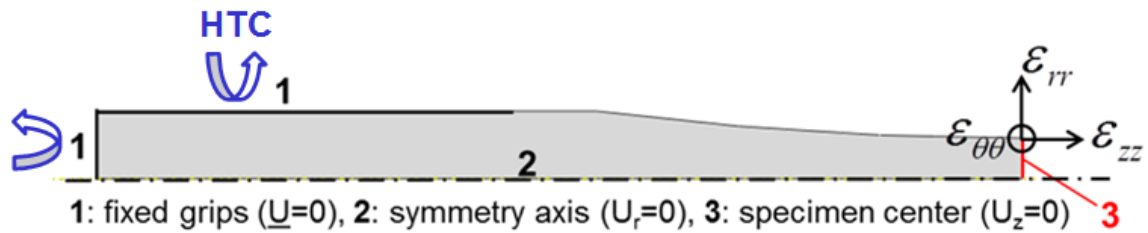


Figure 7-32 - Half of specimen modelled in Abaqus using an axisymmetric model. A Cauchy boundary condition is applied on the grip (surface 1) which is blocked.

Upon cooling, the specimen undergoes thermal contraction but it is constrained by the blocked jaws leading to the build-up of tensile axial stresses in the specimen. This test is similar upon cooling to the Satoh test performed by Zhang *et al.* to retrieve the thermo-mechanical behaviour of aluminium alloys [179].

In the FE simulation, cooling is imposed by choosing a HTC describing the cooling by water-cooled grips. Outputs of the FE simulation are the reaction force at the left extremity of the specimen and the radial displacement at position of TC1 (*Figure 7-32*). The axial stress and the hoop strain at position of TC1 are derived from those outputs using Eq. 4-19.

In the experiments, the cooling imposed in the simulation is reproduced in the Gleeble. The resulting axial stress and the hoop strain measured in the Gleeble are compared to those obtained by FE simulation.

Fast cooling at blocked-jaw

The experimental results of cooling at blocked-jaw are shown in *Figure 7-33*, together with the results by FE simulation using Eq. 4-21 with AA2618 parameters (H , n , K , m) given in *Figure 4-22* and σ_y values identified on tensile loads performed after GC at 20 K/s interrupted at either 500°C, 450°C, 400°C, 350°C, 300°C, 250°C, 200°C, 150°C or 20°C.

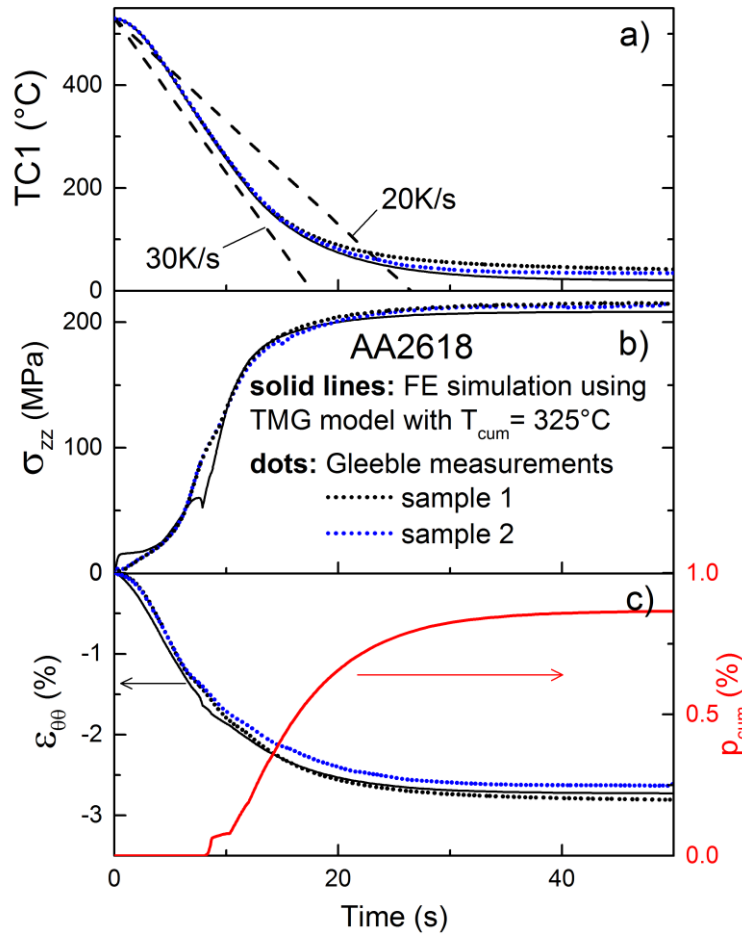


Figure 7-33 – Results of fast cooling at blocked-jaw for AA2618: comparison between measured (short dots) and simulated (solid lines) temperature (a), axial stress (b) and hoop strain (c) evolutions. Two experimental curves are shown since testing is duplicated.

The imposed cooling (solid line in Figure 7-33-a) is chosen to have cooling rates slightly higher than 20 K/s. This justifies the use of σ_y values identified on tensile loads performed after GC at 20 K/s in the Gleeble. The measured temperature (short dots in Figure 7-33-a) is close to the simulated temperature evolution imposed in the Gleeble (solid lines), except at the end where the measured cooling is slightly slower than the imposed one.

As expected by the simulation (TMG model based on Gleeble interrupted quench-tests at 20 K/s), a tensile axial stress (Figure 7-33-b) and a negative hoop strain (Figure 7-33-c) are measured. The stress and strain measurements are reproducible and the agreement between measurements and simulation is excellent which made us confident for the application of the model to non-isothermal unconstrained coolings such as quenches. The predicted value of p_{cum} is almost always increasing during cooling, thus indicating that the specimen plastifies all along the test.

Since the Gleeble measurements in appendix 7.7.4 do not provide a single value for T_{cum} but a temperature interval]300-400°C[, T_{cum} was varied in the FE quenching simulations

(Figure 7-30). This resulted in low RS differences whether 325°C or 325°C are taken for T_{cum} . A value of 325°C was chosen for the FE quenching simulations of forgings.

For the fast cooling at blocked-jaw, this value of 325°C gives a good agreement between predicted and measured stresses in Figure 7-33. The stress evolution as a function of temperature is shown in Figure 7-34 with FE simulations using:

- the TMG model ignoring plastic strain recovery at high temperature ($T_{cum} = 530^\circ\text{C}$),
- the TMG model with plastic strain recovery above either 325°C or 350°C,
- the TM model with plastic strain recovery above 350°C.

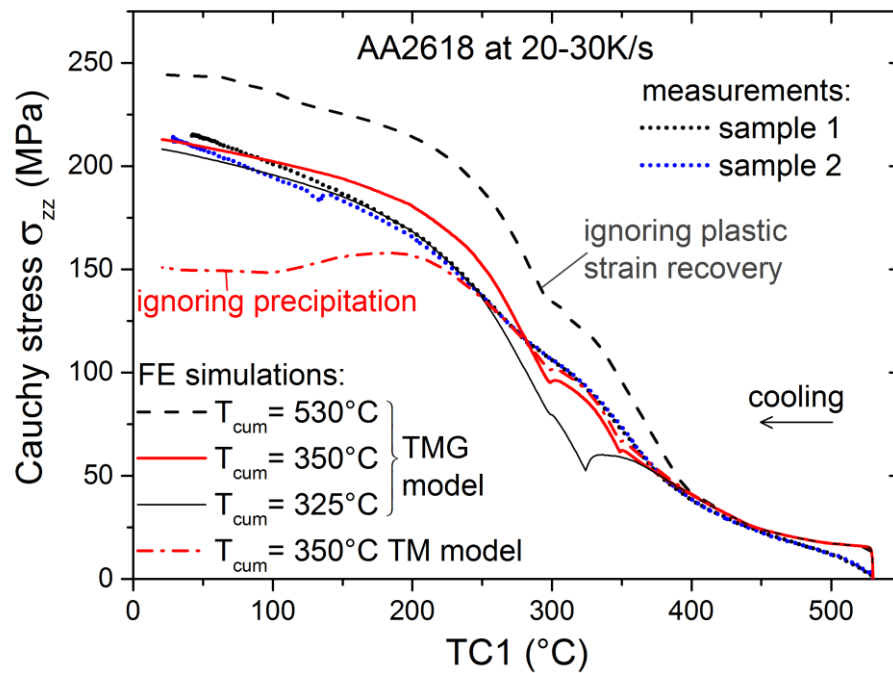


Figure 7-34 – Stress evolution during constrained cooling at blocked-jaw.

The TMG model predicts stresses in relatively good agreement with the measurements when 325°C or 350°C are taken for T_{cum} . Some differences between the stresses predicted using these two values of T_{cum} can be seen in Figure 7-34. On one hand, the value of 350°C instead of 325°C provides a better agreement with the measured stresses between 275°C and 375°C. On the other hand, the agreement between 150°C and 275°C is better with a value of 325°C for T_{cum} . At the end of cooling, the residual stresses predicted by the TMG model with plastic strain recovery above either 325°C or 350°C differ only by 2%.

Ignoring plastic strain recovery ($T_{cum} = 530^\circ\text{C}$ in Figure 7-34), however, leads to RS overestimated by ca. 15% compared to the measured RS.

This fast cooling at blocked-jaw demonstrates for AA2618 that the TMG model calibrated using tensile loads at constant temperature can be applied to non-isothermal tensile loads.

The TM model ignoring precipitation underestimates RS by ca. 25% compared to the measurements. This is due to the fact that precipitation hardening during cooling at 20-30 K/s is not taken into account in the TM model.

In the fast cooling at blocked-jaw, the cooling rate is higher than the critical cooling rate of S phase in AA2618 of ca. 17 K/s. Coarse precipitation is thereby avoided in these tests, which is not the case in forgings where the cooling rates above 300°C are always lower than 5 K/s.

In order to be closer to the cooling conditions encountered during BWQ of forgings, lower cooling rates above 300°C should be applied. Such experiments would help determining the forging size above which high temperature precipitation will significantly affect residual stresses.

7.9. Validation of yield strength model

As explained at the end of section 4.3.6, the interrupted quenches achieved in the Gleeble are imposed in the precipitation model calibrated by P. Schloth [50] for the small precipitates in order to assess the predictability of the calibrated yield strength model for various cooling conditions different from those used for its calibration as shown in *Figure 7-35* and *Figure 7-36* for AA7449 and in *Figure 7-37* and *Figure 7-38* for AA7040.

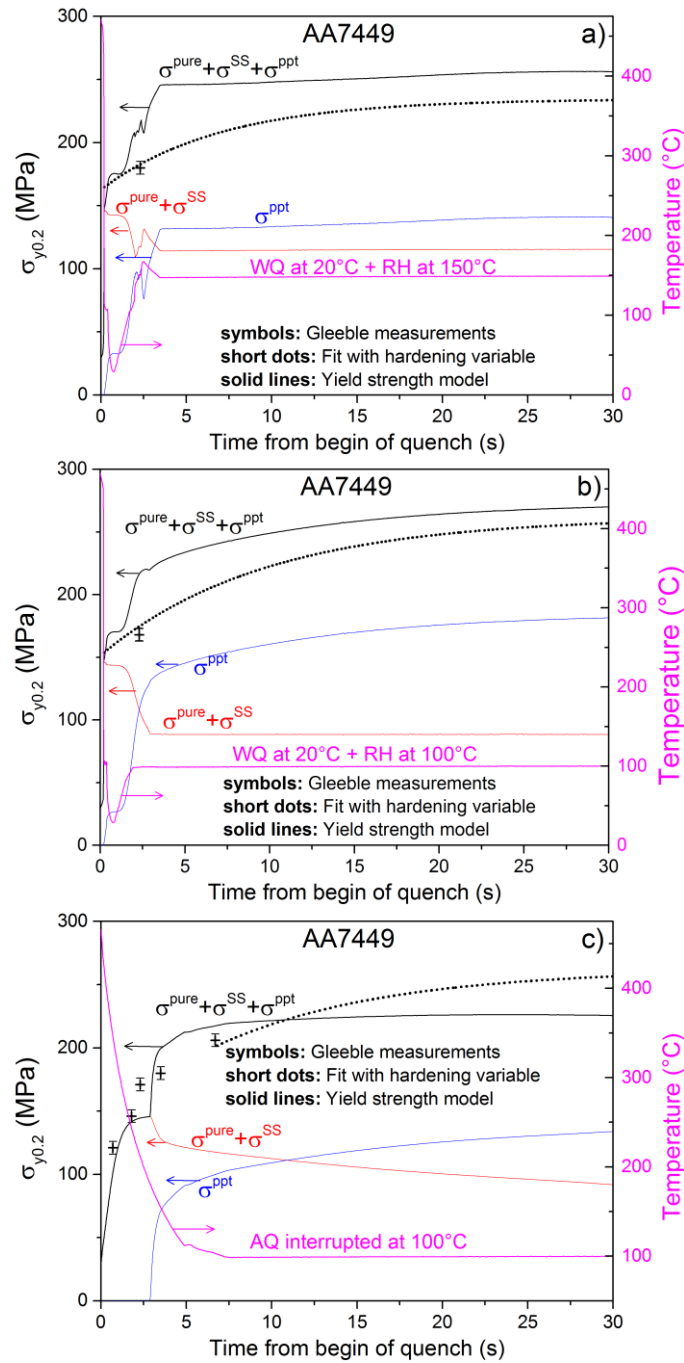


Figure 7-35 – Evolution of $\sigma_{y0.2}$ values obtained experimentally (Gleeble measurements after interrupted quenches), predicted using the fit with hardening variable (Eq. 4-21 and Eq. 4-23 with parameters identified in Figure 4-21-a and b) and predicted using the calibrated yield strength model after various cooling conditions (a), (b) and (c) for AA7449.

After water quench followed by reheat (*Figure 7-35-a and b*), the calibrated yield strength model confirms that precipitation occurs during reheat but predicts $\sigma_{y0.2}$ values much higher (~40 MPa) than the experimental ones obtained after ca. 2 seconds. For longer times, $\sigma_{y0.2}$ values predicted by the yield strength model are higher (~15-30 MPa) than those calculated using the fit with hardening variable (exponential law in *Eq. 4-23*) but the difference between both predictions decreases with increasing time.

After air quench interrupted at 100°C (*Figure 7-35-c*), the $\sigma_{y0.2}$ values predicted by the calibrated yield strength model compare very well with the experimental values for relatively short times (< 10 sec) but are lower (~15-30 MPa) than those obtained using the fit with hardening variable for longer times.

Figure 7-36 shows the overall good agreement between experimental $\sigma_{y0.2}$ values and the predicted values by the yield strength model after surface coolings for AA7449.

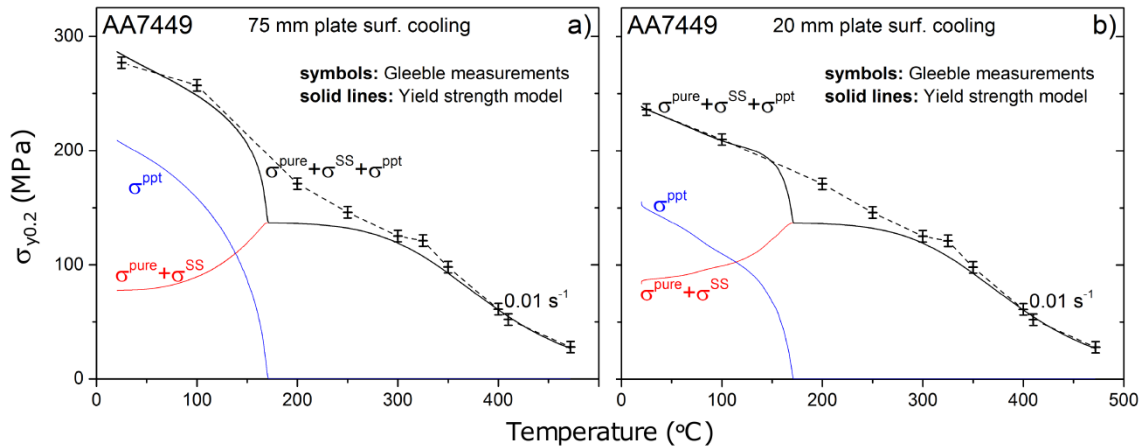


Figure 7-36 – $\sigma_{y0.2}$ values for AA7449 obtained experimentally and predicted by the calibrated yield strength model coupled to the precipitation model for surface cooling of 75 mm plate (a) and 20 mm plate (b). Interpolation of measurements in dashed lines are guide for the eye.

At high temperature (> 300°C), the yield strength model fits almost perfectly the measurements as expected by the good calibration shown in *Figure 4-32*.

At low temperature (< 160°C) where the formation of clusters is taken into account in the precipitation model, the agreement between measured and predicted yield strength is good. This demonstrates the good predictability of the calibrated yield strength for 20 mm and 75 mm AA7449 plate surface coolings.

At intermediate temperature (160-300°C) where precipitation is not considered in the precipitation model, the measured yield strength is higher than the predicted one. This is explained by the fact that precipitation of η' takes place in the measurements but is ignored in the precipitation model above ca. 170°C. This simplification in the precipitation model leads to $\sigma_{y0.2}$ -Temperature curves which are not realistic at ca. 170°C. However, this has no consequence on RS calculations in water-quenched thick plates since deformation is elastic between 150°C and 250°C.

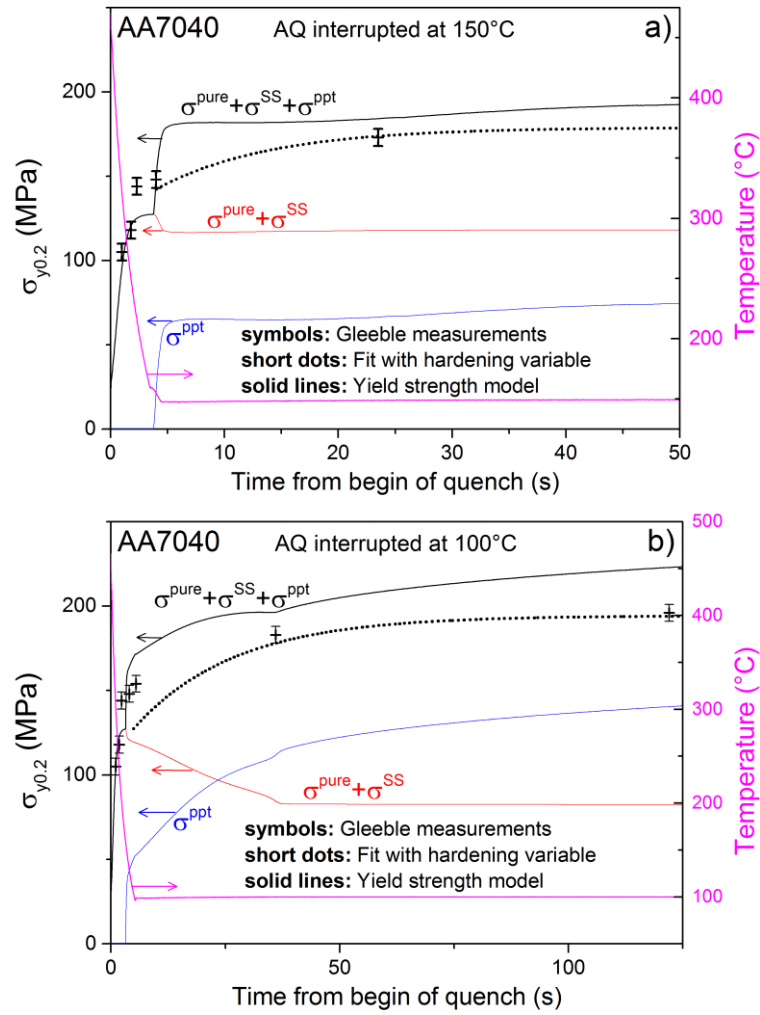


Figure 7-37 – Evolution of $\sigma_{y0.2}$ values obtained experimentally, predicted using the fit with hardening variable (Eq. 4-21 and Eq. 4-23 with parameters identified in Figure 4-21-a and b) and predicted using the calibrated yield strength model after AQ interrupted at 150°C (a) and 100°C (b) for AA7040.

For AA7040 after AQ interrupted at either 150°C or 100°C, the yield strength model compares well with the measurements for short times (< 5 sec) but overestimates (~15-30 MPa) $\sigma_{y0.2}$ values at longer times.

Figure 7-38 shows that the agreement between experimental $\sigma_{y0.2}$ values and the predicted values by the yield strength model after surface coolings for AA7040 is poor below ca. 265°C.

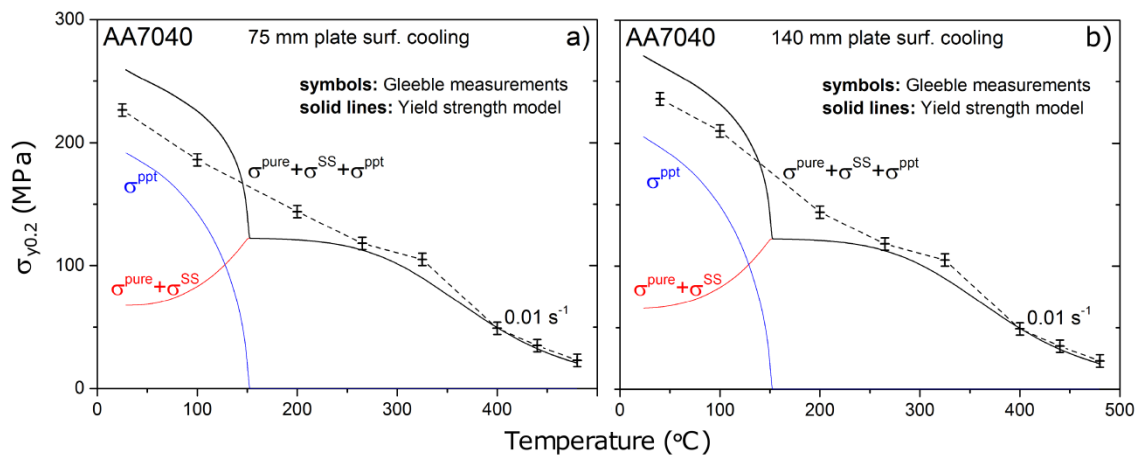


Figure 7-38 – $\sigma_{y0.2}$ values for AA7040 obtained experimentally and predicted by the calibrated yield strength model coupled to the precipitation model for surface cooling of 75 mm plate (a) and 140 mm plate (b). Interpolation of measurements in dashed lines are guide for the eye.

At high temperature ($> 300^\circ\text{C}$), the yield strength model fits almost perfectly the measurements as expected by the good calibration presented in Figure 4-32.

At low temperature ($< 150^\circ\text{C}$) where the formation of clusters is taken into account in the precipitation model, the predicted yield strength values are much higher ($\sim 30 \text{ MPa}$) than the measurements. The origin of this discrepancy is discussed in the SAXS results on AA7040 in section 3.1.3. This shows the poor predictability of the calibrated yield strength for 75 mm and 140 mm AA7040 plate surface coolings. Therefore, the TMM model is not be implemented for cold-water quenching of AA7040 thick plates. Indeed, with the present calibrated precipitation model, the TMM model would overpredict RS in both 75 mm and 140 mm thick AA7040 plates. For accurate RS predictions in AA7040 thick plates using the TMM model, the precipitation model must be re-calibrated to better fit the volume fraction of clusters measured during fast SAXS cooling (Figure 3-3-b).

7.10. Predicted vs measured as-quenched RS in large forging

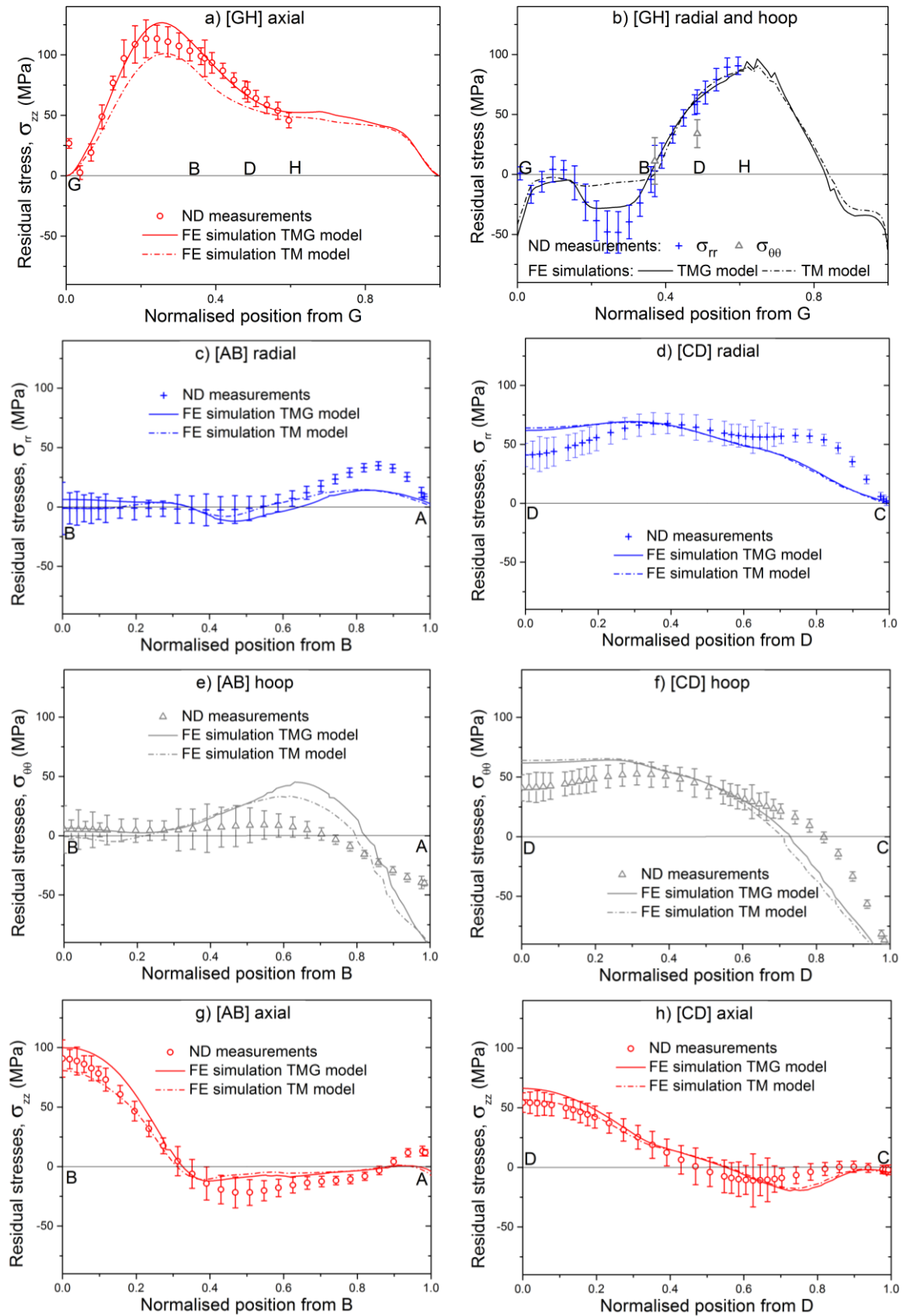


Figure 7-39 – Comparison between measured residual stress components and simulated ones using the TM model and the TMG model along [GH], [AB] and [CD] in as-quenched large forging.

In the as-quenched large forging, the TM model and the TMG model give similar values except in the region where tensile stresses are maximal around B where the simulation ignoring precipitation (TM model) underestimates measurements. The agreement in terms of residual stresses is improved using a TMG model based on Gleeble interrupted quench-tests at 20 K/s, meaning that precipitation hardening during cooling has to be taken into account to predict reasonably well residual strains and stresses.

BIBLIOGRAPHY

1. Pouget, G. and C. Sigli, *Thermal Stability of Al-Cu-Mg Alloys*. Materials Science Forum, 2014. **794**: p. 691-696.
2. Robinson, J.S., D.A. Tanner, and C.E. Truman, *50th Anniversary Article: The Origin and Management of Residual Stress in Heat-treatable Aluminium Alloys*. Strain, 2014. **50**(3): p. 185-207.
3. Jeanmart, P. and J. Bouvaist, *Finite element calculation and measurement of thermal stresses in quenched plates of high-strength 7075 aluminium alloy*. Materials Science and Technology, 1985. **1**(10): p. 765-769.
4. Boyer, J.C. and M. Boivin, *Numerical calculations of residual-stress relaxation in quenched plates*. Materials Science and Technology, 1985. **1**(10): p. 786-792.
5. Prime, M.B. and M.R. Hill, *Residual stress, stress relief, and inhomogeneity in aluminum plate*. Scripta Materialia, 2002. **46**(1): p. 77-82.
6. Dubost, B., et al., *Prediction and Minimization of Residual Stresses in Quenched Aluminium Alloy Die Forgings*. Proceedings of the International Conference on Residual Stresses, Edited by: G. Beck, S. Denis and A. Simon, Springer, 1989: p. 581-586.
7. Godard, D., et al., *Modelling of heat treatment residual stresses. Application to high strength aluminium alloys including precipitation effects*. Proceedings of the 7th International Seminar of IFHT on Heat Treatment and Surface Engineering of Light Alloys, Edited by: J. Lendvai and T. Réti, 1999: p. 249-257.
8. Dumont, D., et al., *Characterisation of precipitation microstructures in aluminium alloys 7040 and 7050 and their relationship to mechanical behaviour* Materials Science and Technology, 2004. **20**(5): p. 567-576.
9. Chobaut, N., D. Carron, and J.M. Drezet, *Monitoring precipitation kinetics in heat treatable aluminium alloys using in-situ resistivity in Gleeble thermomechanical simulator*. Materials Science Forum, 2014. **794-796**: p. 921-925.
10. Schloth, P., et al., *Early precipitation during cooling of an Al-Zn-Mg-Cu alloy revealed by in situ small angle X-ray scattering*. Applied Physics Letters, 2014. **105**(10): p. 101908.
11. Godard, D., et al., *Precipitation sequences during quenching of the AA 7010 alloy*. Acta Materialia, 2002. **50**(9): p. 2319-2329.
12. Shuey, R. and M. Tiryakioğlu, *Quenching of aluminium alloys*, in *Quenching Theory and Technology, Second Edition*, H.M.T. B. Liscic, L. C. F. Canale, G. E. Totten, Editor. 2010, CRC Press. p. 43-83.
13. Mackerle, J., *Finite element analysis and simulation of quenching and other heat treatment processes: a bibliography (1976–2001)*. Computational Materials Science, 2003. **27**(3): p. 313-332.
14. Inoue, T., Z.G. Wang, and K. Miyao, *Quenching Stress of Carburised Steel Gear Wheel," Proc. International Conference on Residual Stresses* Proceedings of the International Conference on Residual Stresses, Edited by: G. Beck, S. Denis and A. Simon, Springer, 1988: p. 606-611.
15. Wang, Y., *Etude et modélisation de l'effet du revenu sur les évolutions des microstructures, du comportement thermomécanique et des contraintes résiduelles de trempe*, PhD thesis INPL, 2006.
16. Denis, S., et al., *Prediction of residual stress and distorsion of ferrous and non-ferrous metals: current status and future developments*. Journal of Materials Engineering and Performance, 2002. **11**: p. 92-102.
17. Godard, D., *Influences de la précipitation sur le comportement thermomécanique lors de la trempe d'un alliage Al-Zn-Mg-Cu*, PhD Thesis INPL, 1999.
18. Deschamps, A., et al., *In situ evaluation of dynamic precipitation during plastic straining of an Al-Zn-Mg-Cu alloy*. Acta materialia, 2012. **60**(5): p. 1905-1916.

19. Gandin, C.A., et al., *Modelling of solidification and heat treatment for the prediction of yield stress of cast alloys*. Acta Materialia, 2002. **50**(5): p. 901-927.
20. Deschamps, A. and Y. Brechet, *Influence of predeformation and ageing of an Al–Zn–Mg alloy—II. Modeling of precipitation kinetics and yield stress*. Acta Materialia, 1998. **47**(1): p. 293-305.
21. Archambault, P., et al., *Prediction of heat treatment residual stresses. Application to quenching of high strength aluminium alloys including precipitation effects*. Proceedings of the 7th International Seminar of IFHT on Heat Treatment and Surface Engineering of Light Alloys, Edited by: J. Lendvai and T. Réti, 1999: p. 249-258.
22. Godard, D., et al., *Mechanical softening kinetics at high temperatures in AlMgZnCu Alloy: experimental characterization and microstructural interpretation*. Proceedings of ICAA6, Edited by: T. Sato, S. Kumai, T. Kobayashi, Y. Murakami, 1998: p. 1033-1038.
23. Drezet, J., et al., *Proceedings of the Symposium Sponsored by the Light Metals Division of The Minerals, Metals and Materials Society (TMS)*, 2010: p. 43-52.
24. Heymes, F., et al., *Development of New Al Alloys for distortion Free Machined Aluminium Aircraft Components*. Proceedings of the First International Non-Ferrous Processing and Technology Conference, St. Louis, USA, 1997: p. 249-255.
25. Robinson, J.S., et al., *Residual stress in 7449 aluminium alloy forgings*. Materials Science and Engineering: A, 2010. **527**(10-11): p. 2603-2612.
26. Tanner, D.A. and J.S. Robinson, *Effect of precipitation during quenching on the mechanical properties of the aluminium alloy 7010 in the W-temper*. Journal of Materials Processing Technology, 2004. **153–154**: p. 998-1004.
27. Rogante, M., P. Battistella, and F. Rusticelli, *Residual stress measurement by neutron diffraction in AA6082 extruded samples submitted to different quenching rates*. Journal of alloys and compounds, 2004. **378**(1): p. 335-338.
28. Li, P., et al., *Simulating the residual stress in an A356 automotive wheel and its impact on fatigue life*. Metallurgical and Materials Transactions B, 2007. **38**(4): p. 505-515.
29. Chobaut, N., et al., *Residual stress analysis in AA7449 as-quenched thick plates using neutrons and FE modelling*. Proceedings of ICAA13, Edited by: Hasso Weiland, Anthony D. Rollett, William A. Cassada, TMS, 2012: p. 285–291.
30. Dumont, D., A. Deschamps, and Y. Brechet, *On the relationship between microstructure, strength and toughness in AA7050 aluminum alloy*. Materials Science and Engineering A, 2003. **356**(1-2): p. 326-336.
31. Archambault, P. and D. Godard, *High temperature precipitation kinetics and TTT curve of a 7xxx alloy by in-situ electrical resistivity measurements and differential calorimetry*. Scripta Materialia, 2000. **42**(7): p. 675-680.
32. Raeisinia, B., W.J. Poole, and D.J. Lloyd, *Examination of precipitation in the aluminum alloy AA6111 using electrical resistivity measurements*. Materials Science and Engineering: A, 2006. **420**(1-2): p. 245-249.
33. Starink, M. and X. Li, *A model for the electrical conductivity of peak-aged and overaged Al–Zn–Mg–Cu alloys*. Metallurgical and Materials Transactions A, 2003. **34**(4): p. 899-911.
34. Staley, J.T., *Quench factor analysis of aluminium alloys*. Materials Science and Technology, 1987. **3**: p. 923-935.
35. Robinson, J.S. and D.A. Tanner, *Materials Science and Technology*, 2011 in press.
36. Banhart, J., et al., *Kinetics of natural aging in Al–Mg–Si alloys studied by positron annihilation lifetime spectroscopy*. Physical Review B, 2011. **83**(1): p. 014101.
37. Micro-measurements, *Tech Note 503 Measurement of Residual Stresses by the Hole-Drilling Strain Gage Method*, 2010.
38. Belahcene, F., *Détermination des contraintes résiduelles par méthode ultrasonore*. Techniques de l'ingénieur, 2002.

39. Drezet, J.M. and A. Phillion, *As-cast residual stresses in an aluminum alloy AA6063 billet: neutron diffraction measurements and finite element modeling*. Metallurgical and Materials Transactions A, 2010. **41**(13): p. 3396-3404.
40. Robinson, J.S., *Measurement and Prediction of Machining Induced Redistribution of Residual Stress in the Aluminium Alloy 7449*, 2010, Experimental Mechanics.
41. Drezet, J.-M., *Measurement of as-cast residual stresses in an aluminium alloy AA6063 billet using neutron diffraction*, 2010, The Minerals, Metals & Materials Society.
42. Fribourg, G., *Precipitation and plasticity couplings in a 7xxx aluminium alloy: application to thermomechanical treatments for distortion correction of aerospace components*, PhD thesis Grenoble INP, 2009.
43. Deschamps, A., et al., *In situ evaluation of the microstructure evolution during rapid hardening of an Al–2.5Cu–1.5Mg (wt.%) alloy*. Acta Materialia, 2011. **59**(8): p. 2918-2927.
44. Maisonnnette, D., *Influences mécaniques et métallurgiques de procédés haute température sur un alliage d'aluminium 6061-T6*, PhD thesis INSA Lyon, 2010.
45. Staab, T.E., et al., *Atomic structure of pre-Guinier-Preston and Guinier-Preston-Bagaryatsky zones in Al-alloys*. Journal of Physics, 2011. **265**(1): p. 012018.
46. Wang, S., M. Starink, and N. Gao, *Precipitation hardening in Al–Cu–Mg alloys revisited*. Scripta Materialia, 2006. **54**(2): p. 287-291.
47. Berg, L.K., et al., *GP-zones in Al–Zn–Mg alloys and their role in artificial aging*. Acta Materialia, 2001. **49**(17): p. 3443-3451.
48. Liu, S., et al., *Investigation of quench sensitivity of high strength Al–Zn–Mg–Cu alloys by time–temperature–properties diagrams*. Materials & Design, 2010. **31**(6): p. 3116-3120.
49. Fischer, G., G. Terlinde, and M. Hilpert, *OTTO FUCHS KG*, patent number 20110008202, 2011.
50. Schloth, P., *Precipitation in the high strength AA7449 Aluminium alloy: implications on internal stresses on different length scales*, PhD thesis EPFL n°6525, 2015.
51. Robinson, J., et al., *Influence of quenching and aging on residual stress in Al-Zn-Mg-Cu alloy 7449*. Materials Science and Technology, 2012. **28**(4): p. 420-430.
52. Dolan, G.P., et al., *Quench factor analysis of aluminium alloys using the Jominy end quench technique*. Materials science and technology, 2005. **21**(6): p. 687-692.
53. Bernardin, J.D. and I. Mudawar, *Experimental and statistical investigation of changes in surface roughness associated with spray quenching*. International Journal of Heat and Mass Transfer, 1996. **39**(10): p. 2023-2037.
54. Faghri, A. and Y. Zhang, *Transport Phenomena in Multiphase Systems*. Elsevier, Burlington, MA, 2006.
55. Tanner, D.A., *Measurement and finite element prediction of residual stresses in aluminium alloy 7010 forgings*, PhD thesis University of Limerick, 1999.
56. Yu, X. and J.S. Robinson, *Measurement of the heat transfer coefficient during quenching of the aluminium alloy 7449*. COMPACT project, 2007.
57. Yazdi Rasouli, S., D. Retraint, and J. Lu, *Study of through-thickness residual stress by numerical and experimental techniques*. Journal of strain analysis, 1998. **33**(6): p. 449-458.
58. Pitts, D.R. and L.E. Sissom, *Theory and Problems of Heat Transfer*. McGraw_Hill, New York, USA, 1977.
59. Michel, G., *Investigation of the build-up of residual stresses in large impellers during quenching*, Internal report ABB, 2014.
60. Rosenthal, D. and J.T. Norton, *A method of measuring triaxial residual stresses in plates*. Welding journal, 1945. **24**(5): p. 295-307.
61. Van Der Veen, S., et al., *Low internal stress Al-Zn-Cu-Mg plates*, 2006, Google Patents.

62. Hutchings, M.T., et al., *Introduction to the characterization of residual stress by neutron diffraction*. 2004: CRC Press.
63. Pawley, G.S., *Unit-cell refinement from powder diffraction scans*. Journal of Applied Crystallography, 1981. **14**: p. 357-361.
64. Fitzpatrick, M.E. and A. Lodini, *Analysis of residual stress by diffraction using neutron and synchrotron radiation*. 2003: CRC Press.
65. Hertzberg, R.W., *Deformation and fracture mechanics of engineering materials*. Wiley, New-York, 1996. **89**.
66. Johnson, M.W. and M.R. Daymond, *Analysis of residual stresses by diffraction using neutron and synchrotron radiation*. in: M.E. Fitzpatrick, A. Lodini (Eds.), Taylor & Francis, London, 2003: p. 146-169.
67. Lu, H., et al., *Precipitation behavior of AA2618*. Metallurgical and Materials Transactions A, 2007. **38**(10): p. 2379-2388.
68. Polmear, I.J., Trans AIME, 1964. **230**: p. 1331.
69. Oguocha, I.N.A. and S. Yannacopoulos, *Precipitation and dissolution kinetics in Al-Cu-Mg-Fe-Ni alloy 2618 and Al-alumina particle metal matrix composite*. Materials Science and Engineering: A, 1997. **231**(1): p. 25-33.
70. Herding, T., et al., *An approach for Continuous Cooling Transformation (CCT) diagrams of aluminium alloys*. Materials Science Forum, 2002. **396-402**: p. 869-874.
71. Milkereit, B., O. Kessler, and C. Schick, *Recording of continuous cooling precipitation diagrams of aluminium alloys*. Thermochemica Acta, 2009(492): p. 73-78.
72. Milkereit, B., et al., *Continuous cooling precipitation diagrams of Al-Mg-Si alloys*. Materials Science and Engineering: A, 2012. **550**(0): p. 87-96.
73. Zhang, Y., et al., *Development of continuous cooling precipitation diagrams for aluminium alloys AA7150 and AA7020*. Journal of alloys and compounds, 2014. **584**(0): p. 581-589.
74. Deschamps, A., et al., *Influence of cooling rate on the precipitation microstructure in a medium strength Al-Zn-Mg alloy*. Materials Science and Engineering: A, 2009. **501**(1-2): p. 133-139.
75. Kessler, O., et al., *Continuous cooling transformation (CCT) diagram of aluminum alloy Al-4.5Zn-1Mg*, in *Materials Science Forum* 2006. p. 1467-1472.
76. Zohrabyan, D., et al., *Precipitation enthalpy during cooling of aluminum alloys obtained from calorimetric reheating experiments*. Thermochemica Acta, 2012. **529**: p. 51-58.
77. Perez, M., O. Lame, and A. Deschamps, *Global Techniques for Characterizing Phase Transformations—A Tutorial Review*. Advanced Engineering Materials, 2010. **12**(6): p. 433-446.
78. Vooijs, S., et al., *Monitoring the precipitation reactions in a cold-rolled Al-Mn-Mg-Cu alloy using thermoelectric power and electrical resistivity measurements*. Philosophical Magazine A, 2001. **81**(8): p. 2059-2072.
79. Dehmas, M., et al., *Experimental study of phase transformations in 3003 aluminium alloys during heating by in situ high energy X-ray synchrotron radiation*. Journal of alloys and compounds, 2005. **400**(1): p. 116-124.
80. De Geuser, F. and A. Deschamps, *Precipitate characterisation in metallic systems by small-angle X-ray or neutron scattering*. Comptes Rendus Physique, 2012. **13**(3): p. 246-256.
81. Deschamps, A. and F. De Geuser, *On the validity of simple precipitate size measurements by small-angle scattering in metallic systems*. Journal of Applied Crystallography, 2011. **44**(2): p. 343-352.
82. Fribourg, G., et al., *Microstructure-based modelling of isotropic and kinematic strain hardening in a precipitation-hardened aluminium alloy*. Acta Materialia, 2011. **59**(9): p. 3621-3635.

83. Schloth, P., et al., *Early solute clustering during cooling in the AA2618 alloy by in situ small angle X-ray scattering*. submitted to Scripta Materialia, 2015.
84. Milkereit, B., et al., *Precipitation kinetics of an aluminium alloy during Newtonian cooling simulated in a differential scanning calorimeter*. Thermochimica Acta, 2011. **522**(1–2): p. 86-95.
85. Shen, P., *The effects of heat treatment on the microstructure and mechanical properties of the AA2618 DC cast plate*, Master thesis Université du Québec, 2012.
86. Samuel, C. and S. Viswanathan, *Specimen configurations for gleeble dilatometry of steels*. Materials Science and Technology, 2008: p. 1872-1883.
87. Ferragut, R., A. Somoza, and I. Torriani, *Pre-precipitation Study in the 7012 Al-Zn-Mg-Cu alloy by Electrical Resistivity*. Materials Science and Engineering A, 2002. **334**(1): p. 1-5.
88. Eon-Sik, L. and Y.G. Kim, *A transformation kinetic model and its application to Cu - Zn - Al shape memory alloys—II. Non-isothermal conditions*. Acta Metallurgica et Materialia, 1990. **38**(9): p. 1677-1686.
89. Starink, M.J., *Kinetic equations for diffusion-controlled precipitation reactions*. Journal of Materials Science, 1997. **32**(15): p. 4061-4070.
90. Ma, S., et al., *A Methodology to Predict the Effects of Quench Rates on Mechanical Properties of Cast Aluminum Alloys*. Metallurgical and Materials Transactions B, 2007. **38**(4): p. 583-589.
91. Serriere, M., *Modélisation des processus de transformation des dispersoïdes dans un alliage d'aluminium 3003. Influence de la description des équilibres thermodynamiques locaux*, PhD thesis INPL, 2004.
92. Gandin, C.-A. and A. Jacot, *Modeling of precipitate-free zone formed upon homogenization in a multi-component alloy*. Acta Materialia, 2007. **55**(7): p. 2539 – 2553.
93. Rappaz, M., et al., *Application of inverse methods to the estimation of boundary conditions and properties*. TMS Publ., 1995: p. 449-457.
94. Godard, D., et al., *Proceedings of the International Conference on Solid-Solid Phase Transformations*, 1999: p. 145-148.
95. Du, Y., et al., *Diffusion coefficients of some solutes in fcc and liquid Al: critical evaluation and correlation*. Materials Science and Engineering: A, 2003. **363**(1): p. 140-151.
96. Krausz, A.S. and K. Krausz, *Unified constitutive laws of plastic deformation*. 1996: Elsevier.
97. Mo, A. and E. Holm, *On the use of constitutive internal variable equations for thermal stress predictions in aluminium casting*. Modeling, identification and control, 1993. **14**(1): p. 43-58.
98. Mo, A. and I. Farup, *The effect of work hardening on thermally induced deformations in aluminium DC casting*. Journal of Thermal Stresses, 2000. **23**(1): p. 71-89.
99. Haafte, W.M., et al., *Constitutive behavior of as-cast AA1050, AA3104, and AA5182*. Metallurgical and Materials Transactions A, 2002. **33**(7): p. 1971-1980.
100. Järvstrå, N. and S. Tjøtta, *A process model for on-line quenching of aluminium extrusions*. Metallurgical and Materials Transactions B, 1996. **27**(3): p. 501-508.
101. Ramberg, W. and W.R. Osgood, N.A.C.A., 1943. **TN 902**.
102. Davis, J.R., *Tensile testing*. 2004: ASM international.
103. Voce, E., *The relationship between stress and strain for homogeneous deformation*. Journal of the Institute of Metals, 1948. **74**: p. 537-562.
104. Mecking, H. and U.F. Kocks, Acta Metallurgica, 1981. **29**(11): p. 1865-1875.
105. Suni, J.P., R.T. Shuey, and R.D. Doherty, *Solute dependence of cold work strengthening in aluminium alloys*. Proceedings of ICAA4, 1994. **1**: p. 521-528.
106. Zolotarevsky, N.Y., et al., *Study of work hardening of quenched and naturally aged Al-Mg and Al-Cu alloys*. Materials Science and Engineering: A, 2009. **502**(1): p. 111-117.

107. Magnin, B., et al., *Ductility and rheology of an Al-4.5% Cu alloy from room temperature to coherency temperature*. Materials Science Forum, 1996. **217**: p. 1209-1214.
108. Reich, M. and O. Kessler, *A Study of the Bauschinger Effect in Undercooled Aluminium Alloys*. Proceedings of the 3rd International Conference on Distortion Engineering, 2011: p. 203-210.
109. Proudhon, H., et al., *The role of internal stresses on the plastic deformation of the Al-Mg-Si-Cu alloy AA6111*. Philosophical Magazine, 2008. **88**(5): p. 621-640.
110. Poirier, J.P., ed. *Plasticité à haute température des solides cristallins*. ed. Eyrolles. 1976.
111. Sherby, O.D. and J. Wadsworth, *Superplasticity—recent advances and future directions*. Progress in Materials Science, 1989. **33**(3): p. 169-221.
112. Sherby, O.D. and P.M. Burke, *Mechanical behavior of crystalline solids at elevated temperature*. Progress in Materials Science, 1968. **13**: p. 323-390.
113. Lagneborg, R. and B. Bergman, *The stress/creep rate behaviour of precipitation-hardened alloys*. Metal Science, 1976. **10**(1): p. 20-28.
114. Garofalo, *Fundamentals of Creep and Creep-Rupture in Metals*. 1985: MacMillan, New York.
115. Sellars, C.M. and W.J. McTegart, *On the mechanism of hot deformation*. Acta Metallurgica, 1966. **14**(9): p. 1136-1138.
116. McQueen, H.J. and N.D. Ryan, *Constitutive analysis in hot working*. Materials Science and Engineering: A, 2002. **322**(1): p. 43-63.
117. McQueen, H.J., *Effect of Solutes and Precipitates on Hot Working Behavior of Al Alloys*. Proceedings of symposium on hot deformation of aluminium alloys, Edited by: T.G. Langdon, H.D. Merchant, J.G. Morris, M.A. Zaidi, TMS, 1990: p. 105-120.
118. Jin, N., et al., *Hot deformation behavior of 7150 aluminum alloy during compression at elevated temperature*. Materials Characterization, 2009. **60**(6): p. 530-536.
119. Sheppard, T. and A. Jackson, *Constitutive equations for use in prediction of flow stress during extrusion of aluminium alloys*. Materials Science and Technology, 1997. **13**(3): p. 203-209.
120. Cerri, E., et al., *Comparative hot workability of 7012 and 7075 alloys after different pretreatments*. Materials Science and Engineering: A, 1995. **197**(2): p. 181-198.
121. Hu, H., et al., *Deformation behavior and microstructure evolution of 7050 aluminum alloy during high temperature deformation*. Materials Science and Engineering: A, 2008. **488**(1): p. 64-71.
122. Alankar, A. and M.A. Wells, *Constitutive behavior of as-cast aluminum alloys AA3104, AA5182 and AA6111 at below solidus temperatures*. Materials Science and Engineering: A, 2010. **527**(29-30): p. 7812-7820.
123. Barlas, B., *Etude du comportement et de l'endommagement en fatigue d'alliages d'aluminium de fonderie*, PhD thesis Ecole des Mines de Paris, 2004.
124. Carron D., et al., *Identification du comportement thermomécanique d'un alliage CuCr1Zr*. Revue de métallurgie, 2010. **107**(10-11): p. 445-448.
125. Le, M., *Approches expérimentale et numérique de la fissuration à chaud dans les soudures en acier inoxydable*, PhD thesis UBS, 2014.
126. Drezet, J.-M., et al., *Étude de la sensibilité à la fissuration à chaud d'un alliage CuCrZr au cours du soudage par faisceau d'électrons*. Matériaux & Techniques, 2010. **98**(4): p. 287-296.
127. Lemaitre, J. and J.L. Chaboche, eds. *Mécanique des Matériaux Solides*. 2e edition ed. 1988, Dunod.
128. Mecking, H. and U. Kocks, *Kinetics of flow and strain-hardening*. Acta Metallurgica, 1981. **29**(11): p. 1865-1875.
129. Estrin, *Dislocation theory based constitutive modelling: foundations and applications*. Journal of Materials Processing Technology, 1998. **80-81**: p. 33-39.

130. Dong, Y., T. Nogaret, and W. Curtin, *Scaling of dislocation strengthening by multiple obstacle types*. Metallurgical and Materials Transactions A, 2010. **41**(8): p. 1954-1960.
131. Friedel, J., *Dislocations*, 1st ed. 1964: Pergamon Press, Oxford, United Kingdom.
132. Kocks, U.F., A.S. Argon, and M.F. Ashby, *Thermodynamics and Kinetics of Slip*. Progress in Materials Science, 1975. **19**: p. 1-288.
133. Deschamps, A., *Précipitation durcissante dans les matériaux de structure, Mémoire d'habilitation à diriger des recherches, Grenoble INP*, 2009.
134. Haasen, P., *Mechanical properties of solid solutions and intermetallic compounds*. Physical Metallurgy, R.W. Cahn and P. Haasen, Eds., Chapter 21, 1983.
135. Cottrell, A.H., *Theory of dislocations*. Progress in Metal Physics, 1949. **1**: p. 77-126.
136. Suzuki, H., Sci. Rep. RITU, 1952. **A4**(455).
137. Fisher, J., *On the strength of solid solution alloys*. Acta metallurgica, 1954. **2**(1): p. 9-10.
138. Bardel, D., *Rôle de la microstructure d'un alliage à durcissement structural sur son comportement et sa tenue mécanique sous sollicitations cycliques après un transitoire thermique*, PhD thesis INSA Lyon, 2014.
139. Doherty, R.D. and J.K. McBride, *Solute enhanced strain hardening of aluminium. 1 - Mechanical properties*. Aluminium Alloys for Packaging, J.G. Morris, H.D. Merchant, E.J. Westerman and P.L. Morris, Eds., TMS, 1993.
140. Bardel, D., et al., *Coupled precipitation and yield strength modelling for non-isothermal treatments of a 6061 aluminium alloy*. Acta Materialia, 2014. **62**: p. 129-140.
141. Myhr, O., Ø. Grong, and S. Andersen, *Modelling of the age hardening behaviour of Al-Mg-Si alloys*. Acta Materialia, 2001. **49**(1): p. 65-75.
142. Simar, A., et al., *Integrated modeling of friction stir welding of 6xxx series Al alloys: Process, microstructure and properties*. Progress in Materials Science, 2012. **57**(1): p. 95-183.
143. Mott, N.F. and F.R.N. Nabarro, *Report of a Conference on Strength of Solids*. Phys. Soc., London, 1948: p. 1-19.
144. Labusch, R., *A statistical theory of solid solution hardening*. Physica status solidi, 1970. **41**(2): p. 659-669.
145. Embury, J.D., *A treatise on materials science and technology*. Vol. 31. 1989: Academic press. 579.
146. Ryen, Ø., et al., *Strengthening mechanisms in solid solution aluminum alloys*. Metallurgical and Materials Transactions A, 2006. **37**(6): p. 1999-2006.
147. Leyson, G., L. Hector Jr, and W. Curtin, *Solute strengthening from first principles and application to aluminum alloys*. Acta Materialia, 2012. **60**(9): p. 3873-3884.
148. Uesugi, T. and K. Higashi, *First-principles studies on lattice constants and local lattice distortions in solid solution aluminum alloys*. Computational Materials Science, 2013. **67**(0): p. 1-10.
149. Deschamps, A., Y. Brechet, and F. Livet, *Influence of copper addition on precipitation kinetics and hardening in Al-Zn-Mg alloy*. Materials Science and Technology, 1999. **15**(9): p. 993-1000.
150. Guyot, P. and L. Cottignies, *Precipitation kinetics, mechanical strength and electrical conductivity of AlZnMgCu alloys*. Acta materialia, 1996. **44**(10): p. 4161-4167.
151. Gerold, V., *Dislocations in solids*, ed. A. North-Holland. Vol. 4. 1979.
152. Deschamps, A., *Influence de la prédéformation et des traitements thermiques sur la microstructure et les propriétés mécaniques des alliages Al-Zn-Mg-Cu*, PhD Thesis Grenoble INP, 1999.
153. Wang, X., et al., *Precipitation strengthening of the aluminum alloy AA6111*. Metallurgical and Materials Transactions A, 2003. **34**(12): p. 2913-2924.
154. Carron, D., et al., *Modelling of precipitation during friction stir welding of an Al-Mg-Si alloy*. Technische mechanick, 2010. **30**: p. 29-44.

155. Myhr, O.R., Ø. Grong, and S.J. Andersen, *Modelling of the age hardening behaviour of Al–Mg–Si alloys*. Acta Materialia, 2001. **49**(1): p. 65-75.
156. Gouttebroze, S., et al., *A new constitutive model for the finite element simulation of local hot forming of aluminum 6xxx alloys*. Metallurgical and Materials Transactions A, 2008. **39A**(3): p. 522-534.
157. Gelin, J. and O. Ghouati, *An inverse method for determining viscoplastic properties of aluminium alloys*. Journal of materials processing technology, 1994. **45**(1): p. 435-440.
158. Aksel, B., W. Arthur, and S. Mukherjee, *A study of quenching: experiment and modelling*. Journal of Manufacturing Science and Engineering, 1992. **114**(3): p. 309-316.
159. Andrade-Campos, A., et al., *On the determination of material parameters for internal variable thermoelastic–viscoplastic constitutive models*. International Journal of Plasticity, 2007. **23**(8): p. 1349-1379.
160. Newman, M.L., et al., *Deformation, residual stress, and constitutive relations for quenched W319 aluminum*. Metallurgical and Materials Transactions A, 2003. **34**(7): p. 1483-1491.
161. Bellini, A., J.H. Hattel, and J. Thorborg, *Thermo-mechanical modelling of aluminium cast parts during solution treatment*. Modelling and Simulation in Materials Science and Engineering, 2006. **14**(4): p. 677.
162. Sheppard, T. and N. Raghunathan, *Modification of cast structures in Al–Mg alloys by thermal treatments*. Materials science and technology, 1989. **5**(3): p. 268-280.
163. J.G., K., *Properties of Aluminum Alloys: Tensile, Creep and Fatigue Data at High and Low Temperatures*. 1999. **ASM International, ISBN: 978-0-87170-632-4**.
164. Alhassan-Abu, A.R. and M.A. Wells, *Determinaton of constitutive behaviour of as cast AA 51 82 for deformations that occur during direct chill casting using the Gleeble 1500 machine*. Materials Science and Technology, 2003. **19**(1): p. 55-61.
165. Reich, M. and O. Kessler, *Mechanical properties of undercooled aluminium alloys and their implementation in quenching simulation*. Materials Science and Technology, 2012. **28**(7): p. 769-772.
166. Kessler, O. and M. Reich, *Mechanical properties of an undercooled aluminium alloy Al-0.6Mg-0.7Si*. Journal of Physics, 2010. **240**(1): p. 012093.
167. Norris, S. and I. Wilson, *Application of 3D numerical modelling for thermal profile optimization on the Gleeble thermomechanical simulator*. Modelling and Simulation in Materials Science and Engineering, 1999. **7**: p. 297-309.
168. Wisniewski, J., *Modélisation thermomécanique de la fissuration à chaud en soudage par faisceau d'électrons d'un alliage de CuCrZr*, PhD thesis UBS, 2009.
169. Zhang, H., et al., *Dynamic and static softening behaviors of aluminum alloys during multistage hot deformation*. Journal of Materials Processing Technology, 2004. **148**(2): p. 245-249.
170. Pilvin, P. and G. Cailletaud, *Identification and inverse problems related to material behaviour*. Proceedings of the second International Symposium on Inverse Problems, Edited by: H.D. Bui, M. Tanaka, M. Bonnet, H. Maigre, E. Luzzato and M. Reynier, Balkema, 1994: p. 79–86.
171. Graff, S., et al., *Finite element simulations of dynamic strain ageing effects at V-notches and crack tips*. Scripta Materialia, 2005. **52**(11): p. 1181-1186.
172. Cavaliere, P., *Hot and warm forming of 2618 aluminium alloy*. Journal of Light Metals, 2002. **2**(4): p. 247-252.
173. Simmons, G. and H. Wang, *Single Crystal Elastic Constants and Calculated Aggregate Properties*. 1971: A Handbook, MIT Press, Cambridge, MA.
174. Sha, G. and A. Cerezo, *Early-stage precipitation in Al–Zn–Mg–Cu alloy (7050)*. Acta Materialia, 2004. **52**(15): p. 4503-4516.
175. Abaqus, *Quenching of an infinite plate*, Abaqus Benchmarks Manual 6.10.

176. Landau, H., J. Weiner, and E. Zwicky, *Thermal stress in a viscoelastic-plastic plate with temperature-dependent yield stress*. Journal of applied mechanics, 1960. **27**(2): p. 297-302.
177. Boley, B.A. and J.H. Weiner, *Theory of thermal stresses*. 2012: Courier Dover Publications.
178. Sigli, C., et al., *Phase diagram, solidification and heat treatment of aluminium alloys*. Proceedings of ICAA6, Edited by: T. Sato, S. Kumai, T. Kobayashi, Y. Murakami, 1998: p. 87-98.
179. Zhang, Z., et al., *A method for retrieving temperature and microstructure dependent apparent yield strength for aluminium alloys*. Computational Materials Science, 2005. **34**(1): p. 35-45.

ACRONYMS AND ABBREVIATIONS

AA	Aluminium Alloys
ABB	Asea Brown Boveri
AQ	Air Quench
as-Q	as-quenched
BWQ	Boiling Water Quench
CCP	Continuous Cooling Precipitation
CRV	Centre de Recherche de Voreppe (now Constellium Technology Center)
CTE	Coefficient of Thermal Expansion
DSC	Differential Scanning Calorimetry
FE	Finite Element
GB	Grain Boundaries
GC	Grip Cooling
GP(B)	Guinier Preston (Bagaryatsky)
HTC	Heat Transfer Coefficient
HV	Vickers Hardness
IQ	Interrupted Quench
ND	Neutron diffraction
neSS	non-equilibrium Solid Solution
NGV	Nominal Gauge Volume
POLDI	Pulse OverLap Diffractometer
PSD	Precipitate Size Distribution
RH	Reheat
RS	Residual Stresses
SALSA	Strain Analysis for Large Scale Engineering Applications
SAXS	Small Angle X-rays Scattering
SHT	Solution Heat Treatment
SRS	Strain Rate Sensitivity
SS	Solid Solution
STRESS-SPEC	STRESS SPECTROMETER
TC	Thermocouple
TM model	Thermo-Mechanical model ignoring precipitation
TMG model	Thermo-Mechanical model with precipitation from Gleeble tests
TMM model	Thermo-Metallurgical-Mechanical model
TTP	Time-Temperature-Properties
WQ	Water Quench

LATIN CHARACTERS

a_{hard}	(-)	hardening variable
a_{soft}	(-)	softening variable
a_i	MPa/(at.%) ^{nss}	parameters of element i in solute strengthening equation
b	nm	magnitude of the Burgers vector
c_p	J.kg ⁻¹ .K ⁻¹	specific heat capacity
d^{hkl}	nm	interplanar spacing for planes hkl
d_0^{hkl}	nm	interplanar spacing of stress-free reference
e	mm	half plate thickness
E	MPa	Young's modulus
f	MPa	yield function
F	N	force for a dislocation to overcome a precipitate
F_p	N	intrinsic resistance force of a precipitate
f_v	(-)	precipitate volume fraction
h	mm	thickness of the layer removal bars
H	MPa	strain-hardening parameter of Ludwig power-law
HTC	W.m ⁻² .K ⁻¹	heat transfer coefficient
J_2	MPa ²	second invariant of the deviatoric stress tensor
K	MPa.s ^{-m}	consistency parameter of Norton-Hoff power law
k	W.m ⁻¹ .K ⁻¹	thermal conductivity
k_1	(-)	natural logarithm of the untransformed fraction
k_2	s	parameter related to the reciprocal of the nucleation site density
k_3	J.mol ⁻¹	parameter related to the energy required to form a nucleus
k_4	Kelvin	parameter related to the solvus temperature
k_5	kJ.mol ⁻¹	parameter related to the activation energy for diffusion
k_B	1.38 10 ²³ J.K ⁻¹	Boltzmann's constant
k_s	(-)	parameter for strengthening by small precipitates
$L = x$		rolling direction
\bar{L}	m	average distance between precipitates
M	(-)	Taylor's factor
M_i	(-)	number of measurement points
m	(-)	strain-rate sensitivity parameter of Norton-Hoff power law
$N = 1/m$	(-)	parameter of Norton-Hoff power law
n	(-)	strain hardening exponent of Ludwig power-law
n_{ss}	(-)	solute exponent
n_{dif}	(-)	diffraction order
n_p	(-)	number of parameters to identify
n_s	(-)	number of alloying elements
n_t	(-)	number of Gleeble tests at a given temperature
\dot{p}	s ⁻¹	equivalent inelastic strain rate

p_{cum}	(-)	equivalent accumulated inelastic strain
q	$W.m^{-2}$	heat flux
Q_{HW}	$kJ.mol^{-1}$	activation energy for hot working
R	$8.314 J.mol^{-1}.K^{-1}$	universal gas constant
R_{end}	$\mu\Omega$	value of the resistance decrease after complete solute depletion of the matrix
R_{start}	$\mu\Omega$	value of the resistance decrease of the neSS
r_g	nm	measured Guinier radius of precipitate
r_{trans}	nm	precipitate size corresponding to peak strength
R_{cyl}	mm	radius of cylindrical Gleeble specimens
s_L, s_{LT}	MPa	average stress in the bars in the L and LT directions
S		Al ₂ Cu Mg precipitates
$\underline{\underline{s}}$	MPa	deviatoric stress tensor
$TC = z$		transverse short direction
$TL = y$		transverse long direction
$t_{soft,0}$	s	initial time before which softening is neglected
$t_{hard,0}$	s	initial time before which hardening is neglected
T_m	Kelvin	melting temperature
T_0	°C	quenchant temperature
T_s	°C	surface temperature
T_n	°C	parameter of $HTC(T)$
T_{cum}	°C	onset of accumulation of inelastic deformation
$\underline{U}(P)$	mm	displacement field at point $P(r,z)$
X_i	at. %	atomic concentration of element i in the matrix
$\underline{\underline{X}}$	MPa	kinematic hardening tensor
Z	s^{-1}	Zener-Hollomon parameter

GREEK CHARACTERS

α_0, α_1	$\text{W.m}^{-2}.\text{K}^{-1}$	parameters of $HTC(T)$
α_2	(-)	parameter of $HTC(T)$
β	(-)	dislocation line tension parameter
ΔE_i^b	eV	characteristic energy barrier of element i at zero Kelvin
$\dot{\epsilon}_0^{in}$	s^{-1}	reference strain rate
ϵ	(-)	total strain
ϵ^e	(-)	elastic strain
ϵ^{in}	(-)	inelastic strain
ϵ^p	(-)	plastic strain
ϵ^{th}	(-)	thermal strain
ϵ_{SG}	(-)	strain gauge reading
ϕ	degree	rotation angle about forging axis
γ_S	J.m^{-2}	interfacial energy between S precipitates and matrix
η		Mg $\text{Zn}_{2(1-z)}\text{Cu}_z\text{Al}_z$ precipitates
λ	nm	wavelength of incident wave
λ_e, μ_e	MPa	Lamé's first and second parameters
μ	MPa	matrix shear modulus
ν	(-)	Poisson's ratio
2θ	degree	scattering angle
θ_{wet}	degree	wetting angle
ρ	kg.m^{-3}	density
ρ_d	m^{-2}	dislocation density
ρ_{NS}	m^{-3}	nucleation site density
ρ_{el}	(-)	relative resistance decrease
σ	MPa	flow stress
$\bar{\sigma}$	MPa	von Mises equivalent stress
σ_L, σ_{LT}	MPa	stress in the plates in the L and LT directions
σ_y	MPa	yield strength at 0% strength offset
$\sigma_0 = \sigma_a$	MPa	threshold stress in the absence of work hardening
σ^\perp	MPa	yield strength due to isotropic work hardening
$\sigma_{y0.2}$	MPa	yield strength at 0.2% strength offset
σ^{LF}	MPa	strengthening contribution due to lattice friction
σ^{GB}	MPa	strengthening contribution due to grain boundaries
σ^{SS}	MPa	strengthening contribution of solid solution
σ^{ppt}	MPa	strengthening contribution of precipitates
$\sigma_{y0.2}^{model}$	MPa	yield strength predicted by the yield strength model
σ_{hard}	MPa	amplitude of hardening
σ_{soft}	MPa	amplitude of softening
τ_{hard}	(s)	characteristic time of hardening
τ_{soft}	(s)	characteristic time of softening
τ_C	(s)	critical time required to form a constant amount of precipitates
τ_{i0}	MPa	shear strength contribution of element i at zero Kelvin
ω	degree	table rotation angle

NOTATION

Tensors

a	Scalar (0 th rank)
\underline{a}	Vector (1 st rank)
$\underline{\underline{a}}$	Tensor (2 nd rank)

Contracted product using Einstein's summation convention:

$x = \underline{a} \cdot \underline{b}$	$x = a_i b_i$
$\underline{x} = \underline{\underline{a}} \cdot \underline{b}$	$x_i = a_{ij} b_j$
$\underline{\underline{x}} = \underline{a} \cdot \underline{\underline{b}}$	$x_{ij} = a_{ik} b_{kj}$
$x = \underline{\underline{a}} : \underline{\underline{b}}$	$x = a_{ij} b_{ij}$

Others

$ a $	Absolute value
\bar{a}	Average value (except $\bar{\sigma}$)
$\delta_{ij} = \begin{cases} 1 & \text{if } i = j \\ 0 & \text{otherwise} \end{cases}$	Kronecker symbol
$\underline{\underline{I}}$	Unit tensor
$\text{Tr}(\underline{\underline{a}})$	Trace
$\underline{\nabla} a = \underline{\text{grad}}(a)$	Gradient using "Nabla" operator
∂_t	Partial temporal derivative
$\ln(a)$ with $a > 0$	Natural logarithm
$\log(a)$ with $a > 0$	Decimal logarithm
$\cot(a) = \frac{\cos(a)}{\sin(a)}$	Cotangent function
$\langle a \rangle = \begin{cases} a & \text{if } a > 0 \\ 0 & \text{otherwise} \end{cases}$	
$Er(a)$	Error $\pm Er(a)$ indicated by the error bars

GLOSSARY

Burgers vector: precise statement of the magnitude and direction of shear that a dislocation produces.

Coherency: relation of orientation with the matrix. Full: 3 directions, semi: crystal lattice continuity along one direction.

Cross-slip: transfer of glide of a screw dislocation from one slip plane to another.

Dispersoids: 10-100 nm, precipitate during homogenisation, inhibit recrystallisation, allow grain size control, influence quench-sensitivity.

Flow stress: yield strength plus hardening.

Homogenising: after casting, alloys are heated to remove any segregation, i.e. to obtain a homogenous composition throughout the alloy.

Intermetallic precipitates: > 1 μm in size, due to impurities during casting, impact on formability and toughness, can be broken during rolling.

Peak-aged state: corresponding to the maximum of yield strength reached during artificial ageing.

Solute loss: matrix depletion due to the formation of precipitates which pump solute elements.

Solutionising (solution heat treatment): before quenching, alloys are heated above the solvus but below the eutectic temperatures to dissolve alloying elements, i.e. to obtain a solid solution at equilibrium.

Stretching: processing step after quenching of plates performed to reduce residual stresses.

Supersaturated solid solution: contains more solute than its equilibrium level.

Nicolas Chobaut
 7 Chemin des Noutes
 1023 Crissier, Switzerland
 +41 (0) 78 774 86 47
 n.chobaut@laposte.net
 Born on 7th June 1987 in Nancy,
 France

PhD Student in materials science
Experimental, modelling and
teaching work at EPFL

Education and diploma

2010 – 2015 Lausanne, Switzerland	PhD thesis at Ecole Polytechnique Fédérale de Lausanne (EPFL) in the group of Prof. M. Rappaz and Prof./MER J.-M. Drezet.
2010 Germany, Saarbrücken Nancy, France	French-German double Diploma of Engineering in Materials Science.
2007 – 2010 Nancy, France	Ecole Européenne d'Ingénieurs en Génie des Matériaux (EEIGM)/European School of Materials Science and Engineering. 2009 – 2010: exchange year in Germany at University of Saarland (UdS) for a specialisation in non-destructive testing.
2005 – 2007 Nancy, France	Classe Préparatoire aux Grandes Ecoles (CPGE) /intensive two-year university course preparing for the entrance examinations to French “Grandes Écoles”, field: physics, Lycée Loritz.

Experience with industrials

2011-2014 Lausanne, Switzerland	Constellium and ABB 4 years project financed by these two industrials on the measurement and modelling of residual stress during quenching of thick heat treatable aluminium components in relation to their precipitation state. The developed model predicts residual stresses close to the measured ones and is useful for industry since a stress relief model has to use residual stress after quenching as its initial state.
2010 Bremen, Germany	Airbus One-year project in R&D on Extended – Non Destructive Testing to detect and assess heat degradation of CFRP used in new composite-based airplanes. A non-conventional method was found to detect heat damage which cannot be detected by conventional non-destructive methods.
Jan. 2009 – Feb. 2009 Saarbrücken, Germany	Halberg Guss Cast Iron production plant Two months internship on the thermal analysis of cast iron solidification to provide experimental data for simulations of casting.
Jul. 2008 – Aug. 2008 Birmingham, England	Ductile Iron heat treatment plant ADI Treatments One month internship on the optimisation of preheating in the austempering of ductile iron to improve productivity.

Expertise and skills

Thermo-mechanical testing	Gleeble machine, DLTMA, DCB (mode I) and SBS (shear) tests.
Non-destructive testing	Ultra-sounds, spectroscopy (FTIR), thermography, resistivity, neutron diffraction on large scale facilities.
Thermal analysis	Calorimetry, Quench Factor Analysis.
Computer-skills	Abaqus, Comsol Multiphysics, Matlab (inverse methods), Origin.
Languages	German: B2/C1 level (18 months in Germany). English: C1 level (2 months internship in UK). Spanish: good understanding (2 months as a volunteer to protect sea turtles at Playa las tortugas, Mexico). French: native.
Teaching	Bachelor courses at EPFL: Continuum mechanics, Modelling of materials and Introduction to materials science. Chess courses in primary schools, part-time employment within CEN program “Contrat Éducatif Nancéien”.

Awards and publications

Awards	Best poster “Residual stress in as-quenched thick heat-treatable aluminium components” at CCMX (Competence Centre for Materials Science and Technology) meeting in 2012. “ Stahl fliegt 2009 ”/“Steel flies”, German competition in lightweight construction of aircrafts, 3 rd place. Winner of the 36th International Chess Open of Barcelona U2000 in 2010.
Publications	N. Chobaut <i>et al.</i> , <i>Quench induced residual stress prediction in heat treatable 7xxx aluminium alloy thick plates using Gleeble interrupted quench-tests</i> . Submitted to JMPT. N. Chobaut <i>et al.</i> , <i>Quench induced stresses in AA2618 forgings for impellers: a multi-physics and multi-scale problem</i> . Accepted in JOM, TMS, 2015. N. Chobaut, D. Carron and J.M. Drezet, <i>Monitoring precipitation kinetics in heat treatable aluminium alloys using in-situ resistivity in Gleeble thermomechanical simulator</i> . Materials Science Forum, 2014. 794-796 : p. 921-925. N. Chobaut <i>et al.</i> , <i>Residual stress analysis in AA7449 as-quenched thick plates using neutrons and FE modelling</i> . Proceedings of ICAA13, Edited by: H. Weiland, A.D. Rollett, W.A. Cassada, TMS, 2012: p. 285–291.